CRANFIELD UNIVERSITY

MAXIME CARLIN

DESIGN, MANUFACTURE, AND HIGH TEMPERATURE BEHAVIOUR OF α-PHASE BONDCOAT FOR THERMAL BARRIER COATING

SCHOOL OF APPLIED SCIENCES

PHD THESIS

CRANFIELD UNIVERSITY

SCHOOL OF APPLIED SCIENCES

PHD THESIS

ACADEMIC YEAR 2007

MAXIME CARLIN

DESIGN, MANUFACTURE, AND HIGH TEMPERATURE BEHAVIOUR OF α-PHASE BONDCOAT FOR THERMAL BARRIER COATING

Supervisor: Professor J.R.Nicholls

This thesis is submitted in fulfilment of the requirements for the degree of Doctor of Philosophy

To my Grandfather, prof. Max Bausset,

Acknowledgments

I would like to acknowledge the people who have assisted my throughout my Ph.D. studies at Cranfield, and without whom this work would not have been possible.

At first, I would like to express all my gratitude to my academic supervisor, Prof. John Nicholls. For all the advices, scientific discussions, and support during the entire project. He was always present for encouraging me during the all project, with his well known enthusiasm. I am as well grateful to him for having allowed me to present this work in many conferences over the UK, Europe or the US. He is a lot more than a supervisor to me.

This work would not have been possible without the full support from Snecma, especially people of the Materials department as B.Saint-Ramond, F.Bourlier and J.Y.Guedou. I would like to acknowledge them for their trust and their interest in new manufacturing routes for high temperature coatings.

Many people from the staff at Cranfield contributed to this work, by technical advices and sharing their experience:

Mr Tim Pryor for his knowledge and enthusiasm. He was always here to help with heat treatment and high temperature facilities. Mr Andrew Dyer, Mrs Christine Kempston, Mr Colin Matthews and Mr Mattew Kershaw for sharing their knowledge and having a lot of patience during the time I spent carrying out analyses in their lab. Mr Tim Rose for his technical experience and his ability in fixing all kind of apparatus. Mr Tony Gray for his work on EB-PVD deposition. Dr Jeff Rao, Mr K.Lawson, for their scientific experience and Mr Potter, Mr Stallard for their technical support in coating manufacturing. And last but not least, I would like to acknowledge Mrs Sharon McGuire for her kindness.

I would like to acknowledge as well Regine Molins from the Ecole des Mines de Paris for welcoming me in their lab and carrying out the TEM analysis.

My years at Cranfield would not have been the same without all the friends I met there. French, British, Italians, Portuguese, German, Mexicans, or South African mates… :a very special thank to all of them!!

At last, I would like to thank my family. They were always here during good and difficult times, especially Lorène who, I am sure, enjoyed writing up as much as I did.

Abstract

In order to improve jet engine efficiency and performance, manufacturers have been trying over the last five decades to increase the working temperature of gas turbines. This was achieved by improving materials performance and component design. The latter technological breakthrough is known as Thermal Barrier Coating (TBC), which consists of applying a ceramic insulating layer on the internally cooled parts of the turbine. This technology is now applied in military and civil aircraft engines, and allows temperature improvement up to 150°C. However, understanding degradation mechanisms and improvement in manufacturing still remain important activities in turbine development.

This PhD thesis was founded by a turbine manufacturer, Snecma, with the aim of developing a new type of high temperature coating. The ceramic topcoat of TBC's is currently deposited on typical binary platinum aluminide diffusion coating or NiCoCrAlY overlay, called bondcoat, which stands at the component/ceramic interface. In this work, a new kind of intermetallic was studied, a ternary compound of the Ni-Al-Pt system, called α-phase, and a manufacturing route to deposit it as an overlay coating was developed.

The main result of this thesis is the achievement of a reliable, reproducible, and controlled manufacturing process of α-phase coatings. This process is based on sputtering multlilayers of pure metals, followed by the annealing of the layered coating. Produced coatings are thinner than commercial systems as they are richer in platinum (typically 5 µm instead of 70µm), hence the so-called name of "low mass bondcoat".

Such high temperature intermetallic coatings were characterised during this project (by XRD, SEM, EDS, FIB and TEM), as well as their isothermal and thermal cycled oxidation behaviour at high temperature. These systems were topped with a commercial ceramic layer in order to assess their potential as bondcoats for a full TBC system. Lifetimes are relatively promising, and failure modes, which will be described and discussed, are very specific compared to state of the art coatings. This specificity is proven to be due to the non conventional deposition route rather than to the new compound used as a bondcoat.

Table of Contents

List of Abbreviations

Chemical elements are abbreviated according to the periodic table (e.g. Fe for iron…)

BlzXX : XXth batch realised in the Balzers coater

BSE: Back-Scattered Electrons

CMAS: Calcium-Magnesium-Alumino-Silicate

CTE: Coefficient of Thermal Expansion

CVD: Chemical Vapout Deposition

DG: Detonation Gun

DSC: Differential Scanning Calorimetry

DTA: Differential Thermal Analysis

EB-PVD : Electron Beam Physical Vapour Deposition

EDS: Energy Dispersive Spectrometry

FIB: Focused Ion Beam

GDMS: Glow Discharge Mass Spectroscopy

HVOF: High Velocity Oxy-Fuel

LPPS: Low Pressure Plasma Spray

PS: Plasma Spray

PSLS: Photo Stimulated Luminescence Spectroscopy

PVD: Physical Vapour Deposition

SEM: Scanning Electron Microscope

SIMS: Secondary Ion Mass Spectrometry

TBC: Thermal Barrier Coating

TCP phases: Typically Closed Pack phases

TEM: Transmission Electron Microscope

TET: Turbine Entry Temperature

TGA: Thermo-Gravimetric Analysis

TGO: Thermally Grown Oxide

VPS: Vacuum Plasma Spray

XRD: X-Ray Diffraction

YSZ : Yttria Stabilized Zirconia

Introduction

Increasing the working temperature of gas turbines in jet engines has always been a major objective for industrials manufacturers as this is directly linked to the efficiency and the performance of the engine. Since the first engines after the Second World War, many improvements were achieved, such as the development of nickel based superalloy offering high temperature creep resistance. Improvement in components casting were also a key achievement, with simple internal air cooling first, followed by the development of always more complex internal cooling circuits and cooling holes on leading and trailing edges of high pressure nozzle guide vanes and blades. These resulted in a film of cooler air protecting the surface of the parts. Directional crystal and single crystal casting improved even more the high temperature creep resistance by dramatically reducing the metal plasticity by removing grain boundaries.

The latest achievement in this race for increasing the turbine entry temperature (TET) is the development of Thermal Barrier Coatings (TBC's). These have now been in service on military and civil aircrafts for over a decade. This breakthrough technology consists in applying a ceramic coating over the component metal, in order to improve even more the thermal gradient, therefore either improving the part lifetime as it works at lower temperature, or increasing efficiency and performance by increasing the TET.

TBC's are in fact a triplex system. First a bondcoat is deposited onto the superalloy based part. This bondcoat is high temperature protective coating i.e. it grows a protective oxide scale, called thermally grown oxide (TGO). Alumina is chosen for its slow growth rate, and very high stability at high temperature. State of the art bondcoat are either platinum aluminides (rather developed by GE, Rolls-Royce or Snecma) or NiCoCrAlY overlays (rather developed by Pratt and Whittney).

Platinum aluminide bondcoats are deposited as follow: an overlay of platinum (typically 7 to 10µm) is deposited, typically by electrodeposition. This layer is then diffused into the superalloy by a short high temperature heat treatment (typically 1h at 1100°C under vacuum). This platinum enriched surface is then aluminised by various process, all based on chemical vapour deposition mechanism: Aluminium is chemically transported to the surface of the part (by the mean of an gaseous aluminium halogenure); Aluminium is then adsorbed on the surface and diffuse into the substrate while reacting with the underlying structure to form an aluminide. Aluminides are intermetallic compounds: ordered, dense and thermodynamically stable. The resulting coating is a diffused multiphase platinum modified aluminide, which forms a stable alumina scale at high temperature by consuming the aluminium

reservoir reacting with the oxygen of the environment. NiCoCrAlY overlays are simply deposited onto the part by thermal spraying the relevant powder mix (this is generally followed by a heat treatment in order to reduce the coating porosity) or it can be deposited by electron beam physical vapour deposition (EB-PVD) from a rod of the relevant composition.

The bondcoat is topped by a thick ceramic layer (typically 100 to 250µm) aiming at thermal insulation of the part. This ceramic is in fact deposited onto the early TGO, hence the triplex system bondcoat/TGO/ceramic that makes a TBC.

State of the art TBC consist in depositing yttria stabilised zirconia (YSZ) by EB-PVD. This ceramic offers many advantages which are key points from the TBC design. First such a coating has a relatively low thermal conductivity (0.8 to 2.2 W/m.K depending on its microstructure), second it is crystallographically stable at high temperature thanks to the yttria addition, at last, it has a high coefficient of thermal expansion (CTE=$10x10^{-6}°K^{-1}$), which quite close from the superalloy CTE ($15.10^{-6}°K^{-1}$), hence drastically reducing the stress induced by thermal cycling the ceramic/metal system. At last, its properties are well established as YSZ is used in many other materials engineering applications.

Although EB-PVD deposition route is rather cost effective compared to others (thermal spraying for instance), it gives a very specific columnar microstructure with excellent strain and stress compliance as a very low surface roughness. This is a key property as the coated component faces high mechanical loading, and excellent aerodynamic of the shape is required.

Today's main issue about TBC is the understanding of its failure mechanism of this complex system. Lifetime of TBC's is affected by many parameters such as stress generated by thermal cycling of the triplex scale, or by the TGO growth, by the degradation of the bondcoat microstructure which occurs by interdiffusion mechanism with the substrate and by aluminium consumption to form the oxide scale, or by the ceramic degradation by high temperature reactions or erosion with gas particles.

Another major field of development of TBC's is manufacturing, which is the main concern of this work. The present study focuses on the manufacturing of a new type of bondcoat technology. First, a novel intermetallic phase of the (Ni-Pt-Al) ternary system has been investigated: the α-phase. This compound was only recently discovered and literature is very poor compared to other intermetallic from the (Ni-Pt-Al) system. This phase is a platinum rich ternary intermetallic centered on the 50Pt25Al25Ni stoichiometry. Bulk samples of this compound were manufactured and studied by energy dispersive spectrometry (EDS), Xray diffraction (XRD) and differential thermal calorimetry (DSC) in order to have a better knowledge of its physical properties.

In a second step, the manufacturing route of this intermetallic as a coating on superalloy was developed. This is based on some previous works carried out at Cranfield. The process is based on

stacking thin layers of pure metal followed by a soft heat treatment under protective atmosphere aimed at reacting the layers together to form the expected intermetallic compound. Improving the adherence, the reproducibility and the control of the process was the major objective of this work.

Once this process successively optimised, high temperature behaviour of these coatings were investigated. At first, bare bondcoat oxidation tests at 1100°C in air were performed. Analyses and understanding the ageing mechanism of these typical systems was carried out. Then, a commercial type ceramic topcoat was deposited by EB-PVD onto these bondcoats. These systems were thermal cycled at 1100°C in order to asses lifetime of these TBC's compared to commercial ones. Microstructures of the coatings after failure were as well analysed in order to propose a possible degradation mechanism.

The first chapter of this thesis is a literature review covering current state of the art of TBC systems, coating manufacturing processes, degradation modes, and current development in new type of high temperature protective coatings.

The second chapter will describe in detail the project that led to this study.

The third chapter describes the analysis tools and the special processes used during this study.

The fourth chapter focuses on the study of the intermetallic α-phase that was carried out prior to manufacture coatings. This part aims at a better knowledge of this material as literature is very poor, and at building a XRD data base that would allow a better quality control of the manufactured coatings.

The fifth chapter deals with understanding and optimising the specific deposition route used in this work. It explains encountered difficulties and how one overcomes those. It results in a "on shelf" manufacturing process to make controlled and reproducible α-phase coatings.

The sixth chapter focuses on the isothermal oxidation of these system, depending on the deposition parameters. Samples were exposed at 1100°C in air and analysed by scanning electron microscopy (SEM), EDS and transmission electron microscopy (TEM).

The seventh and last chapter deals with thermal cycling of bare bondcoats, rapidly shifted to the lifetime assessing of full TBC systems. Over 40 samples were cycled with various bondcoat deposition parameters. Microstructures of failed TBCs were analysed by SEM. These TBC systems have a very specific degradation mode, likely to be linked to the deposition route rather than to the alumina former intermetallic compound which both differs from conventional systems.

Chapter I

Literature review

The development of ever more efficient gas turbines has always been dependant of the results of research and development in the field of design and materials technology. Improved structural design and airfoil cooling technology, applied to higher strength-at- temperature alloys, cast by increasingly complex methods, and coated with steadily improved coating systems, have led to remarkably efficient turbine engine for aircraft propulsion and power generation.[1]

I.1 Introduction

Gas turbine systems are mainly used for power generation plant or for aeronautic propulsion, jet or helicopter engines. Their design is in four main stages: compressor, combustion, turbine and exhaust. The most thermo-mechanically solicited part is the turbine stage as it is positioned right after the combustion chambers were the compressed air from the intake is burnt with kerosene. The first stage of turbine blades face gas flows with temperatures up to 1700°C, while rotating at high speed, up to 30000rpm on the latest military engines. Engines manufacturers have always worked to increase the turbine entry temperature which would then increase the thermodynamic efficiency of the combustion hence reduce the global fuel consumption for a given power. Therefore the main driving forces for turbine materials engineers were about improving mechanical performance, especially creep resistance, for always higher temperature capable materials while reducing the density of the selected materials in order to reduce the total weight/thrust ratio of the engines (though this parameter is not as critical for power generation turbines). In the following paragraphs, the main improvement on turbine stage materials and processing will be briefly described.

The first engine turbines were manufactured with classical austenitic steel, but were quickly replaced by Nickel alloys, which offer really high temperature strength capabilities and a better oxidation resistance than iron. These capacities have been upgraded by the development of Ni based superalloys in the 60's, which can be used under high loads up to 80% of their melting point (in °K). This outstanding performance is due to the specific microstructure and the complex composition of these alloys, each element playing its own role. The microstructure of superalloys is usually described as a γ/γ' composite: γ matrix is a face centred cubic (FCC) nickel based phase, which can contain in solid solution Co, Mo, Cr and W; γ' is a Ni_3Al intermetallic compound (detailed later in this chapter), which forms coherent precipitates with the matrix, reducing the movement of dislocation during high temperature creep.

The next stage in the development of turbine blade was the use of an internal cooling system from the late 60's. Hollowed blade were made possible thanks to the improvement of the superalloys mechanical behaviour, a "cold" air flux (around 700°C) taken from the compressor stage is injected through the inner side of the blade and flows along the trailing edge of the blade through rows of cooling holes. Another main improvement of turbine blade material was given by enhanced casting

methods. Directional solidification in the 70's and monocrystal casting in the early 80's reduced the negative effect of grain boundaries of the blade materials, improving once again high temperature creep resistance. The current improvements on the actual blade material deal mainly with the composition, new generation superalloys now content rhenium or ruthenium, and manufacturers keep on working on better control and efficiency of the single crystal casting process.

The main developments on turbine stage components are nowadays more and more focused on complex coating design to provide environmental and thermal protection.

I.2 High temperature protective environmental coatings

High temperature components are usually made from materials selected for their high temperature mechanical properties and their manufacturability. There is therefore a need for optimising the surface, and subsequent interfaces so generated of the parts depending on the various threats it will have to face. For metallic compounds, the main source of degradation is chemical as reactions kinetics are exponentially increased with temperature: reaction with the oxygen from the environment (oxidation), reaction with the mineral salts from the environment in combination with oxygen (corrosion), interdiffusion mechanisms within the microstructure of the material (phase transformation, precipitation, nucleation)…These transformations will generate mechanical issues with stress fields growing at the interface of these reactions, which are likely to lead to the failure of the component.

In order to increase the life time of high temperature components, environmental protective coatings were developed. Such protective coatings do not function as inert barrier: they provide protection by interacting with oxygen to form a dense oxide scale that inhibits the inward diffusion of damaging species into the substrate[2].The first part of this literature review chapter will describe various coating manufacturing processes, as well as the compounds commonly used for high temperature protection. Thermal Barrier Coating systems will then be presented with their key features and issues. Finally some degradation mechanisms that apply to environmental coatings and TBC's will be reviewed. At last, the final part of this chapter describes some of the new developments in high temperature protection of metals.

I.2.1 Deposition process of protective coatings

As explained, high temperature coatings were developed to protect materials which were not primilarly selected for their oxidation resistance. These coatings are extensively used in high temperature parts of power generation units or gas turbine for aircraft propulsion.

The principle of an environmental protective coating is relatively simple: the protective material deposited onto the part by various methods must lead to the formation of a more stable oxide than the substrate when it is in contact with the working environment of the component. The main systems used by the manufacturers are chromia and/or silica formers, and alumina formers for higher temperatures.

This coating will act as a sacrificial layer, oxidizing instead of the substrate, allowing the actual part to keep its integrity with time.

Some key performance parameters may strongly differ depending on the deposition process:

- ✓ The resulting microstructure of the coating
- ✓ The deposition rate
- ✓ The homogeneity in thickness/line of sight deposition issues
- ✓ Temperature of the substrate during deposition
- ✓ The surface state of the substrate needed (roughness, cleanliness…)
- ✓ The type of material which can be deposited

The deposition processes can be divided into two main categories: diffusion coating and overlay coatings. The principle of diffusion coating is to penetrate the substrate and to modify the chemistry of the first tens of microns of the material in order to change its oxidation behaviour. These processes lead to very adherent systems, but their performance is strongly driven by the compatibility with the substrate. Alternatively, overlay systems are not supposed to interact with substrate, providing a sacrificial top layer: those give a better compositional flexibility than the previous diffusion coating systems. [3-5]

I.2.1.1 Chemical Vapour Deposition

Chemical vapour deposition (CVD) is widely used in the materials engineering industry. For the concern of high temperature environmental coating, this process is applied for the manufacturing of diffusion coatings (detailed in the next part of this chapter).

The general principle of CVD involves that the material to be deposited be in the gaseous state, called the precursor. The precursor flows over the substrate, the element to be deposited is released form the gas state by a chemical reaction, usually catalysed by the surface, growing a film on the part to be coated. The reacted gas is then ejected from the deposition chamber. The precursor is usually a hydride, a halide or an organometallic; the main considerations concerning the precursor are its volatility (for process flow and security issues), and its reactivity (strength of the bond, stability of any compound formed) [6-9].

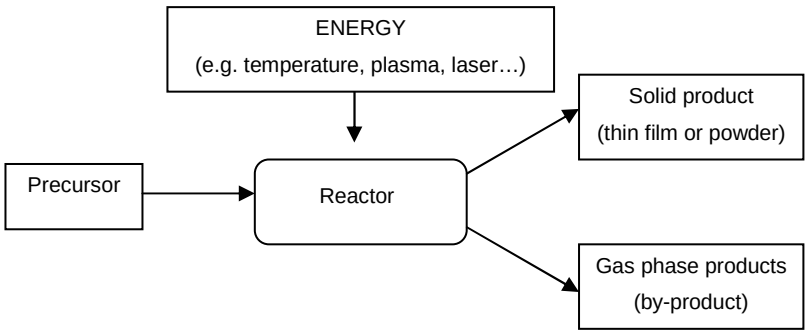

Figure 1 Schematic of CVD principle

The main steps of CVD are:

- ✓ *Vaporization* and *Transport* of Precursor Molecules into the Reactor
- ✓ *Diffusion* of Precursor Molecules to the Surface
- ✓ *Adsorption* of Precursor Molecules on the Surface
- ✓ *Decomposition* of Precursor Molecules on the Surface and Incorporation into a Solid Films
- ✓ *Recombination* of Molecular Byproducts and *Desorption* into the Gas Phase

The advantages of CVD process are:

- ✓ Not a line of sight process: complex 3D shaped parts can be coated
- ✓ Many components can be coated per batch
- ✓ Good adhesion to the substrate thanks to chemical bonding

Limitations:

- ✓ Production of chemical waste which may have environmental issues
- ✓ The substrate needs to be heated (more or less depending on the presence of an alternative energy source)
- ✓ Medium deposition rates

I.2.1.2 Physical Vapour Deposition (PVD)

Physical vapour deposition (PVD) is a very versatile process: it enables the deposition of virtually any inorganic materials (metals, alloys, intermetallics, ceramics) as well as some polymers. It is used widely; in microelectronic, optic or tooling industries or even for decorative applications. Deposition rates vary from 10^{-3} up to 75µm/min for the latest electron beam evaporated films (EB-PVD). The first

evaporated thin films were probably done by Faraday in 1857, and Joule heating evaporation was discovered at the end of the 19th century[10].

The PVD process follows three steps which can be independently controlled, giving a great degree of flexibility:

- ✓ Synthesis of the material to be deposited: transition from a condensed phase(usually called a target in sputtering or a source in evaporation; is often a solid, but can sometimes be liquid) to the vapour phase
- ✓ Transport of the vapour between the source and the substrate
- ✓ Condensation of vapours followed by film nucleation and growth.

There are three types of PVD process: evaporation, sputtering and ion plating. Evaporation by EB-PVD will be described in the next part of this chapter. There are several advantages of PVD processes over CVD or thermal spraying:

- ✓ Versatility in composition of the deposit.
- ✓ The ability to produce unusual microstructures and crystallographic properties (e.g. amorphous, texture…).
- ✓ The substrate temperature can be varied over a very wide range.
- ✓ Very high purity of deposit.
- ✓ Ability to control thickness down to the nm level.
- ✓ Surface finish can be equal to that of the substrate.
- ✓ No chemical waste is produced, unlike CVD methods.

Limitations are:

- ✓ Line of sight process: impossible to coat inner parts of a complex shaped substrate and shadowing effects are a significant factor during deposition.
- ✓ Relatively low deposition rates for sputtering PVD (1µm/min is quoted as a maximum).
- ✓ Poor ratio between material consumed from target and quantity deposited onto the substrate.
- ✓ Vacuum systems with high degree of sophistication are required, hence a higher initial cost.
- ✓ Stress can be induced in the coating during the growth of the film, this may be either tensile or compressive.

I.2.1.2.1 Evaporation

Evaporation PVD relies on the saturating vapour pressure of materials: when heated, the partial pressure of the material increases, hence creating the atomic vapour. The material can be deposited from solid state (sublimation) or from liquid. The material to be deposited is placed in a crucible which is usually heated by Joule effect. The crucible is either metallic (usually Mo or W), or a metal coated with alumina. The deposition rate may be controlled by the change of resonance frequency of a quartz disc (standing next to the substrate) due to its mass gain. This entire process is set in a high vacuum chamber in order to prevent oxidation of the parts during processing.[3;10;11]

I.2.1.2.2 Sputtering

Sputtering deposition results from the ejection of atoms from a condensed matter target, as a result of the impact of other particles onto the target. The impacting particles are usually heavy ions coming from a plasma sustained above the surface of the target or from an ion gun focused on the target. The plasma is triggered by applying a negative bias on the target, while the overall deposition chamber is earthed. The gas to be ionised is usually heavy and inert, Argon is typically used for such applications. A plasma contains roughly the same number of ions and electrons, having therefore an average neutral charge at the macroscale. The plasma is sustained by a constant ionisation of Ar atoms caused by inelastic collision with electrons.[12-15]

Sputtering is a purely mechanical process: the Ar^+ ions from the plasma are accelerated towards the target by the bias applied to the target, impacting its surface, leading to momentum exchange with the target atoms. Various interactions can be listed:

- ✓ Ejection of an atom from the target: this is the actual sputtering process.
- ✓ Implantation of the bombarding ion into the target material lattice known as ion implantation.
- ✓ Reflection of the ion, with or without neutralisation, with loss of kinetic energy.
- ✓ Emission of a secondary electron, extracted from an atomic orbital of a surface atom.
- ✓ Cascade effect: impact energy spreads into the first few atomic layers of the material lattice, which could lead to the ejection of another atom, than the impacted one.

The sputtering process is quantified in terms of the sputtering yield, defined as the number of target atoms ejected per incident particle. The yield depends on the target species, the target nature, the available energy, and the angle of incidence of the bombarding species.

Direct current (DC) glow discharge is the most widely used sputtering configuration: a negative DC bias is applied to the target (cathode), while the chamber is earthed. The plasma is triggered and

sustained by the DC bias itself. The requirement for sustaining such a discharge is that each primary electron must produce sufficient ions to release one further electron from the cathode. The current crossing the target is therefore directly related to the number of impacts that occur, hence the actual deposition rate.

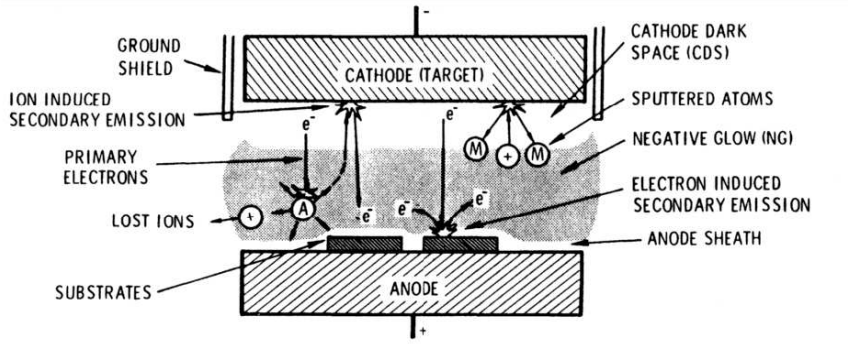

Figure 2 Planar diode DC sputtering[12]

DC sputtering implies the target has to be a good electricity conductor. Radio frequency sputtering (RF) is used when the material to be deposited is either insulative (some ceramics or polymers) or dielectric. In order to prevent charge build up on the surface of the biased target, the polarity of the cathode/diode is changed at high frequency (13.56 MHz or 27 MHz which are the only two allowed frequencies for both medical and scientific applications). When the bias is inverted, positive charges are removed from the surface of the target by the impacting electrons: no sputtering occurs, as the mass hence the energy of impacting electron is not sufficient. Moreover, at these frequencies, the ions are motionless because of their mass. Therefore, under equilibrium conditions, the RF signal is assymmetrical: it has a DC component that is negative.

Pulsed DC is sometimes used as well, as it gives more parameters to control the deposition process (power, frequency, and asymmetry of the signal).

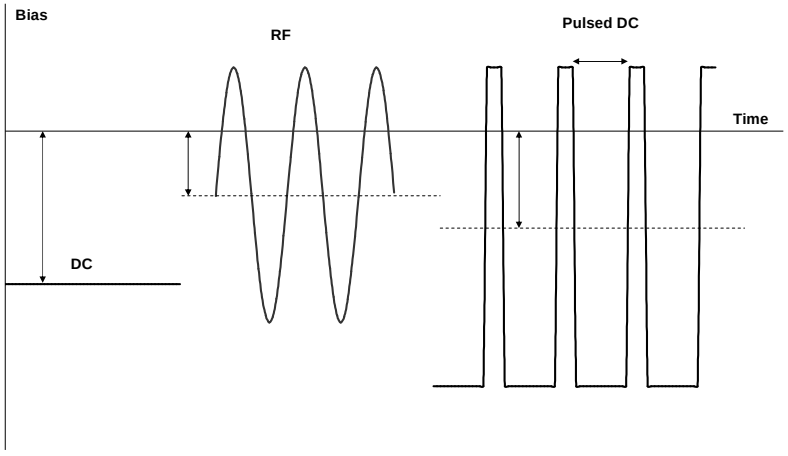

Figure 3 Direct current (DC) Radio frequency (RF) and pulsed DC bias profiles

In order to enhance the deposition rate, a magnetic field is often incorporated into the target electrode: it confines the charged particles to follow a predfined track along the B field lines, hence improving the impacts per surface. More than improving the deposition rate, this device permits deposition at lower working pressures in the chamber. However, because the erosion is not uniform over the target surface, it leads to an erosion track, meaning that a large part of the target materials will stay unused, when the total thickness of the target is crossed. The target is usually cooled by a water flow at the backside of the target material or its copper backing plate, in order to prevent local overheating. Such devices are called Magnetrons, and are nowadays systematically used except for special cases, for instance when the sputtered material is very precious and that waste due to the erosion ring would be costly.

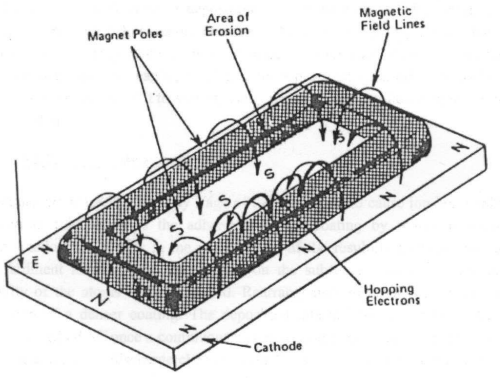

Figure 4 Magnets disposal in a rectangular magnetron[13]

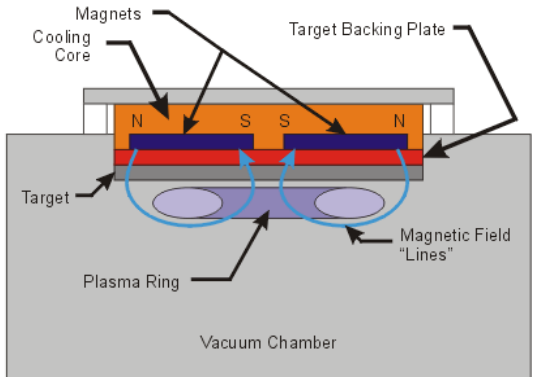

Figure 5 Cross section of a sputtering cathode with magnetron

Improvement in sputtering technology is coming from many industries, especially the optical and microelectronic industries, leading to new systems, reduced operating cost, especially regarding to the material loss due to the erosion ring[16].

Alloys can be as well sputtered; however the composition of the target will initially differ from the expected composition of the coating: the relative yield of the alloying element has to be taken into account. But after some time the system will stabilise, with sputter yields producing the expected target composition.

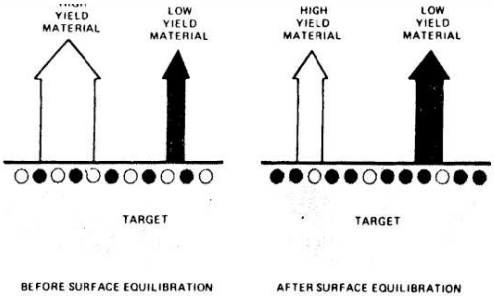

Figure 6 Sputtering of alloys[12]

I.2.1.2.3 Structure of PVD films

As explained before, for PVD films the deposited material arrives on the substrate surface in an atomic form. The atom fist diffuses on the surface with a motion determined by its binding energy with the substrate and this is influenced by the nature of the surface as well as the temperature of the substrate.

The film builds up with a typical nucleation/growth mechanism ruled by the reduction of the surface energy of the primary formed islands. Those grow and coalesce a continuous film is formed. On single crystal substrate, the growth and coalescence can lead to a single crystal film. This phenomenon, called epitaxy, occurs however only above a specific temperature.

The structure of the film therefore depends on the surface energy of the substrate, hence its temperature; this was modelled by Mochvan and Demchishin in 1969[17], and called the Structure Zone Model. Depending on the T/T_m ratio (T is the substrate temperature and T_m is the coating material melting point in °K).

- ✓ Zone 1:$T/T_m<0.3$: tapered crystallites, usually following a crystallographic orientation with the denser closed pack planes at the edges of the domes
- ✓ Zone2: $0.3<T_m<0.45$: typical columnar grains with a smooth surface
- ✓ Zone3: $T/T_m>0.45$: equiaxed grains with a smooth surface can form

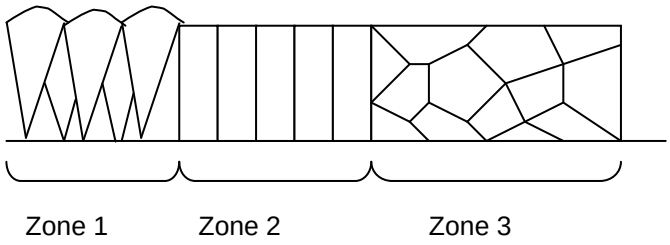

Figure 7 Mochvan and Demchishin structure zone model[17]

This model was later generalised by Thornton in 1973, to account for the structures expected to be seen in sputtering. This he achieved by adding the effect of the Argon pressure on the film microstructure[18].

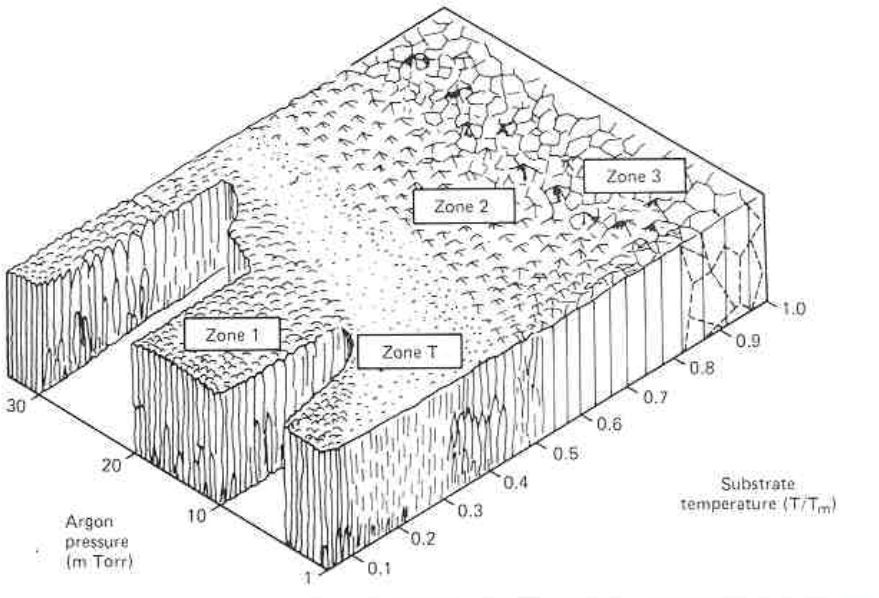

Figure 8 Thornton's Model (1973)[18]

Zone 1 corresponds to a state where atoms do not have enough energy to diffuse properly across the substrate surface, leading to localised shadowing of islands with each other. It occurs for low T/T_m ratio and high Ar pressures. It results in a columnar structure with a crystal diameter increasing with thickness, and a rounded tops. Crystal interfaces are quite weak and show some porosity. The diameter of crystal increases with T/T_m, and the surface roughness of the coating will follow the surface state of the substrate due to preferential nucleation on local defects. Usually these films are under tensile stress.

Zone T corresponds to densely packed fibrous grains, which would correspond to a Zone 1 type on a perfectly smooth substrate. Zone T films exhibit a high compressive internal stress.

Zone 2 corresponds to the thermodynamic state where surface diffusion of atoms is controlling the growth. It corresponds to purely columnar grains with dense interfaces.

Zone 3 corresponds to a high T/T_m ratio: here the bulk diffusion of the coating species controls the microstructure: grains maybe equiaxed as it corresponds to a minimisation of the surface energy of the crystallites, if stress is sufficient to initiate recrystallisation.

I.2.1.3 Thermal spraying

Thermal spraying is a general term used for coating produced from molten or semi-molten powder, accelerated at high speed onto a substrate. The coating is made of layers of overlapping splats (flattened droplets): unlike PVD, the transported particle is not at atomic scale. There are many type of thermal spraying, depending on the way the droplets are melted and accelerated, amongst them the three most common are: Plasma spray (PS), detonation gun (DG) and high velocity oxy fuel (HVOF)[19].

PS is the most widely used process for thermal spraying aerospace quality coating. The plasma torch of PS consists of a tungsten cathode and a copper anode creating an arc, sustained as a plasma by flowing an inert gas through the system (usually argon). The anode serves as a constricting nozzle. The power varies from 5 to 120 kW: the temperature of the core of the plasma may exceed 30,000°C, and the molten droplet velocity can vary from 100m/s up to almost supersonic. The powder used is usually between 40 and 150μm diameter.

The coatings produced by thermal spray are more porous and rough compared to CVD or PVD films, and some oxidation is likely to occur during the process. However, low pressure plasma spray (LPPS) and vacuum plasma spray (VPS), which are carried out in reduced pressure, reduce the formation of oxide during spraying.

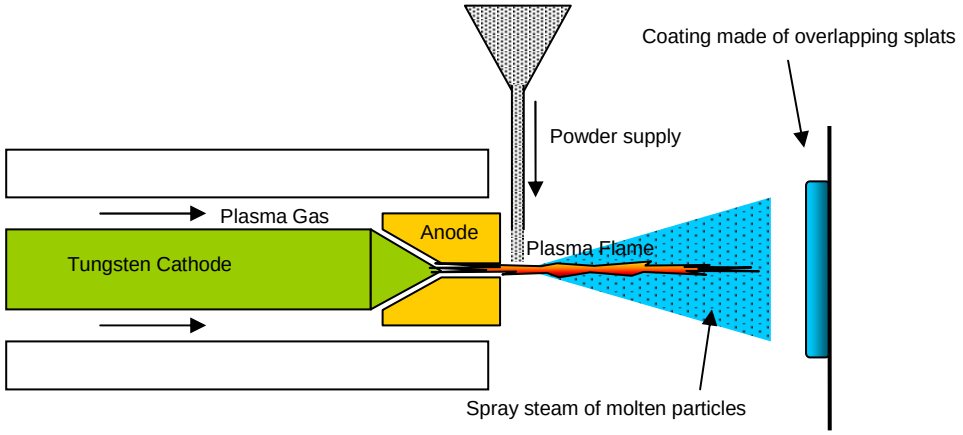

Figure 9 Schematic of a plasma torch used in APS

Kinetic and thermal energy can be provided to the powder by other means than a plasma: DG and HVOF use fuel (usually acetylene for the DG) to produce high velocity combustion flames. The DG is not a continuous process: the pressure of fuel builds of in the barrel and then is ignited between 4 to 10 times per second, whereas HVOF consists in a continuous flow of burnt fuel. These two processes give a greater velocity to the powder than PS, between 500 and 700 m/s.[20;21]

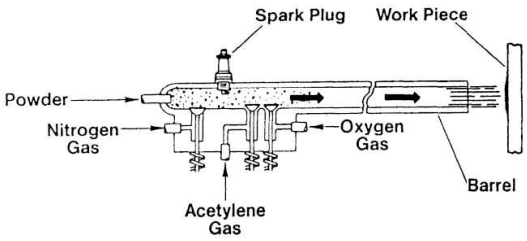

Figure 10 Schematic of a detonation gun

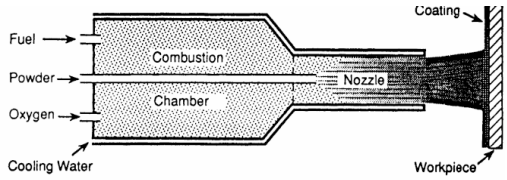

Figure 11 Schematic of a HVOF

The main advantages of thermal spraying are:

- ✓ Versatility of the composition of the film.
- ✓ Very high deposition rates.
- ✓ Possibility to grade the coating with various powder mixes during the same deposition process.
- ✓ Ability to coat very large components.
- ✓ Less expensive than EB-PVD (for TBC application for instance).
- ✓ The typical porous structure of the coating lowers the thermal conductivity of the film.

The limitations of these processes are:

- ✓ Line of sight process (no possibility to coat complex 3D shaped component, shadowing issues)
- ✓ Inability to deposit thin films (30 μm is a minimum)
- ✓ Poor surface finish which usually requires some post machining
- ✓ Poor erosion resistance due to the in plane micro-cracks
- ✓ Presence of oxidised particles within the coating, non homogeneity of the splats due to temperature/speed difference between each powder grain
- ✓ For turbine components, blades cooling holes can be obstructed

I.2.1.4 Coating from aqueous solutions

Coatings produced from aqueous solution are used as well, widely, in the aeronautic industry. The most known are electrodeposition, anodising, and electroless deposition[22]. These processes are cost effective but are less versatile, regarding the type of material which can be treated or deposited. Moreover, their use may raise environmental issues due to the use of large quantity of solvent and chemicals.

The general principle of electrodeposition is to load the component to be coated into an ionic solution as a cathode, with the metal to be deposited as the anode. When a DC or a RF power supply is applied to the electrode/electrolyte system, the metal ions will segregate to the cathode and re-precipitate forming a continuous film. This method is fast and very cost effective, but can only be applied to a limited range of materials material: the component must be electrically conducting and the coating must be metallic, and having a free enthalpy which allows the reduction of the metal oxide to a metal ion in an acqueous solution(Aluminium for instance can not be electroplated under normal condition of temperature but can be deposited from molten salts). Electroplating is not a line of sight process enabling to coat complex shapes, and leads to films which are smoother than the substrate. However if some parts do not need to be coated, they need to be insulated from the electrolyte, usually by an organic wax. The plating of platinum when fabricating platinum modified coating is typically deposited by this process.

Anodising is used when the metal to be protected forms a stable oxide layer, typically aluminium or magnesium alloys. An oxide scale is artificially grown by applying a positive bias to the part to be coated in a relevant ionic oxygen rich electrolyte. Anodising is usually used to improving the wear resistance of the component. Recently, some research is currently carried out to make thicker coatings,

by applying intense bias and creating some arcing. This improves the mechanical properties of the scale, and generates structures which could be used as a specific TBC. The commercial name of such "plasma electrolytic oxide" coatings is Keronite[23].

Electroless deposition differs from electroplating as there is no current required to grow the film: the metallic coating is created by chemical reduction of ions within the aqueous solution. Usually the chemical reaction is made possible due to a self catalysing mechanism, which is self sustained by the grown film. Phosphorous, boron or hydrazine may be used to autocatalyse the reaction.

I.2.1.5 Summary

The described deposition techniques can be summarised in the following chart.

	evaporation	*Ion plating*	*Sputtering*	*Chemical vapour deposition*	*Electro-Deposition*	*Thermal spraying*
Mechanism of production of deposition species	thermal energy	Thermal energy	momentum transfer	chemical reaction	deposition from solution	from flames or plasma
deposition rate	can be very high (up to 75µm/min)	can be very high (up to 25µm/min)	low except for pure metals (e.g. Cu 1µm/min)	moderate (0.2 to 250nm/min)	low to high	very high
depositing specie	atoms and ions	atoms and ions	atoms and ions	atoms	ions	droplets
throwing power for:						
a. complex shaped object	poor line of sight coverage except by gas scattering	good but nonuniform thickness distributions	good but nonuniform thickness distribution	good	good	no
b. into small blind holes	poor	poor	poor	limited	limited	very limited
metal deposition	Yes	Yes	Yes	Yes	Yes, limited	Yes
alloy deposition	Yes	Yes	Yes	Yes	Quite limited	Yes
refractiry compound deposition	Yes	Yes	Yes	Yes	limited	Yes
energy of deposit species	low	can be high (1-100eV)	can be high (1-100eV)	can be high with plasma aided CVD	can be high	can be high
bombardment of substrate/deposit by inert gas ions	0.1 to 0.5KeV	Yes	depending on geometry	possible	no	Yes
substrate heating (by external means)	Yes normally	Yes or no	not generally	Yes	no	normally not
growth interface perturbation	Not normally	Yes	Yes	Yes by rubbing	no	No

Figure 12 Summary of deposition techniques[11]

I.2.2 Types of coating used for high temperature protection

I.2.2.1 Diffusion coatings

I.2.2.1.1 Simple aluminides

For high temperature coating manufacturing, two routes are usually followed in order to aluminise the part: in pack cementation and over pack CVD.

Pack cementation has been used since the beginning of protective coating development in the 1950's[24]. It is still nowadays extensively used in the market for the protection of turbine blades, probably up to 80% of the components coated[5]. This process consists in immersing the part to be coated into a mixture of powder at high temperature (between 650°C and 1100°C):

- ✓ 2-5% activator, usually a halide
- ✓ up to 25% of donor, which is the actual metal to be deposited (i.e. aluminium)
- ✓ Balanced with an inert filler which prevents the pack from sintering and allows the carrier gas to flow through the pack (usually alumina)

The carrier gas is usually Argon, in order to prevent early oxidation of the donor and substrate. Pack cementation is in fact a CVD process, the reactive gas being synthesised in situ through the pack[25]:

$$6NaCl_{(g)} + 3Al_{(l)} = \left(AlCl_3 + AlCl_2 + AlCl\right)_{(g)} + 6Na_{(g)}$$

The volatile aluminium halides are reduced on the substrate surface. Interdiffusion between the depositing aluminium and the substrate alloy results in the formation of the intermetallic coating. The deposition rate and morphology of the coating depends on the pack activity, process time and temperature.

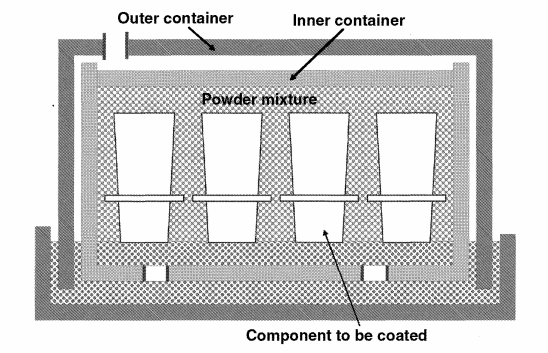

Figure 13 Schematic of the layout of pack cementation aluminising[25]

High activity coatings are obtained at moderate temperature (<950°C, LTHA: Low Temperature High Activity): the process is controlled by the inward diffusion of aluminium, leading to the formation

of Ni_2Al_3 and β-NiAl. Usually a post heat treatment is carried out to convert Ni_2Al_3 into β-NiAl as it is a brittle intermetallic. The final morphology is characterised by:

- ✓ An outer layer of β-NiAl with some precipitates from elements of the substrate (carbides and α-Cr) as well as impurities from the cement
- ✓ A zone constituted of cleaner equiaxed β-NiAl above the original surface of the substrate
- ✓ An interdiffusion zone constituted of nickel-depleted alloy.

Low activity coatings are obtained at higher temperatures, up to 1100°C (HTLA: High Temperature Low Activity): the process is controlled by the outward diffusion of nickel into the depositing aluminium, the original surface of the substrate remains in the middle of the β-NiAl layer. No post heat treatment is required for this type of aluminizing. The final morphology is characterised by:

- ✓ A clean layer of β-NiAl with some impurities from the cement
- ✓ An internal zone formed from the underlying superalloy depleted in nickel and rich in precipitation of elements which are not soluble in β-NiAl: carbides, α-Cr, and topologically close packed phases (TCP: σ, η)

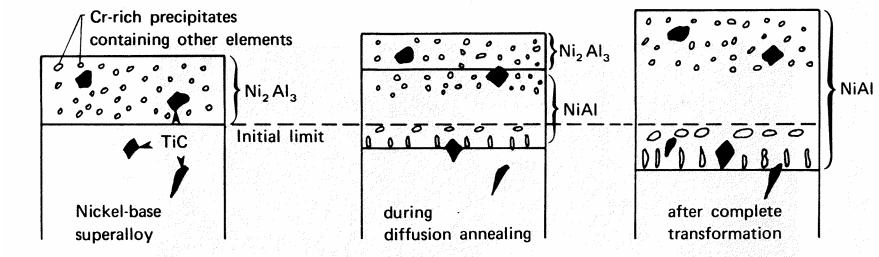

Figure 14 High activity aluminising followed by high temperature annealing[26]

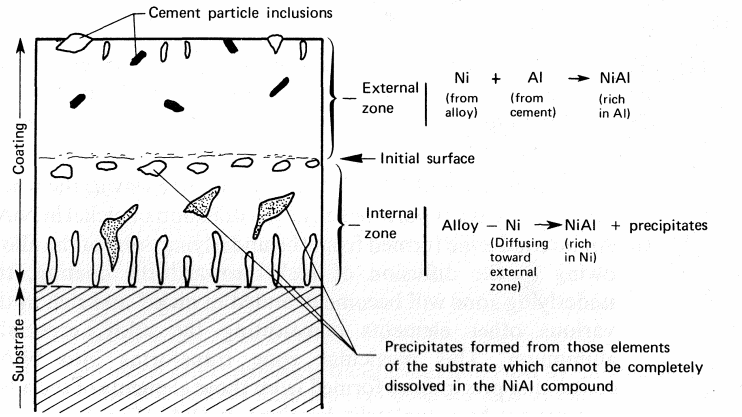

Figure 15 Schematic of a low activity NiAl coating[26]

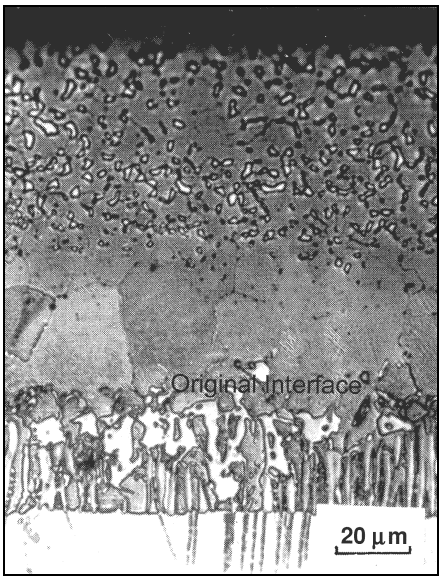

Figure 16 Micrograph of a high activity simple aluminide after heat treatment[27]

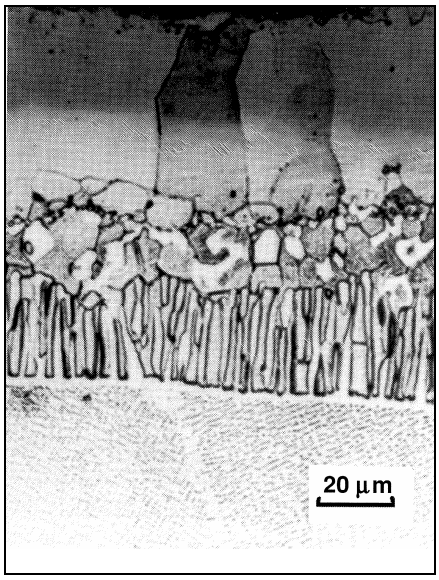

Figure 17 Micrograph of a low activity simple aluminide[27]

Two other processes were developed later for aluminising. Over pack aluminising is similar to pack cementation except for the active mix which is not in direct contact with the part to be coated, which is the process used at SNECMA. The second one is called out of pack CVD or vapour aluminizing[28]: the vapour phase is activated before entering the retort and flowing onto and around the parts. This prevents inclusion of impurities from the pack, and allows to coat uniformly inside the internal cooling system of the blade[9] as well as outside.

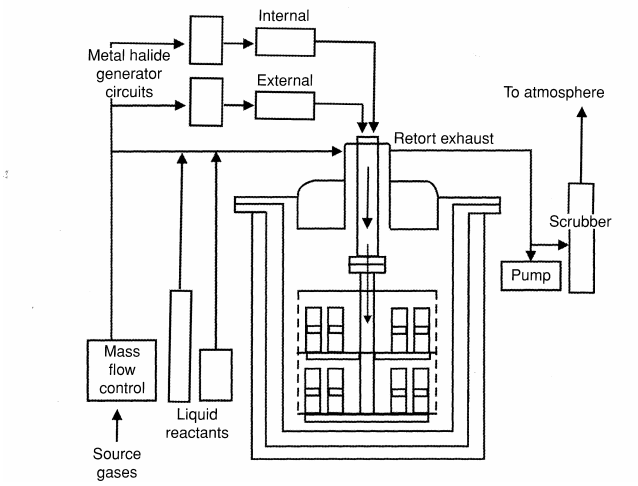

Figure 18 Schematic diagram of a CVD aluminising process[25]

Typically aluminide coatings contain in excess of 30wt% of aluminium and are deposited with thickness between 30 and 70µm[5].

I.2.2.1.2 Modified aluminides

Aluminide diffusion coating performance was enhanced by adding other elements such as chromium, silicon, reactive elements, or precious metals[29].

Chromium (and eventually Silicon) modifications were at first applied to improve corrosion resistance of those coatings over wider range of temperature, especially at lower temperature in more chemically aggressive environment such as land based gas turbines[1;30;31]. It is usually codeposited with aluminium in a pack cementation or vapour phase process.

Platinum modified aluminide was the main breakthrough in oxidation resistant coatings, improving drastically the adherence of the oxide, therefore improving the cyclic oxidation lifetime of the turbines blades. These systems were patented and commercially produced in the early 70's by Lehnert and Meinhardt[32] under the name of LDC-2. The principle of platinum modified coating manufacture is to coat the part with a single layer of Pt, typically between 6 and 10µm by electrodeposition, followed by a diffusion aluminising treatment. Depending on the process parameters, the platinum modified aluminide coatings can show several microstructures[9;33-35]:

- ✓ LDC-2 type of coating: deposition of platinum, followed by a pack low activity aluminising (around 1050°C). It results in a bi-layered coating with a continuous top layer of $PtAl_2$, above a thicker β-(Ni,Pt)Al layer, followed by an interdiffusion zone containing β-(Ni,Pt)Al with precipitates of σ-CoCr intermetallics.
- ✓ RT 22 type of coating: deposition of platinum followed by a heat treatment (over 1000°C) in order to diffuse Pt inward into solid solution within the superalloy γ-Ni matrix. Intermediate activity aluminising, controlled by the inward diffusion of Al is then carried out, followed by a homogenisation treatment. The resulting microstructure is similar to LDC-2 excepting the $PtAl_2$ intermetallic compound is dispersed instead of being continuous.
- ✓ CN91 type of coating: deposition of platinum followed as well by a heat treatment to diffuse platinum. Aluminising is carried out by a vapour phase process instead of a pack cementation, with an outward diffusion of the Ni: it results in a single phase β-(Ni,Pt)Al layer over the interdiffusion zone.

RT and CN are the commercial prefix for Chromalloy coatings. The protective coatings currently used by Snecma are of the CN91 type, produced by Snecma Service or Chromalloy UK.

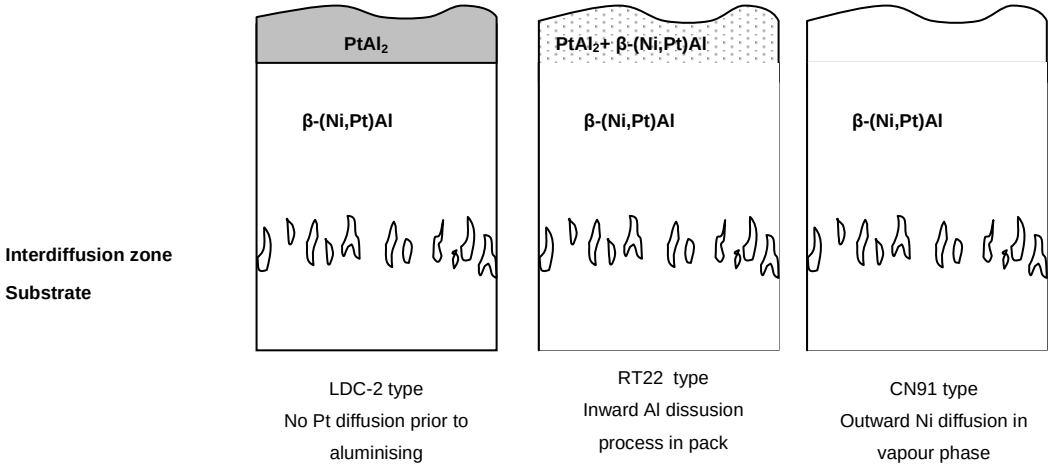

Figure 19 Main types of Pt modified aluminide coatings

Krishna et al.[36] reviewed the effect of varying the thickness of platinum (from 1 to 15µm by electroplating) deposited prior to high activity aluminising and found that the resulting microstructure depends on the original thickness: for less than 1µm Pt is completely dissolved in solid solution in NiAl, for more than 10µm, a continuous layer of $PtAl_2$ is found on the surface. The overall cyclic oxidation behaviour improves when increasing the platinum content to a minimum of 6µm of precious metal[37].

The effect of Pt diffusion prior to aluminising is questioned in a study published in 2004 by a French team[38], working on the vapour phase process used by Snecma, on a Snecma commercial superalloy AM1. It is shown that the thickness of electrodeposited platinum and the choice of an Al poor donor for the CVD reaction are critical to lead to a $PtAl_2$ free coating.

I.2.2.2 Overlays

Diffusion coatings, by the nature of their formation, imply a strong interdependence on substrate composition in determining both their corrosion resistance and mechanical properties; hence, the possibility of depositing a more nearly ideal coating, with a good balance between oxidation, corrosion and ductility, has stimulated much research interest since the early 70's[39]. These coatings have been deposited by EB-PVD or thermal spray (usually PS and HVOF, but more recently DG coatings were manufactured[20]) processes. They are usually referred as MCrAlY's:

- ✓ M stands for Ni and/or Co:it is the balance of these coating, reducing the interdiffusion with the Ni/Co based substrate, and reducing the ductile to brittle transition temperature (DBTT).

- ✓ Chromium is added for hot corrosion resistance especially type II (650-800°C) by the formation of a stable layer of chromium oxide.
- ✓ Aluminium protects at higher temperature, as alumina layer gets denser and chromia volatilizes above 1000°C
- ✓ Yttrium is the most used of the reactive element family. The beneficial effect of reactive elements are to improve the local adherence of alumina, and to reduce the oxidation rate (see details later in this chapter)

The usual microstructure of an MCrAlY consists of β-NiAl and α-Cr grains dispersed in a γ/γ' matrix. The main advantage of MCrAlY is the versatility of the composition, which allows tuning the oxidation/corrosion properties, as well as the DBTT value[29].

The better high temperature oxidation behaviour of NiCrAlY over NiCoCrAlY has been experimentally proven[40]. Corrosion/oxidation resistance of coatings is often compared with the following chart:

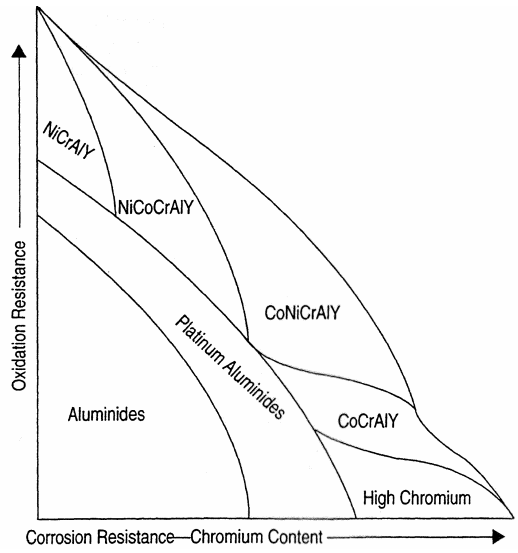

Figure 20 Comparison of oxidation and corrosion resistance of high temperature standards coatings[29]

I.2.3 Intermetallics (nickel and platinum aluminides)

This paragraph gives details on the intermetallic compounds regularly discussed for nickel base high temperature protection

I.2.3.1 Nickel aluminides

The thermodynamically stable nickel aluminide intermetallics can be listed thanks to the binary diagram of Nickel and Aluminium. One can see five major intermetallic compounds are present: γ'-Ni_3Al, Ni_5Al_3, β-NiAl, δ-Ni_2Al_3, and $NiAl_3$.

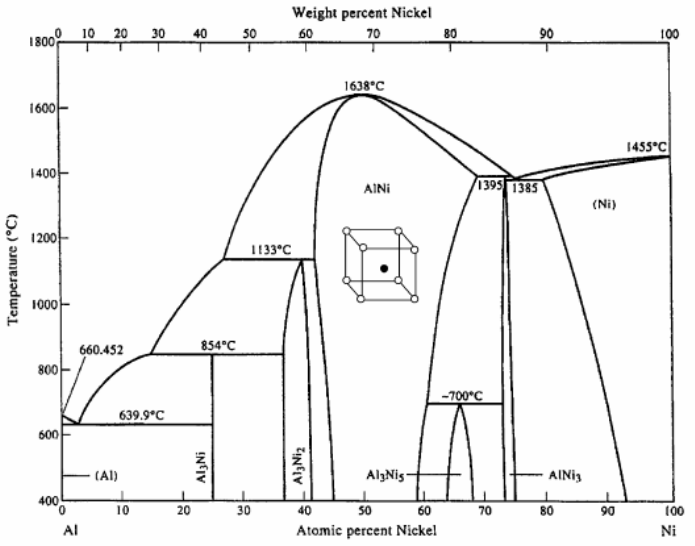

Figure 21 Nickel Aluminium binary diagram[41]

I.2.3.1.1 β-NiAl

β-NiAl is extensively used for high temperature protection as it has a very wide stability field, melts at very high temperature (1638°C, higher than Ni and of course Al), and is fairly rich in aluminium, therefore providing a consistent reservoir for the formation of a stable alumina scale during its ageing. As its melting temperature indicates, this compound is very stable with an important enthalpy of formation of approximately -62kJ/mol [42].

The unit cell of the β-NiAl phase, with B2 (CsCl-type) structure consists of two interpenetrating simple cubic sublattices and at the equiatomic composition all Al atoms occupy the cube corners of one sublattice, and Ni-atoms occupy the corners of the other sublattice[43]. The deviation from stoichiometry is accomplished by essentially two mechanisms. On the Ni-rich side, antisite defects are created: Ni-atoms can occupy the Al-sublattice, whereas on the other side of the stoichiometry, structural vacancies are present on the Ni-sublattice. The Al-sublattice is therefore always occupied.

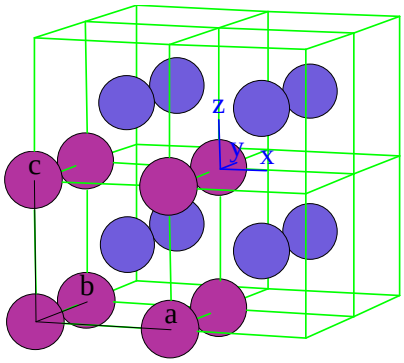

Figure 22 The two sublattices of β-NiAl

I.2.3.1.2 γ'-Ni_3Al

This intermetallic is the compound used in superalloys for high temperature strengthening. Actually, γ' has a very low lattice mismatch with γ-Ni, allowing an homogeneous nucleation of γ' precipitates in the Nickel matrix, with a very low surface energy[44].

γ'-Ni_3Al has an ordered $L1_2$ structure that consists of two sublattices, i.e., the a-sublattice (the face centres) and the b-sublattice (cube corner), with the a-sublattice having three times the number of lattice sites than the b-sublattice. In its perfectly ordered state at stoichiometric composition, the a-sublattice is entirely occupied by Ni and the b-sublattice entirely by Al atoms. Unlike the β-NiAl compound, the constitutional point defects in binary Ni_3Al alloys are antisites on both sides of stoichiometry: Al antisites in Al-rich and Ni antisites in Ni-rich Ni_3Al[45].

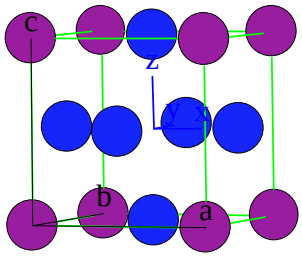

Figure 23 $L1_2$ structure of the γ'-Ni_3Al compound (Al sites at the corners)

Recent studies concerning the alloying of γ' have shown that Pt always prefers Ni sites, while Cr and Hf always prefer Al sites in Ni_3Al. The site preference of Ir was found to be strongly composition-dependent: Ir prefers Ni sites in Al-rich and Al sites in Ni-rich Ni_3Al, and shows no site preference in stoichiometric Ni_3Al[46].

I.2.3.2 Platinum Aluminides

The aluminium-platinum binary system is much more complex, with various narrow composition field compounds. The most described of these compounds is $PtAl_2$, as it is commonly observed after aluminising of platinum modified coatings (see previous paragraphs). Certain phases are well established (Pt_8Al_{21}, $PtAl_2$, Pt_2Al_3, Pt_5Al_3 and Pt_3Al), while others are not (Pt_5Al_{21}, PtAl, β-PtAl, Pt_2Al *LT* and Pt_3Al *LT*). A number of metastable phases have also been observed ($PtAl_4$ for instance).

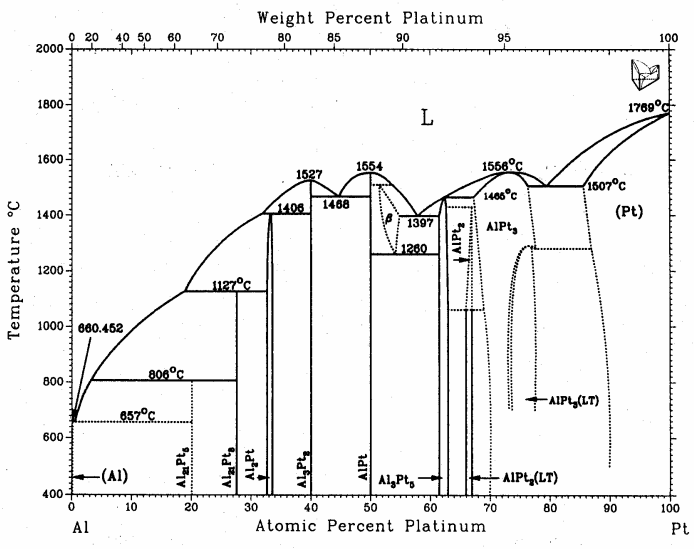

Figure 24 Platinum-Aluminium binary diagram[41]

The crystal structure of the Pt-Al phases are listed below:

Table1 Crystal structure of Pt-Al phases (m=metastable phase)[47]

Phase	*Pearson Symbol*	*Space group*	*Prototype*
Pt_5Al_{21}	c**I**416	…	…
$PtAl_{4\,(m)}$	h**P**90	$P6_322$	…
Pt_8Al_{21}	t**I**116	$I4_1/a$	Pt_8Al_{21}
$PtAl_2$	c**F**12	Fm3m	CaF_2
Pt_2Al_3	h**P**10	P3m1	Pt_2Al_3
Pt_2Al_3	h**P**5	P3m1	Ni_2Al_3
PtAl	c**P**8	$P2_13$	FeSi
β-PtAl	c**P**2	Pm3m	ClCs
Pt_5Al_3	o**P**16	Pbam	Ge_3Rh_5
Pt_2Al	o**P**12	Pnma	Co_2Si
Pt_2Al (LT)	o**P**24	Pmma	$GaPt_2$
Pt_3Al	c**P**4	Pm3m	$AuCu_3$
Pt_3Al (LT)	t**P**16	P4/mbm	$GaPt_3$

I.3 Thermal Barrier Coating

I.3.1 Description of Thermal Barrier Coatings

I.3.1.1 General concept

As explained in the introduction, jet engine manufacturers are always trying to improve the high temperature performance of the materials used in gas turbines. The development of Thermal Barrier Coatings (TBC's) follows this global trend although this technology appears like a real breakthrough in capability to increase the turbine inlet temperature: an increase of 170°C can result in increases in thrust of 5% and efficiency increases of the order of 1%[48]. The strategic challenge of the TBC is obvious when the gain in the blade working temperature is compared with previous technological development (Figure 25).

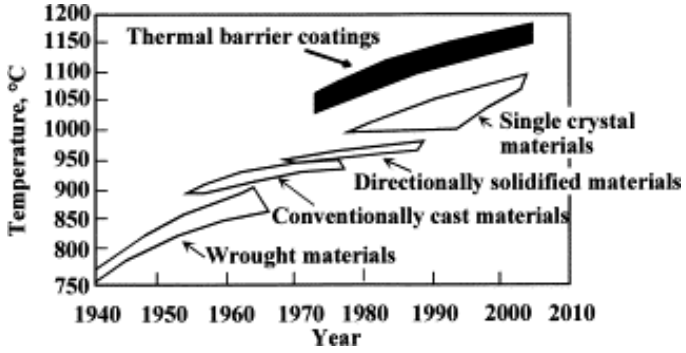

Figure 25 Turbine blade working temperature improvement and years of introduction[49]

The concept of a TBC first appeared roughly three decades ago, or even earlier in former USSR aerospace research laboratory[50]. The principle is to coat the blade with an insulating layer, usually between 100µm and 250µm, with a low thermal conductivity, such as a ceramic. This ceramic topcoat improves the thermal gradient between the hot combusted gas flow and the metal part of the component which is internally cooled.

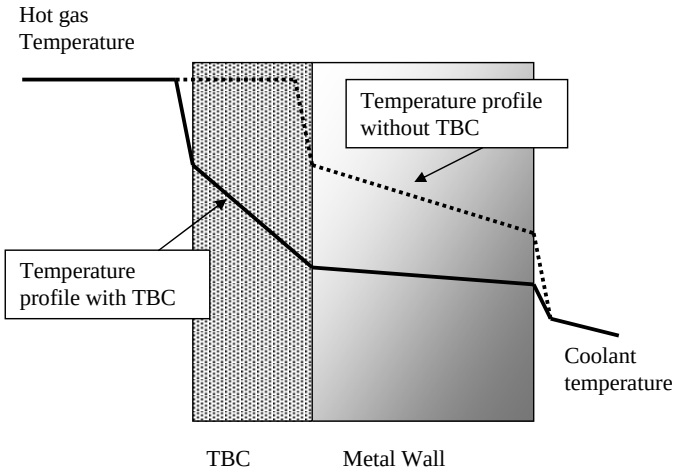

Figure 26 Schematic of the thermal gradient across a component with and without TBC[51]

However, the ceramic topcoat will not protect the metal from becoming oxidised as it is transparent to oxygen: it is deposited on a sub-coating, called a bondcoat, whose aim is to provide high temperature oxidation protection. Actually, the ceramic is bonded to the growing oxide scale of this bondcoat, called the Thermally Grown Oxide. A Thermal Barrier Coating is therefore a triplex system: topcoat/TGO/bondcoat overlying the superalloy substrate (Figure 27).

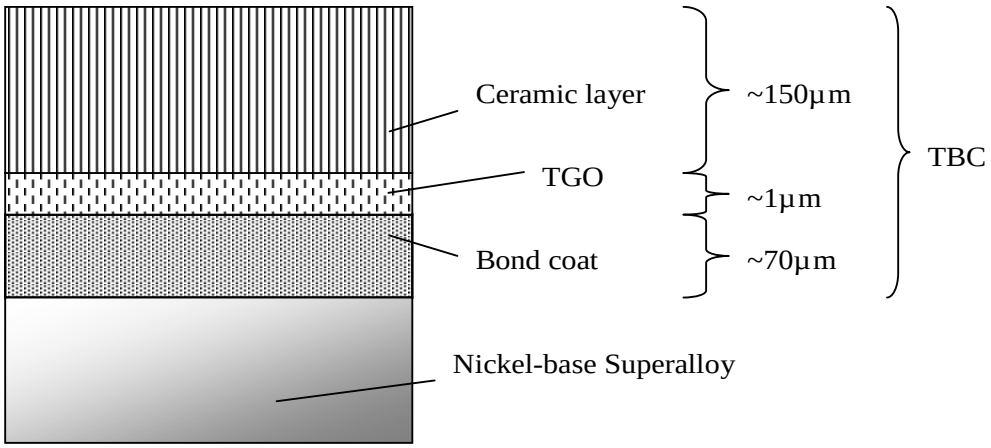

Figure 27 TBC typical triplex structure with typical thicknesses (sketch not in scale)

Each part of this system will be described in detail later in this chapter, but one can see that the critical issue of such system stands on the heterogeneity in properties (physical, thermal, chemical and mechanical) of each of these layers, making it inherently more complex than any individual component that are all metallic or all ceramic[52]. The overall system must withstand extreme temperature, periodic temperature cycling (take off/cruise/landing/thrust reversal/stand by for a commercial jet engine), and interaction with foreign objects from the combustion. The failure mechanisms are numerous and still not entirely understand by the scientific community. The four main failure mechanisms are:

- ✓ The thermal expansion mismatch due to the difference of coefficient of thermal expansion (CTE) for each of the TBC components. Thermal cycles induces various strain for each part at cooling and heating, leading to thermal fatigue ageing
- ✓ The oxidation of the bondcoat. This mechanisms leads to the growth of the TGO with time at high temperature. This growth will induce stress at the interfaces with the topcoat and the bondcoat, which usually results in a roughening of the oxide scale until spallation occurs at the bondcoat/oxide interface or, as a consequence, within the undulating ceramic.
- ✓ The physical and chemical decomposition of the different layers. The ceramic coating microstructure will evolve with time (densification, sintering), altering its mechanical strain tolerance. The material of the ceramic itself will decompose with time as it is usually not in the thermodynamic stable state. Degradation of the bondcoat will occur with time, like any environmental coating, by interdiffusion with the superalloy substrate, and formation of the TGO.
- ✓ Interaction with foreign objects. Erosion due to particles impacting the ceramic layer leads to the cracking and failure of the topcoat. Moreover, the ceramic can react at high temperature with chemicals from the gas flow (calcium magnesium alumino-silicate: CMAS), to form low melting point compounds.

I.3.1.2 Required properties, benefits and limitations

I.3.1.2.1 Properties

Required properties vary with the turbine component needing to be coated. TBC for instance are deposited on combustion chambers walls, transition ducts, nozzle guide vanes and rotating blades. Temperature is greater in combustion chambers, but the mechanical load is lower than for rotating blades. TBC ceramic topcoats are therefore deposited by thermal spray for the combustion cans, as it gives lower thermal conductivity for a cost effective process. However, these ceramics cannot withstand the strain tolerance required for rotating parts such as turbine blades: the ceramic is deposited by EB-PVD. This thesis will now focus on TBC's for rotating blades only (nozzle guide vanes are sometimes produced with the same kind of TBC as blades).

The key properties required for the ceramic topcoat are:

- ✓ Low thermal conductivity
- ✓ CTE as close as possible to the substrate
- ✓ Strain tolerant microstructure at high temperature
- ✓ Chemically stable at high temperature (phase transformation, reaction with CMAS)
- ✓ Physically stable microstructure (densification, sintering)
- ✓ Good aerodynamic surface finish
- ✓ Compatible with the cooling holes (either a deposition process that does not fill them, or a possible machining after ceramic deposition)
- ✓ Remain adherent during the thermal cycling of the component, with a maximum lifetime, and if not, then compatible with scheduled maintenance of the engine
- ✓ Repairability of the ceramic if only partially spalled on the component

The ceramic commonly used nowadays is Yttria stabilised Zirconia (YSZ): ZrO_2+8wt%Y_2O_3, and it is usually deposited by EB-PVD for rotating blade applications (see "Manufacturing of TBC's")

The key properties required for a Bondcoat are:

- ✓ Being an alumina former: at temperatures above 1000°C, it is the only protective oxide
- ✓ TGO growth should be as slow as possible
- ✓ Withstand a TGO as thick as possible (when the TGO fails, the overlying topcoat fails as well)
- ✓ Form a TGO as uniform as possible (allotropic form, porosity)
- ✓ Mechanical properties compatible with the superalloy and the topcoat (ductile to brittle transition temperature, CTE)

As a consequence, the bondcoat must:

- ✓ Have a consequent aluminium reservoir to form only alumina on the scale(at least 10wt%, or 5wt% if there is more than 15wt% Cr)[29]
- ✓ Have a consequent and significant aluminium activity at the Metal Oxide interface
- ✓ Act as a diffusion barrier towards refractory element from the substrate, whose behaviour toward oxidation is very poor
- ✓ A microstructure compatible with the complex γ/γ' microstructure of the superalloy
- ✓ A deposition process which would not affect the high temperature mechanical properties of the substrate

The bondcoats used nowadays by industrials are in fact high quality environmental coatings: β-(Ni,Pt)Al, or MCrAlY obtained as described earlier by diffusion or overlay (thermal spray or EB-PVD) processes.

I.3.1.2.2 Benefits

TBCs for rotating blades are regarded as a major technological breakthrough as were directional and single casting at their time. Gradients between 100°C to 150°C can be achieved thanks to the ceramic insulating layer. This is critical regarding to the fact that creep life of turbine blades is halved for every 10 to 15°C increase in metal peak temperature. Actual metal surface temperatures are about 1000°C with short-term peaks as high as 1100°C.

The potential benefits of TBCs for blades are schematically outlined in Figure 28: Improvement in component life, engine performance or engine thrust can be achieved:

- ✓ Performance improvements by allowing a reduced cooling (reducing the cool flow intake from the compressor)
- ✓ Lifetime improvement of the components by reducing the metal temperature at a given cooling air flow
- ✓ Thrust improvement by allowing higher gas temperature at a given cooling airflow

These benefits have to be added to the continuous improvement of turbine manufacturers towards engine fuel consumption, reduced maintenance, NOx emission levels and noise pollution of new generation engines. The industrial choice for turbines with TBC coated blades would be a complex tuning between these 3 parameters, depending as well on the use of the engine (typically military engines with high level of maintenance would rather concentrate the benefits of Thrust improvement).

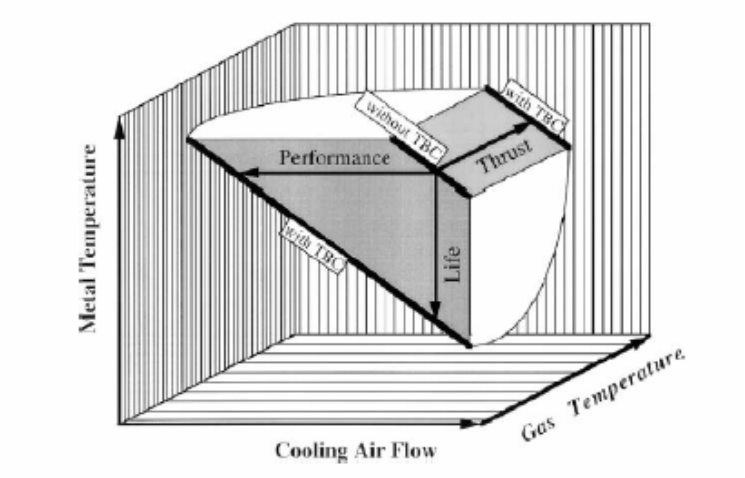

Figure 28 The use of TBCs in gas turbines: improved engine performance or component lifetime[53]

Moreover it has been shown that the use of TBC's on rotating blades reduced local creep distortion on the pressure side which was originally due to non uniform temperature distribution on the surface of the blade[54].

I.3.1.2.3 Limitations

However, TBC systems have some inherent drawbacks, added to the current difficulty to have failure resistant systems (TBC failure modes will be described later).

- ✓ Increase in surface roughness

First generations of TBCs were deposited by thermal spraying (see later section). This method was fast cheap and quite reliable; however mechanical performance of such coating was extremely poor, driving the choice of the industries to shift to EB-PVD deposited ceramic. This choice was helped as well from the roughness point of view: plasma spray coating are very rough and needed post machining. EB-PVD deposited ceramic are very smooth in comparison (Ra≈1-2µm), and do not induce high loss in aerodynamic performance[55;56].

- ✓ Alteration of aerodynamic performance due to a higher load on the blade

Increasing the ceramic topcoat thickness increases the overall thermal insulation, however, it would add a load on the blade, which is critical for high speed rotating components[54]. Moreover the gain in thickening the topcoat is not that straightforward: it has been observed that failure could be accelerated with thicker coatings (CTE mismatch), and the gain in thermal insulation is not linear with thickness, the main insulation being provided by the inner part of the ceramic top coat[57].

- ✓ Modification of the superalloy high temperature behaviour

The manufacturing of TBC can affect the superalloy microstructure, such as heat treatment for the bondcoat manufacturing or the ceramic deposition. Interdiffusion between the bondcoat and the superalloy does occur during the ageing of the system, which could modify the superalloy mechanical properties, at least over the 100 first microns of superalloy in contact with the bondcoat[58].

- ✓ Alteration of the cooling holes geometry

EB-PVD deposition is a process usually described as non obstructive for the cooling holes. This is usually in comparison with thermal spraying which is catastrophic for holes closure. However the outer shape of cooling holes is modified by the ceramic layer, and it has been considered to re-drill the cooling holes after ceramic deposition by laser drilling as one solution[59-61].

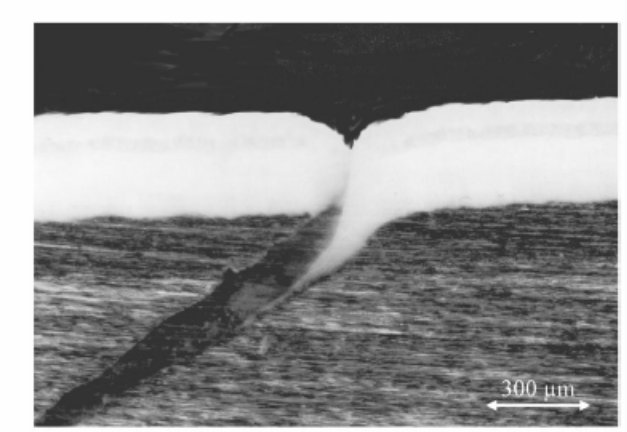

Figure 29 Cross section of a 56° tilted hole with a 330 µm thick EB-PVD deposited TBC with rotation[60]

- ✓ Failure induced particles

The presence of TBCs on gas turbine component increases the probability of foreign object particles within the gas flow. This is particularly true with ceramic deposited onto combustion cans walls, which can create foreign object erosion issues for the following components of the engine.

I.3.2 Manufacturing of conventional TBCs

This part presents the TBC systems as it currently stands on production lines for gas turbine manufacturers. However, in addition many novel systems have been developed and some of these are very close to being integrated into the next generation of engines, such as a new generation of ceramics or low cost bondcoats, which are said to be tested on industrial demonstrators. These new systems, amongst others, are described in the "upcoming technologies" part of this chapter.

I.3.2.1 Conventional bondcoats

As explain earlier the ceramic topcoat is transparent to the oxygen, hence the main purpose of the bondcoat is to provide high temperature oxidation protection for the superalloy. The natural choice was therefore to use environmental coatings such as MCrAlY's and platinum modified aluminide. The bondcoat is grit blasted and degreased prior to ceramic deposition. The alumina scale is formed during the preheating in the EB-PVD deposition chamber. The ceramic topcoat will nucleate on the alumina grains of the scale. Ideally the scale should be α-alumina, the most stable and dense allotropic form. The adherence between the topcoat and alumina is good as their CTE is close at high temperature. The

bonding of a TBC therefore stands on the capability of the bondcoat to have a tough metal/oxide interface.

I.3.2.2 Conventional ceramic topcoat

I.3.2.2.1 Deposition process

As explained earlier, early TBC systems were deposited by thermal spraying. However, the lamellar structure of such coatings is not compatible with high strains involved for rotating aerofoil. Electron Beam Physical Vapour Deposition (EB-PVD) gives a typical columnar structure which offers a better strain tolerance to the ceramic, a better surface finish and does not close the cooling holes. However, EB-PVD is very costly it is a vacuum batch process (like any PVD process, as described earlier), and the thermal conductivity of the resulting coating is higher than a plasma sprayed TBC. The tapered structure of EB-PVD ceramic coating does not block photons as efficiently as the porous and lamellar microstructure of plasma sprayed TBC. Advantages and limitation of both processes are given in Table 2.

Table 2 Structural and processing comparison of Plasma spraying and EB-PVD[62]

	Plasma Spraying	*EB-PVD*
Structure	Lamellar	Columnar
Surface finish	Good, but needs extra polishing	Excellent
Bondcoat roughness	Grit blasted (10μm)	Smooth (1μm)
Bonding mechanism	Mechanical	Chemical
Typical ceramic thickness	0.2-3mm	0.1-0.3mm
Cooling hole closure	Poor	Excellent
Large part predicable	Favourable	Little closure
Investment cost (%)	100	100-400
Parts per charge	1	1-10

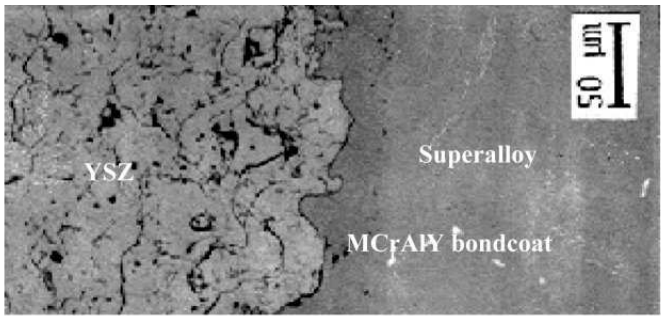

Figure 30 Microstructure of a plasma sprayed TBC

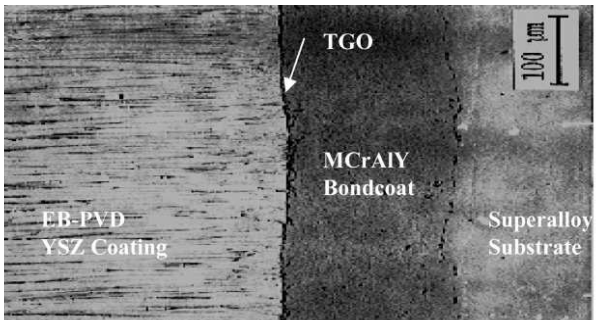

Figure 31 Microstructure of an EB-PVD TBC

Of course EB-PVD follows the main PVD deposition processes principles, as exlained previously in the literature review. The heating source is an electron beam generated by a gun installed in the deposition chamber. The beam scans the surface of the target material, sitting in a crucible, or cast as an ingot. The material is evaporated from the ingot into a cloud that will nucleate on the substrate. As any PVD method the deposition is carried out in a vacuum chamber, with a rotating substrate holder (PVD is a line of sight deposition process).

The EB gun is usually a tungsten filament electron emitter, with the electrons accelerated by a cathode/anode dipole. Electron are accelerated through the electrical field and directed towards the ingot by a coil induced magnetic field. The power of the beam is directly related to the heating of the filament. Commercial coaters for TBC systems have a typical power of 150kW, for an ingot diameter of 75mm. The temperature at the impact point of the beam is around 5000°K[63], hence the scanning to prevent the ingot from thermal induced fracture. It is usually admitted that the beam is powerful enough to melt through the depositing chamber wall in a few second, hence the need of an accurate control of its path. The ingot holder is made of copper and is water cooled to prevent it from melting. The ingot is fed upwards during the deposition time, with the aim of keeping the melt pool surface at constant level.

For TBC deposition, the gas mixture in the chamber is oxygen rich in order to stabilize the coating as an oxide. The pressure is typically 10^{-2}mbar. Moreover, the substrate is heated in order to get the expected columnar microstructure of the film, usually to 1000°C. In industrial coaters, the heat is directly provided by the radiation of the evaporating ingot, onto preheated components.

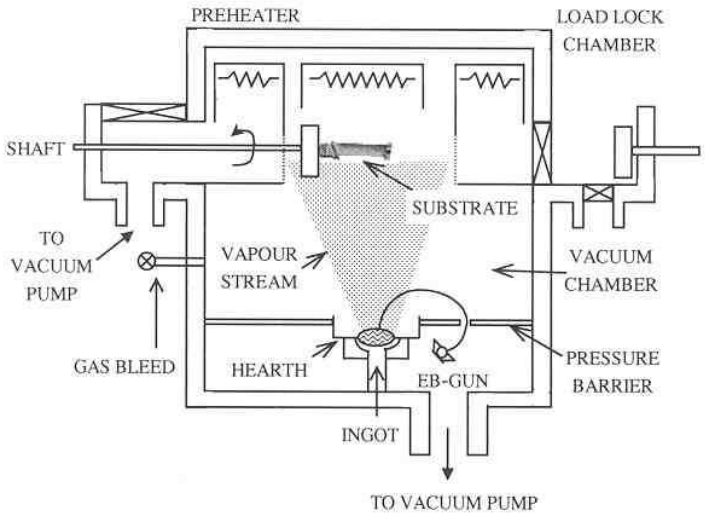

Figure 32 Schematic diagram of a commercial EB-PVD coater system[64]

Like any PVD deposition process, the operator can adjust various parameters to control the film microstructure. The TBC microstructure follows the Thornton model given in Figure 8: the most strain tolerant structure corresponds to the Zone T.

- ✓ The chamber partial pressure, which must stay compatible with the stability of the electron beam (usually the beam is generated in a lower pressure part of the chamber), and with the stability of the vapour stream.
- ✓ The substrate temperature (in situ heater or preheating + radiation from the melting ingot)
- ✓ The substrate rotation speed
- ✓ The beam power is not easily tuneable, especially for high power systems, the beam scanning mode and the rod feeding are more easier to control.

An article published in les Embiez proceedings of 1996 by Schulz *et al.*[65]deals with the deposition parameters of the EB-PVD coated zirconia: the effect of process temperature and rotation. The different microstructures are observed and there performances are compared by thermocycling at 1100°C. Elevated temperature accelerates surface diffusion of atoms, leading to higher column diameter and a more regular structure (see Figure 33). An increase of rotation speed has the same consequences. The microstructures presenting the less perfection (lower process temperature and lower rotation speed) give the best lifetime to thermal cycling.

More recently, Schulz published a whole study[66] comparing the microstructure and the texture of EB-PVD topcoat, under different rotation mode, modifying the vapour incidence pattern. This study compares the mode A (sunrise-sunset pattern) and the mode P (conical pattern). All the orientation are <100>, but columns are narrower in mode A, and larger “pipe-like” in mode P.

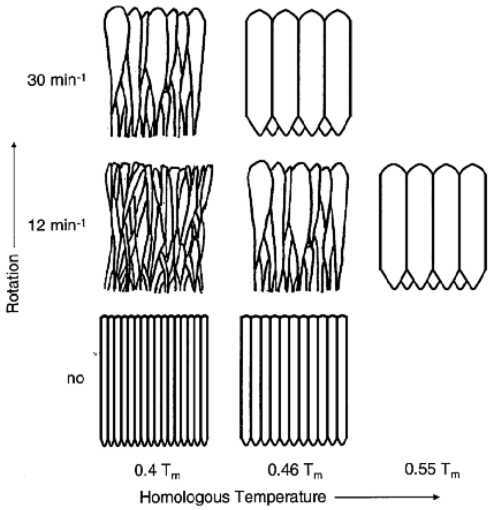

Figure 33 Effect of rotation and temperature of the substrate on EB-PVD TBC microstructure[65]

I.3.2.2.2 Ceramic choice

Early works on TBC's were focused on enamel, alumina or zirconia-calcia topcoats, however these systems were rapidly changed to modified zirconia (ZrO_2) based systems. Alumina based systems had poor performance due to the transient alumina transformation and zirconia-calcia had phase instability issues. Zirconia has a low thermal conductivity coefficient and one of the highest CTE of ceramic materials ($\approx 11.10^{-6}K^{-1}$), closer to the superalloy ones ($14.10^{-6}K^{-1}$), reducing therefore the mismatch strain and the thermal cycling failure[52]. Moreover, ZrO_2 is a very stable oxide with a high melting point (2710°C). Figure 34 compares CTE and thermal conductivity of TBC related materials.

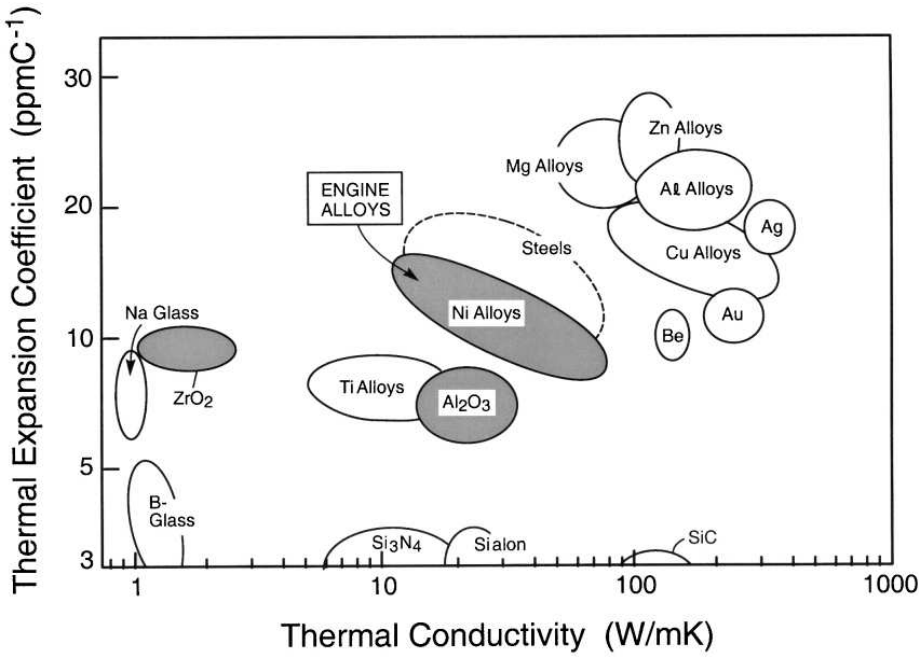

Figure 34 Cross plot of the thermal expansion coefficient and thermal conductivity of the major material constituents in the TBC system[67]

However, the main drawback of ZrO_2 is its polymorphism: 3 allotropic forms are stable at various temperatures:

- ✓ Monoclinic (m) up to 1170°C
- ✓ Tetragonal (t) between 1170°C-2370°C
- ✓ Cubic (c) above 2370°C

The reaction between monoclinic and tetragonal occurs close to the temperatures relevant for aerofoil application. This phase transformation is detrimental as it is linked with a change in volume,4-5%, leading to stress cracking and failure of the ceramic under thermal cycling[68].

Stabilizing the tetragonal structure of zirconia coating was developed in the mid 70's for thermal spray and late 70's for the EB-PVD systems[69]. The first stabilising agent were calcia (CaO) or magnesia (MgO), but these where rapidly changed for yttria (Y_2O_3), which had better toughness and cyclic lifetime as a result. Adding yttria stabilises the tetragonal phase at temperatures below 1170°C, preventing the detrimental t→m transformation. This stabilised phased is commonly called t' as this is not a thermodynamically stable phase. This phase has a complex microstructure (containing twins and antiphaseboundaries) which resist crack propagation and transformation into the monoclinic phase (4% volumechange) upon cooling. The result is a thermomechanically tough TBC layer with a room temperature,grain size dependent, thermal conductivity of 2.2–2.6W/m K in the densest form[70;71].

The initial yttria partially stabilised zirconia (YPSZ) TBCs contained up to 20% of yttria. It is nowadays acknowledged that yttria level around 6-8wt%Y_2O_3 gives the best thermo-mechanical performance, although a higher yttria level reduces the thermal conductivity.

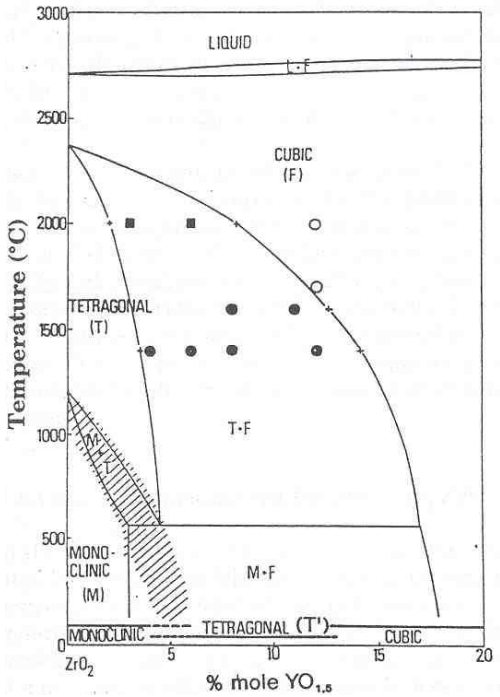

Figure 35 Low yttria region of the ZrO_2-Y_2O_3 phase diagram[72]

I.3.2.3 Industrial approach

The EB-PVD TBC process sequence at the industrial scale is described in Figure 36.

Surface preparation is a key step, carried out prior to each deposition: degreasing in a solvent+ultrasonic bath and grit blasting. These operations have to be realised less than 24h before deposition. Grit blasting roughens the surface and is subject to many discussions in the literature, see the following paragraph.

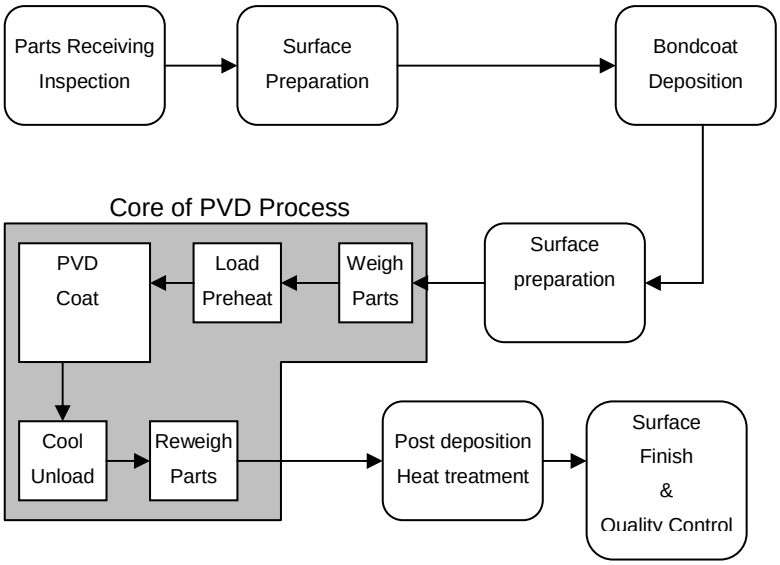

Figure 36 Schematic of TBC deposition process sequence[63]

Parts are weighed before and after the deposition as part of a non destructive quality control of the process. EB-PVD is a line of sight process; the control of the deposited thickness along the shape of the part is done by the design of complex shaped masks holding the blade[73]. Some parts such as the root of the blade or the shroud of the blade have to be protected not to get coated. As explained earlier the parts are mounted on rotating substrate holder in order to control the coating microstructure.

Figure 37 Blade holder in an industrial EB-PVD coater[74]

Preheating is carried out in a loading chamber, usually by a controlled furnace. During the deposition, the temperature is usually kept constant by the radiation from the hot melt pool. A post deposition heat treatment is usually carried out in controlled atmosphere in order to release stress from the deposition, and also readdress the stoichiometric zirconia-oxygen ratio.

I.4 Degradation mechanisms and current research

As shown earlier, industrial needs have led to the use of more and more complex alloys. The complexity of the superalloy+coating systems compared to usual reference materials leads to very complex oxidation mechanisms[75]. The fourth part of this chapter relates the main degradation mechanisms observed for high temperature environmental coatings as described in the literature, followed by issues specific to TBC systems. The understanding of the failure mechanisms is critical, especially for TBC's, as these coating are specifically known for having scattered lifetime for similar systems. Reliability is today's key issue of TBC's[2], and can be improved by understanding the lifetime affecting mechanisms and modelling.

First the degradation of intermetallic coating with oxidation will be developed, as this occurs during the ageing of the overall TBC system. The thermal cycling ageing of TBC, bondcoat and ceramic will be then presented.

I.4.1 Degradation of environmental coatings and bondcoats

I.4.1.1 Introduction

As bondcoats and environmental coatings are often similar, this part gathers degradation behaviours in common between both types of coatings.

At high temperature, these intermetallic coatings are subsjected to many phenomena. First, the growth of the oxide scale. This follows the rules of thermodynamics and is subjected to kinetic laws. The issue of transient oxides will be presented. Secondly, the coating microstructure changes due to the many diffusion driving force such as consumption of metal to form the oxide scale, interdiffusion with the substrate, or precipitation of compounds at high temperature. At last, the effects of some elements such as platinum, sulphur or reactive elements will be presented. Stress related degradation will be included in the part concerning TBC's.

I.4.1.2 Growth of the oxide scale

I.4.1.2.1 Thermodynamically stables oxides

The high temperature oxidation of a metal can be first approached from a thermodynamic point of view. The global reaction of oxidation of a metal M can be simply be written as:

$$M(s) + O_2(g) = MO_2(s) \quad [1]$$

At the thermodynamic equilibrium the chemical activities of solid are taken as unity, the Gibbs free energy of the reaction (ΔG^0) can therefore be linked to the oxygen partial pressure at which metal and oxide coexist i.e. the dissociation pressure of the oxide ($p_{O_2}^{M/MO_2}$):

$$\Delta G^0 = RT \ln p_{O_2}^{M/MO_2} \quad [2]$$

Where T is the temperature in Kelvin and R the universal gas constant.

From the equation [2], the value of ΔG^0 can be plotted for various metal/oxide systems as a function of the temperature. This plot was first described in 1944[76], and is now commonly called Ellingham diagram.

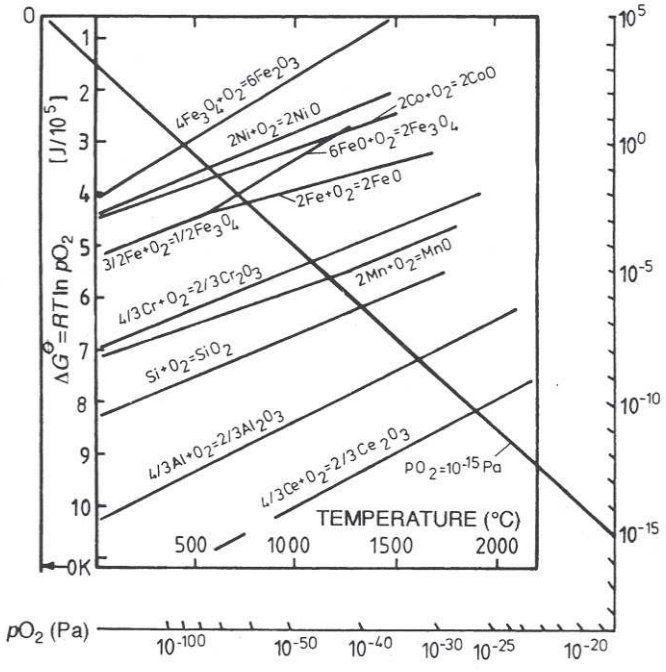

Figure 38 Ellingham Diagram[25]

This diagram can be qualitatively interpreted like so: when the temperature and the partial pressure of oxygen are such as they fit within the plot of a metal/oxide system, then, the both species are thermodynamically stable. Above this line the stable state of the chemical element is in its oxidised

form, below the line, its stable state is metallic. This part of the diagram shows only the systems whose oxides are stable under normal conditions. Precious metals such as Au or Pt would be positioned above the $\Delta G^0=0$ axis: they do not develop an oxide scale under normal conditions. One can notice than some metals have very stable oxides such as Mg, Al, Cr, Ti or Si.

The oxidation reaction will obviously lead to a solid/solid/gas thermodynamic system: Metal/Oxide/Oxygen. For the reaction to proceed further, many mechanisms may be possible, as the reactants have to cross the oxide layer i.e. metal cations through the oxide to the oxide/gas interface or oxygen anions through the oxide scale to the metal/oxide interface. Many transport mechanisms are described in the literature involving cations, anions and vacancies displacement in the atomic structure, their relative kinetics will rule the overall evolution of the system with time.

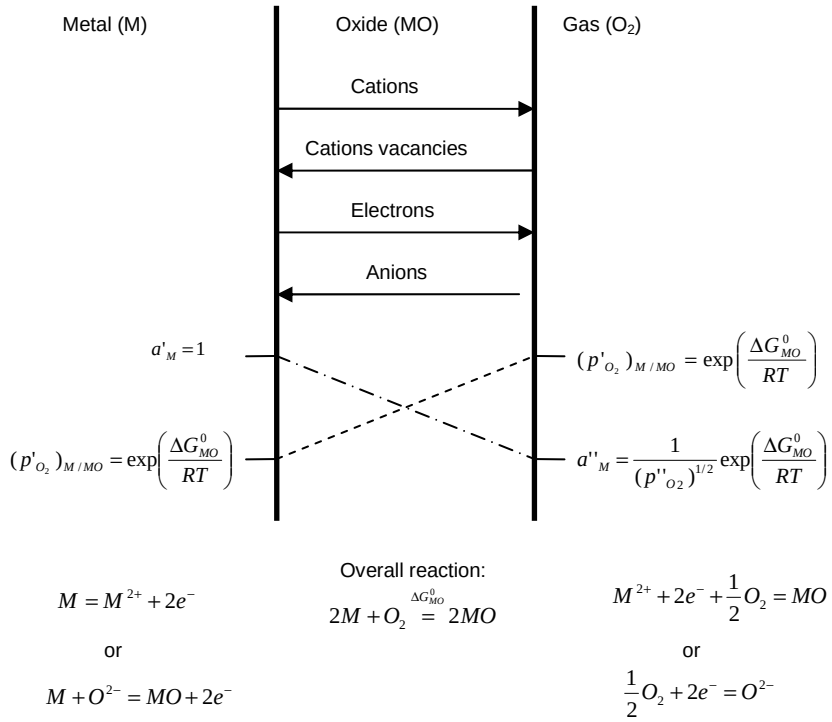

Figure 39 Metal/Oxide/Gas interfaces thermodynamic[25]

When the diffusion of cations controls the kinetic of the reaction, Fick's law can be applied to the outward cation flux $j_{M^{2+}}$ which is opposite to the inward vacancies flux, and related to the oxide thickening. This leads to the commonly known parabolic growth rate of the oxide layer, established by Wagner in 1933[77]:

$$j_{M^{2+}} = -j_{V_M} = D_{V_M} \frac{C''_{V_M} - C'_{V_M}}{x} = \frac{1}{V_{Ox}} \frac{dx}{dt} \Leftrightarrow \frac{dx}{dt} = \frac{K}{x} \Leftrightarrow x^2 = 2Kt$$

I.4.1.2.2 Oxidation of alloys

The oxidation of alloys or intermetallics is more complex, and widely described in the literature[25;78-80]. The first type of alloy corresponds to a reactive metal (B) alloyed with a noble metal (A) : typical of the platinum aluminide type. If B is quite diluted in A and oxygen soluble in A, then it oxidises internally (Figure 40). Above a critical atomic concentration of B, with the assumption of BO being a stable oxide and the diffusion coefficient of the metal B being negligible compared to the diffusion of oxygen: then a continuous oxide scale grows on the surface (Figure 41).

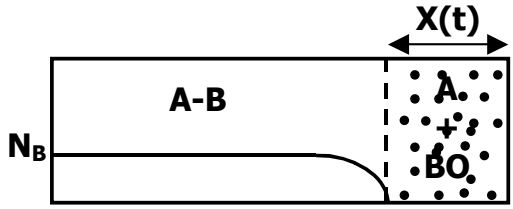

Figure 40 Oxidation with a noble metal and a low concentration of B

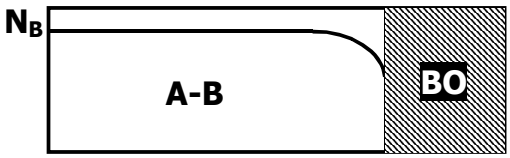

Figure 41 Oxidation of a A-B type alloy with high concentration of B

More generally both A and B form stable oxides, which is the case of MCrAlY type coatings. Considering AO being less stable than BO then the system oxidises as followed. For a low content of B (below a critical atomic concentration), AO scale forms at the surface and BO precipitates internally (Figure 42). Above this critical content, the formation of a continuous BO layer will prevent the formation of internal AO oxide (Figure 43).

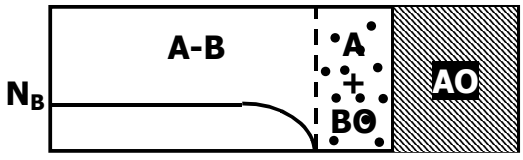

Figure 42 Oxidation of A-B without noble metal and low B content

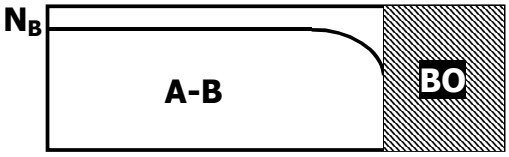

Figure 43 Oxidation of A-B without noble metal and high B content

I.4.1.2.3 Growth of the oxide scale and transient alumina

The growth of the oxide scale occurs as follow. At first the oxidant adsorbs on the clean surface of the metal. At high temperature, all possible oxides start forming as nuclei which will then grow laterally until it forms a continuous scale. In the mean time, the oxidant may dissolve in the alloy or coating.

The first oxidation sequence is called the transient phase. The oxide with the greatest stability continues to grow laterally, until the alloy surface is covered with a continuous layer of this oxide. From this point, the growth of the other metal oxides stops and the oxidation rate is controlled by transport through and growth of the predominant oxide. This final oxidation phase is often referred as to the selective oxidation, to develop a protective scale of the most stable oxide[81].

Alumina possesses numerous transient phases. The most stable alumina, corundum, is referred as α-alumina and has an hexagonal structure: It is the ultimate stable slow growing scale of alumina forming alloys.

During the first steps of oxidation of alumina forming alloys, or at lower temperatures, one may observe the growth of the transient alumina, such as δ, γ (cubic structure) or θ (monoclinic structure). Above 1000°C the transformation into α-Al_2O_3 at the metal oxide interface. The formation of transient alumina is proposed as follow in the literature[79;82;83]:

$$\gamma - Al_2O_3 \xrightarrow{800°C} \delta - Al_2O_3 \xrightarrow{900°C} \theta - Al_2O_3 \xrightarrow{1000°C} \alpha - Al_2O_3$$

The oxidation rate of transient alumina is sensibly higher than corundum (two orders of magnitudes for θ-Al_2O_3[84].

Moreover, the difference in density between θ-Al_2O_3 and α-Al_2O_3 is consequent, leading to volume shrinkage of 10% during the last transformation[85]. This shrinkage leads to internal stress which may cause the scale to spall. Therefore research works often focus on limiting the formation of transient alumina. This was shown to be possible by preoxidising at high temperature, changing the surface roughness or modifying the surface preparation[86;87]. θ-Al_2O_3 microstructure is typically needle, platelet shaped or whiskers like growth. This is due to the fast cationic growth mode. On the other hand, α-Al_2O_3 is a dense columnar scale, typical form cationic growth[80]. The use of isotopic oxygen tracers is often used to understand the growth mode of the scales[88;89].

Furthermore, the phenomena of oxidation implies the formation of some cavities underneath the oxide scale, reducing therefore its adherence. These voids are thought to be implied by the outward diffusion of vacancies, consequence of the difference in diffusion flux between inward Ni and outward Al[81]. This is often referred to Kirkendall effect.

I.4.1.2.4 Sulphur effect

The presence of sulphur has been proven to be detrimental to the scale adhesion by many research works. However the mechanism associated is not yet fully understood. The sulphur contamination may come from the superalloy cast, the specimen handling and storing, the aluminising equipment or Pt electroplating[90-93].

It has been suggested that sulphur, even at very low concentration, would segregate at the metal oxide interface. The chemical bonding of the scale is reduced by the sulphur, causing early spalling of the oxide[94]. The sulphur level has to be very low in order to limit these dramatic consequences: below 1ppm is often referred as a critical concentration. These levels are achieved industrially by H_2 annealing at high temperature (typically 100h between 1100°C and 1200°C)[95]. Nowadays, superalloys have typical sulphur content below 0.5ppm. According to Grabke et al.[96], sulphur segregates to the interface when voids are forming beneath the surface. These voids are then expanding creating more metal free surface acting as a driving force for the sulphur to segregate[97].

I.4.1.3 Phase transformations

The degradation of the β-(Ni,Pt)Al phase into γ'-$(Ni,Pt)_3Al$ is commonly described as the degradation mechanism due to the outward diffusion of aluminium to form the alumina scale and inward diffusion of aluminium into the superalloy plus the outward diffusion of nickel from the superalloy[34;98;99]. This transformation leads to several consequences. First internal stress is induced by the volume shrinkage of the β→γ' transformation, around 16%[100]. This stress is described as a possible cause for rumpling of the system (see dedicated paragraph). Secondly, the growth of the oxide scale is affected: the density and the quality of the scale is lower, particularly in the absence of Pt[99].

Another modification of the system microstructure is the formation of Typically Closed Pack phases (TCP phases), within the superalloy, having high Re and W content, resulting in a γ'/TCP composite in the outer surface of the superalloy[101]. This highlights the drawback of diffusion coating which degrade the structure of the underlying substrate, reducing therefore its high temperature mechanical properties.

I.4.1.4 Role of Platinum

As described earlier in this chapter, platinum is widely used by industrials for bondcoat. despite these system are much expensive (cost of platinum, cost of adding manufacturing steps). This choice is made by the strong effect of platinum in increasing lifetime of the bondcoat, hence the TBC system.

The main effect of Platinum is described by Pettit in the 80's or Tawancy et al.[102;103]: Platinum prevents refractory elements outward diffusion. Hence improving performance as these elements have detrimental oxidation behaviour. This effect on refractory elements is even noticeable during the aluminizing step of the coating manufacturing[8].

Moreover, platinum has a strong effect on Al atoms in the β-NiAl and γ'-Ni_3Al intermetallic phases: it reduces the activity of Aluminium (i.e. the chemical bond between Al and Pt is very strong, stronger than that between Al and Ni)[104]. Delaying the β to γ' transformation improves the overall lifetime of the system. Moreover the rapid growth of α-alumina after spalling is enhanced by the improved diffusion of aluminium in the coating[105].

Altering the diffusivities in the coating also inhibits the formation of voids at the metal oxide interface[36;92;106]. However no clear mechanism is proposed in the literature. The most recurrent explanation is the reduction of sulphur segregation[107]. Platinum would segregate at the interface, therefore inhibiting sulphur segregation, up to 60%[91].

Adding platinum in the coating also has a strong influence on the growth stress of the oxide scale[108]. In fact it reduces the CTE mismatch between the intermetallic and the growing scale.

At last, another effect of Pt reported in the literature is its effect on the oxidation kinetics of the system. It is sometime reported that oxidation rates are not as good as simple aluminides. However, lifetime before spalling in cyclic oxidation mode is improved: this proves the adherence of the scale in presence of platinum is enhanced.

I.4.1.5 Role of reactive elements

Many studies have evaluated the effect of reactive element (RE) by implementing them by various routes (e.g. ion implantation, co-deposition…). However, results have to be taken with care, the effect of reactive element being dependant of the implantation process. Moreover too much reactive element is not always good, for instance the formation of Hf rich pegs under the alumina scale can be observed for high content of this reactive element, reducing the oxide adherence[109].

It is now established that adding few ppm of reactive elements improves the oxide scale adherence and increases the coating lifetime by a factor 2 to 3[109].

Many possible explanation of this positive effect are described in the literature:

- ✓ RE segregate to the alumina grain boundary and reduces the outward diffusion of Al^{3+}, therefore slowing the scale growth[110]. This mechanisms as well reduces induced growth stress[111;112].
- ✓ Presence of reactive element at the metal/oxide interface would improve scale adhesion[113]
- ✓ Reactive elements would limit the negative impact of sulphur by trapping sulphur at grain boundaries in the substrate[97;114]

- ✓ As a consequence, adding RE limits the formation of voids under the oxide scale[97]
- ✓ RE would slow the reaction of alumina scale from θ to α-Al_2O_3 [115]

A direct application of these effect is in MCrAl bondcoat, where adding Y is very beneficial. Three main mechanisms have been identified that may affect the oxidation behaviour[116]: the formation of Y_2O_3 rich pegs in the α-alumina scale which may improve the scale adherence; the presence of Y in solid solution in the TGO; and lastly the segregation of Y to the alumina grain boundary, that could reduce its growth rate.

An excellent paper published by the ORNL in 1998[111] compares the effect of Hf and Zr bondcoat doping, but also the effects of sulphur and platinum. Tests were carried out on René N5 superalloy (desulphurized or not) with a commercial platinum aluminide bondcoat, but also on NiAl-Zr or-Hf , (Ni,Pt)Al-Zr or -Hf and PtAl coupons, directly YSZ EB-PVD coated. Cyclic oxidation tests of 1 hour at 1150°C or 1200°C were done. Results for Zr doped NiAl (0.04 at.%) are outstanding (Figure 44), and discussed in the term of the Zr segregation to the metal-scale interface and at grain boundaries, and also to a better stress repartition along the scale. In conclusion, the addition of reactive elements further improve scale adhesion compared to just a Pt addition alone (Figure 45).

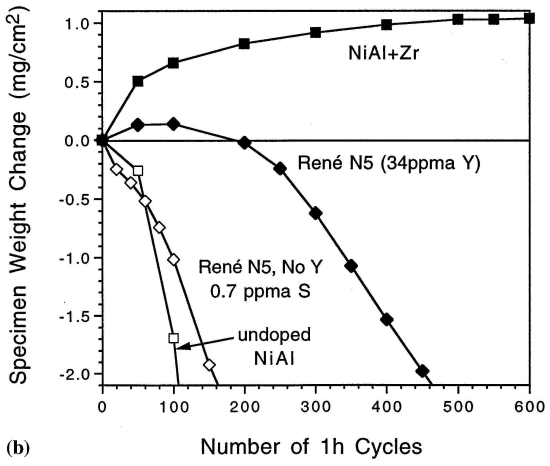

Figure 44 Weight change at 1200°C of uncoated alloys[111]

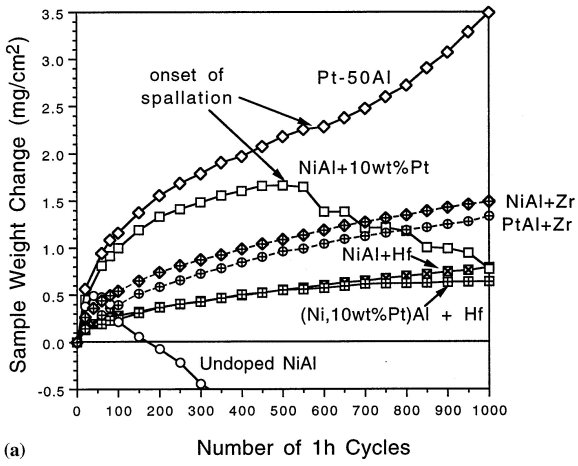

Figure 45 Weight change of doped systems at 1150°C[111]

B. Warnes published in 2001[117] a way to produce a diffusion platinum aluminide coating with reactive elements additions (Hf, Zr, Si). These coatings are said to give four time better oxidation resistance than classical platinum modified diffusion aluminides. The principle is to simply add three separated sources of reactive elements, giving a coating gas composed of 3.5%$AlCl_3$, 0.5%$SiCl_4$, 1.5%$HfCl_4$, 1.5%$ZrCl_4$, 15% Ar and the balance hydrogen. A similar study was published recently[118].

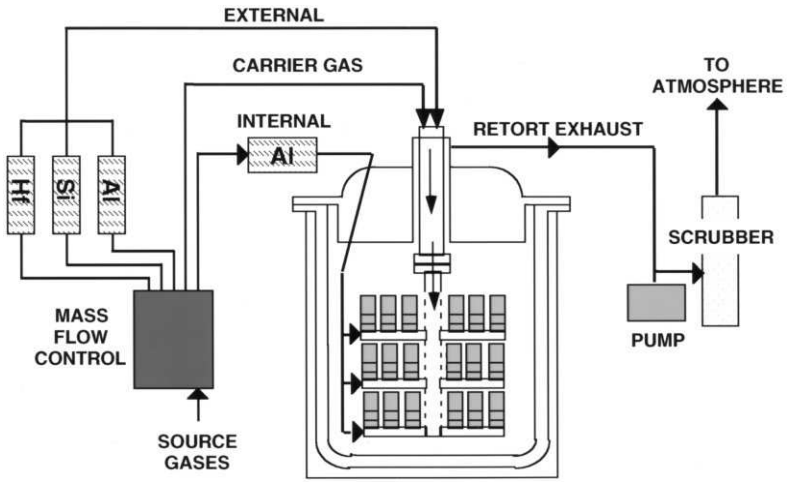

Figure 46 CVD low activity co-deposition of Al and one or more reactive element[117]

A systematic study of oxidation performances of NiAlPtHf systems (Ni: 47%-78%, Al: 22%-53%, Hf: 0%-0.045%, Pt: 0%-29.5%) was carried out by Pint in 2004[119]. These tests were done on bulk intermetallics (melted and cast within a chilled copper mould, and annealed 4h at 1300°C in a quartz bulb at 10^{-6}Torr), loaded on a cyclic oxidation rig (1h at varying temperature and 10 min cooling in a flowing O_2 environment). He discusses the effect of reducing the Al content, of a Hf addition, of a Pt addition and the good performances of γ/γ' coatings (low Al and high Pt content). The addition of Hf to the alloys showed the best possible oxidation resistance that can be expected from these compositions. The addition of Pt was found to increase the selective oxidation of Al (i.e., reduce the formation of Ni-rich oxide). A γ/γ' cast alloy showed excellent oxidation resistance, comparable to aluminides with much higher Al contents (see Figure 47).

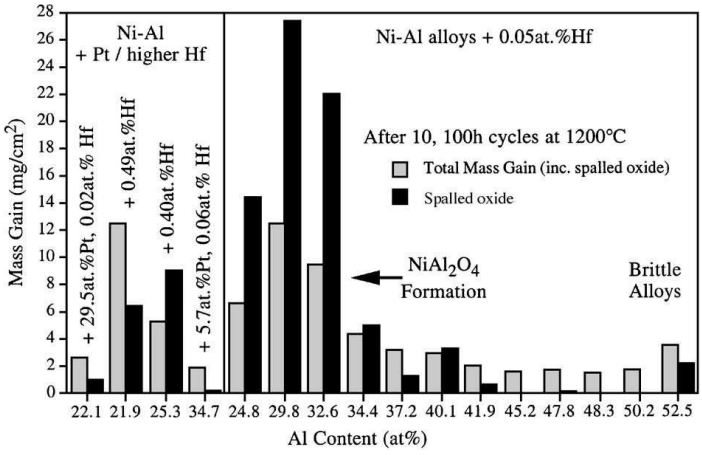

Figure 47 Total mass gain and amount of spalled oxide after 10, 100-h cycles at 1200°C for various Ni–Al–Hf alloys. Increased Hf contents were not as beneficial as a Pt addition for low Al content compositions.[119]

The role of Hafnium on low cost bondcoat systems was recently studied by Zhang[120], and later confirmed by B.Gleeson's team in Iowa State University. Low cost bondcoat behaviour being extensively substrate dependant, it was chosen to cast directionally solidified superalloy René 142 with various Hf

content, then coated by a Platinum γ/γ' low cost bondcoat. Hafnium was proven to be very efficient in improving oxidation behaviour, proportionally to the added content ("A":0.02, "B":0.76, "C":1.37 wt%). However, oxide adhesion was not as good as for β-(Ni,Pt)Al, probably due to the higher dissolution of refractory metals in the γ/γ' structure.

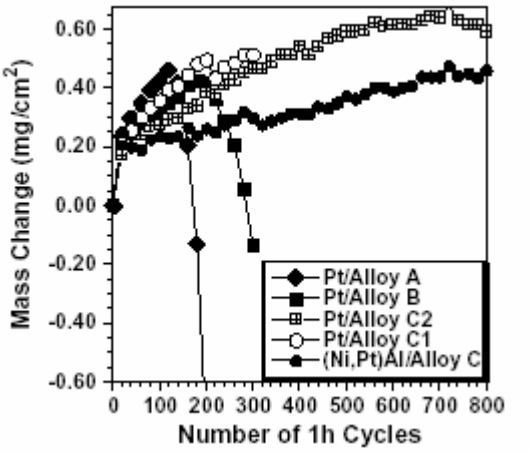

Figure 48 Weight change on cyclic oxidation testing of Hf enriched Rene142 with Pt γ/γ' coating and (Ni,Pt)Al reference.

I.4.1.6 Behaviour specific to cyclic oxidation

I.4.1.6.1 Rumpling

Many papers are published about the bondcoat rumpling phenomenon[121;122]. Rumpling is described as the roughening of the bondcoat-TGO surface after thermal cycling, initiating cracks, reducing the lifetime of TBC systems. This has been observed for both MCrAlY and aluminide bondcoats. The mechanism of this phenomenon is not fully understood, and the different hypotheses focus on CTE mismatch between the coating and the substrate or the oxide behaviour itself. The initial stress within the bondcoat may trigger this phenomenon. Other hypotheses are based on the martensitic transformation of the bondcoat at each cycle, leading to volume expansion. Moreover the thinner the coating the more it rumples: the undulation amplitude to wavelength decreases with the coating thickness[123].

Tolpygo and Clarke[124] discussed a lot on this phenomenon[125]. These authors try to assess the current supposed mechanisms (basically mismatch of the CTE or martensitic transformation) by observation, and by changing the oxidation parameters, and the roughness:

- ✓ Rumpling of the bond coat does not require pre-existing surface undulations.
- ✓ It also occurs during thermal cycling in vacuum with virtually no oxidation.

- ✓ The extent of rumpling strongly depends on the cycle length (therefore contradicting the theory of CTE mismatch between the bondcoat and the superalloy).
- ✓ The surface of a bulk (Ni,Pt)Al alloy, having a composition similar to that of the bond coats, does not rumple.
- ✓ Deliberate roughening of the bulk alloy, in order to produce surface undulations prior to cyclic oxidation, does not lead to rumpling.
- ✓ The reverse martensitic transformation in the bond coat during thermal cycling has no discernible effect on rumpling for the bond coat composition studied.
- ✓ Surface rumpling is accompanied by thickening (swelling) of the bondcoat.

Hence, according to these latest work from Santa Barbara team, the rumpling could not be due to a problem of CTE mismatch or martensitic transformation of the bondcoat alone, but rather to a phenomenon related to the interdiffusion between the bondcoat and the superalloy.

I.4.1.6.2 Martensitic transformation

An investigation of the martensitic transformation of NiAl leading to surface rumpling was published by Zhang *et al.* in 2003[126]. This paper shows the martensitic reaction occurs after Al depletion from the coating to form Al_2O_3. It also points out the role of superalloy elements modifying the β stability, and so the transformation temperature, M_s, complicating the issue of martensitic transformation because of their diffusion into the coating.

The phase transformation β (B2 structure) → γ' ($L1_2$ precipitates) might be due to the nickel outward diffusion from the substrate[127].. Also, the formation to a martensite ($L1_0$ structure) at lower temperature, retransforms to β at higher temperature. Martensitic transformation is confirmed to occur during the heating and cooling stage of cyclic oxidation.

The thermo-mechanical behaviour of a diffusion aluminide bondcoat during thermal cycling is studied in a paper published in 2003 in association with GE company[128]. It gives the measurement of the CTE, the Young modulus, DDBT and as well an elevated temperature stress relaxation. It also relates these properties to the martensitic transformation of the bondcoat which occurs during each cycle.

I.4.1.6.3 Compared effect of cycled oxidation and isothermal oxidation

A comparison between isothermal and cyclic oxidation (80h at 1200°C) of platinum modified aluminide coating on CMSX-4 was published in 2003[129]. The transformation of β-(Ni,Pt)Al into γ'-(Ni_3Al) was observed, precipitates of μ-phase in the interdiffusion layer and σ-phase (Cr and refractory element rich phase) in the substrate are also described. The relative proportion of γ' formed in the coating is larger in the cyclic tests. The microstructure of μ-phase and σ-phase is also changing: the first

ones are deeper into the interdiffusion zone, the second take a needle shape that is not observed in the isothermal exposed samples. Another type of oxidation analysis is also described: the "accelerated oxidation" consisting in gritting the TGO layer every 10 hours, increasing the oxidation rate.

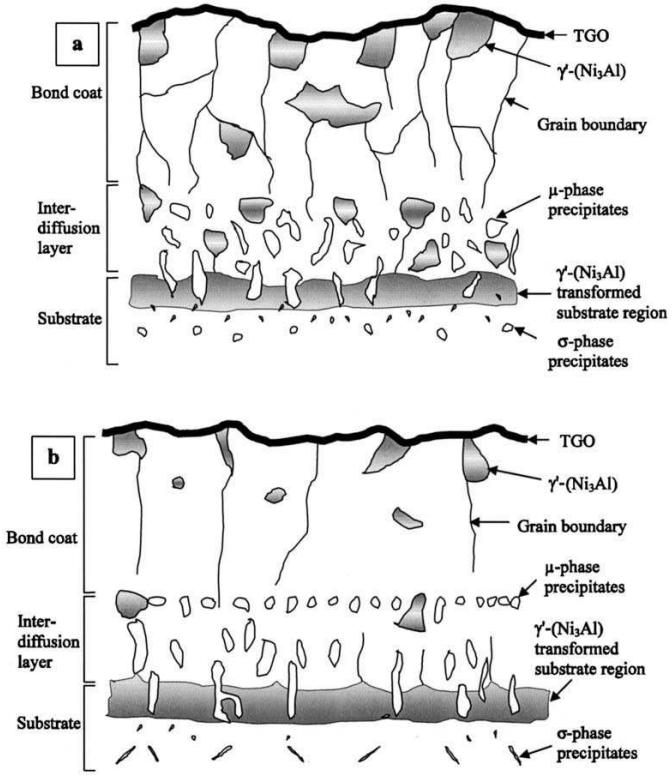

Figure 49 Microstructure of a Pt-modified coating after 80h at 1200°C, isothermal (a) and cyclic (b)[129]

I.4.2 Degradation specific to Thermal Barrier Coatings

The entire TBC system suffers from the bondcoat degradation routes described in the previous paragraph (phase transformation, void formation, rumpling, aluminium reservoir depletion…) plus the entire set of degradations induced by the duplex bondcoat/ceramic system (mainly mechanical degradation) and the degradation of the ceramic on its own (chemical and mechanical). The main degradation route for TBC's are shown in Figure 50 [67]. However this drawing by Evans does not mention degradations of the ceramic itself (sintering, corrosion), which will be presented later in this chapter.

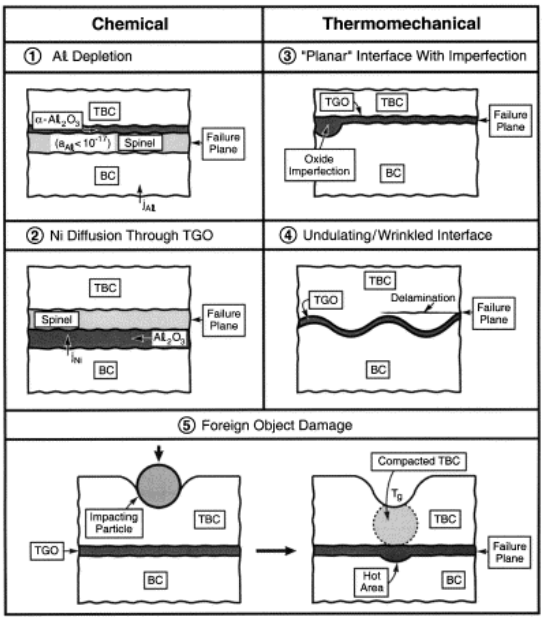

Figure 50 Five of the major failure categories for TBC[67]

I.4.2.1 Stress in Thermal Barrier Coatings

By all means, failure of TBCs is driven by stress generation. This part deals with general mechanical considerations, and how stress increases with time. Failure will occur when stress reaches a critical value. This critical stress level inducing failure will as well reduce with time: the oxide scale being less protective, hence less tough, or the ceramic being less stress compliant, or the bondcoat structure evolving with time…these points will be expanded in the following paragraphs.

Main source of stress within TBC's are:

- ✓ Stress induced by thermal expansion mismatch between the bondcoat, the TGO and the ceramic topcoat. Those are generated by thermal cycling, upon cooling
- ✓ Stress induced by the TGO growth (in plane stress and thickening due to oxidation). This stress is induced even under isothermal exposure. Stress up to 5GPa are sometimes measured within the oxide
- ✓ Stress generated by chemical reactions: transient oxide, phase transformation in the bondcoat, phase transformation in the ceramic
- ✓ Stress induced by the environment: mechanical loading of the part, impact of foreign objects
- ✓ Stress induced by the specific geometry of the component (difference of thickness of the substrate across the component, edges, holes…).

At high temperature, at steady state, the overall system is generally stress free as the bondcoat can plastically deform under creep. This plastic deformation leads to compressive stress within the ceramic and the TGO upon cooling. These are in plane stress.

However, when local defects are present or changes in geometry of the component, this stress would become out of plane and initiate interfacial cracks. This is a driving force for TBC spallation.

I.4.2.2 Bondcoat pretreatment

The effect of grit blasting is intensely discussed in the literature. Some describe it as a very efficient process to remove surface chemical impurities due to the aluminisation (S, C, or N), reducing the void growth (due to sulphur) during oxidation, and so accelerating the formation of α-alumina[90]. Grit blasting seems as well to reduce the formation of transient θ-alumina, therefore reducing the stress in the growing scale. Early failure seems to happen when the surface of the bondcoat is too smooth.

On the other hand, some author are more suspicious about the advantages of bondcoat grit blasting prior to ceramic deposition[130]. It is argued that the grit blasting process contaminate the surface with alkali and alkaline-earth elements (coming from the grit blasting media), modifying the oxygen and/or aluminium diffusivity and resulting in an increase the oxidation growth. And, as said before, the roughing of the bondcoat surface leads also to a greater rumpling while oxidised, reducing therefore the TBC lifetime.

To limit the effect of embedded particles after grit blasting, a "cleaning" method has been described by Warnes *et al.* [131]. This study focused on the cleaning after grit blasting the superalloy substrate, and not the diffusion coating itself. This cleaning stage is carried out in a molten potassium hydroxide bath for 5 to 10 min (US Patent # 6,194,026-B1, Feb.2001). Low activity platinum aluminide coated samples were tested and compared by thermo-mechanical fatigue tests: a 47% lifetime improvement is said to be obtained.

A very complete paper published by U. Schulz team and MTU aeroengines compares thermal cycling performances of various EB-PVD systems (50min in air at 1100°C/10min forced air cooling)[87]. Two types of bondcoats (EB PVD NiCoCrAlY, and pack diffusion (Ni,Pt)Al), two types of superalloy substrates (IN100 and René142), and two heat treatments prior to the deposition of the topcoat (in vacuum or in Ar-H) were used during these experiments. Results are quite scattered (Figure 51), but the effect of the pre-treatment is significant. Vacuum pre-treatment gives better performances for a NiCoCrAlY bondcoat and Ar-H pre-treatment for the platinum aluminide one. Moreover, René142 is a third generation superalloy: it contains 5W6.4Ta1.5Hf2.8Re and no Ti, which is opposite to the IN100.

The Hf is said to form Hf-pegs at the bondcoat-TGO interface that strongly increase TGO adherence. At last the roughness of the bondcoat (and therefore the TGO) is said to reduce dramatically the performance, the platinum aluminide system being more susceptable to this phenomenon than NiCoCrAlY.

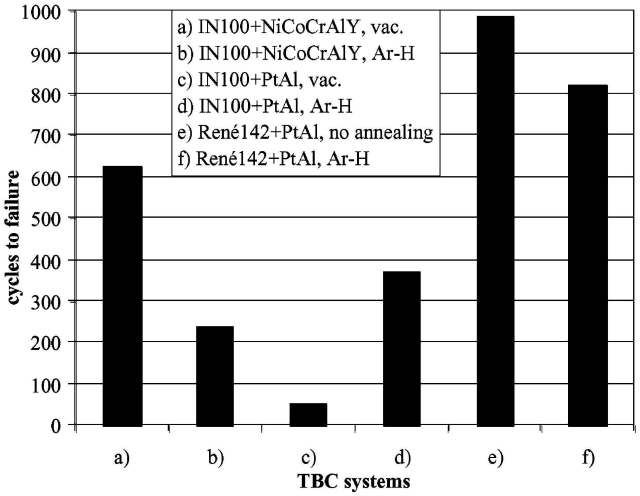

Figure 51 TBC lifetime (50min in air at 1100°C/10min forced air cooling at 10% ceramic spallation) for different substrates-bondcoat-pretreatment systems [87]

I.4.2.3 TGO degradation and a mixed zone

The mixed zone corresponds to the external region of the as deposited TGO where particles of entrapped ZrO_2 are observed. This feature is not described by all the research teams and still subjected to caution[132]. It is sometimes said this mixed zone reduces the lifetime of the TBC, by weakening the ceramic-TGO interface[133].

This mixed zone is described in a paper published by the ORNL and Alcoa in 2001[134]. This study was carried out on platinum aluminide bondcoat topped with an EB-PVD TBC. The TGO structure was observed with High Resolution SEM and TEM, and the presence of the different alumina allotropic forms studied by photo-stimulated luminescence spectroscopy (PSLS). This method allows analysing through the TBC, using a Raman spectrometer. The TGO was observed just after the TBC deposition, and shows two layers: an inner continuous γ-Al_2O_3 and an outer "mixed zone" containing a mix of alumina (γ-, θ-, and α-) and zirconia. The discussion explains the formation of this duplex structure by a first outward growth of an irregular γ-Al_2O_3. This alumina partially converts to θ- and α- aluminas. This structure is then filled by the YSZ during the TBC deposition process leading to this mixed zone. The discussion finishes by assuming this TGO will convert to α-alumina during high temperature exposure, leading to the 3.5-4 GPa stress usually observed.

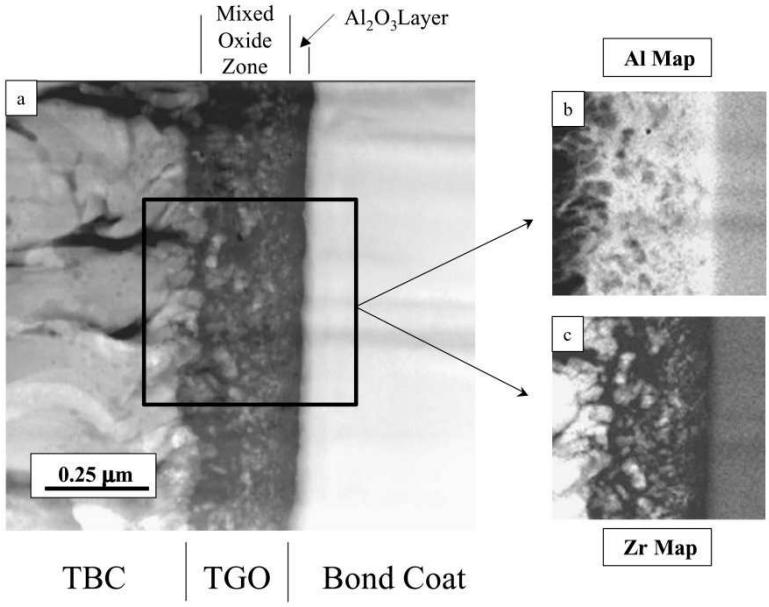

Figure 52 STEM dark field image and Al/Zr mapping of the (Al_2O_3-7YSZ) mixed zone in the TGO [134]

It is even possible to track the formation of this zone during the ceramic deposition: this was carried out by Laxman *et al.* in 2004[135], on (Ni,Pt) Al bondcoats, they removed the samples during the deposition process to make a TEM section by FIB, and then loaded it again in the coated to continue with the deposition. They found that only α-alumina was formed on grit blasted bondcoats, even during the very early stage. On the contrary, θ-, and γ-alumina were formed on non-mechanically activated bondcoats, with a mixed zone at the very beginning, and later, a dense and continuous layer of α alumina was formed on the bondcoat surface, topped with this mixed zone.

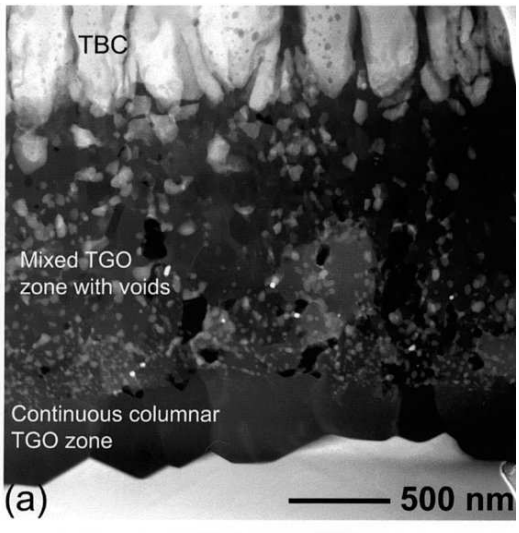

Figure 53 STEM micrograph of TGO on a non grit blasted bondcoat after 50 h@1100°C[135]

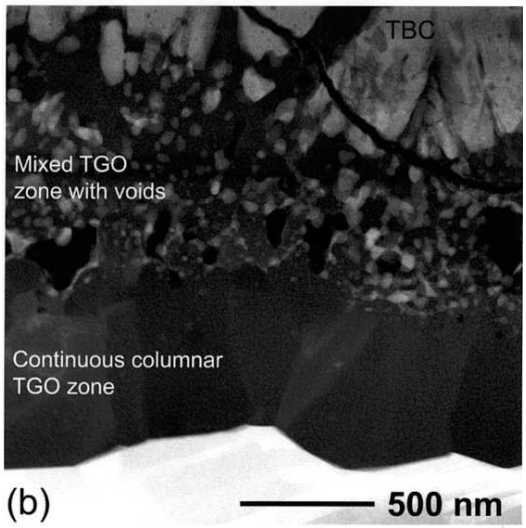

Figure 54 STEM micrograph of TGO on a grit blasted bondcoat after 50 h@1100°C[135]

The residual stress of the TGO is another source of TBC failure described in the literature. Works on TGO stress were greatly improved thanks to the development of Photo Stimulated Luminescence Spectroscopy, PSLS, see analytical tool paragraph.

The effect of surface roughness and TBC thickness on residual stress within the TGO is studied by Atkinson *et al.*[136] in a study funded by RR and Chromalloy UK. Measurements were performed with PSLS and piezospectroscopy. The ceramic topcoat is said to reduce and uniform the stress repartition in the TGO. The roughness also relaxes the TGO stress. The effect of reactive elements (Y, La, Ce) is described as minor. A stress mapping is also described by the same authors[137]in 2003: the evolution and the propagation of stress is therefore possible on the whole sample area, rather than on local points. A similar study was also published by Xie *et al.*[138] in 2003.

Any residually compressed thin film on ductile substrate is susceptible to out of plane displacement instabilities. The "Ratcheting" and the "Wrinkling" are the resulting phenomenon on the TGO respectively for isothermal and thermocyclic heat treatment. The ratcheting is well described by He[139] *et al.* in 2000. The hypothesis is that pre-existing undulations in the film initiate the instability. The cyclic plasticity leads to an increase of the undulation amplitude. The author points out the existence of a critical undulation amplitude below which ratcheting doesn't occur. This value depends on the CTE misfit, the substrate yield strength and the growth strain in the film per cycle. The wrinkling of a TGO on FeCrAl alloys is described by Tolpygo and Clarke[140]in 1998. This study highlights the lateral stain associated with oxide growth, leading to internal stress measured by piezospectroscopy. A FeCrAlY alloy does not wrinkle but internal stress is still induced by the oxide growth.

I.4.2.4 Degradation linked exclusively to the Ceramic layer

I.4.2.4.1 Phase transformation

As explained before, the standard YSZ ceramic topcoat consists in a metastable t' phase. During thermal ageing of the ceramic, this phase structure decomposes into equilibrium phases : tetragonal and cubic phases. The tetragonal phase would later transform into monoclinic phase while cooling to room temperature.

This transformation leads to volume changes inducing stress within the coating, therefore to leading possible spalling of the topcoat. It will as well influence the mechanical properties

(strain compliance), thermophysical properties[141], or sintering capabilities of the ceramic columns.[142]

Moreover, these transformations may be driven by the stress applied to TBC's during service on blades. Actually, it has been reported to observe this phases transformation on concave zones of aged TBC coated blades, whereas no reaction occurred on flat surfaces (such as blades platforms) or convex surfaces (e.g. pressure side of a blade). The *t*-to-*m* transformation of YSZ occurs more easily under a compressive stress than in tension.[143]

I.4.2.4.2 Sintering

As any non fully dense ceramic, the topcoat suffers from sintering at high temperature. This behaviour is generally triggered at exposure temperature over 1150°C. The typical feather like structure is degraded, leading to the reduction of the stress compliance of the coating[142;144-146].

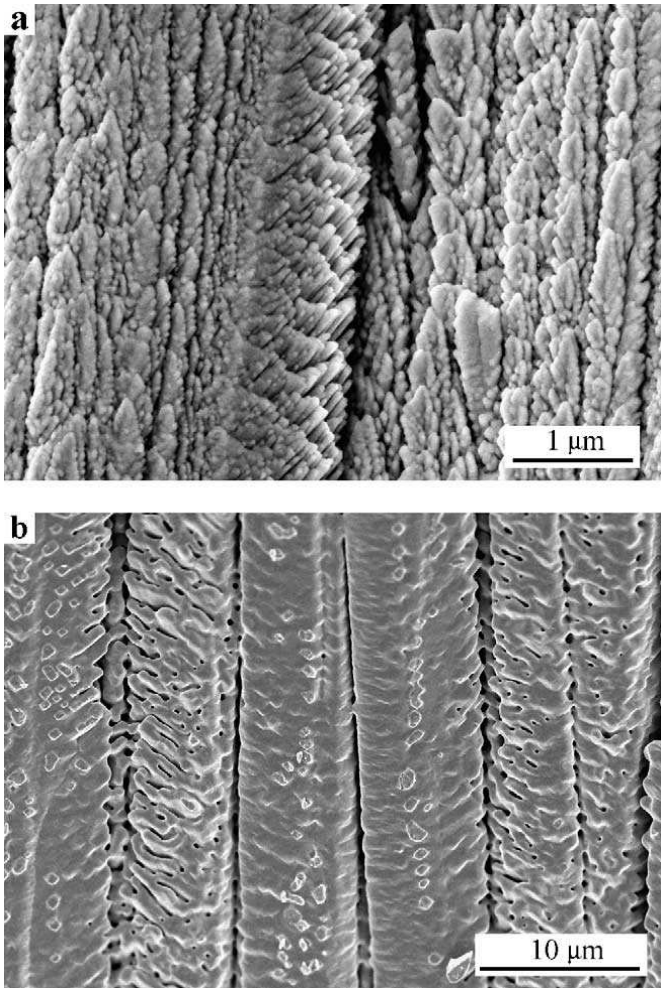

Figure 55 Surface morphology of TBC columns: as deposited (a) and after 50h at 1200°C (b)[142]

I.4.2.4.3 Erosion

Erosion degradation results from particles present in the air flowing through the turbine parts. These particles can be present in the atmosphere or induced by spalling of materials of the engine itself before the turbine stage (wear resistant coating on compressor blades or ceramic coatings from the combustion chamber)[56;147;148].

There are two type of damage induced by particles:

- ✓ FOD (Foreign Object Damage) when the TBC is removed down to the bondcoat. This generates local hot spots where the substrate could be severely damaged. Cracks can then initiate and propagate from those hot spots leading to the whole TBC spallation.
- ✓ Erosion thinning, the ceramic thickness is locally reduced by wear. The substrate remains protected but at a lower level, oxidation rates increase locally. There is a synergy between oxidation and erosion mechanism, but erosion remains a secondary lifing factor.

Erosion damages result in material removal: the ceramic is removed from the coating leading to a local increase in heat transfer to the component. This is measured by the erosion rate, which is the removed quantity of coating material for a given quantity of erodent impacting. Morever it may lead to a deterioration of surface finish, which influence the aero-thermal heat transfer process. The subsequent surface roughening is accompanied by a change in the blade geometry which in turn results in significant aerodynamic efficiency loss.

The erosion behaviour of TBC systems are dependent on parameters such as component temperature, particle size, particle velocity and the impact angle[134;149].

I.4.2.4.4 CMAS

The interaction of the YSZ topcoat with calcium-magnesium-alumino-silicate (often refered as CMAS) was only recentently discovered[150]. This degradation is based on the adsorption of these silicates on the top of the topcoat tips. At high temperature (typically above 1250°C), these silicates react with the YSZ to form low melting point eutectics. These compound then penetrate the interstitial gap between the column at high temperature. During cool down and re-solidification, this eventually leads to the failure of the contaminated ceramic by volume change. A typical structure of a simulated CMAS exposure in laboratory is shown in Figure 56.[68;150-152]

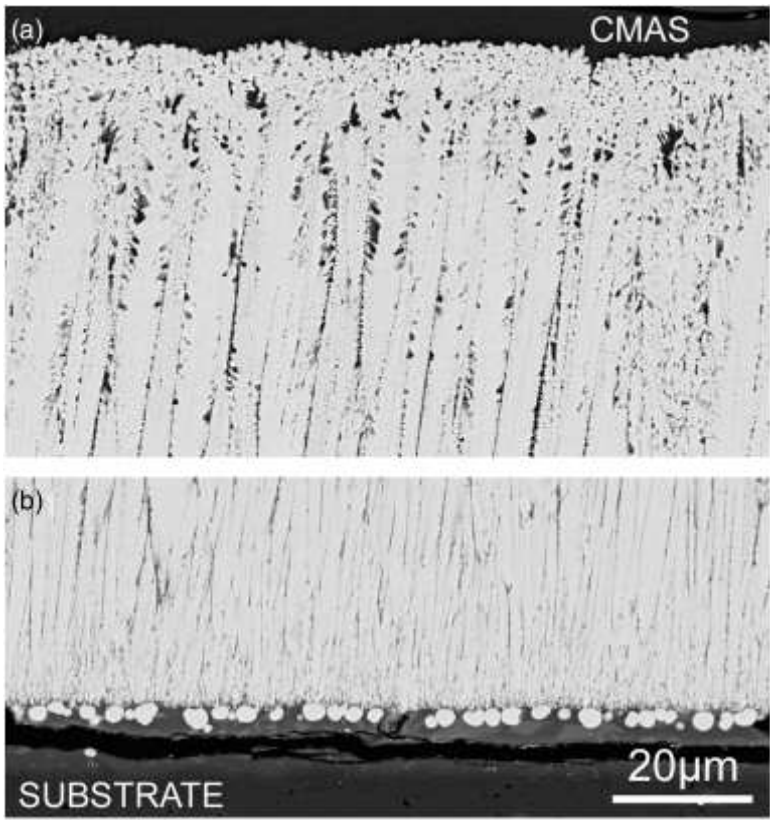

Figure 56 TBC after exposure to CMAS at 1300°C for 4h, highlighting the regions of severe attack near the outer surface (a) and the TBC substrate interface (b)[152]

I.4.2.5 Effect of the superalloy composition

Many types of superalloys are currently used by industrials: there compositions influence the TBC lifetime, especially regarding to the sulphur content, or the presence of typical elements such as reactive elements, refractory elements or rhenium.

The effect of refractory element in superalloys can be evaluated on M247 (15.1 wt% refractory elements), CMSX-4(16.2 wt% refractory elements) and CMSX-10 (19.5 wt% refractory elements) the proportion of Cr for each type is consequently varying in the other direction. Moreover, both APS and EB PVD TBC processes were compared. Performances are evaluated by cyclic oxidation. It is of course found that the greater the refractory element proportion the poorer the oxidation resistance[153].

Current generation superalloys clearly outperform older systems: a comparison of NiCoCrAlY bondcoat/ EBPVD YSZ TBC systems on last generation rené N5 and CMSX-4 superalloys was carried out in a study published in 1999 by the DLR German laboratory and the ORNL[154]. Lifetimes are increased by a factor 7 at 1150°C, and a factor 2 at 1100°C. These results

are said to be mainly due to the presence of Ti in CMSX-4 diffusing into the bondcoat (N5 does not contain titanium).

Titanium and Tantalum are acknowledged as reducing the overall lifetime of TBC's due to the formation of Ti/Ta rich oxide particles at the bondcoat interface[155].

On the other hand, reactive elements such as Hf are very beneficial as they improve the TGO adhesion. A study by Schulz *et al.*[58] from DLR compares this effect on various superalloy systems. Results are very clear as outlined in the two following table and chart.

Table 3 Superalloys studied in[58]

Alloy	*Condition*	*Co*	*Cr*	*Al*	*Mo*	*W*	*Ta*	*Ti*	*Hf*	*Re*	*C*	*B*	*Other*
IN 100 DS	DS	14	9	5	2.3			5			0.18	0.015	0.05Zr,1V
Rene 142	DS	12	6.8	6.1	1.5	5	6.4		1.5	2.8	0.12	0.015	0.02Zr
MAR M002	DS	10	9	5.5		10	2.5	1.5	1.5		0.15	0.015	0.05Zr
PWA 1483	1st gen SX	9	12.2	3.6	1.9	3.8	5	4.1			0.07		0.002Zr
CMSX-4	2nd gen SX	9	6.5	5.6	0.6	6	6.5	1	0.1	3			

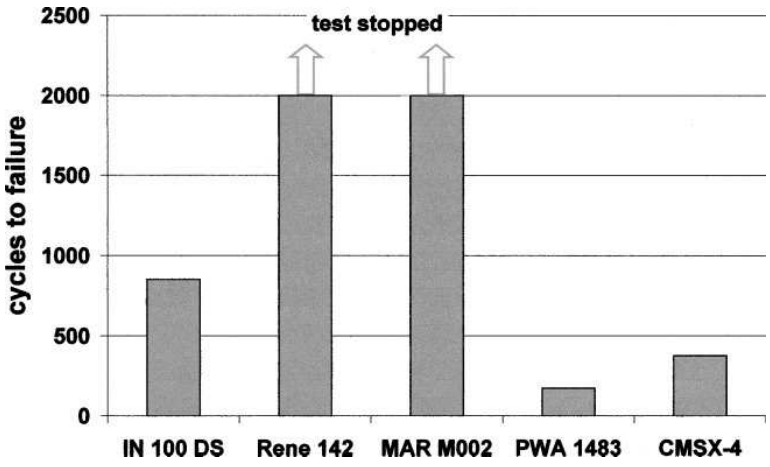

Figure 57 Cycles to TBC failure[58] at 1100°C (1h cycles) for the superalloys described in Table 3

I.5 Upcoming technologies

The objective of this final part is to cite some ongoing work on TBC systems, focused on various parts such as bondcoat, ceramic, processes, analysis…As the present study is focused on new approach for bondcoat manufacturing, it is thought to be interesting for the reader to have an overview of some works of other research teams on high temperature protection.

I.5.1 Bondcoats

I.5.1.1 Modified aluminides

Palladium has been studied for environmental coatings because this metal is more affordable than platinum, whereas their chemistry are quite similar. An article published in 1990 by Alperine *et al*[156]*.* shows that hot corrosion resistance of aluminides is improved by the adding of palladium, with performances close to the platinum modified ones. This study is based on high activity, low activity and vapour phase diffusion coatings, tested at 1100°C for thermal cycling and 850°C in air plus 0.01%SO_2 for hot corrosion. Low activity pack cemented coating have equivalent performances under thermal cycling at 1050° with similar conclusions[157].

A new bondcoat has been recently developed by Rolls-Royce, the patent was deposited in 1997[158;159]. The principle is to electroplate platinum, and heat treat the system at very high temperature (1100°C-1200°C) to fully diffuse it in the substrate. *No aluminisation is carried out*. This methods leads to a vertically oriented graded coating, with an outer Pt enriched γ-phase and an inner Pt enriched γ'-phase. The YSZ is then EB PVD deposited on this "γ-γ'" bondcoat (sometimes also called low cost bondcoat).

Pint published in 2000 a Lockheed-Martin funded study on oxide doped β-NiAl diffusion coatings[112]. Y_2O_3, ZrO_2, TiO_2, HfO_2, Al_2O_3 and La_2O_3 were dispersed into the coating by powder metallurgy technique. Reactive elements have sometimes been said to reduce the oxidation rate by forming more stable oxides at grain boundaries, slowing the oxygen ingress into the coating. Therefore, Pint tried to directly add and disperse these oxides in the coating thickness, and tested

the alumina scale adhesion after thermocycling at 1200°C. Each doping gives very different results: addition of Y_2O_3 and ZrO_2 improves the adhesion; TiO_2 and HfO_2 modify the surface morphology but did not affect the global performances; Al_2O_3 addition clearly reduces the adhesion, forming whiskers on the surface; and La_2O_3 which was tested at 1vol% addition lead to a large weight loss (however, Pint cites references of works at lower concentration that gives improvement of the scale adhesion, and concludes that overdopping is detrimental).

A recent study[160;161] describes the possibility of manufacturing a NiAl-0.1%Hf overlay coating on CMSX-4 by DC sputtering (400W, 10mTorr, 20µm thick). The target was fabricated by an arc casting and forging process. The coating was annealed in vacuum at 1000°C for 1hr in order to increase its adherence by the formation of an interdiffusion zone. Unfortunately this work only studies the coating mechanical properties (E and Hv) evolution with oxidation time, and not oxidation performances. It may be worth keeping a watch on new publications concerning this process.

A paper published in 2004, in the Journal of Alloys and Compounds by a polish team[162] offers a new route for depositing overlay intermetallics. The authors do not make any link with possible applications in the turbine industries. They succeeded to coat steel with Ni/Al intermetallics by electrodeposition of Ni with metallic powder of Al added in the galvanic bath. The resulting coating is quite thick (150 to 320µm), with pure Al particles embedded in a Ni matrix. After heat treatment in an Ar atmosphere at 700°C, the two metals reacted in the solid state to form a NiAl+Ni_3Al system. This work is therefore based on the same concept as the studies carried out at Cranfield, except for the actual deposition process used. If platinum can be added to this bath, which is theoretically possible, it means that platinum aluminides could be deposited by this method on superalloy, leading to the applications we know. Bath composition and a schematic of the experiment are given in Figure 58 and Table 4.

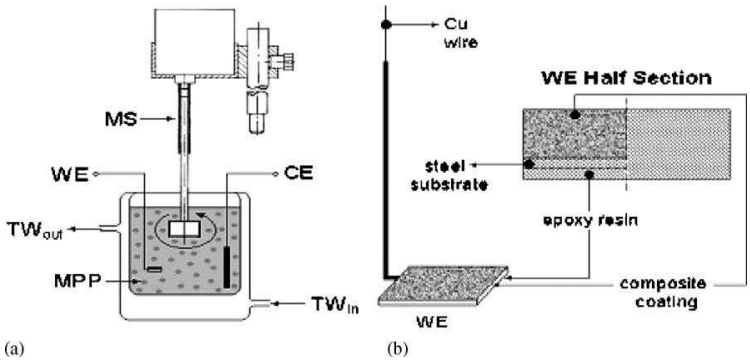

Figure 58 Schematic diagram of the experimental set-up: electrodeposition cell (a) with a platinum counter electrode (CE), the working electrode (WE) of the coating under study, agitation of the electrolyte

containing metal powder particles (MPP) using mechanical stirring (MS), and a constant temperature by thermostated water (TW), and WE detail (b)[162]

Table 4 Bath characteristics and operating conditions for electrolytic deposition of Ni+Al coatings[162]

Bath composition	$Ni(SO_3NH_2)_2,4H_2O$, 56g.dm^{-3} $(NH4)_2SO_4$, 15g.dm^{-3} CH_3COONa, 15g.dm^{-3} H_3BO_3, 9g.dm^{-3}
Al powder	20-140g.dm^{-3}
pH	4
Temperature	293K
Current density	200-450mA.cm^{-2}
Duration	30-100min
Agitation	150rpm
Weight of deposit	0.24-0.36g.cm^{-2}
Thickness of deposit	150-320µm

I.5.1.2 Overlays

In order to reduce the grain size of a MCrAlY bondcoat, a pulsed Electron Beam treatment is describe in 2001[86]. Thanks to the high cooling rate (10^7°K/s), this localized heat treatment on a MCrAlY coating deposited by LPPS, before the EB-PVD TBC was deposited, increased the homogeneity of the TGO and reduced the formation of spinels in the α-alumina scale. This treatment was achieved with a facility providing a beam diameter of approximately 10cm.

Schmitt-Thomas *et al.* [149]proposed in 1999 a duplex design for the bondcoat itself: a 120µm LPPS CoNiCrAlY topped with a 28µm Pt-modified aluminisation (electroplating+CVD). This results in a biphase diffusion coating: $PtAl_2$ (outer)/β-(Co,Ni,Pt)Al (inner). This system was zirconia coated (APS) and tested. Microstructure after isothermal oxidation was observed and compared with a classical diffusion bondcoat.

The concept of smart overlay coatings (SMARTCOATS) was developed jointly between the University of Birmingham and Cranfield University[163]. These environmental coatings are based on a graded composition to improve either high temperature oxidation resistance (formation of alumina) or hot salt corrosion (formation of chromia). The basic coating is a MCrAlY composition designed for type I and II hot corrosion resistance. This coating is pre-treated to form an intermediate chromium rich layer and then it is aluminized to form an aluminium rich β-NiAl layer on the surface, providing a high temperature resistance.

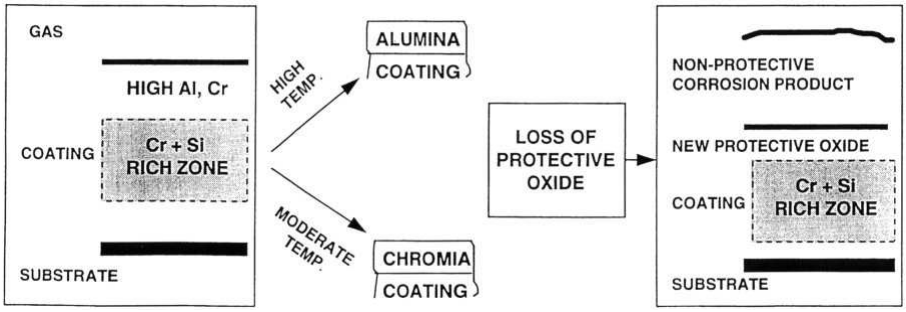

Figure 59 Smart overlay coating concept[163]

A study published in 1995[164] discussed the addition of Ti in order to reduce the CTE of MCrAl coatings. The lowest CTE values are for a Al to Ti ratio less than unity. Adding Si improves the oxidation resistance at temperature below 1000°C: the lowest oxidation rates are achieved with 17.5%Cr and 4%Si. Cr also reduces the CTE value by forming α-Cr precipitates, but chromia formation reduces the oxide adherence.

Air plasma and Low pressure plasma sprayed TBCs are already well known for their low cost, low thermal conductivity, poor mechanical properties, and for the possibility to coat both the bondcoat and the ceramic in one batch. Some recent papers relate the production of TBCs by "detonation gun" spraying process. The resulting coatings have finer microstructure than APS or LPPS ones apparently resulting in good resistance to thermal shocks[165] with thermal conductivity as low as 1 W/mK. Some experiment were also carried out to test the oxidation performance of a triplex system deposited by detonation gun: NiCrAlY/NiAl/YPSZ (thicknesses in µm: 80-100//5-10//250-300) compared with a typical NiCrAlY/YPSZ. The triplex gave better isothermal oxidation resistance at 1150°C[166].

I.5.1.3 Diffusion barriers

The development of diffusion barriers between the environmental coating or bondcoat and the superalloy substrate is described by Cremer *et al.*[167] in 1998. In this study, the barrier consists in a ternary Al-O-N film deposited by Al reactive sputtering between a CMSX-4 substrate and an MCrAlY overlay coating. These films, after 4 hours annealing in Argon, consisted in an AlN-α-Al_2O_3 compound, and no refractory elements of the superalloy were found in the MCrAlY layer.

An interesting approach is presented by Muller *et al.* in 2003[168]: in order to reduce interdiffusion of refractory elements from the superalloy to the bondcoat, a layer of α-alumina was deposited between the substrate and the MCrAlY bondcoat. This oxide was chosen because it is a dense hcp crystal structure stable from room temperature to its melting point. A TiN thin layer was firstly deposited in order to have a dense alumina layer, and prevent the formation of whiskers. Both alumina and TiN were deposited by a CVD process with respectively $TiCl_4$, N_2, H_2 and $AlCl_3$, CO_2, H_2 , HCl, Ar gas mixtures. TiN and α-Al_2O_3 are respectively 1µm and 3µm thick. The diffusion of Ti from the substrate was measured after 100h at 1373K in Argon. Qualitatively, this system seems promising. However, it may have been worth analysing the diffusion of other refractory elements and testing this multilayer coating in an oxidation atmosphere, the formation of the TGO being a driver to the diffusion of species.

An Iridium-tantalum modified aluminised coating is described by Wu *et al.* in 2003[169]. The first layer of Ir-74%Ta alloy is deposited on the superalloy by EB-PVD, and then it is aluminised with a classical low-activity pack cementation. This result in a triplex layer structure: an Ir-Ta layer, NiAl, and an Al diffusion zone. Thanks to the closed pack structure of the Ir-Ta alloy, this system acts as a very efficient diffusion barrier towards Ni or Al movements implying a slower precipitation of refractory element based phases. Cyclic oxidation performances are compared with simply aluminised samples, and TGO growth is significantly lower for the Ir-Ta system. However, this study does not compare results with a commercial Pt-modified aluminised coating.

The concept of improving the « diffusion barrier » performances of bondcoats or environmental coatings is developed in a paper from the Oak Ridge team[170]. The aim of having a diffusion barrier is to reduce the inward diffusion of Al, which reduces the coating aluminium reservoir, and the outward diffusion of refractory elements from the superalloy. The authors deposited a layer of Hf or Hf/Pt by magnetron sputtering prior to conventional CVD low activity aluminising. These layers are less than 7 µm, and form Ni_3Hf or $HfPt_3$ after aluminizing. Results are not convincing when compared with reference to aluminised coatings. Only the 1µm thick Hf intermediate layer gives similar cyclic oxidation performances. These poor results are thought to be due to the limited high temperature stability of the intermediate layers produced.

Enriching the substrate with chromium prior to aluminizing is being currently studied in Hokkaido University team[171]. There works are based on synthesising an α-Cr rich diffusion barrier plus sigma phase (TCP type phase) under the aluminium reservoir.

I.5.2 Ceramic topcoat

The main goal in this field is to reduce the thermal conductivity. This can be achieved by the study of new kind of materials or new deposition routes leading to alternative structures.

I.5.2.1 New generation ceramics

About the selection of materials for TBC applications, Clarke published in 2003 a thermal properties comparison between different oxide systems[172]. This paper summarises the different models for thermal conductivity variation with temperature and compound chemical properties. These models are then applied to the typical high temperature conditions of turbine blades. This study doesn't take in account the stability of the compound as a coating on a superalloy, with the thermomechanical, the erosion, or the microstructure evolution issues.

The addition of La_2O_3 to the EB-PVD YSZ recently described by Matsumoto *et al.*[173] is said to reduce the sintering of the columns during the deposition process and TBC ageing. Lanthania is added thanks to a sintered ingot of ZrO_2 and $La_2Zr_2O_7$, resulting in a La_2O_3 doping proportion up to 5mol%. After 50hrs annealing time at 1200°C, the thermal conductivity of an undoped TBC is measured (laser flash method) at 2.1 W/mK and only 1.3 W/mK with 5mol%La_2O_3 additions. Unfortunately, the phase transformations that may occur are not taking in account in this study.

New ceramics for thermal barrier is an important field of the current research. Pyrochlore based TBCs are particularly studied for their promising performances in sintering reduction. Saruhan *et al.* from DLR describe an EB-PVD based process to manufacture $La_2Zr_2O_7$ pyrochlore based TBCs (manufacture using an APS process was already successfully performed in 2000). Pyrochlore compounds are $A_xB_yO_z$ where A is a rare earth metal cation (typically La, Gd, Nd…), B is a metal cation of Zr, Hf or Ti. The structure of $La_2Zr_2O_7$ is cubic with six ZrO_6 octahedras connected by La^{3+} ions; vacancies are randomly distributed at La^{3+}, Zr^{4+} and O^{2-}sites[174]. The EB-PVD process is based on either a single source rod of pure pyrochlore or 3 wt. % Y_2O_3 doped pyrochlore. Some compositional variations are observed during the process: they are said to be due to the gas pressure change and to the 3 order of magnitude difference in partial vapour pressure between La_2O_3 and ZrO_2 (using a jumping beam EB-PVD may be a solution, see process and manufacturing section). No preferential orientation was observed for pure pyrochlore, which had

a branched columnar microstructure; the Y_2O_3 doped coating displayed some pyramids and a slight <100> preferential orientation (explained by the smaller ionic radius of Y^{3+}).

In order to reduce the thermal conductivity of the TBC zirconia ceramic topcoat, recent studies proved the efficiency of rare earth doping, such as dysprosia (Dy_2O_3) or gadolinia (Gd_2O_3) combined or not with the usual yttria stabilizer. An original paper written by Portuguese teams[175] focuses on the evolution of the allotropy of the ceramic topcoat, the local stress and the surface roughness with thermal ageing depending on the doping in gadolinia. The deposition of the ceramic was carried out by reactive magnetron sputtering.

I.5.2.2 Ceramic deposition process

The production of dense vertically cracked TBCs is a recent concept aimed at having a pseudo columnar microstructure on plasma sprayed ceramic coating in order to improve mechanical performance. Cyclic oxidation tests were recently published by the University of Connecticut[176] and show that the main cause for failure is the bondcoat (NiCrAlY) rumpling and thickening. The formation of chromia observed at the bondcoat/ceramic interface might play a role as well. Lifetimes to failures are quite good, around 600 1h cycles at 1100°C, but drops dramatically at higher temperature: only 100 cycles at 1150°C.

Another concept is to change the EB-PVD microstructure in order to decrease its thermal conductivity. A team at the University of Virginia published some papers on the study of zig-zag columnar YSZ coatings[71]. By altering the inclination angle and the dwell time at each position, films with a low relative density (porosity up to 85%) and zig-zag pore morphologies were produced. In order to improve the deposition efficiency, these were deposited by EB-DVD ("D" stands for directed) with a flux of He carrying the vapour onto the surface. Resulting coatings had an excellent thermal conductivity: between 0.8W/mK and 1W/mK thanks to the porosity. However, such coatings keep the good mechanical properties of a columnar microstructure. The deposition parameters leading to different porosity designs, of the type I, II, or III (see Figure 61), was studied by a Monte Carlo modelling[177], and the consequences on the thermal conductivity was studied by finite elements analysis[178]. After discussion with Professor Nicholls, the erosion resistance of this type of coating is expected to be quite poor due to the 45° inclination of the columns.

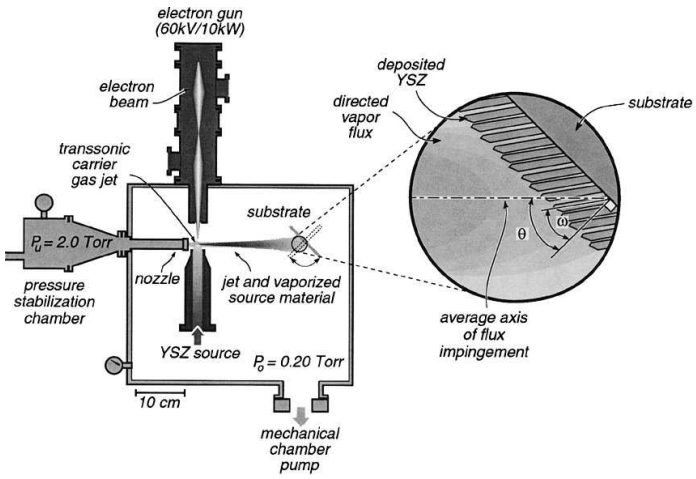

Figure 60 EB-DVD process for zig-zag TBCs[71]

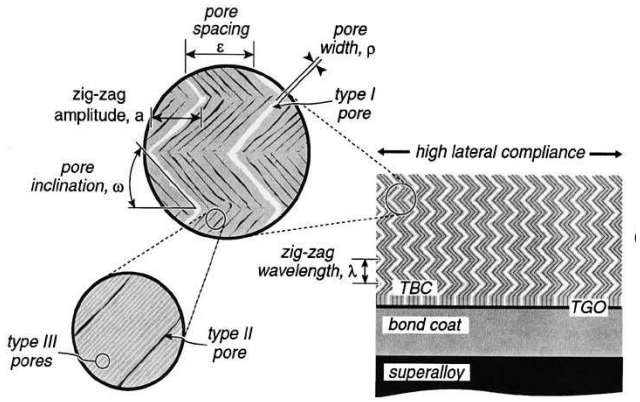

Figure 61 Microstructure of zig-zag TBCs[71]

In order to reduce the thermal conductivity of EB-PVD TBCs, Wolfe *et al.* (2005)[179] describe a "tailored" microstructure of the columns. The principle is to make layers on the ceramic by periodically interrupting the condensing of the vapour, i.e. periodically remove the substrate from the vapour flux ("in and out"), or "shutter" it. Similar works were achieved by Nicholls *et al.* in 1998[51]. First, layering creates interfaces acting like chicanes for photons of the radiated heat; second, it increases the global porosity of the ceramic, hence reduces the thermal conduction. The "shutter" method has less influence on the global TBC microstructure as the substrate surface is not as cooled before redeposition as it is for the "in and out" method. However it still gives interesting results, with thermal conductivity reduced to 1.2W/mK for the best configuration. Moreover, the shuttered process gives better result on cyclic oxidation lifetimes than traditional TBCs (this last point is not very well discussed by the authors). The advantage of this process is that it can be easily shifted to the industrial process, by adding a shutter in the deposition chamber. Moreover, it can be combined with new generation ceramic TBCs (pyrochlore based or stabilised with gadolinia, or dysprosia).

On the process of ceramic deposition itself, some recent papers focused on a Metal-Organic CVD (MOCVD) route[180]. The coatings of YSZ are produced from different organo-complex of Zr and Y with $Zr(org)_4$ and $Y(org)_3$ stoechiometries (where org can be acetylacetonate (acac), dipivaloylmethanate (dpm), 2, 2, 6, 6, -tetramthyl-3, 5, -heptanedionate (thd)). The coating microstructure is columnar (see Figure 62), and the deposition rate is quite fast, up to hundreds of microns an hour (really faster than conventional halide CVD with a $ZrCl_4$ precursor). The crystal structure of the film changes with the content of Y_2O_3 (m+t at 0-2mol%, t only at 2-8 mol%, and c above 8 mol%). This route is promising due to the numerous advantages of CVD from the manufacturing point of view compared with PVD deposition processes (e.g. batching, energy costs, no high vacuum…).

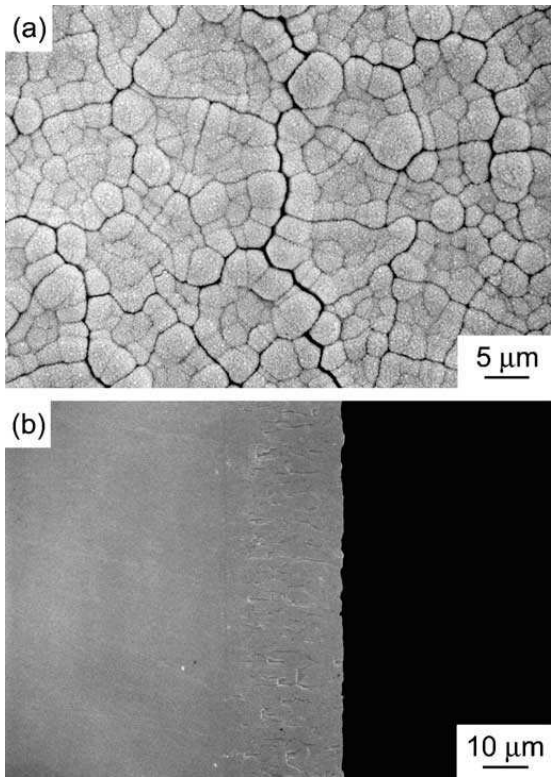

Figure 62 Morphology of a YSZ film prepared by MOCVD[180]

I.5.3 Analytical tools

Non destructive analysis is a key tool for industrials by allowing reliable quality control of the production. Moreover, TBCs are intrinsically complex

Taylor *et al.* published in 1999 a comparative study[181] of different techniques of TBC thermal conductivity measurement: the laser flash, the 3-omega and the photoacoustic methods. Sensitivity and accuracy of the three processes are discussed.

Two articles published by Feist[182;183] are not directly dealing with high-temperature coating analysis, but they may be quite interesting to be quoted: A new way of TBC surface temperature measurement is described. This method is based on doping the EB-PVD ceramic with a phosphorescent element, dysprosium, then exciting it with an UV emission laser (YAG:Nd) and finally measuring the photon reemission with an UV spectrometer. The transition energy and the decay time from an excited quantum level to the stable one, the luminescence, can then be measured, and the values compared for different temperatures. This method gives an alternative to the "in service" temperature control with a precision of +/- 2.6% from 534°K to 950°K as described in Feist *et al.* paper (recent presentations from the author give a temperature in excess of 1125°K). This method allows also an imaging of the ceramic degradation with time.

The use of rare earth element doping for photoluminescence analysis after excitation of TBC by a laser in order to make temperature sensing is also discussed in a paper from Santa Barbara team[184]. The concept was described is similar to the work from Feist. The authors of this paper also discuss about problems in phase compatibility and concentrations of chromophore elements leading to absorption phenomenon.

Glow discharge mass spectrometry is a powerful (but destructive) way to analyse depth profile (in the range of 1-100µm). This was applied by Spitsberg *et al* [185] from *General Electric*s to detect the presence of sulphur, potassium and calcium in β-NiAl platinum modified coatings. These impurities are mainly due to the processing route.

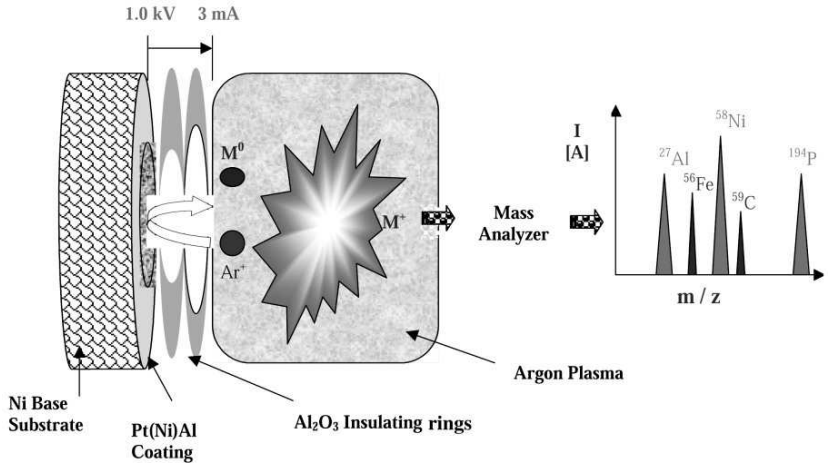

Figure 63 Glow discharge mass spectroscopy principles[185]

The powerful PSLS analytical method which is now well used for TGO studies was clearly described in a paper by Clarke *et al.*[186] in 1997. This non destructive piezopectroscopy analysis is based on the luminescence of Cr^{3+} dopants in the TGO. The luminescence effect is triggered by a laser beam whose energy is high enough to go through the YSZ, and corresponds to the optical absorption band of Cr^{3+}. The spectrum of re-emitted photons is then recorded. This method enables to detect the presence of transient alumina through the TBC thickness: the spectral peaks are characteristic for each allotropic form. α-alumina shows two typical R1 and R2 peaks roughly at 14370cm^{-1} and 14415cm^{-1} sometimes called the "R-line" θ-alumina also produces peaks in different energy bounds, therefore phase transformation within the TGO during oxidation tests can be detected. Moreover, the magnitude of the in plane-stress of the oxide is able to be measured because the re-emitted photons energy will be shifted in wavelength. The frequency shift is directly proportional to the stress: 7.61 cm^{-1}/GPa for the R2 peak. Peak broadening is due to a stress gradient in the analysed volume.

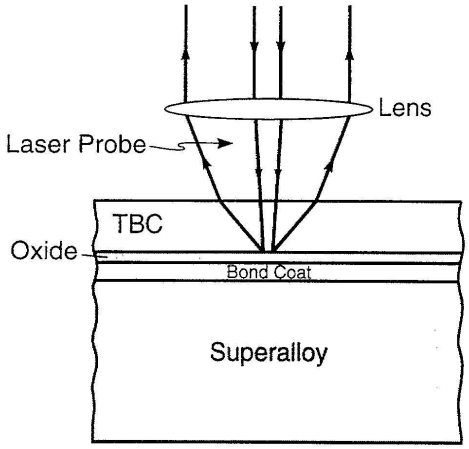

Figure 64 Optical arrangement to excite and collect the R-line[186]

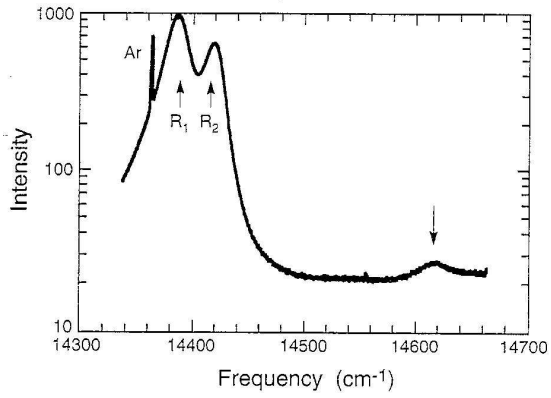

Figure 65 Typical luminescence logarithmic spectrum; R1 and R2 standing for α alumina, the arrow showing a θ-alumina peak[186]

The luminescence analysis of the TGO was used by Tolpygo *et al.* in 2004[187] to make a non destructive analysis of the TBC failure at the microscopic scale. The failure of the interface (triggered by bondcoat rumpling for instance) results in a steady release of the elastic strain in the TGO, which can be monitored by luminescence spectroscopy. The correlation between the TGO/bondcoat damage and the shift in TGO luminescence frequency was demonstrated in this

paper by cross section observation. Finally, the PLPS allows to see the difference between stress change due to θ to α transformation and the stress built during the TGO growth[188].

An alternative to piezospectroscopy analysis for predicting TBC failure is infrared monitoring. This method was described by the team of Stuart Saunders, from the National Physics Laboratory, UK, during the TBC workshop of November 2004, and in a paper published in 2005 by an American team[189]. It was previously used in 2000 by the team from Oak Ridge[190] for APS TBC damage monitoring during mechanical testing. The principle is to heat the TBC coated coupon, and to observe the infrared radiating, whose intensity changes depending on the good interface between the ceramic insulative layer and the metal, hence the failure zone can be monitored. This analytical method is non destructive and is far easier to set up than piezospectroscopy, the analysis time being seconds instead of hours. The spatial resolution is better than spectroscopy (around $0.5mm^2$)[189], but the infrared radiation offers a poor quantitative result, and if area that will fail can be detected, it is still tricky to know when it will occur. At least, the piezospectroscopy gives a quantitative value of the TGO stress.

The third non destructive method for TBC degradation monitoring which is widely described is impedance spectroscopy. The concept is to link the state of degradation of the TBC with its electrical properties, an equivalent AC circuit can be drawn (see Figure67: R_s refers to the resistance of the electrolyte solution, $R_{YSZ}C_{YSZ}$ refer to the topcoat resistance and capacitance, R_PC_P to those of the pores in the ceramic, and R_TC_T to those of the bondcoat). The first paper describing this method is from a Japanese team, published in the *NDT&E International*[191] [192]. This method was then used by other teams, such as Song *et al.* on a degraded TBC cut from an after service turbine[193] or, more interesting, Jayaraj *et al.* who made some impedance analysis during cyclic and isothermal oxidation of TBC's. One of the main results of this latter study is that the TGO thickness, measured by weight gain is clearly inversely proportional to its capacitance[194] (Figure 66).

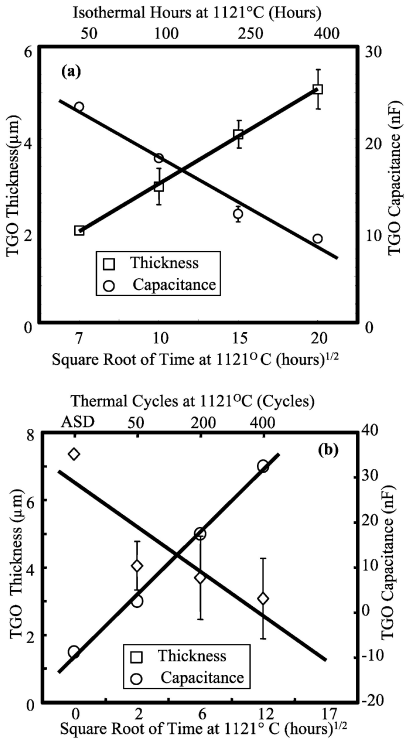

Figure 66 Comparison between TGO thickness and capacitance as function of time for isothermal and cyclic oxidation

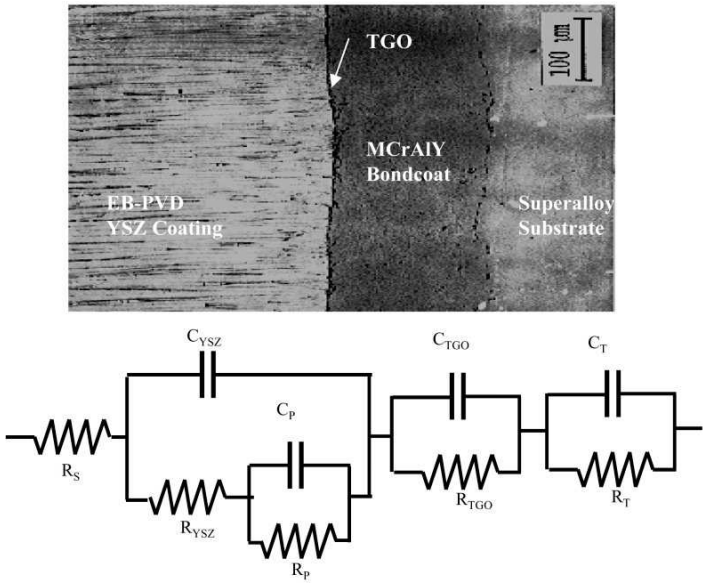

Figure67 Picture and corresponding AC circuit for MCrAlY/EB-PVD YSZ TBC

Another non destructive method is X ray and neutron imaging. While conventional microscopy (SEM and TEM) studies reveal the nature of the microstructural features in TBCs, quantitative microstructural information is sought using high-resolution X-ray microtomography (XMT) along with ultra small-angle X-ray scattering (USAXS) and small-angle neutron scattering (SANS). The goal is to obtain insights into the microstructure with respect to porosity, its dimensions and the pore size distributions of open and closed porosity in 3D along with the porosity gradient[195].

Continuous thermogravimetry of cyclic oxidation is a very powerful analytical tool recently developed in the Cirimat at Toulouse by Monceau *et al.* The facility itself was described during Les Embiez Conference in May 2004. A very complete paper was published in *oxidation of metals*[196] and describes a new methodology shifted from the isothermal thermogravimetry, in order to determine the net and the gross mass gain, the total mass of spalled oxide. It also allows to carry out TGA while conducting thermal cycling of TBC systems.

I.5.4 Processes and Manufacturing

An industrial-size cathodic arc evaporation device was described in 2003 by Ducros *et al.*[197]. This facility was designed for cutting tools multilayer hard coatings, but may be interesting when thinking to the industrial shift of Low Mass Bondcoats production. Cathodic arc evaporation will still be a batch process, but present an alternative to the sputtering process.

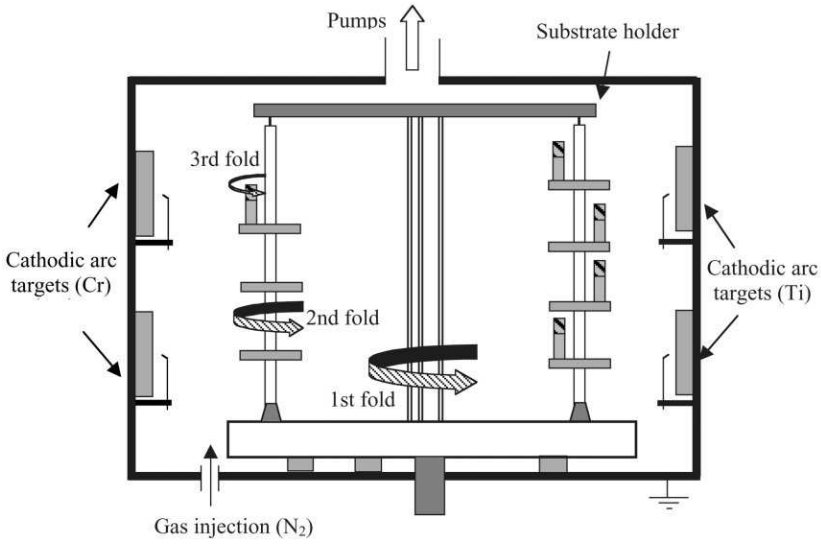

Figure 68 Large size arc evaporation PVD coater (here for TiN/CrN multilayers)[197]

Multilayer coatings can be achieved by EB-PVD method by different ways:

- ✓ with a single rod with a single beam: if the rod is an alloy, a pulsed modification of the beam intensity leads to a pulsed modification of the vapour composition and therefore a variation in the coating composition along the thickness
- ✓ With two rods and two beams: it is equivalent to a double plain EB-PVD coater (but two beam guns costs a lot of money)
- ✓ With two rods and one beam: this is the jumping beam technology

The first system is limited by the difference of vapour pressure and melting point of the rod compounds and the jumping beam clearly described by Schulz *et al.* in a paper published in 2000[198] is a cheap and good alternative. The beam frequency is the most critical parameter and has to be set up with consideration of the freezing time of the rod materials, see Figure 69 (as long as the top is liquid, the vapour deposition is still running). This system has been used in the reported study for the manufacturing of ZrO_2 and CeO_2 multilayers: these oxides have 3 order of magnitude different vapour pressure values at 2500°C (respectively 4.10^{-5}atm and 2.10^{-2}atm). Multilayer

coating obtained with the jumping beam have a less scattered concentration of Ce along the thickness.

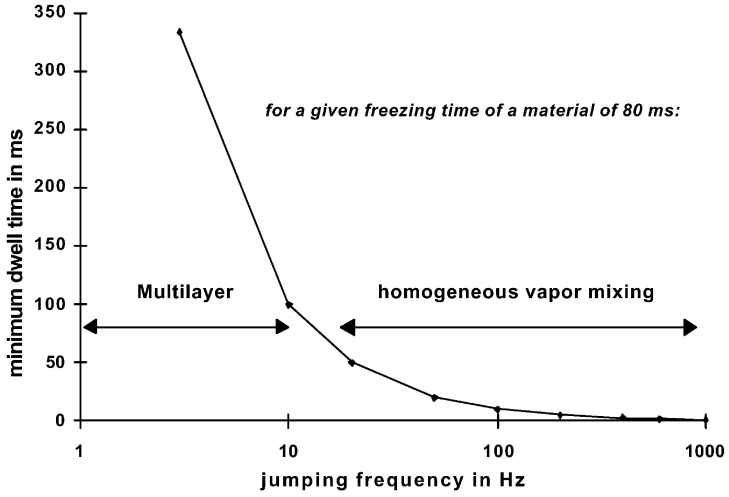

Figure 69 Influence of the jumping frequency on the coating microstructure[198]

Plasma Enhanced Chemical Vapour Deposition (PECVD) is a promising alternative technique to the EB-PVD for TBC deposition. A study published by Préauchat *et al.*[199] from the ONERA describes this method and its advantages. The deposition is carried out at 700°C or 900°C and its rate is quite high (>250µm/h); the microstructure is more porous than EB-PVD resulting in a lower thermal conductivity when the deposition temperature is 700°C (1.3+/-0.3 $W.m^{-1}.K^{-1}$ instead of 1.5-1.8 for the EB-PVD). However these coating are more susceptable to the phase transformation of the t' tetragonal phase into a low (t) and a high (t'_1) yttria tetragonal phase .t'→ t + t'_1. These coatings are therefore said to be excellent candidate for application as TBCs below 1000°C.

The production of TBC by a one step (bondcoat and ceramic) EB-PVD process is described by Mochvan and Yakovchuk in 2004[200]. The idea is to manufacture an ingot having the materials for both the bondcoat (in this study NiAl or NiCoCrAlY) and the ceramic (in this study YSZ or YSZ+ GdSZ or HfSZ). The interest of this process on a manufacturing point of view is obvious (1 step only for a full TBC deposition process), but the design of the ingot is complex, and a single ingot can be used only for one single batch. The design of the ingot is described in Figure 70 and Figure 71.

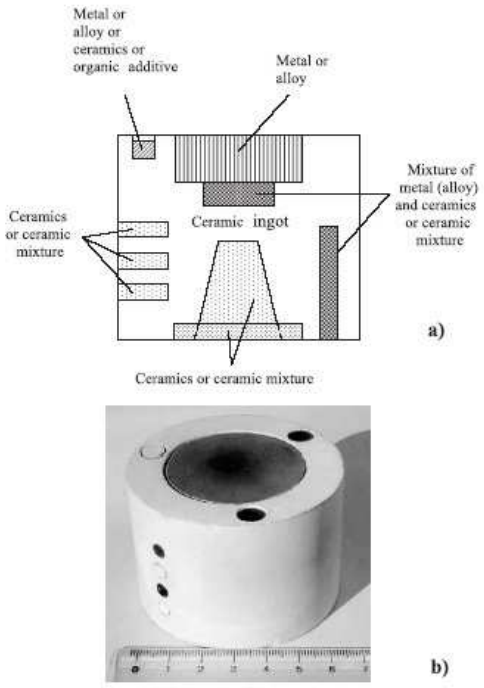

Figure 70 Structure of a composite ceramic ingot for graded TBC[200]

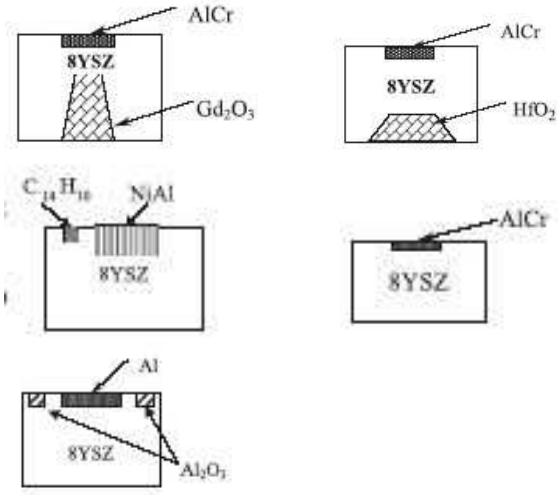

Figure 71 Ingot design for 5 types of graded TBCs[200]: NiCoCrAlY/YGdSZ; NiCoCrAlY/YHfSZ; NiAl/YSZ;NiCoCrALY/YSZ;NiCoCrAlY/NiAl+Al_2O_3/YSZ

Resulting coatings are named "graded TBC" and show two transition zones, between the superalloy and the substrate and between the bondcoat and the ceramic. Moreover, performances are said to be better than classical two steps EB-PVD TBCs (more than 400 cycles at 1150 °C instead of 250). However this process is not competitive for platinum modified bondcoat systems: it would waste too much noble metal.

Chapter II

Project description

II.1 The ternary system Ni-Al-Pt at high temperature

II.1.1 Brian Gleeson work

Brian Gleeson et al. presented a key paper at Les Embiez conference in 2004 concerning the effect of Pt on nickel aluminides[104]. Before this paper only two version of the ternary diagram of the Ni-Pt-Al system were available, a speculative version at 1060°C[8], and a version at 1100°C from informal discussion with Gleeson in 2002 (Figure 72).

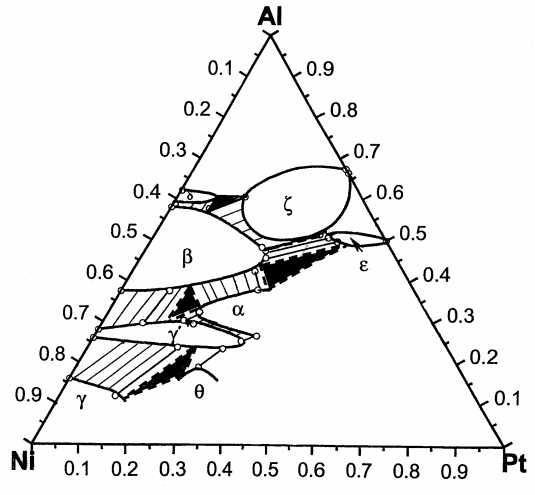

Figure 72 Al-Pt-Ni diagram as informally proposed by Gleeson in 2002

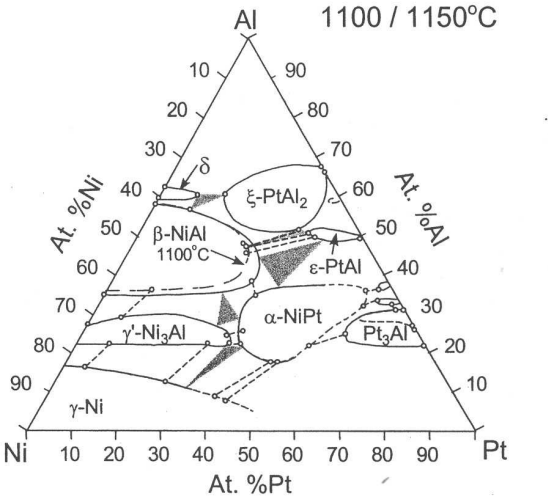

Figure 73 Ni-Pt-Al ternary diagram as proposed by Gleeson in 2004[104]

As one can see these diagrams show the main compounds used for platinum modified compounds used in high temperature oxidation protection. The high solubility of Pt in NiAl, γ, and γ' is outlined by these diagrams as the very large stability field of $PtAl_2$. These diagrams show as well the presence of a platinum rich phase, poorly described so far: the α-phase (see next paragraph).

The point of Gleeson study was to demonstrate by diffusion couple experiment the role of Pt in γ'. It was proven that Pt modified γ-γ' compound add excellent oxidation performance due to the fact that Pt reduces the Al activity in this phase. As a consequence, uphill diffusion of Al was observed in a γ-γ' diffusion couple. The main objective of this work was to support the

development of the Pt modified γ+γ' coating. It proved at the same time that adding a reactive element would further improve the TGO adherence and reduce the oxidation kinetic.

Two ternary diagrams were published more recently, during the HYPERCOAT European research project, and in a paper published by Hayashi et al.[201] (both from Gleeson's team). The first one (Figure 74) shows a double stability field for the α-phase: α'' and α'. Though it was not possible to discuss this with the author as this diagram is part of a specific research project, the presence of these two phase fields is arguable. The structure of the α-phase compound is $L1_0$ (see next paragraph and chapter IV), which corresponds to the structure of the martensitic phase of β-(Ni,Pt)Al. Gleeson chose to differentiate this phase onto the diagram, close to the β phase stability field, α'', which is likely to extend its stability "under" β at lower temperature, when the martensitic transformation occurs. Moreover, this α'' corresponds to the $AuCu_3$ type structure of the binary Ni-Pt at 25 at% Pt and the α' phase would corresponds to the AuCu structure compound (see chapter IV). This latter phase corresponds to the one which will be related as the "α-phase" in this thesis. It is the ternary intermetallic described in the chapter IV.

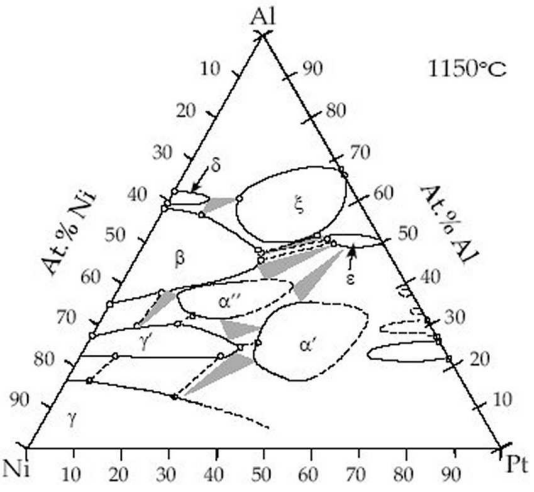

Figure 74 Ni-Pt-Al ternary diagram at 1150°C from HYPERCOAT

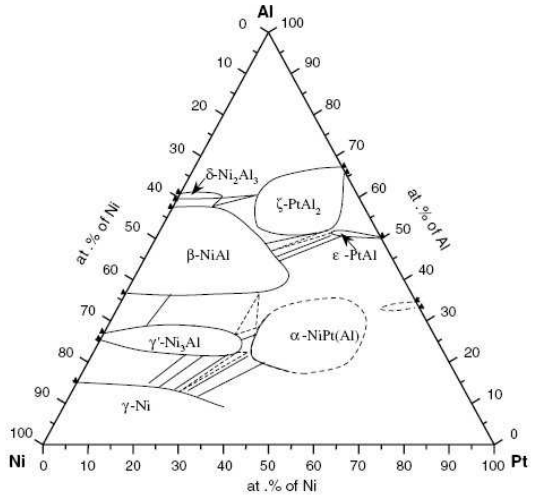

Figure 75 Ni-Pt-Al ternary diagram at 1100°C[201]

As one can see, very few information was released on the Ni-Pt-Al system at high temperature until 2002, which was not relevant to the fact that platinum modified aluminides have been for years before. On the opposite, many information was released since, pushed by the interest of industrials in Pt modified γ+γ' compound for high temperature oxidation protection. The first of this diagram is one of the starting point of the thesis because it outlined the presence of this new compound poorly described in the literature: the α phase.

II.1.2 The alpha phase

The earliest paper describing this compound was published in 1994 by Kamm et al.[202]. The point of this study was to study the evolution of structures between the two $L1_2$ structures Ni_3Al and Pt_3Al when balancing the Ni/Pt content for a fixed content of Al at 25at% after an annealing at 1100°C for 7 days. The authors discovered that from a Pt content greater than 25at%, a new compound started to form, with a $L1_0$ structure (the maximum solubility of Pt in $(Ni,Pt)_3Al$ being therefore 25 at%. From ≈35 at% Pt, no $L1_2$ is left, only this $L1_0$ phase is observed. The athors didn't find the $L1_0$-Pt_3Al stability limit. The structure proposed for the $L1_0$ phase is a tetragonal cell, with Al entirely placed on the corner sites. Ni atoms stand on the middle of the (001) faces and Pt atoms on (100) and (010) faces. This ordered structure is similar to Pt_2CuAl.

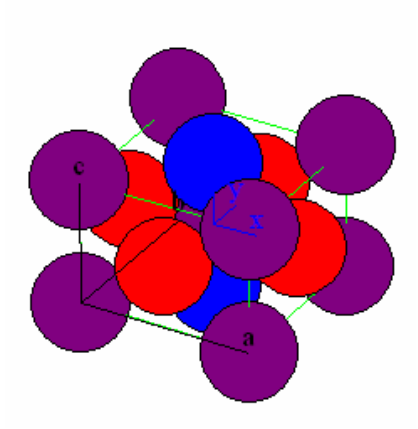

Figure 76 Structure of the $NiPt_2Al$ compound by Kamm et al. (Al in purple, Ni in red, Al in blue)

More recently, in 2003, Meininger et al. published a similar study [203]. These authors were tracking a solid solution between the two compounds Ni_3Al and Pt_3Al, but always formed this ternary compound with the $NiPt_2Al$ stoichiometry. A precise XRD pattern of this phase was published at this time. The study concludes by comparing the distortion of the lattice to a tetragonal system with the parameters $c/a<1$, similar to the Pt-Cu-Al and Pt-Ga-Al systems.

In May 2005, Brian Gleeson's team which is clearly involved in the investigation of high Pt content modified aluminides published a study entirely focused on the $NiPt_2Al$ compound[201].

More details on the α-$NiPt_2Al$ compound can be found in the Chapter IV of this thesis with experiments which were carried out during this project.

II.2 Manufacturing intermetallic coatings

II.2.1 Synthesis of intermetallics by solid phase diffusion.

Intermetallic compounds can be obtained by crystallisation form the liquid state and also as a result of reactions in a solid phase. The formation of intermetallics due to reactive diffusion, at solid state, is a typical first order transition[204]. This formation is realised by the formation and growth of at least one new phase due to diffusive interaction between two initial phases. In the simplest case of interaction between two metals A and B, only one intermetallic phase AmBn is formed at the interface. This is the method used in the characterisation of a thermodynamic system by diffusion couples.

However, once an intermetallic is formed at the interface, the reaction can carry on if there is enough reservoirs in each side of the formed intermetallic. It becomes a mechanism controlled by diffusion in the intermetallic structure.

II.2.2 Platinum aluminides: Colgan's work

Evan G. Colgan published a study on overlay platinum aluminide coatings in 1987[47]. The context of this study is thin film technology for micro-electronic application; the author worked later in IBM research centre. The point of this study is to manufacture diffusion barrier based on Pt/Al multilayer on Si/SiO_2 wafers. Colgan studied the effect of the relative thickness of the Pt/Al layer and the heat treatment to form platinum aluminides. Depending on the temperature, various compounds from the Pt-Al binary system are manufactured, based on the relative stability of each of these compounds. The layers were deposited by evaporation PVD, and analysed after reaction bt XRD and Rutherford backscattering spectrometry (RBS).

The initial phase formed when Pt and Al reacted was always Pt_2Al_3, at 225°C. The reaction proceeds until all the Pt or Al is consumed. Then the next more Pt or Al rich compound is formed depending on the overall stoichiometry. However, it shows that thermodynamic driving force is

not related to the phase formation sequence of the next compounds. In overall at temperatures over 450°C, the Pt-Al system ends up with the formation of Pt_3Al.

An interesting result demonstrated in this study is that the phase formation is rather controlled by the Al content as it is the dominant moving species. It was measured by RBS that after a 60 min annealing at 250°C, for every Pt atom which moved by a marker, approximately 90 Al atoms did.

II.2.3 Intermetallic coatings at Cranfield University

A Ph.D. thesis was carried out at Cranfield University between 1991 and 1995 by M.J. Deakin on intermetallic coatings for Ti alloys[205]. The aim of this study was to manufacture diffusion barriers between an oxidation protective overlay and the Ti alloy substrate. These diffusions barriers were produced to limit the oxygen ingress into the Ti alloy, detrimental for mechanical properties. Intermetallics were chosen for their high temperature stability, and ordered structure, such as binary aluminides. $PtAl_2$, TiAl and $MoAl_3$ compounds were applied by different process. The most promising system is $PtAl_2$, as it was the best system in preventing diffusion of Ni from the Ni20Cr overlay towards the substrate at 800°C and has an inherent oxidation resistance as an alumina forming system. This $PtAl_2$ was deposited by a sequential PVD sputtering route for pure Al and pure Pt films with the relevant thickness ratio, followed by an annealing at low temperature triggering the reaction of the metal layers. This method was protected by a patent[206], but is no longer available.

II.2.4 Low Mass Bondcoat at Cranfield University

II.2.4.1 Bertrand Saint-Ramond

Bertrand Saint Ramond worked 2 years on developing the low mass bondcoat concept at Cranfield, in 2000 and 2001[207]. The aim of his study was to demonstrate it was possible to manufacture a platinum aluminide coating by sequential sputtering of Pt-Al multilayers on Ni based superalloy substrate. The main difference with Deakin's works is the temperature at which these coating were tested: over 1100°C as these systems were tested as potential environmental

coatings for turbines hot parts. Moreover, the work was focused both on increasing the number of layer in the sequential sputtering and investigating other binary platinum aluminides (such as $PtAl_2$, PtAl, Pt_2Al_3, Pt_8Al_{21}) as potential high temperature environmental coatings.

B. Saint-Ramond did some work on tracking the reaction of the metal layers into intermetallic compound. He sputter coated a 1.5µm thick foil of Al with Pt, with the relevant thickness corresponding to $PtAl_2$ and PtAl, and loaded this sample in a differential thermal analysis (DTA) facility. The exothermic reaction peaks were observed for temperatures comprised between 350°C and 500°C, depending on the number of layer (AL/Pt or Pt/Al/Pt systems) for both stoichiometries, see Figure 77. $PtAl_2$ forms at lower temperature than PtAl which is relevant with their relative enthalpy of formation, PtAl being more stable than $PtAl_2$. Moreover the more layers the lower the triggering temperature, outlining the fact that increasing the number of interfaces increases the potential energy in the system making it more reactive.

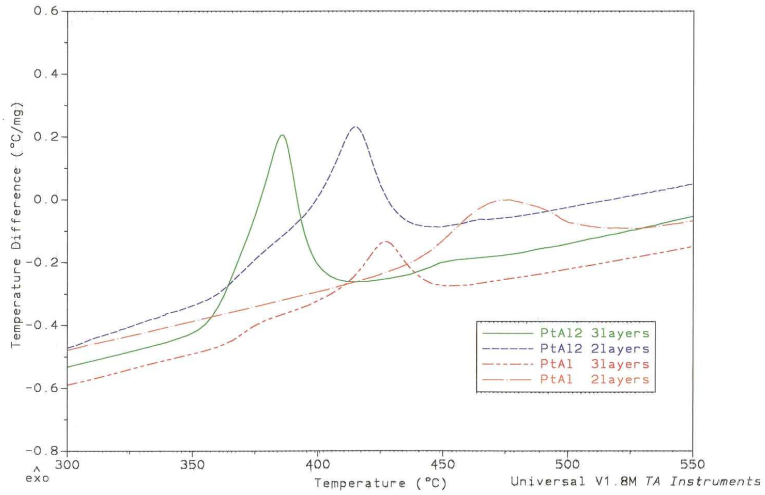

Figure 77 DTA results on PtAl and $PtAl_2$[207]

As platinum aluminide are alumina former they can be used for high temperature oxidation or as a bondcoat for TBC. These coatings are very thin because of the low deposition rate of PVD, and because of the high Pt content. Their main potential application is therefore in avoiding the patent protecting the traditional bondcoat manufacturing for TBC, as bondcoats are less exposed than environmental coating to degradation form external source such as erosion, which would be detrimental for an overlay of 10 µm roughly.

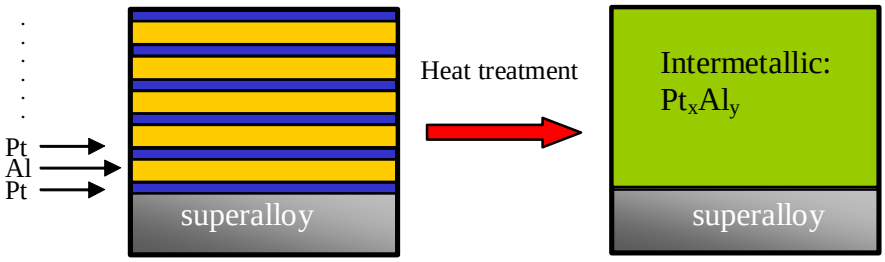

Figure 78 Concept of multilayer sequence for intermetallic coating manufacturing

The multilayer sequential deposition of Pt and Al layers on superalloy coupons was developed in this study and called "low mass bondcoat" due to their relative lightness compared to commercial systems. Systems up to 300 layers were manufactured, but the main study focused on systems with typically 9 layers of metals. The effect of annealing temperature and time was studied.

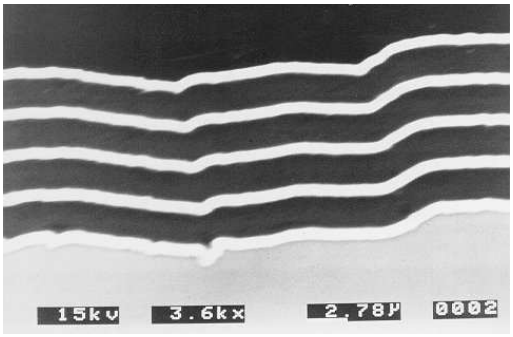

Figure 79 9 layers system (Pt/Al/Pt...Pt) with $PtAl_2$ stoechiometry on superalloy[207]

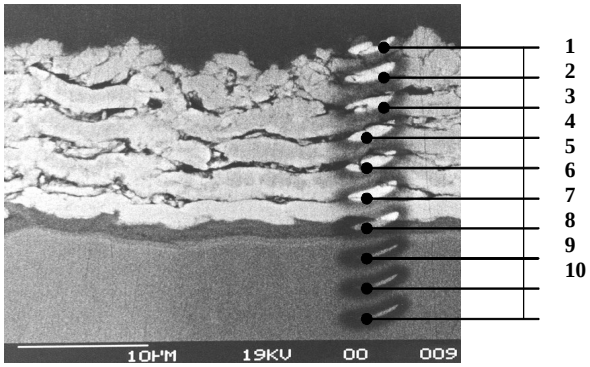

Figure 80 9 layers system after 2hrs at 700°C[207]

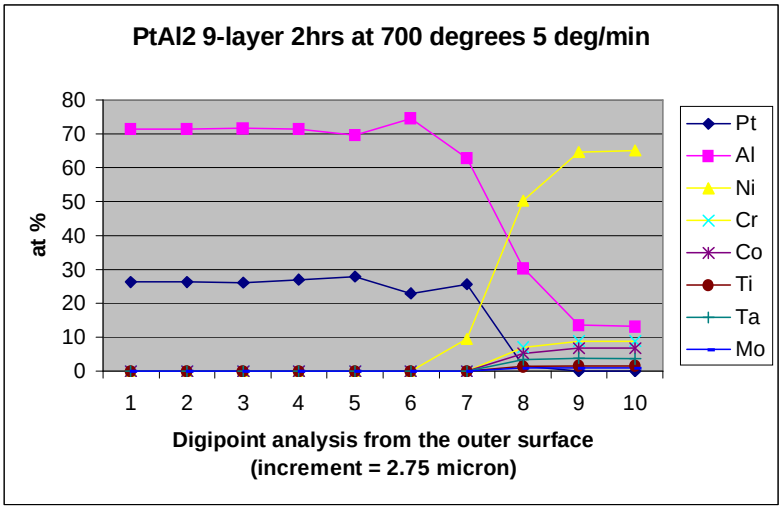

Figure 81 Concentration profile across the 9 layers system after reaction[207]

The PVD gives very homogeneous overlay across the thickness (Figure 79). However this method produces coatings with some remain of the multilayer pattern after the reaction occurred during the annealing at 700°C under vacuum (Figure 80). The composition control though is excellent, with a constant stoichiometry across the coating though a 2µm interdiffusion zone is observed.

In order to assess the potential of these PVD coatings as bondcoats for TBC systems their cyclic oxidation behaviour was tested at 1100°C in air. Figure 82 gathers weight gains under cyclic oxidation of CN91 commercial systems, and $PtAl_2$ and PtAl low mass bondcoats with of 7.5µm total thickness.

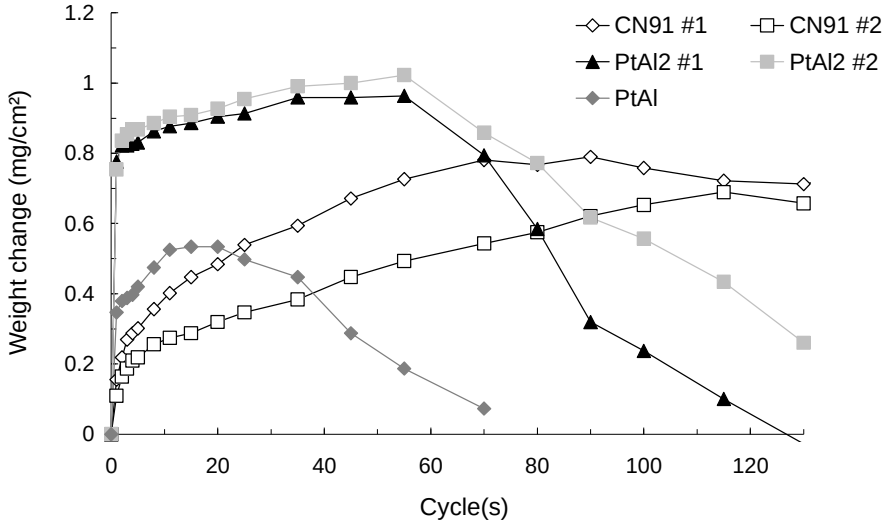

Figure 82 Some cyclic oxidation weight gains at 1100°C for some aluminides coatings[207]

As observed in Figure 82, the first sample to spall is the Low Mass Bondcoat PtAl, then the Low Mass Bondcoats $PtAl_2$ and finally the CN91 samples. For ten times thinner systems, Low Mass Bondcoats exhibit a critical oxide thickness of the same order of magnitude as CN91, or even better for the $PtAl_2$ stoichiometry. Furthermore, Low Mass bondcoats exhibits an initial rapid oxide growth followed by a slower parabolic growth: the scale reaches virtually its final thickness during the first few cycles and then grows very slowly. Such oxidation behaviour is consistent with an initial rapid transitional alumina formation and then a rapid transformation to a protective α-alumina scale.

II.2.4.2 Manuel Silva

Manuel Silva worked at Cranfield on Low Mass Bondcoat systems in 2001 and 2002[208]. His study was more focused on the ageing mechanism of platinum aluminides manufactured by the sequential sputtering method. He tested the high temperature behaviour of various intermetallics from the Pt-Al binary system with a ceramic topcoat to form a complete TBC system.

The main difficulty M.Silva was confronted with was poor adhesion of the thin films due to roughness of the superalloy substrate (Snecma nickel based, AM1). After a systematic study on the substrate roughness, he concluded that:

- ✓ For coatings with a total thickness below 4µm, R_a should be comprised between 0.023 and 0.140µm
- ✓ For higher thicknesses, R_a should be greater than 0.040.

A surface finish of 600 grit, which corresponds to the surface finish of a turbine blade after machining, is a good compromise as it stands within these specification and minimise the required surface treatment.

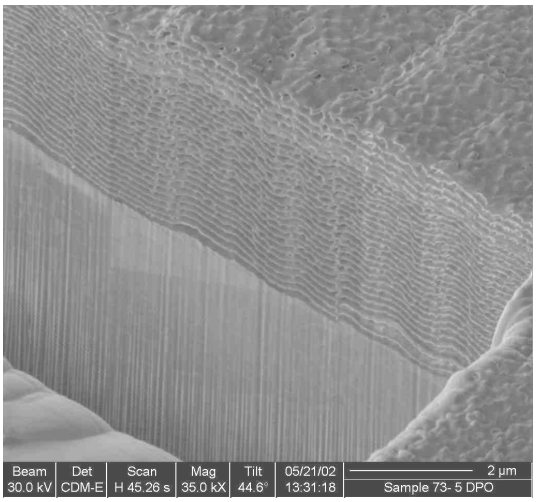

Figure 83 FIB section of a 50 layers low mass bondcoat system ($PtAl_2$)[208]

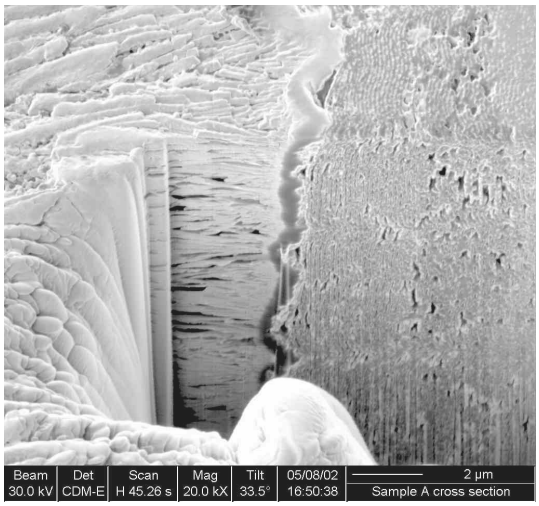

Figure 84 FIB section of the same system topped with EB-PVD deposited YSZ[208]

Cyclic oxidation tests were carried out on different bondcoats topped with EB-PVD yttria stabilised zirconia: CN91 diffusion bondcoat and three different Low Mass Bondcoat compositions, PtAl, $PtAl_2$, and Pt_2Al_3 (Figure 85). In order to compare results, corresponding aluminium reservoirs of all the systems are plotted (19.9 mg/cm² for CN91). Thermal cycling lifetime is not proportionally linked to the Al reservoir, but the Pt_2Al_3 bondcoat exhibits roughly the same

performance as CN91 although it is ten times thinner and aluminium rich. The $PtAl_2$ bondcoat, which is only 2.5 µm thick, and contains 40 times less aluminium than CN91, has a lifetime above 600 cycles at 1100 °C. The PtAl composition shows less promise, with performances comparable to the 2.5 µm thick $PtAl_2$ despite it being 8 µm thick and contains more aluminium (1.12 mg/cm^2).

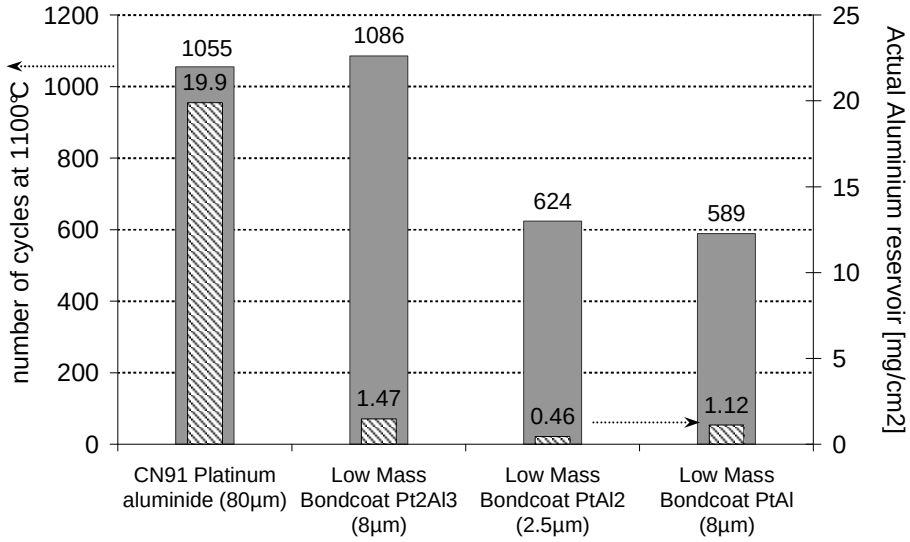

Figure 85 Lifetime of TBC systems for 20%ceramic spallation and corresponding Al reservoir[209]

These thermal cycling lifetime are very promising indeed, and shows the potential of low mass bondcoat as an industrial alternative to tradiational diffusion bondcoat systems.

II.3 Current project objectives

The ternary diagram of Pt-Ni-Al at 1100°C and the low mass bondcoat deposition process are the two starting point of the current project. The α-phase has to be investigated as a new potential high temperature protective compound. This phase is a potential bondcoat for TBC systems because:

-It seems to be a stable phase for the diffusion system, because it was observed during oxidation tests of platinum aluminide overlay bondcoats.

-It is rich enough in Al to be a good alumina former.

-It seems to be wide enough to prevent short-time phase transformation by the augmentation of Ni (from the substrate) and diminution of Al (to the TGO)

-It also seems to be wide enough in composition to provide a reproducible industrial production process.

-This intermetallic phase can be tested at laboratory scale by the low mass bondcoat sputtering process developed during the first studies.

-We already know an important drawback: this phase is Pt rich and will therefore be expensive compared to the β-(Ni, Pt)Al phase. In comparison, CVD processes for complex platinum aluminides use an average of a 7µm thick platinum layer. But this high cost can be decreased by the low mass system that uses less material.

Thus the aim of this Ph.D. study is to identify the α-phase, its structure and its thermodynamical, mechanical, chemical properties. The first stage is to determine the stability field of this phase, on the ternary diagram at 1100°C. During this work, crystallographic symmetry and lattice parameters will be measured.

The second stage is to test the ability of this composition to be coated as were platinum aluminides in B. Saint-Ramond and M. Silva studies. This implies using the low mass bondcoat process, with aluminium platinum and nickel multilayers, and afterwards triggering the in situ exothermic reaction that takes place between the mono-elemental coated layers, during heat treatment at an average of 700ºC. The reproducibility of the process has to be assessed, with cheaper nickel-chromium alloys first, and then on nickel based single crystal superalloys.

Once α-phase based coatings have been successfully manufactured, performances of such systems have to be measured. Cyclic and isothermal oxidation are the classical testing method for oxidation resistant systems. These experiments will be carried out on simple α coated systems, and full TBC coating, with a ceramic layer. For that purpose, the process with rotating samples will be adapted in order to coat both faces of the substrate.

The parameters of α-based Low Mass Bondcoats manufacturing process (e.g. global composition, number of layer, alternation pattern, adding a fourth element…) will be optimised for better oxidation and TBC lifetime performances. And, at last, the process will have to be switched to a higher productivity process, more compatible with an industrial activity.

Every main step of the project is described in the following work breakdown structure chart.

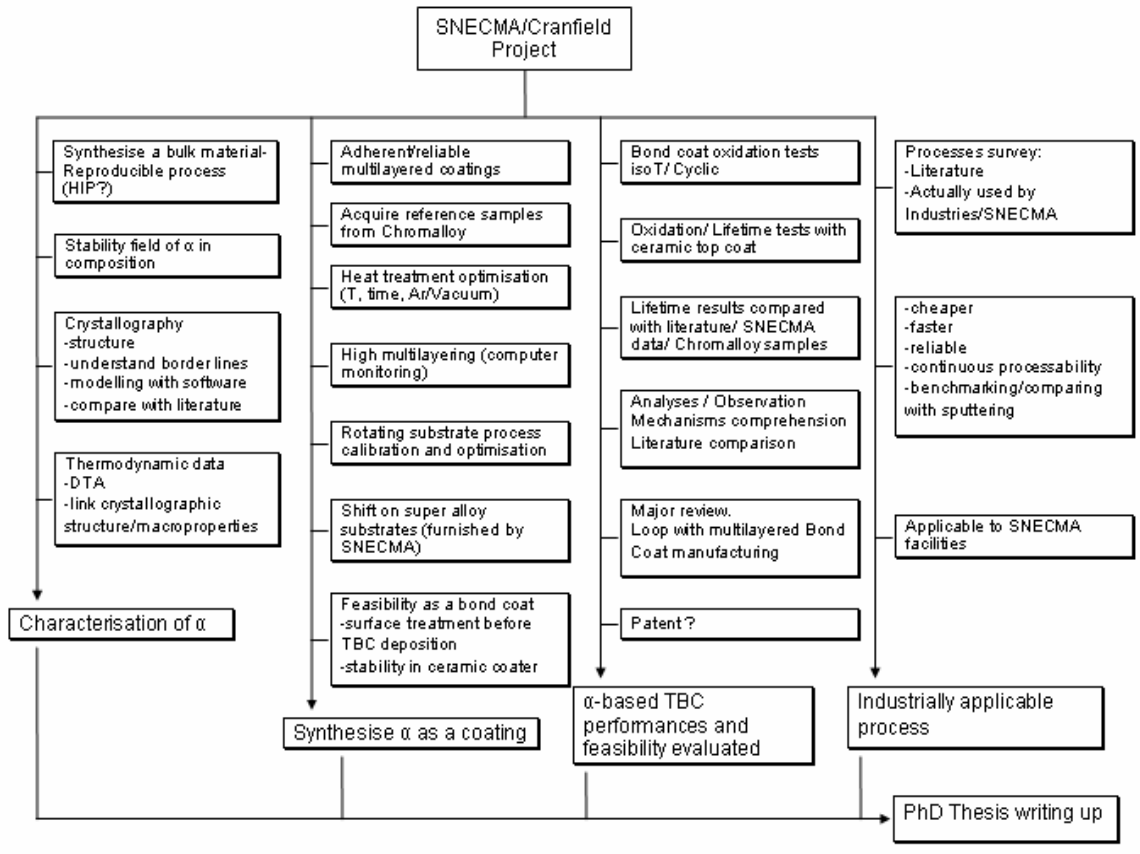

Figure 86 Work breakdown structure chart for the current project

Chapter III

Experimental Procedures & Facilities

III.1 Intermetallic coatings deposition procedure

III.1.1 Substrates specification and preparation

Coatings were produced either on Nickel-Chromium alloy (Nimonic 75) or on single crystal superalloy AM1 low sulphur, from Snecma. NiCr alloy is cheaper and was used initially in this study. NiCr samples were cut in square from a raw 1.5mm thick sheet. AM1 samples were cast at Snecma with the same procedure as HP single crystal blades. Superalloy sample were machined from a single crystal rod into 2 and 3mm thick discs, 24mm diameter. Compositions of both alloys are given in Table 5.

Table 5 Chemical composition of Nimonic 75 and AM1 in at% (data from manufacturers)

	Ni	*Cr*	*Al*	*Ti*	*Si*	*Mg*	*Fe*	*Cu*	*C*	*Co*	*Mo*	*W*	*Ta*
NiCr	Bal	18-21	-	0.2-0.6	<1.0	<1.0	<5.0	<0.5	0.08-0.15	-	-		
AM1	Bal	7-8	5.1-5.5	1-1.4	-	-	0.2	-	-	6-7	1.8-1.2	5-6	7.5-8.5

When cutting was needed, it was carried out on a precision saw "ATA brilliant 220" with a SiC wheel and water base lubricant. Wheel rotating speed was set at 2800rpm and sample translation at 1mm/min. When cutting a coated sample, the sample was laid out so the wheel cuts "into" the coating in order to prevent any spalling.

Samples were either ground or grit blasted prior to deposition. Grinding was carried out with SiC grinding paper at 240grit and then 600grit. Few samples were ground up to 4000grit finish; this was achieved with a grinding at 1200grit, then 2500grit and finally 4000grit. Grinding was carried out on manual or automated polisher.

Grit blasting was performed manually with 220grit brown alumina in a clean grit blaster. Compressed air pressure was set to 3.5bar and distance from the nozzle was 10cm. Grit blasting was performed for approximately 10second per side to prepare.

III.1.1.1 Generalities

The sputtering chamber is a German make (Balzers) commercial laboratory size facility. The main general specifications of this coater, that will be called "Balzers" later in this thesis, are listed below. Some were not used in these works, e.g. the heating of the substrates.

- ✓ It holds up to 4 different targets (metal, ceramic or polymer) within the deposition chamber
- ✓ It has a 4 gas lines manifold with mass flow controllers
- ✓ The chamber walls, the targets and the top lid are water cooled
- ✓ Depositions may be carried out on planar substrate or 3D substrates via a rotating substrate holder
- ✓ The substrate holder revolution in front of each target position can be controlled with an automated stepper drive
- ✓ The substrate can be heated (up to ≈500°C) with an halogen lamp heater
- ✓ Plasma are generated by RF(1 position), and DC or pulsed DC power supplies (on the 3 other positions)
- ✓ High vacuum is generated with a turbopump

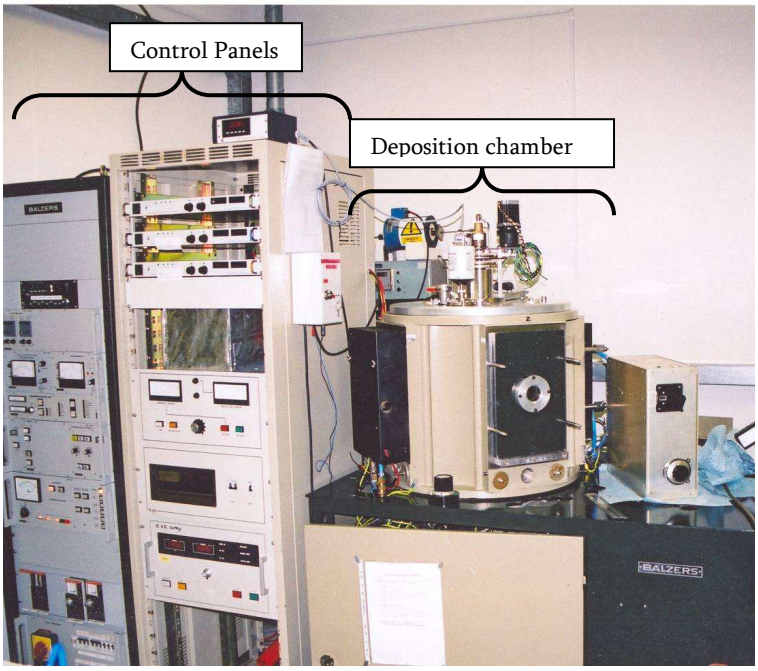

Figure 87 Overall picture of the Balzers coating facility

The Balzers is situated in a clean room in order to prevent impurities from polluting thin films. Targets are laid out so the substrate can rotate alternatively facing each target, hence in

front of each plasma (Figure 89). For this study, it was loaded with three rectangular (4×6 inches) targets:

- ✓ Commercially pure Nickel (Ni200)
- ✓ Commercially pure Al
- ✓ Pure Pt (same target which was used during M.Silva's works)

Each target is clamped on a magnetron and connected to a power supply: DC and pulsed DC for Ni and Al, and an RF power supply for Pt. The substrate holder is connected to a DC power supply in order to provide a negative bias which will enable ion plating during the process.

The use of a turbopump, which holds high speed rotating blade stages (600Hz), gives a clean vacuum prior to injecting Argon into the chamber to trigger the plasma, see vacuum system in Figure 88. Before starting any deposition and injecting the Argon, the chamber is reduced to a high vacuum, called base pressure. This pressure is typically below 5.10^{-6}mbar, that corresponds to an overnight pumpdown. Vacuum is controlled via two gauges: a penning gauge for high vacuum reading, situated at the bottom of the chamber, and a Baratron for pressure control during the deposition. The Baratron is more precise but has a limited range between 1 and 0.001Torr and is situated at the top of the chamber.

The Argon flow is controlled with a mass flow controller on the inlet line. The Argon is purified by the use of a getter furnace situated on the gas line before entering the chamber. The line is locally stuffed with titanium chips which are heated at around 700°C. At this temperature, the titanium will trap the few oxygen atoms from the gas to form a stable titanium oxide, hence purifying the Argon.

The substrate holder was connected to a computer controlled stepper motor drive in order to program deposition runs requiring a high amount of position alternation in front of each target (it was used for depositions with more than 50 alternations).

Substrates were either hooked onto the substrate holder by NiCr wires or clamped on a designed substrate holder. It was decided not to use any Kapton® tape as some users do: it may degas some organic compound into the system during the deposition as the run are relatively long in time (between 5 and 7 hours for the typical 5µm coatings). Kapton® tape was only used for shadowing glass slides when carrying out calibration runs.

The overall system is constantly water-cooled: each magnetron is connected to the water cooling circuit so the back of the metal target is cooled. The chamber walls and lid are water cooled as well as the turbopump.

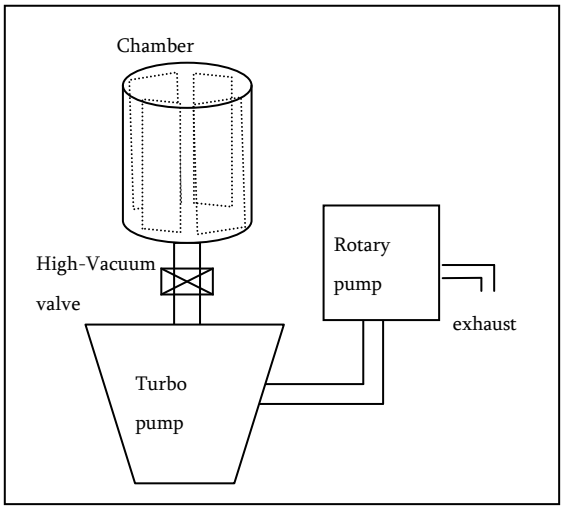

Figure 88 Vacuum system of the Balzers

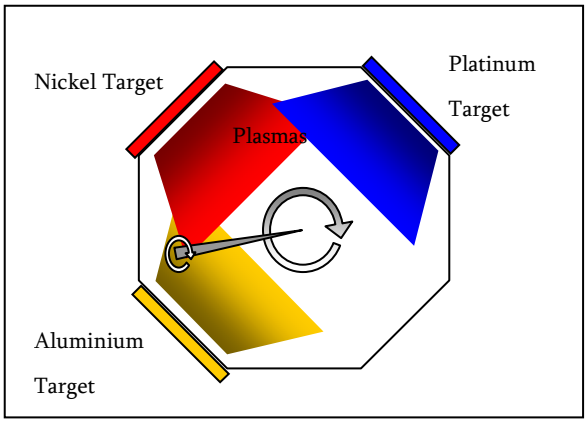

Figure 89 Targets layout in the chamber

III.1.1.2 Targets

The system is loaded with the three metallic targets, each of them being clamped on a magnetron. The magnetron holds magnets in order to enhance the plasma density. It sometimes get polluted with corrosion product from the water cooling flow, as shown in Figure 90. A copper backing plate is placed between the target and the magnetron (Figure 91). This plate prevents the target to be directly in contact with the water cooling hence preventing its possible corrosion. The use of copper is obvious for improved thermal conductivity, without altering the magnetic field. However, the Platinum target is glued on a stainless backing plate in order to shunt the magnetic field. This annihilates the magnetic field created doughnut shape of the plasma, giving a better homogeneity of the metal consumption without erosion track ring. However it drastically reduces deposition rates. The typical magnetron induced erosion track ring is shown on the aluminium target in Figure 92 whereas the platinum target layout is shown in Figure 93.

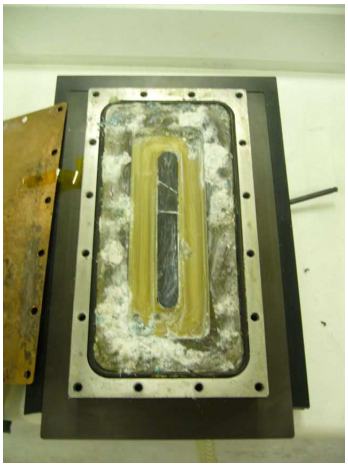

Figure 90 Magnetron and corrosion

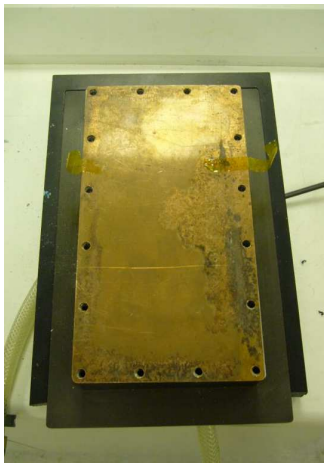

Figure 91 Copper backing plate

Nickel being paramagnetic, it tends to shunt as well the magnetic field. It was therefore needed to machine a target thinner than usual: it is only 5mm thick. Another consequence of this property is denser plasma with a smaller but deeper erosion track ring on the target surface (Figure 94).

Targets are clamped on the side of the deposition chamber the vacuum sealing being obtained by using bakelite frames with rubber O rings. The magnetrons are then connected to the water cooling system and to the correspondent power supplies.

Figure 92 Aluminium Target

Figure 93 Platinum target

Figure 94 Nickel target (in position in the chamber

III.1.1.3 Substrates layout

The deposition is carried out vertically, the substrates must therefore be hooked vertically on the planar or 3D substrate holder. This was realised either by clamping them onto a metallic mesh which was clamped itself to the holder or by the use of a specific holder later on in this study as explained in the corresponding chapter of this thesis. A general view of the chamber with the open lid is shown in Figure 95 as a view of the inside of the chamber from the top in Figure 96, with the halogen heater mounted in front of a ceramic target. The central pillar in this later picture corresponds feeds the substrate holder electrical connection; this being connected once the lid being closed.

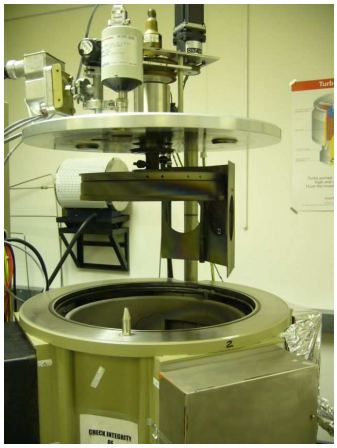

Figure 95 Chamber lifted lid

Figure 96 Inside view of the deposition chamber

Figure 97 Clamping system

Figure 98 Clamping system with samples

The clamping system used for better reproducibility of the positioning of the substrate is shown in Figure 97 and Figure 98. It is a NiCr plate machined to the size of the discs, with an

inner step to hold them. The clamping is accomplished with NiCr wires put in tension on each side of each disc. The overall system is screwed on the vertical holder and is very stable as no falling ever happened even for deposition runs with 900 successive rotations

III.1.1.4 Calibrations of deposition rates

Results of deposition rates calibration are given in detail in the corresponding chapter. Two procedure of calibration were used in this study. The first is a traditional method which was used earlier on by previous PhD students at Cranfield, and still used for thin films manufacturing in the department of Materials.

This procedure consists in depositing a monolayer of sputtered material onto a glass slide. The glass side is partially shadowed with Kapton® tape in oreder to create a step between the bare glass and the film. This is carried out for each metal for given process parameters such as power and Argon pressure. The step height is electromechanically measured by using a stylus moving across the step and measuring the deflection (Figure 99). This facility is called Dektak, and has a resolution of 1nm.

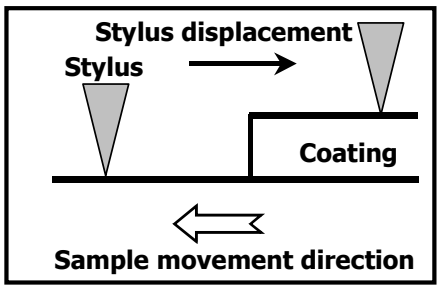

Figure 99 Principle of the Dektak

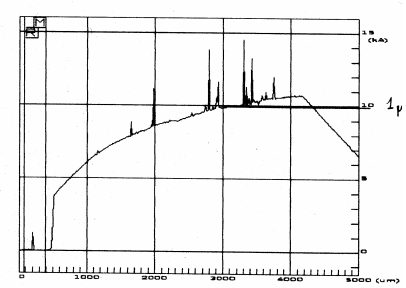

Figure 100 Typical step profile obtained with the Dektak

As one can see in Figure 100, one of the main draw back of this method is that the measured step is not always strictly flat, hence a difficult reading of the thickness of the produced coating. In order to solve this issue, weight gain calibration was used later in this project. This method is described in the relevant chapter. Weight gain calibration was chosen as it is more appropriated to the type of produced coating, with the same accuracy and a better control of the composition of the film across an entire disc sample.

III.1.1.5 Powers Supplies

Aluminium and Nickel were connected to DC supplies . The control of the deposition power is based on the current rather than the bias as current is directly proportional to Argon ion impacts on the target. Platinum target was connected either to a pulsed DC or to an RF power supply. Powers used were not greater than 350W: above this value the heat produced locally on the target is relatively high, and water cooling limit is reached. Working above 350W can lead to the melting of the bakelite frames as experienced by M. Silva.

III.1.1.6 Automated rotation

Automated rotation was used for coatings having more than 50 layers, as it gives a better control and reproducibility than manual rotation. The substrate holder is linked to a stepper motor drive by a rubber chain. The overall design is pictured in Figure 101. The stepper motor is linked to a computer which drives it with a fortran type program. The user can set the actual alternation of rotation between each target, the dwell time in front of each target, and the total number of loop of this alternation pattern.

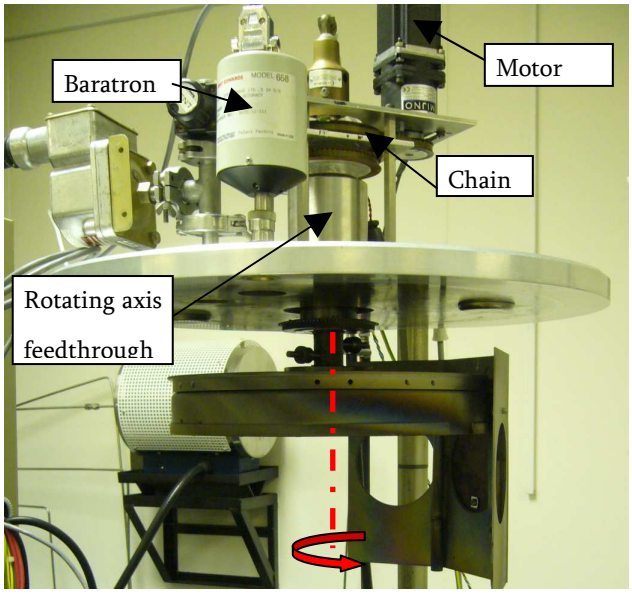

Figure 101 Substrate table rotation design

III.1.1.7 3D substrate holder

In order to coat both face of a disc or to coat cylindrical samples, a substrate holder with self rotation of the substrate was used. The holder consists in 4 pairs of rotating pins, each situated in front of a target. Only one pair was used as it had after to rotate in front of each target position. The rotation movement is transferred to the pin via a stainless bicycle like chain from the central main gear, connected to an electric motor to 4 smaller gears, controlling each pin pair. The salmples to be coated are simply hooked to each drilled pin with NiCr wire. The overall design is pictured in Figure 102.

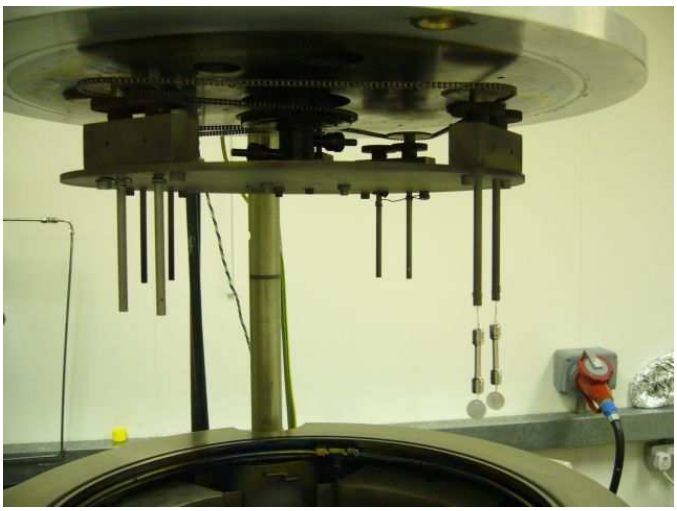

Figure 102 3D substrate holder with chain and gears

III.1.1.8 Typical sputtering run

The unfolding of the manufacturing of a batch of multilayered Al/Ni/Pt coating comes as follow:

- ✓ Choosing the deposition parameters: substrates type and surface finish, number of layers, thickness of each layer alternation pattern, power for each target, argon pressure.
- ✓ Carrying out calibration run (whatever the calibration method) for each of the metal. As the chamber needs to be vented each time, and takes a night to pump down, this step is quite time consuming.
- ✓ Preparing the samples (grinding or grit blasting, then cleaning)

- ✓ Loading the samples and program the alternation sequence on the stepper motor drive, each dwelling time being calculated with the deposition rates obtained during the calibration runs.
- ✓ Pump down the chamber to a sufficient base pressure (at least 5.10^{-6}mbar)
- ✓ Switch the pumping system to a throttle mode in order to reduce the pumping flow and switching on the getter furnace.
- ✓ Let the argon flow into the chamber in order to get a suitable pressure to trigger the plasmas (typically between 0.01-0.02 Torr)
- ✓ Each target needs to be sputter cleaned prior to start the actual deposition run. Power is gradually increased for each target and the plasma is left to run in order to remove the first atomic layers from the target surface which could have been contaminated during their exposition under air. The sputter cleaning time varies with the metal: 3min are sufficient for Pt as it is poorly reactive; 15min of sputter etching is carried out on both Ni and Al which are more likely to develop an oxide scale at their surface.
- ✓ The actual run is started with the use of ion plating during the first 15min as explained in Chapter 5, followed by the sequence of dwell between each target. For high multilayer runs, the unused targets power was not switched off during the run.
- ✓ Once the run is finished, power supplies and Argon are switched off the chamber being pumped back to its original base pressure.
- ✓ The system is left to cool down before unloading the samples.
- ✓ Once samples are removed, the chamber is always left under vacuum in order to prevent adsorbed pollutant on the targets and the chamber walls.

III.2 Ceramic deposition

This study focuses on the manufacturability of α-$NiPt_2Al$ as a potential bondcoat system for TBC. Therefore, no specific developments were carried out on the process of depositing the ceramic toplayer, except few adaptations to the specificity of the low mass bondcoats.

III.2.1 Sample preparation

Commercial reference bondcoats are grit blasted 24h before carrying out the deposition of the ceramic. Grit blasting is carried out at 3.5 bar with 220 grit brown alumina with a distance to nozzle of 10cm. Obviously the thin multilayer bondcoats were not grit blasted prior to the deposition. Cleaning of the samples in ultrasonic bath with acetone is carried out prior to clamping the samples on the substrate holder.

III.2.2 EB-PVD deposition chamber

The chamber used for the ceramic topcoat is the laboratory scale facility of the lab: it has two rotating holders, an EB gun of 15kW, and a dual vacuum chamber, a lower chamber for the beam and a deposition for the substrates. Samples are clamped on a rotating substrate holder above the ceramic ingot. The electron beam is generated in the bottom low pressure chamber and gets to the deposition chamber through an aperture. It is deflected onto the ceramic ingot with a magnetic field.

The substrates are positioned inside an arc shaped furnace in order to heat them prior to the deposition (commercial coaters have powerful EB gun which self sustains the high temperature). Figure 103 shows the layout of the substrate holders, positioned on the two rotating axis, the ceramic ingot is clean, and loaded on a mechanical feeder so it raises during its consumption throughout the deposition run. Figure 104 shows two blades mounted in the chamber, the arc shaped furnace is only half opened. The surface of the tip of the ingot is a glossy black corresponding to the molten and re-solidified YSZ.

Figure 103 Deposition chamber of the EB-PVD

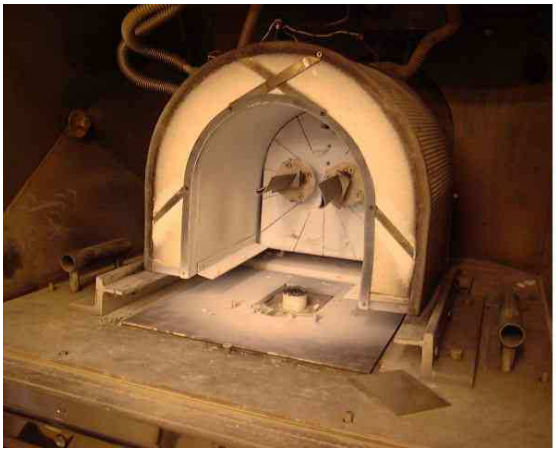

Figure 104 EB-PVD coater after deposition

A typical topcoat deposition with the EB-PVD coater follows these steps:

- ✓ The samples are clamped on the holder and placed on the rotating axis, the $ZrO_2$8wt%Y_2O_3 standard ceramic rod is loaded, and the furnace is put in place.
- ✓ The chamber is pumped down to a high vacuum level (typically between 10^{-5} and 10^{-7} mbar).
- ✓ The furnace is heated up to about 500°C.
- ✓ A gas mixture of 10% argon and 90% oxygen is introduced until the working pressure of 10^{-2} mbar is obtained. Oxygen is used in order to saturate the coating with oxide so no oxygen vacancies are formed in the ceramic structure. Vacancies would not drastically change the intrinsic properties of the coating, but it would not be white anymore (this is the reason why the top of the molten ingot is black): this is called aesthetic treatment by the industrials.
- ✓ Prior to the deposition, the furnace temperature is increased to 850°C.
- ✓ The sample rotation is started.
- ✓ The electron beam gun, placed in the lower chamber at 6.10^{-4} mbar, is then triggered (10kV/0.54A). This raises the temperature to about a 1000°C (deposition temperature).
- ✓ The evaporation of ceramic onto the component is carried out for the time required (60 minutes to deposit 120µm thick TBC).
- ✓ The ceramic rod evaporation is controlled through the control aperture and raised approximately every 5 minutes.
- ✓ Once the run is finished, samples are left to cool down. Fans can be added if assisted cooling is required.
- ✓ Samples are kept in a desiccator prior to analyses or ageing experiments.

III.3 Oxidation tests and annealing furnaces

III.3.1 Annealing furnaces

As explained in the project description chapter, the manufacturing route of intermetallic coatings consists in reacting sputtered metallic thin multilayers in a protective atmosphere. Two devices were used during the project for this purpose: a vacuum and an argon furnace. One will notice that further developments demonstrated that reacting the layers in situ of the EB-PVD coater during the heating of the substrates induced no change in the thermal cycling lifetime of TBC systems.

III.3.1.1 Vacuum furnace

The vacuum furnace consists in a vacuum chamber equipped with a conventional rotary/diffusion pumping system. The chamber can reach a vacuum level of around 10^{-7}mbar, although it increases with temperature up to roughly 10^{-5}mbar. Heating is provided by carbon electrodes sitting in square on each side of the alumina substrate table (roughly 25cm^2). Carbon elements are used because of the vacuum atmosphere: the heating energy is therefore mainly radiative. Heating rate is excellent: up to 30°C/min; cooling is fast thanks to the water cooling of the chamber walls (roughly 15°C/min between 700°C and 400°C and then 4°C/min between 400°C and 100°C).

Thermal annealing experiments were carried out between 700°C and 1000°C, with a start up sequence. This sequence is carried out prior to the actual annealing dwell and aims at burning possible organic pollutant, and limiting the degassing during the dwell that would reduce the vacuum level. The total sequence is as follow:

- ✓ 10°C/min until 40°C; 2 min dwell.
- ✓ 30°C/min until 200°C; 10 min dwell.
- ✓ 18°C/min until 310°C; 10 min dwell.
- ✓ 15°C/min until annealing temperature; annealing dwell (typically 120min)
- ✓ Fastest cooling (no power transferred to the heating electrodes) until room temperature.

III.3.1.2 Argon furnace

The argon furnace is a standard horizontal tube furnace loaded with 6 SiC heating elements situated around the inner alumina tube. The two extremities of the alumina tube are joined to stainless steel vacuum sealed gates. One end of the tube is connected to a manometer pressure gauge, to an overflow valve and to a roughing pump line. The other end is made of a screw clamped cap with O ring, to access the inner tube and load the samples on an alumina tray. This cap is equipped with a gas line inlet. The gas line goes through a Ti getter furnace in order to purify the Argon (U purity) from oxygen. The heating of the furnace is controlled by a traditional power supply with two thermocouples situated in the middle of the inner tube.

A typical run in the argon furnace consists in:

- ✓ Loading the samples (up to 3 AM1 discs) onto an alumina tray, pushed to the middle of the tube.
- ✓ Purge the tube with the rotary pump to a rough vacuum level and fill the tube with the deoxygenated the Argon gas.
- ✓ 3 purges are carried out in total.
- ✓ The Argon is left on, flowing through the tube with an average flow of 10cc/min.
- ✓ Heating is very slow, 5°C/min maximum, due to the thermal inertia of the alumina tube and the risk of thermal failure.
- ✓ Despite this low heating rate, it was decided to keep the annealing dwell time starting when the furnace does actually reach the intended annealing temperature.
- ✓ Cooling down is extremely slow as the tube is not water cooled: heating elements are simply switched off, it takes typically over 10 hours to reach a temperature below 100°C when the samples could be unloaded (5°C/min cooling down from 700°C to 500°C decreasing to 0.5°C/min between 200°C and 100°C).

III.3.2 Isothermal oxidation

III.3.2.1 Box furnace

Isothermal oxidation experiments were carried out under air (laboratory atmosphere) at 1100°C. Standard box furnaces were used for this purpose. Samples are placed onto an alumina tray and loaded into the furnace already stabilised at 1100°C. The furnace is equipped with rapid heating elements and recovers 1100°C after less than a minute from the opening of the door (temperatures drops roughly to 950°C when opening the doors). Samples are unloaded after the determined time and left to cool down on the alumina tray at room temperature under laboratory atmosphere.

III.3.2.2 Thermogravimetry

Some thermogravimetry experiments were carried out with a high temperature thermobalance device. The model of this device is a Setaram Setsys Evolution 16. The principle of isothermal oxidation thermogravimetry is to continuously measure weight change of a sample throughout its exposure at high temperature in an oxidant atmosphere. This method gives the kinetic of oxidation of the analysed compound.

The sample is hanged in a small high performance furnace, and linked to a high precision balance above the furnace. The furnace is heated with carbon elements set around an alumina tube. The chamber is filled with flowing air from a gas bottle. The balance measuring device consists in a tilting beam with the sample hanged on a side and counter weights on the other side. The beam is kept horizontally with copper induction bobbins: the current required to keep the beam horizontal is proportional to the mass difference between the two sides of the beam.

Figure 105 Visual of the TGA facility

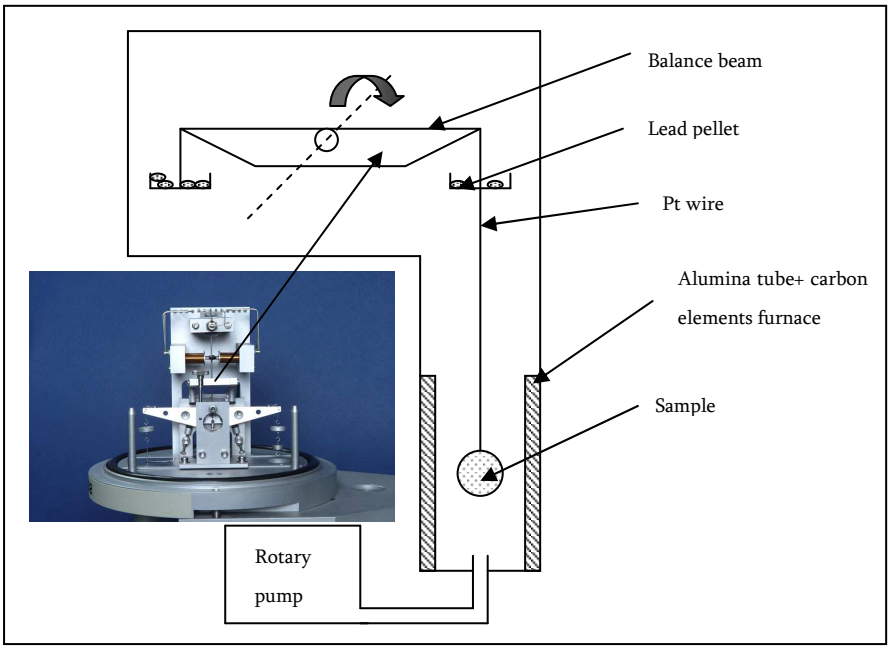

Figure 106 Principle of the TGA

A typical run of TGA consists in:

- ✓ Hooking the sample to the Pt suspension wire, with a hand made Pt basket
- ✓ Set a mass equilibrium between the two sides of the beam with counterweights. For this purpose, lead pellets are used for gross equilibrating and alumina chip for fine tuning. The mass difference between the two sides is set to below 1mg.
- ✓ The overall system is air sealed
- ✓ Air from a gas bottle is injected with a flow of 10mL/min
- ✓ The furnace is rapidly heated to 1100°C (30°C/min)
- ✓ The isothermal dwell is carried out under the flowing air. Mass change is acquired by the change in current in the bobbins controlling the beam tilt.
- ✓ Cooling is carried out at 30°C/min
- ✓ Sample is weighted prior and after the test in order to check the relevance of the weight gain curve.

The resolution of the weight change is 0.03µg. There are two sources of noise with this facility. A typical buoyancy effect occurs during the heating and cooling steps: the buoyancy value changes with the ambient air change in temperature (the equivalent air mass of the sample volume decreases with temperature). Hence, TGA results were only considered during the isothermal dwell. The second source of noise is the environment of the facility. As this is a precision device,

fine changes in room temperature or humidity leads to change in mass reading. The alternation of night and days due to central heating was clearly observed during our experiments.

III.3.3 Cyclic oxidation

Cyclic oxidation or thermal cycling (this latter terminology is rather used for TBC testing) is a typical test used for turbine high temperature components. The aim is to simulate thermal cycles endured by the components, and comparing their behaviour with isothermal exposure. For TBC systems, it emphasises the failure generated by thermal stress generated at each cycle due to the difference in CTE between the superalloy, the bondcoat, the TGO and the ceramic topcoat. The principle is quite trivial: the sample is moved from a "cold" position (laboratory temperature with or without pulsed air to improve cooling) to a "hot" position, inside a tube furnace. The tube furnace consists in a standard alumina tube surrounded with six SiC heating elements. Typical cycles are 1h at high temperature followed by a cold dwell of 10 to 15min. Industrials sometimes use more complex cycles in order to simulate cycles for military engines, with high temperature variation corresponding to an attack configuration of a fighter jet.

In this thesis, hot dwell are set to 1100°C, failure of a TBC sample being defined by the failure of 20% of the ceramic surface. For cyclic oxidation tests of bare bondcoats, the samples are periodically removed from the holder and weighted on a precision balance (resolution of 0.01mg).

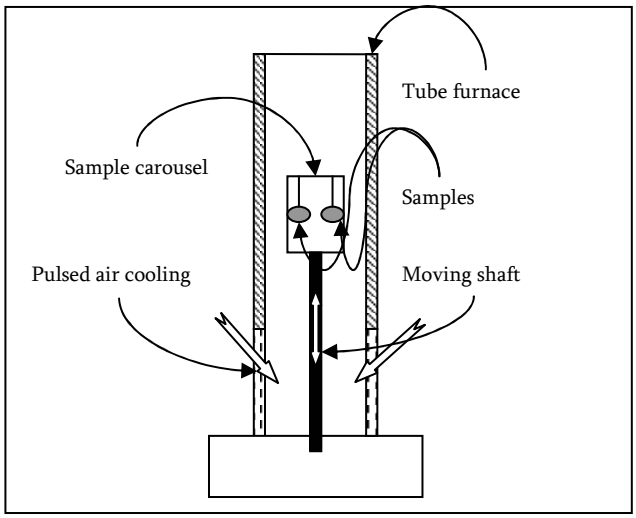

Figure 107 Principle of thermal cycling

Two thermal cycling rigs were used. The "old" one corresponds to the rig used by previous students at Cranfield. It was mainly used to assess lifetime measured on the new rig, and to

compare data bases. The new rig offers a better cooling rate and higher sample content. The new rig was designed and acquired during this project in collaboration with the Pyrox furnace manufacturer.

III.3.3.1 Old Thermal Cycling Rig

This rig was used during previous projects on TBC systems, in particular B.Saint-Ramond and M.Silva works. It is able to cool the samples with water, hence the large base which contains the water tank. This option was not used during this project. The cycle used on this rig is the same as M.Silva: 1hour at 1100°C followed by 15min of cold dwell without forced air.

Calibrations were carried out in order to measure the cooling rate of this rig. Three thermocouples were hooked to the carousel and submitted to one cycle. The first was a plain thermocouple junction, the second, an AM1 disc with a thermocouple welded on the surface, and the third was a small metallic cylinder (5mm diameter, 10mm height). Thus, the effect of the sample mass on the heating and cooling inertia was measured.

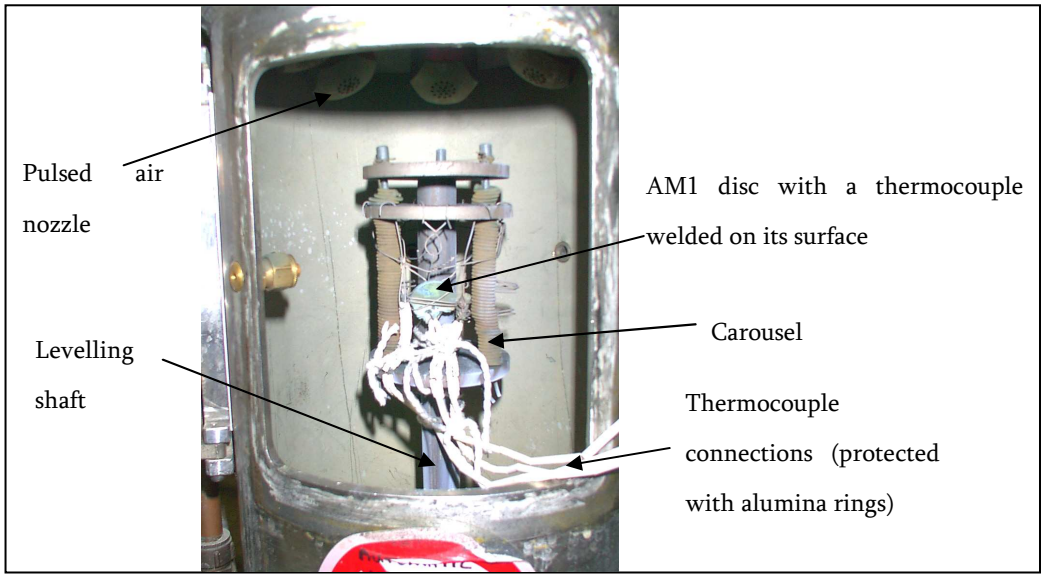

Figure 108 Samples layout for calibration

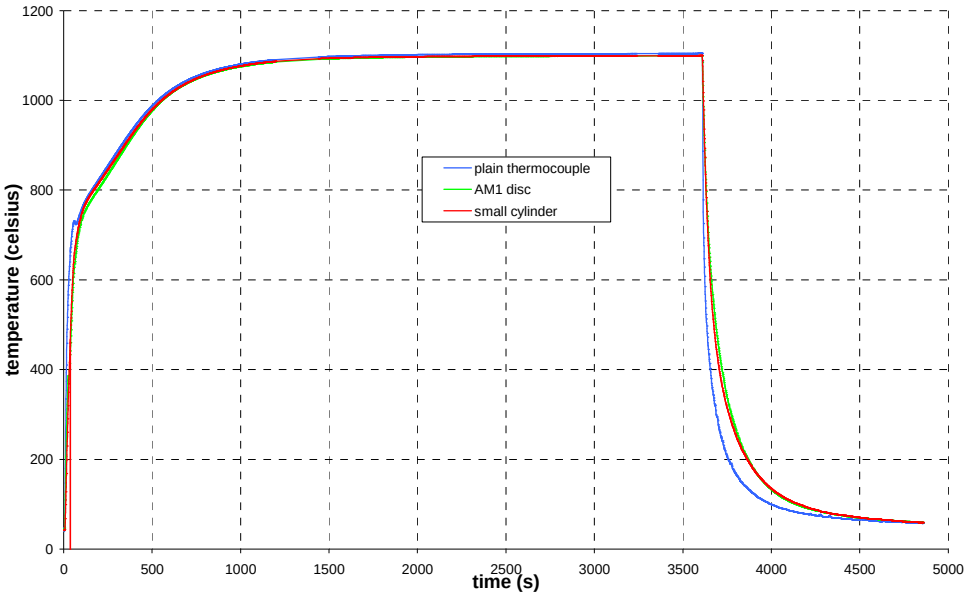

Figure 109 Calibration curves for the old rig

III.3.3.2 Pyrox Thermal Cycling Rig

Two new thermal cycling rigs were issued by PYROX in August 2005. These rigs can go up to 1450°C, with a substrate holder moving in and out of the furnace by a pneumatic device. Four electric fans are blowing into vertical nozzles which are installed in front of the substrate holder on the lower position to create a cooling air vortex. The carrousel holds two decks to hook the samples. The fan rotating speed can be adjusted with a potentiometer.

One of the rigs was calibrated in order to have a homogeneous cooling rate between the two decks of the substrate holder. The chosen solution was to set a metallic mesh in front of the four nozzles.

Figure 110 Picture of one of the cycling rigs

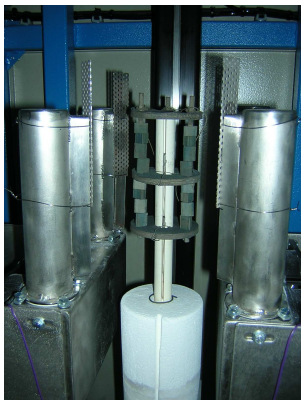

Figure 111 Zoom on the substrate holder

Two thermocouples were loaded on each deck of the substrate holder in order to make the acquisition of the cooling speed of the rig. The meshes have been optimised so the cooling rate is the same between the two decks when the fans are at full speed. The data are given in Figure 112 and compared with the cooling curves of the original thermal cycling rig installed at Cranfield, and compared with Snecma's rigs.

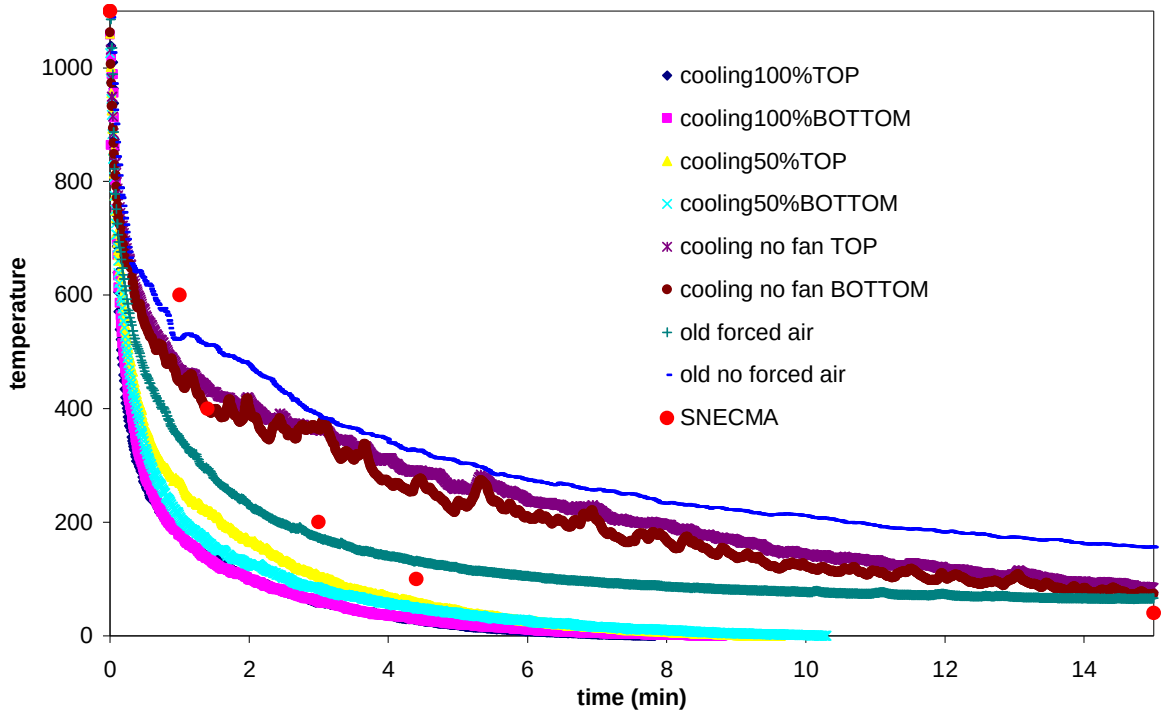

Figure 112 Cooling curves of pyrox rig, at fan full speed, half speed, and no fan for the two decks

The cooling rate of this rig is faster than the original Cranfield or Snecma's ones. This is why it has been chosen to make only 10 minutes long cooling stage during the cycling experiment. The data were acquired on plain thermocouples, so a mathematical correction from precedent acquisitions was applied in order to take in account the theoretical thermal inertia of superalloy discs. The results are given in and compared with Snecma data

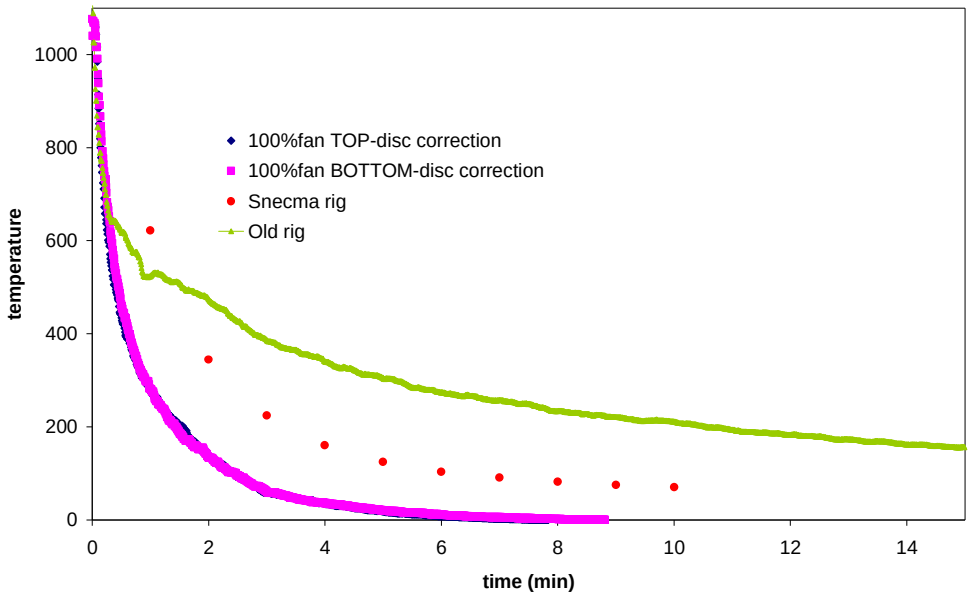

Figure 113 Cooling curve with mathematical correction for disc samples

One can notice that after 9 minutes of forced cooling, the temperature indicated by the thermocouples gives negative values. This intriguing fact was observed for both thermocouple, and checked with a secondary thermocouple reader. None of the thermocouples was found faulty after this test. The temperature reaches the lab temperature of 20°C after 25minutes of cooling. This is likely to be an artefact due to local water evaoparation at the welded join of the thermocouples. It was decided to consider the temperature as constant and equal to 20°C when it reaches this temperature at first i.e. after 5min (with the disc mathematical correction).

III.4 Analytical and observation tools

III.4.1 Microscopy Techniques

Microscopy was used for observing surface and cross sections of as deposited samples or samples exposed to oxidation in order to understand ageing behaviour of the coating produced during this project.

III.4.1.1 Optical Microscopy

Optical microscopy was hardly used during this study as the thickness of the coating produced is not relevant with the maximum magnification of 60X offered by the opticl microscope. It was mainly used for general aspect of an oxidised surface or checking the quality of the samples polishing. The facility used is a Nikon direct optical microscope equipped with a JVC CCD sensor camera for picture acquisition.

III.4.1.2 Scanning electronic microscopy

III.4.1.2.1 Principle

Scanning electron microscopy (SEM) is a typical analysing tool use din Materials science so the principles will be only briefly described. SEM was extensively used in this study as sample preparation is fast and high magnification (in theory up to 300,000X) corresponds to the scale of the thickness of low mass bondcoats.

The principle is to load the sample in a vacuum chamber and taking advantage of the high frequency of electrons (compared to light photons in optical microscopy) to reach high magnification. Electrons are produced in an EB-gun, by a heated filament or a field emission gun. They are accelerated with a voltage comprised between 10 and 30kV, and then focused with electromagnetic lenses while scanning the sample surface. Secondary electrons or backscattered electrons can be detected to form a picture of the sample. Secondary electrons give topographic

information, whereas backscattered electrons are dependant on the observed material as they reacted with the atoms of the surface. Samples have to be conductive in order to prevent charge build up on the surface of the electron bombarded sample;

Three various kind of SEM were used in this study:

- ✓ A classical SEM with a W filament as an electron source. This SEM is a Cambridge 2000 (and is roughly 20 years old. It was used during the first year of the project in order to get confident with SEM technology and mechanisms.
- ✓ A SFEG-SEM (FEG stands for Field Emission Gun): FEI XL30 SFEG. This alternative source of electrons gives a much narrower electron beam allowing high resolution pictures, up to X300,000. This is a recent facility which offers the advantage of a full computer controlled system.
- ✓ A ESEM (Environmental Scanning Electron Microscope): FEI KL30 ESEM. This SEM uses a classical source of electrons, but the chamber can be filled with water vapour, which allows observation to be carried out in a relatively low vacuum. It makes as well possible the observation of non conductive materials, as water vapour prevents electron charge build up: this was used for oxidised samples surface observation. However the resolution of this SEM is not as good as the SFEG which was used for the observations of cross sections.

III.4.1.2.2 Sample preparation

For oxide surface observation, no specific sample preparation was carried out as ESEM was used to observe non conductive oxidised surfaces.

Cross sections were produced as follow:

- ✓ Mounting of the sample in cold epoxy resin with a metallic or plastic clip to hold the sample vertically.
- ✓ Mounting plus sample cylinder were cut using the precision saw
- ✓ The section was polished using the automatic grinder: at grit 240, 1200, 2500 and 4000 with SiC paper, then down to 3µm using alumina colloidal suspension on a smooth cloth.
- ✓ The polished surface was coated with a thin layer of carbon (below 50nm) to provide electrical conduction (the cold epoxy resin is isolating)
- ✓ Silver paint was used to connect the edge of the sample cross section to the back side of the mounting cylinder.

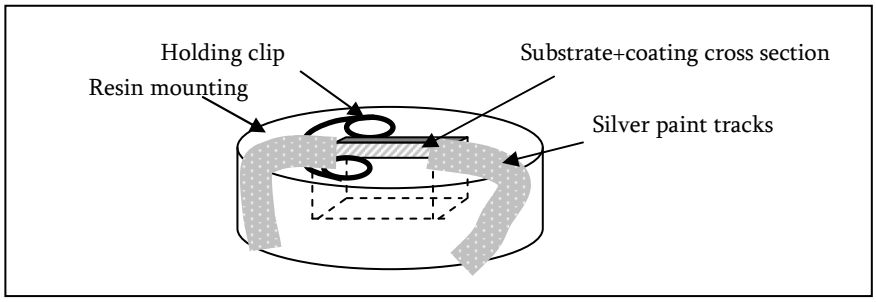

Figure 114 Cross section mounting for SEM observation

III.4.1.3 Focused ion beam

Focused ion beam (FIB) systems have been produced commercially for approximately ten years, primarily for large semiconductor manufacturers. FIB systems operate in a similar way to a SEM except, rather than a beam of electrons and as the name implies, FIB systems use a finely focused beam of gallium ions that can be operated at low beam currents for imaging or high beam currents for site specific sputtering or milling.

Figure 115 shows the apparatus available at Cranfield University: it is a single beam Fei FIB200.

Figure 115 The Fei FIB200 at Cranfield

As Figure 116 shows, the gallium (Ga^+) primary ion beam hits the sample surface and sputters a small amount of material, which leaves the surface as either secondary ions (i^+ or i^-) or neutral atoms (n^0). The primary beam also produces secondary electrons (e^-). As the primary beam

scans the sample surface, the signal from the sputtered ions or secondary electrons is collected to form an image.

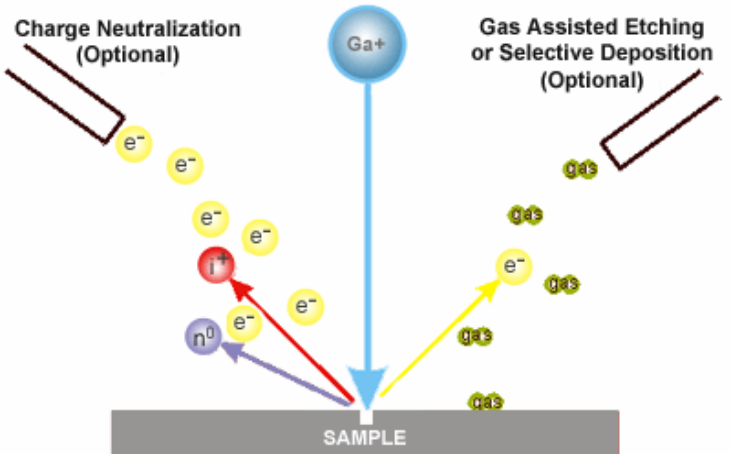

Figure 116 Principle of the Focused Ion Beam facility

An electromagnetic aperture situated after the ion gun allows the user to choose beam currents from 1pA to 11500pA. At low current, typically between 1 and 70pA, FIB is used for imaging, as the sputtering yield is very low for these values. Above 70pA, the beam is energetic enough to noticeably mill the substrate. The higher the current the higher the energy transeferred to the surface: for a given milling depth, increasing the current reduces the milling time but increases the thermal affected zone around the milled section.

If the sample is non-conductive, a low energy electron flood gun can be used to provide charge neutralisation. In this manner, by imaging with positive secondary ions using the positive primary ion beam, even highly insulating samples may be imaged and milled without a conducting surface coating, as would be required in a SEM.

In addition to primary ion beam sputtering, FIB system permits local "flooding" of the specimen with a variety of gases. These gases can either interact with the primary gallium beam to provide selective gas assisted chemical etching or selective deposition of either conductive or insulating material by decomposition of the deposition gas by the primary ion beam. For instance Pt-organometallic gas is used to manufacture thin protective Pt strips (1 to 3µm thick) on the surface.

The FIB facility at Cranfield is a single beam FIB: more recent systems have a dual beam with integrated SEM in the chamber. This allows the user to observe the sample while it is sputter etched by the ion beam. This feature is particularly useful for transmission electronic microscope (TEM) sample manufacturing. On Cranfield apparatus, the operator works “blindly”: imaging of

the sample at low current, then program the milling pattern, and close the detector when actually milling (the high contrast created by high energy milling would burst the single secondary electron detector).

FIB was extensively used in this study to make cross sections. FIB sections can be considered as non destructive as the affected area is very small compare to the total sample size. Moreover it does not have the artefacts of classical cross sections (mounting, cutting, and polishing). Therefore typical procedure is to establish a step section at high energy, and then mill planar sections while decreasing gradually the energy of the beam (Figure 117 and Figure 118).

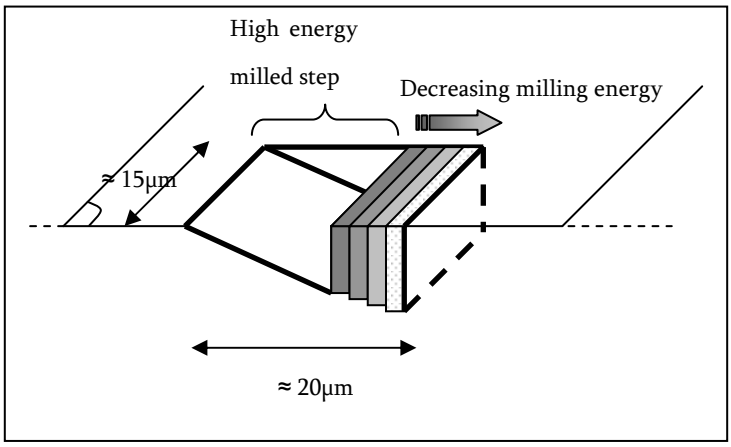

Figure 117 Principle of FIB section

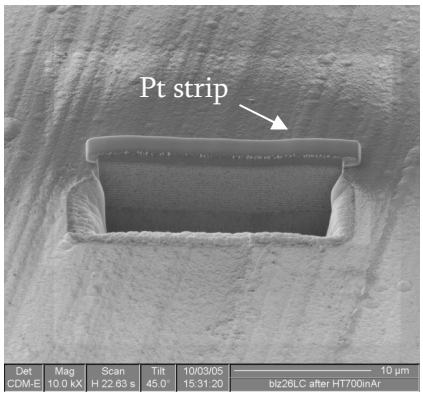

Figure 118 Example of FIB section (with Pt protective strip)

III.4.1.4 Transmission electronic microscopy

III.4.1.4.1 Principle

Transmission electronic microscopy (TEM) is used for high resolution imaging, up to 1,000kX in transmission mode with the facility used. TEM was not extensively used in this study, and observations were carried out with a specialised operator, therefore few details on this facility will be given. Many references deal with TEM[210-212].

The TEM used in this study is at the *Ecole de Mines de Paris*: the model is a Tecnai F20 SFEG TEM. Briefly, the principle or TEM is to analyse a sample in transmission i.e. the electron beam crosses through the analysed substrate. For this purpose the sample has to be extremely thin (see next paragraph), and electrons having high energy. The beam is driven through a series of electromagnetic lenses, through the substrate and then focused onto a screen (see manufacturer pictures in Figure 119).This model uses a SFEG source for electrons and the acceleration voltage is

200kV. Various imaging mode were used: direct TEM (bright field and dark field), STEM (Scanning TEM) with HAADF detector (High Angle Annular Dark Field, ideal for tomographic highly contrasted pictures).

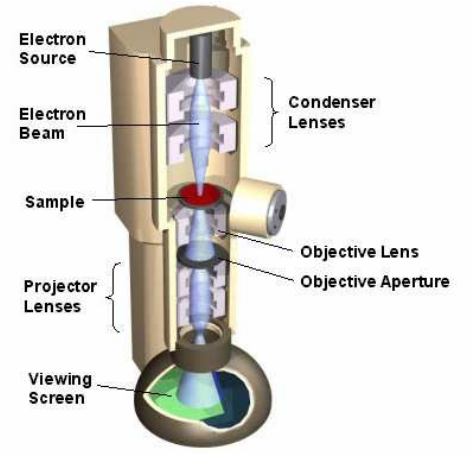

Figure 119 Principle of TEM

III.4.1.4.2 Sample preparation

More details are given on sample preparation, as this was carried out at Cranfield, without previous experience at the University on the use of FIB for TEM sample preparation of metallic or intermetallic materials with coatings. This preparation is very delicate and took few months to set up by myself. First tries took more than 10 working hours with the FIB to produce a single section; latter developments lead to a typical 4 hours of working hours under the FIB to achieve a section ready for lift out. The lift out technique is more subjected to failure, as only 25% of the prepared samples were successfully mounted, ready for TEM observation.

The coated sample is loaded in the FIB; a Pt strip (20*2*1 µm) is deposited with the gas injection system in order to protect the surface of the future TEM section. Two steps are produced at high beam current (6000pA) at a distance of 3µm from the Pt strip edge in order not to affect thermally the material which will be later observe under TEM.

Planar millings at medium power (beam current≤1000pA) are then carried out to thin the section at the thickness of the Pt strip (Figure 120). Planar millings have always to be programmed so 1/3 of the box sits before the actual section edge seen on the imaging mode. At these power values, the detector had to be switched off during the etching so no continuous control is possible, and ruining the section can occur in case of an unexpected shift. This does sometimes occur due to poor electrical conductivity of the surface or to successive change in the beam aperture. At 1000pA, it is possible to "grab" a single picture in order to check the positioning i.e. a single scan

of the working area :the beam would eventually sputter some material at this power but the Pt strip act as a sacrificial layer, the high contrast transmitted to the detector is acceptable at this current for a single exposure.

From a 2µm thick section, currents of 350pA to 150pA are used for milling. This extends dramatically the milling time, but it reduces the thermal effect on the observed material and allows the operator to continuously monitor the milling. The FIB being single beam, no actual picture of the sample being milled can be obtained. However, an oscilloscope is linked to the detector so the raster box of the ion beam can be observed continuously, and a ghost picture of the position of the section is observable by contrast difference (corresponding to the presence or not of material to be milled at the sample surface). The beam can be adjusted manually during the milling on the FIB control panel.

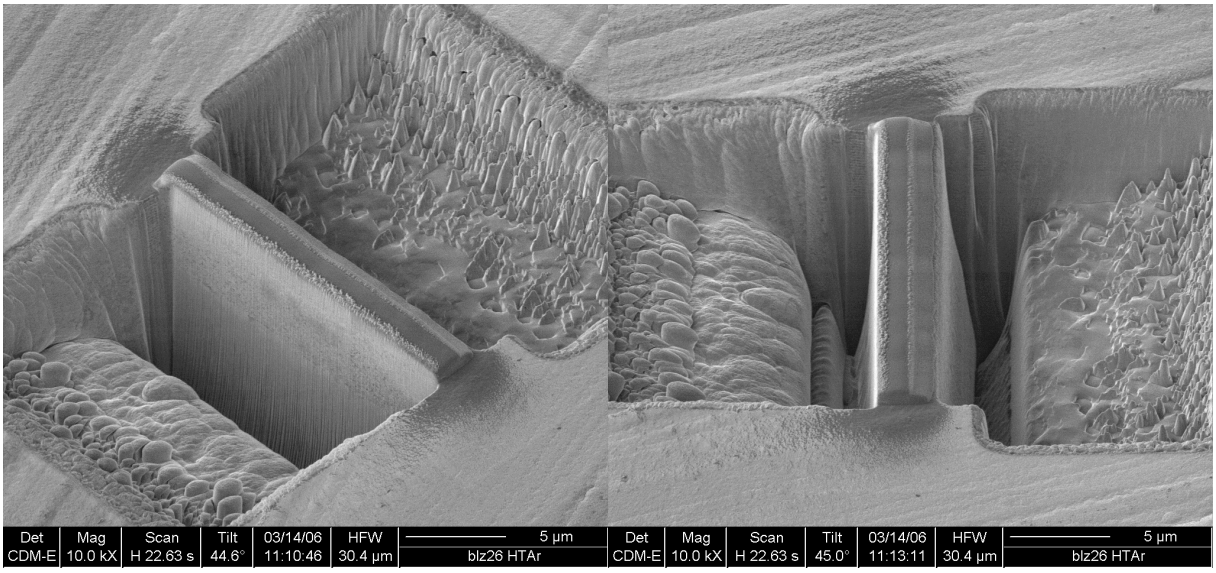

Figure 120 Section after gross thinning

When the section is roughly 1µm thick, the sample is tilted in order to cut the section so it is almost free standing. This leads to the formation of a sectioned "flag" held on a side only (Figure 121). This milling must not be carried out on thinner sections, as acquisition of pictures of tilted sample would pollute it with implanted Ga ions. Generally when working on a section below 1µm thick, it is advised not to scan the sample but rather taking few grabbed pictures.

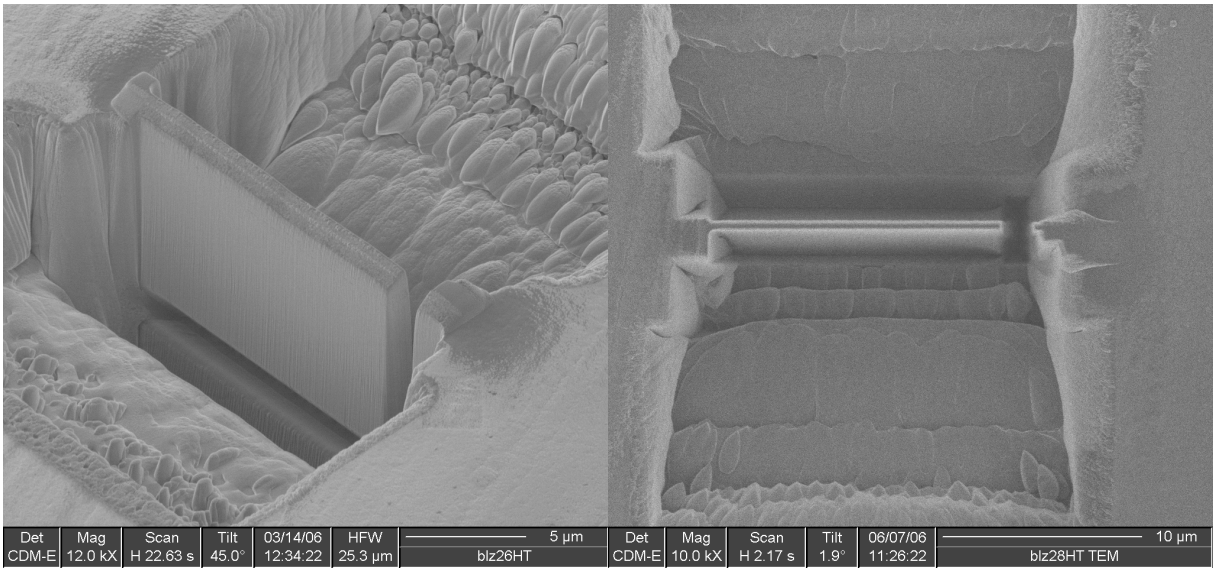

Figure 121 Thick and thin flag

The final thinning of the flag is a very delicate part (Figure 122): the section thickness must be below 100nm to be electron transparent in the TEM. This fine milling is carried out at 150pA with visual control on the oscilloscope. Only half of the length of the flag is finely milled so that if the section is blasted, the operator can take a second chance on the second half of the flag.

Once an apparent thickness of 100nm or below is obtained (the operator can only have a top view of the sample), the last pillar of the section is milled. This milling must be carried out at 350pA so it is fast enough but still controllable with the oscilloscope signal: the milling must be stopped as soon as the section actually falls into the trench. This part is very critical. First the section can fall into a position such as it could be blasted by the ion beam, or deep in a trench so it would be difficult to lift out. Second it happens often that during the fine millings some material re-deposited on the side of the flag, re-sealing it to the substrate. It becomes then very difficult to find this welded joints and to cut them while limiting the exposition of the section the Ga^+ beam which would destruct the thin section in few seconds (it is needed to operate at 1pA, which gives very poor resolution, to find the joints while being careful not to scan the working area of the section).

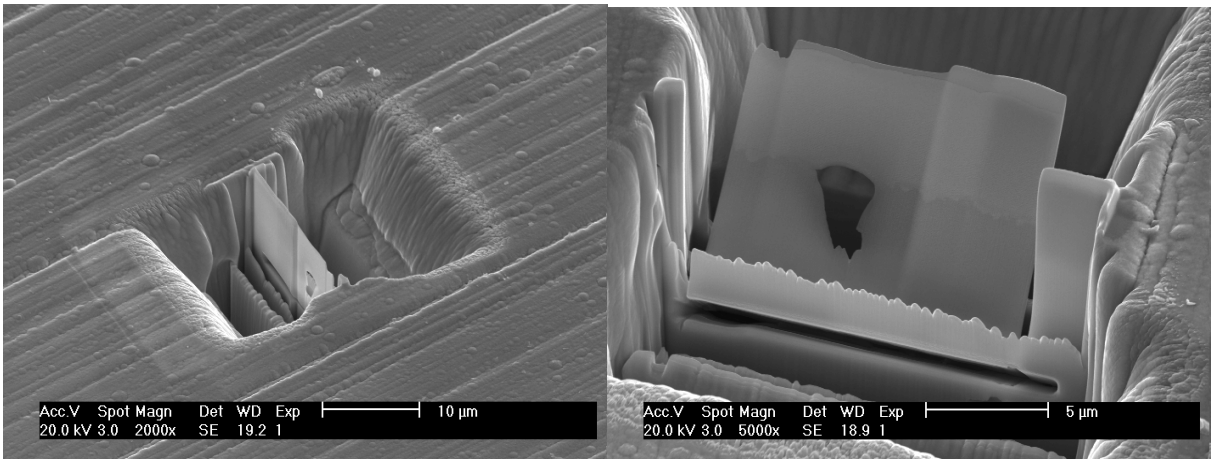

Figure 122 Flag final milling and final cut

Few general remarks: it is advised to alternate frequently the side of the section being milled in order to prevent the bending of the section to compressive stress being implemented on a single side (Figure 124). Moreover, having a clean steps and preliminary planar sectioning reduces the formation of heterogeneity and deep trenches around the section, which reduces the risk of re-welding and/or loss of a cut section deep in a trench. On Figure 123, the left hand side trench is relatively smooth whereas the right had side one shows deep and rough edged trenches likely to trap the section once cut.

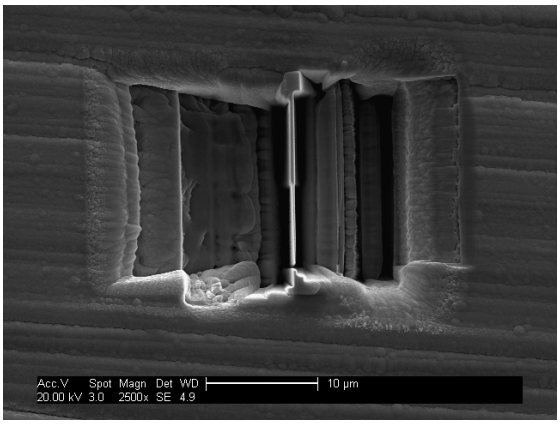

Figure 123 Uniformity of the area surrounding the section

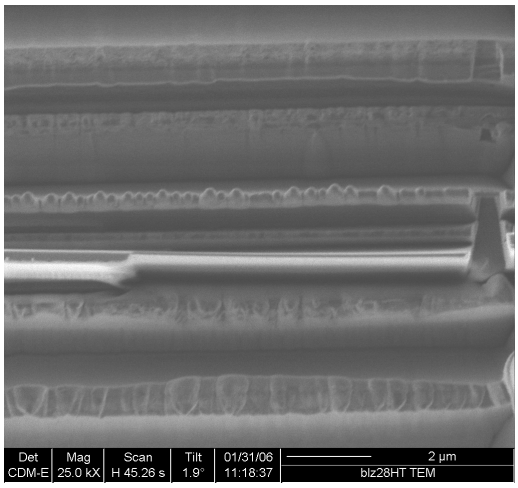

Figure 124 Bending of the section

Typical defects implied by manufacturing TEM section with a FIB are:

- ✓ An homogeneity of the thickness: the FIB beam is not perfectly square (V shape), so the section gets thicker deeper in the trench. This can be seen on the second micrograph of Figure 120.

- ✓ A "waterfall" effect: due to heterogeneity in the milling: this effect leads to non-flat sections. It usually occurs deeper in the milling, when some of the sputter etched material is re-deposited deeper on the section (see Figure 125).
- ✓ Partial milling of the top edge: due to the V shape of the beam: the top edge is sometimes sputter etched while trying to thin further the deeper part of the section. This is difficult to apprehend when the section is imaged from a top view.
- ✓ Formation of inner holes at weak points inside the coating, triggered by the input of energy in the section (see the second picture of Figure 122).

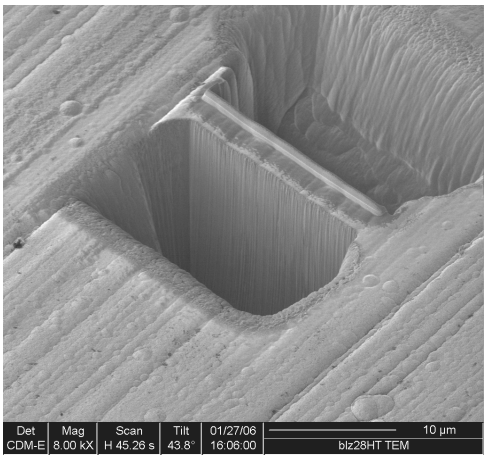

Figure 125 Waterfall effect

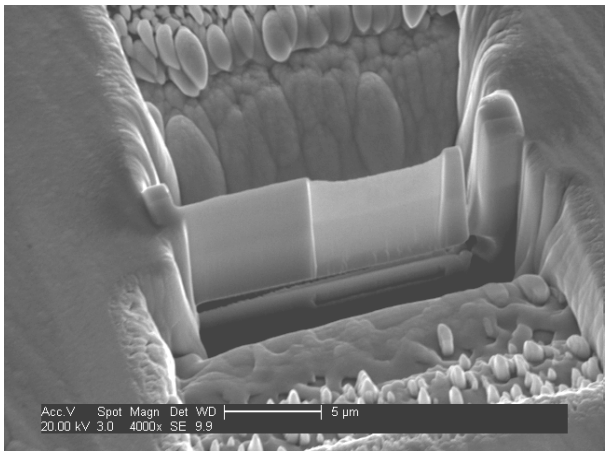

Figure 126 Partial milling of the top edge

Once the section is free standing, it stays in contact with the substrate with a surface contact and static electricity mechanism. The sample is then loaded under an optical microscope and a micro manipulator with a micro glass capillary stick. The glass stick is carefully inserted in the trench until the cut section jumps on the tip of the stick. The section is then dropped onto a TEM copper grid substrate holder (2mm diameter). A fine formvar® film is laid on the grid so the sample does not lay on a copper part.

This operation is extremely delicate as the magnification of the microscope (60X) is just enough to see the FIB trench, and the tip of the glass tip is large compare to the size of the trench. The risk is to break the glass tip against the edges of the trench, or pierce the section. Moreover the section can jump away from the trench and lost when manipulated. The moisture in the laboratory air does as well affect the ability to attract the section by static electricity. Only 33% of the samples were successfully lifted out with this method.

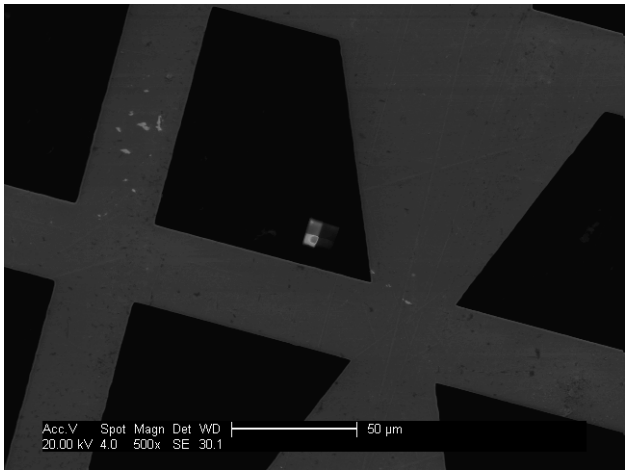

Figure 127 TEM section successfully laid on the formvar film

III.4.2 X-ray diffraction

X-Ray Diffraction (XRD) was extensively used in this project as an analytical tool. XRD of coated samples, as deposited, reacted or oxidised were carried out in order to make a quantitative analysis of the compounds or oxides in the system. Some powder diffraction was as well occasionally carried out in order not to have texture effect on the diffraction spectra. Quantitative analysis was carried out, especially for measuring d spacing and cell parameters on various samples.

The diffractometer was mainly used with a typical θ/2θ layout. The facility is a Siemens D5005 loaded with a Cu K-alpha X-ray tube. Bragg's law was applied in order to measure cell parameters from diffracted peak. When a given (hkl) crystal plane diffracts at a given incidence angle θ_{hkl}, the distance between two consecutive planes d_{hkl} follows Braggs Law [1]. When applied to an orthorhombic structure (lattice angles are 90° but *a*, *b* and *c* parameters differ), it gives equation [2]. The studied alpha phase is tetragonal, hence *a* and *c* parameter can be calculated from two different peaks [3].

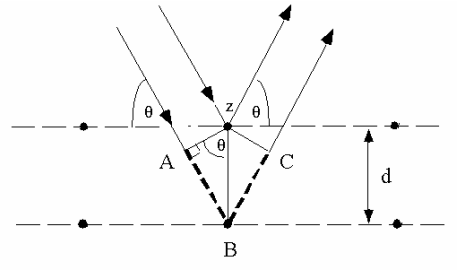

Figure 128 Bragg's law

$$n\lambda = 2d_{hkl}\sin\theta_{hkl} \quad [1]$$

$$\frac{1}{d_{hkl}^2} = \frac{h^2}{a^2} + \frac{k^2}{b^2} + \frac{l^2}{c^2} \quad [2]$$

$$\frac{1}{d_{hkl}^2} = \frac{h+k}{a^{é}} + \frac{l}{c^2} \quad [3]$$

The motion of the goniometer is set so a scan from 2θ=20° to 95° takes roughly 30 min with enough count at each step i.e. a step of 0.040° with a step time of 1s.

III.4.3 Chemical analysis

III.4.3.1 Energy Dispersive Spectrometry

Energy Dispersive Spectrometry (EDS) or Energy Dispersive X-ray Analysis(EDX) is a powerful chemical analysis tool. It was extensively used in this study in order to quantify chemical species in the substrate, the coatings or the oxide scale. This device is included in SEM or TEM chamber, and takes advantage of the bombardment of the material with electrons which excites electrons from the electronic cloud of the atom. The atoms of the material react to the electron irradiation by releasing a photon during the energy relaxation of electrons from the electronic cloud surrounding the atom core. The energy of the dispersed photon is equal to the difference in energy level between the excited and the standard status of the concerned electron, which is typical for each element of the periodic table.

For SEM the typical size of the pear of interaction is 1µm2 whereas spatial resolution of EDS is 0.2nm in TEM. Single point quantitative analysis, concentration profiles or mapping were carried out.

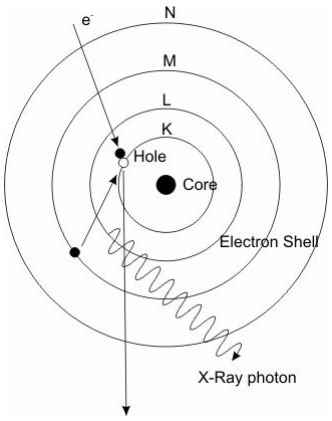

Figure 129 Scheme of EDX principle

III.4.4 Thermal Analysis

III.4.4.1 Principle

The principle of the Differential Thermal Analysis (DTA) is to measure the difference of temperature ΔT between the sample and a reference (usually alumina), both subjected to the same heat treatment. When an exothermic reaction occurs, the temperature of the sample increases more than should be expected, resulting in an increase of ΔT (e.g. solidification of a liquid): see Figure 130. On the contrary, when an endothermic reaction occurs on the sample, ΔT decreases. The heat treatment is usually a slow heating or cooling (typically a couple of °C). Usually ΔT is plotted against time.

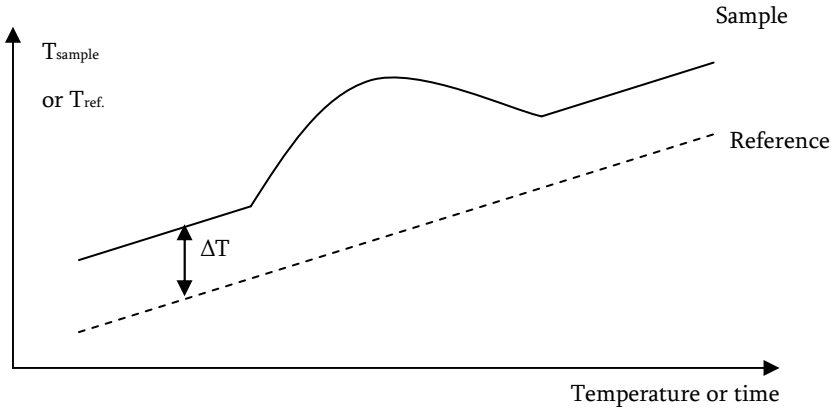

Figure 130 Principle of DTA for an exothermic reaction

The Differential Scanning Calorimetry (DSC) is based on the same principle as the DTA except the sample and the reference are placed in small calorimeter crucible. This method is better on the quantitative point of view, and gives the actual enthalpy of a reaction by the integration of the peak.

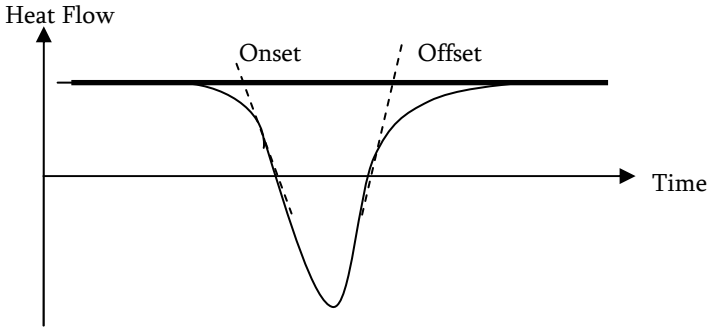

Figure 131 DSC of an endothermic reaction and peak integration

The baseline depends on the heat capacity of the sample (vertical shift of the base line) and on the thermal conductivity of the sample (rotation of the baseline). The onset of the reaction is calculated at the intersection of the baseline and the tangent of the peak. The integration of the peak between the onset and the offset gives the enthalpy of the reaction.

The apparatus is a "SETSYS Evolution 16" manufactured by Setaram. It is designed for both DTA/DSC and thermogravimetry. The heating is provided by a high performance graphite furnace, running up to 1600°C. The sample and the reference are placed in two small alumina crucibles (100µl) in the centre of the furnace. The reference is alumina (roughly the same weight as the sample in order to limit the difference of inertia due to the mass).

The heating rate has to be the same for calibration and experiments: 2°C/min

The sample is first heated beyond its melting point and then cooled around 30°C below it before actually starting the acquisition. This is done in order to homogenise the sample.

III.4.4.2 Calibrations

The facility has to be calibrated both for the temperature and for the heat flow signal. Seven elements were chosen in order to perform this calibration.

Table 6 Melting points and enthalpies of fusion of calibration elements

	Pb	*Zn*	*Al*	*Ag*	*Au*	*Ni*	*Pd*
Melting point (°C)	327.5	419.6	660.3	961.8	1064.2	1455	1554
Enthalpy of fusion (J/g)	23	107.4	401	104.8	64.5	300	162

The typical heat treatment for calibrations tests is described in (Tm is the theoretical melting point of the calibration material).

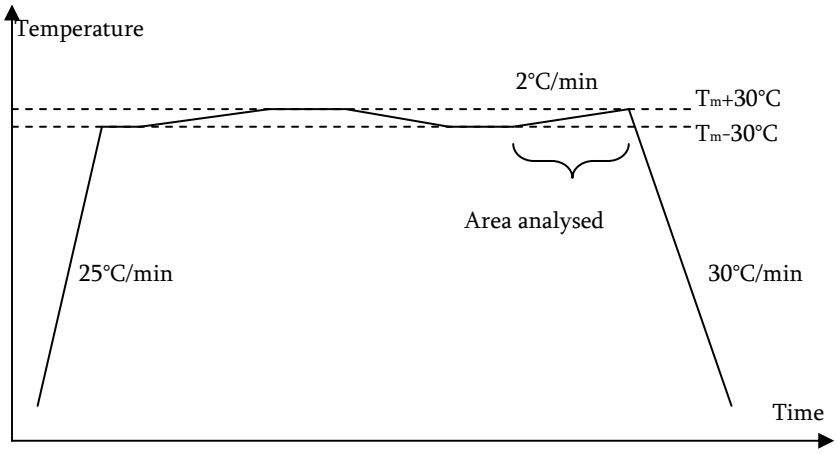

Figure 132 Heat treatment for DSC calibration

In order to link the signal provided by the apparatus to the theoretical values and draw the calibration lines, the dT_i and K_i values are calculated. dT is the shift in temperature of the melting point T_m (the compounds being pure crystalline materials, the onset temperature is the one corresponding to T_m). K is the coefficient between the integration of the heat flow and the actual enthalpy of the melting reaction.

Table 7 Calibration results

sample	*T onset*	*T peak*	*T offset*	*integration (µV.s/mg)*	*dTi*	*Ki (µV/mW)*
AG1	956.8438	960.3215	961.1329	28.7435	-4.9562	0.27427004
AG2	958.6783	961.9811	962.8581	28.8629	-3.1217	0.27540935
GOLD1	1066.686	1073.04	1074.076	6.8754	2.486	0.10659535
GOLD2	1068.987	1073.912	1075.141	6.3699	4.787	0.09875814
NI1	1448.005	1453.237	1454.331	5.5974	-6.995	0.018658
PD1	1558.073	1563.119	1564.104	5.9642	4.073	0.03681605
Ni2	1450.082	1455.058	1455.852	8.3865	-4.918	0.027955
AG3	962.0052	969.2983	970.433	15.2827	0.2052	0.14582729
ALU1	661.019	668.1811	669.4006	80.6861	0.719	0.20121222
PD2	1558.747	1563.182	1563.829	6.2515	4.747	0.03858951
NI4	1449.518	1453.912	1454.972	10.1484	-5.482	0.033828
ALU3	659.8	666.9	668	76.9339	-0.5	0.19185511
ZINC1	418.71	424.46	425.75	26.167	-0.89	0.2436406
LEAD1	326.35	328.07	329.02	6.6117	-1.15	0.28746522
AG4	962.18	967.81	968.67	18.3853	0.38	0.17543225
ZINC2	418.36	423.97	425.22	27.1776	-1.24	0.25305028
LEAD2	325.8516	328.2965	329.35	6.1042	-1.6484	0.2654
ALU4	660.3135	667.7562	668.8506	82.0756	0.0135	0.20467731

The three first experiments were not taken in account because the weight of the reference crucible was different from the sample one.

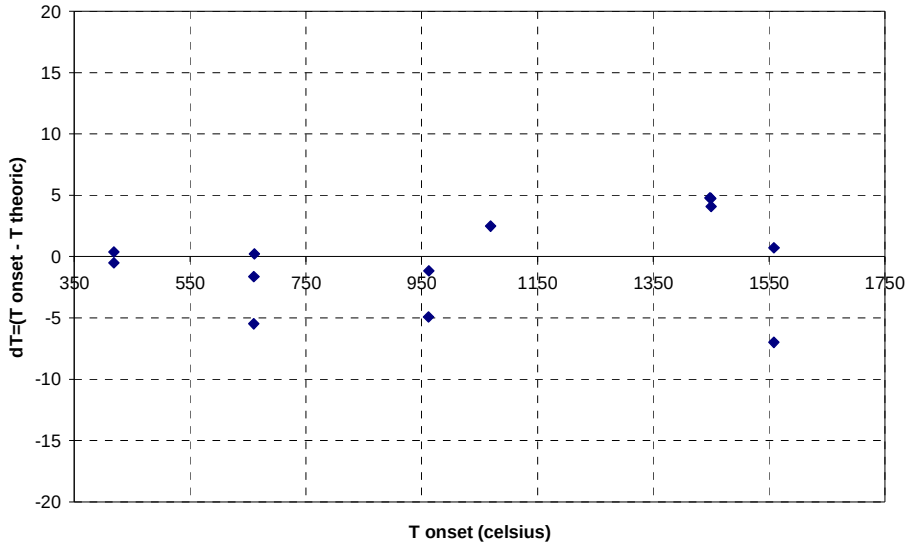

Figure 133 Plot of the variation between theoretical and experimental onset temperature

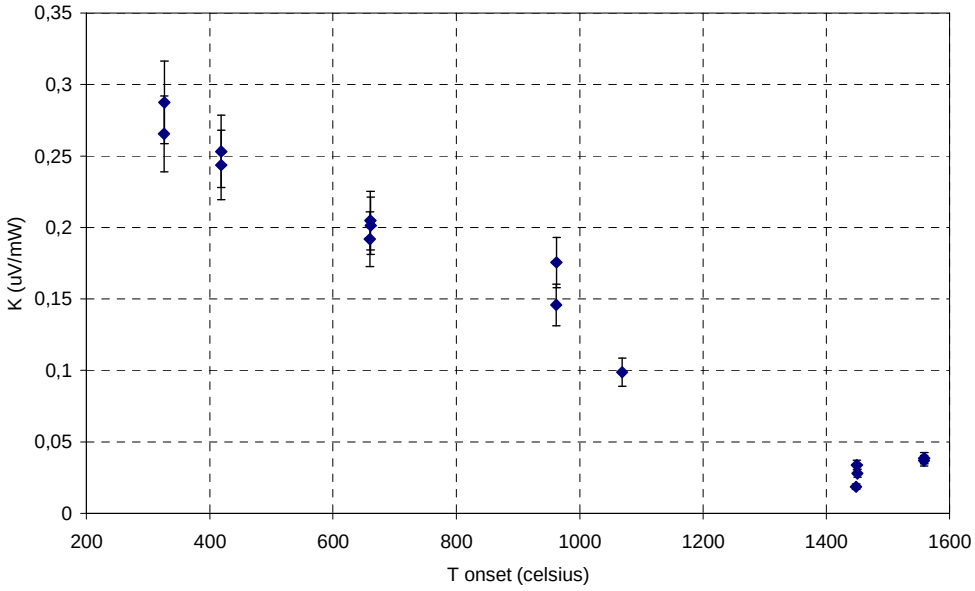

Figure 134 Calibration on the value of K function of the onset temperature

The manufacturer gives an accuracy of 10% for the enthalpy measurement. dT=f(T) is expected being a straight line, and K=f(T) a polynomial law of order 6. The calibration quality is satisfactory, even if some scattering is observed, particularly on dT for Al and Pd and on K for Ni. Ni and Al samples don't actually form a droplet after the melting, certainly due to the protective layer of oxide on the surface. The calibration samples keep therefore the wire shape, being maybe the reason of the scattering of data.

Chapter IV

Study of the α-phase

IV.1 Bulk samples of α-phase

IV.1.1 Manufacturing of bulk intermetallic samples

Intermetallics can be quite difficult to manufacture as bulk materials, and people tend to use vacuum casting facility to manufacture pure intermetallic coupons. No such facilities being available at Cranfield, it was decided to take advantage of the high thermal stability of intermetallics to synthesise some compound from the pure metal. Intermetallic are highly stable structures, having an ordered lattice different from the base metals[213]. They can therefore be produced by adding energy to the metals in contact, at solid state, triggering the exothermic formation of the intermetallic. Although platinum has a very high melting point (T_m^{Pt}=1769°C), the energy released during the exothermic reaction [1] can be used to self sustain the synthesis of the intermetallic compound.

$$xPt_{metal} + yAl_{metal} + zNi_{metal} = (Pt_xAl_yNi_z)_{i\,\mathrm{int}\,ermetallic} \quad [1]$$

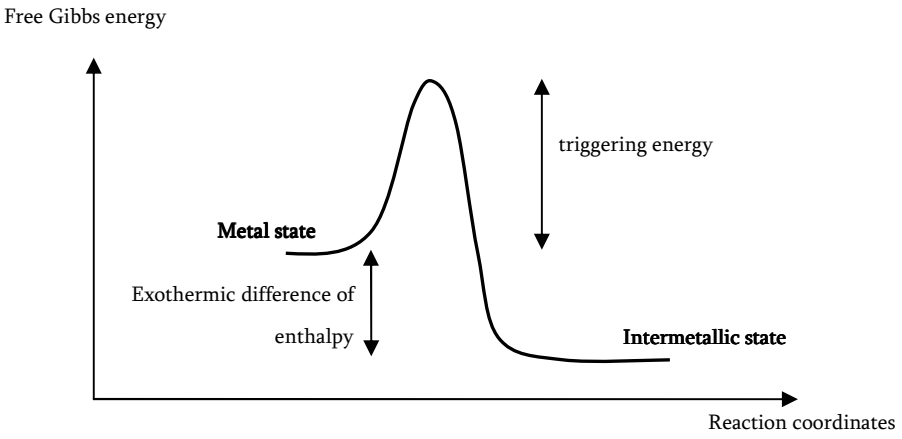

Figure 135 Energy profile for the metal intermetallic reaction

The exothermic reaction at solid state was expected to occur at relatively low temperature (about 600°C) between Ni, Al and Pt.

The heater has to stand in a vacuum chamber in order to prevent samples from oxidation, especially for Aluminium. A classical resistive evaporator was therefore used to heat treat the

samples. This system comprises an alumina coated tungsten boat (or bridge) in a vacuum chamber. The boat is heated by Joule's effect with high intensity current (up to 150A).

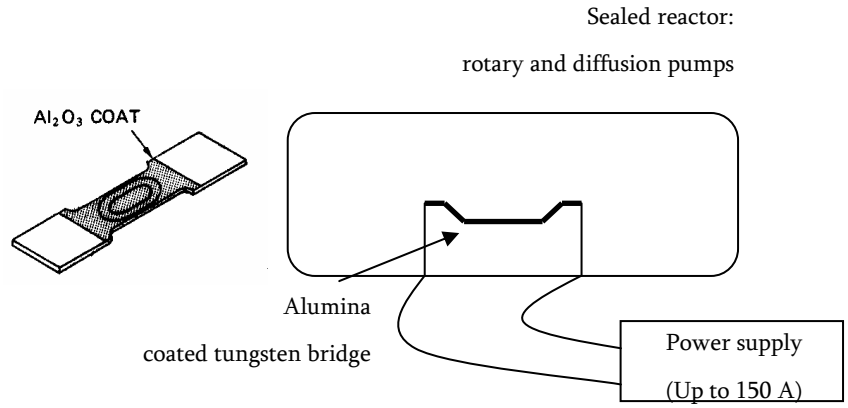

Figure 136 Experimental setup for bulk intermetallic synthesis

High purity Pt wire, Al wire and Ni wire were used for these melts. The pressure during the experiments was below 10^{-5}mbar. Because of the exothermic reaction and the expensive price of raw materials, the minimum required weight has been used. The total weight of each sample was 500mg.

The metallic wires were mixed close together like a wool ball, and loaded on the alumina boat. The evaporator is window equipped allowing observation of the inside of the chamber during the process. When the current grows, the temperature of the boat rises, and the bridge becomes extremely shining (so that protective dark glasses are necessary during observation). At an indicated current, materials react suddenly and violently in an intense firelight with projections out of the boat. The sample then looks like a drop of dark red melted metal. After two hours cooling under vacuum, the drop shows some cooling scares are cracks (Figure 137).

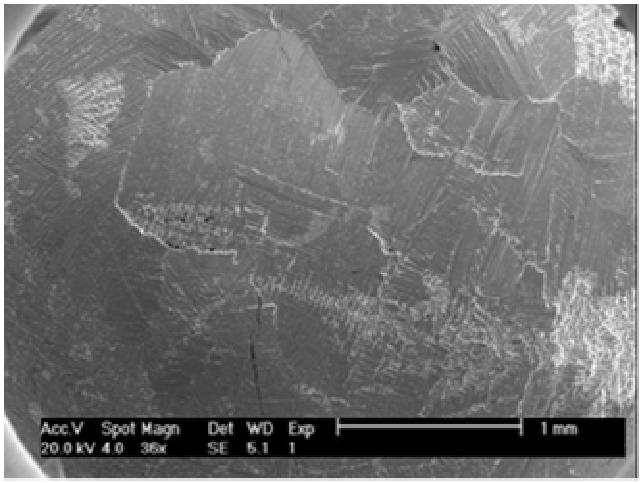

Figure 137 SEM micrograph of a solidified droplet of bulk intermetallic

Due to the violence of the reaction and the losts of some of the material, there is a shift between the expected composition and the actual composition of the droplet. EDS was carried out on mounted and polished section of the droplet after 4 hours annealing at 1100°C with fast cooling in a vacuum furnace (10^{-7}mbar). The microstructure of the reacted sample is homogeneous, an EDS on a large surface of a polished section of the sample can be considered as the overall composition of the sample. The concentrations obtained after reaction are gathered in Table 8 and plotted versus the Ni-Pt-Al diagram at 1100°C (Figure 138 corresponding to the ternary diagram that was available at the time of the experiments).

The diagram plotted in Figure 139 corresponds to the ternary diagram released by Gleeson's team in 2005[201]. Data points are exactly plotted by the mean of an Excel program turning ternary coordinate onto an orthonormal plot, the picture of the diagram is simply added over the plot.

The labelling corresponds to chronological order, though some samples did not react in the chamber, and are therefore not plotted on the diagram. The labelled experiment are plotted over Glesson's2004 version diagram in .One can realise the scattering of the data due to the loss of material during the reaction. Data points #1, 4, 9 and 3 fit inside the α-phase stability field. Data point #2 sits close to the γ'-$(Ni,Pt)_3Al$ Data points #11, #11bis, #12, #8 and #14 sit in a platinum richer region. The compositions produced differ from those planned due to the unpredictable loss of aluminium during melting. This is linked to the low melting point and lightness of the aluminium wire, affected by the high temperature before melting: some bits of material are blown from the melt pool when the exothermic reaction occurs.

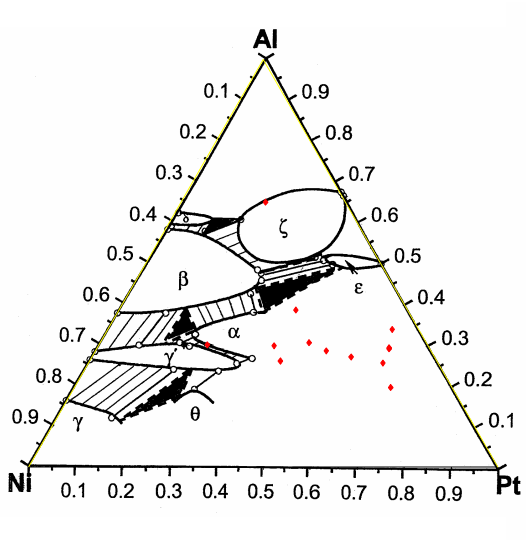

Figure 138 Composition plot overlapping Gleeson's 2003 ternary diagram

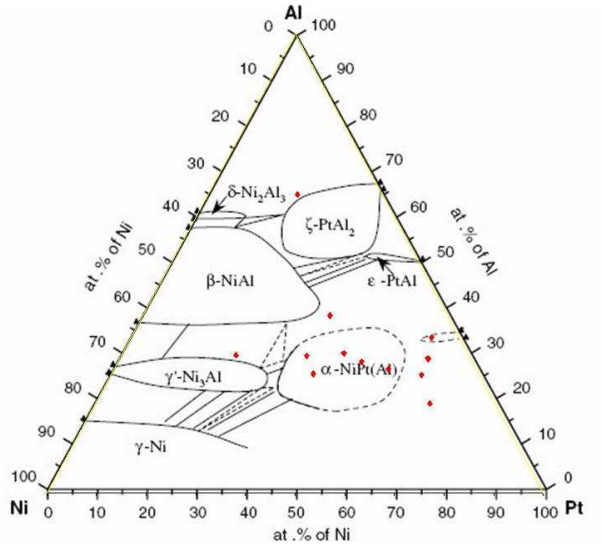

Figure 139 Composition plot overlapping Gleeson's 2005 ternary diagram

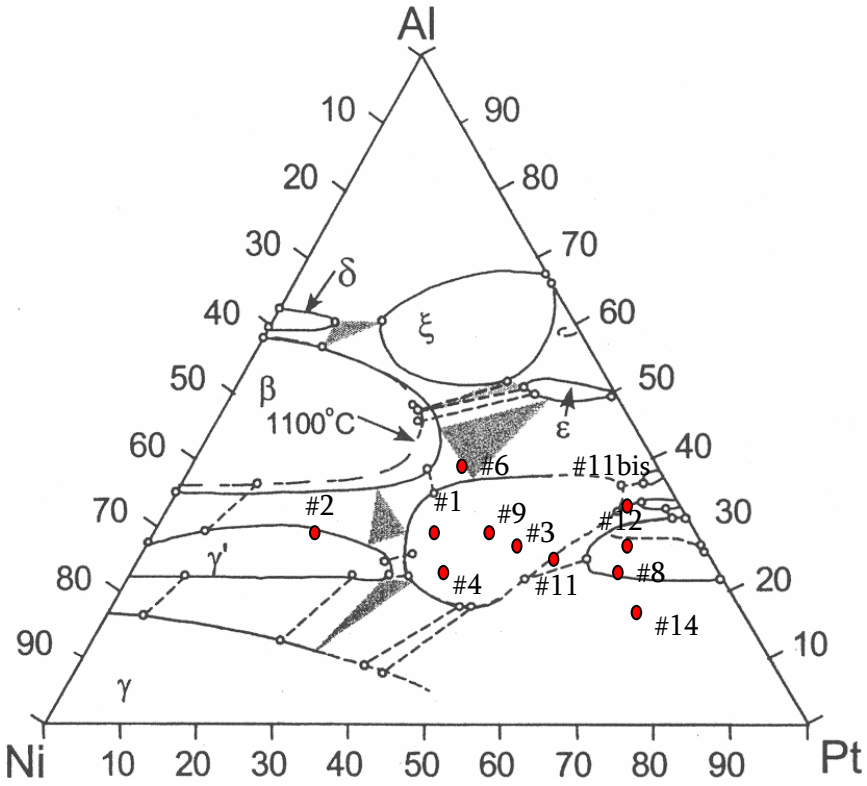

Figure 140 Data plotted with labels over Gleeson's 2004 version diagram

IV.1.2 Considerations on the intermetallic structure

IV.1.2.1 X-ray diffraction and discussion on the structure of α

Samples were reduced to powder by liquid nitrogen quenching of the droplet followed by a milling with a mortar and pestle. The powder was loaded on sticky glass slides, and analysed in a X-Ray spectrometer with a standard θ-2θ setup. Samples whose composition fit within Gleeson's α-phase field show relevant peak distribution (Figure 141), with some change in the relative intensity, and slight shift in peak values due to the various stoechiometries changing therefore the crystallographic lattice parameter value.

The peaks distribution corresponds to a tetragonal structure from the P4/mmm space group, of the AuCu type which corresponds to a tetragonal primitive cell with a C_4 rotation axis and three mirrors planes (Figure 148). XRD spectrum of sample #9, whose composition is the closer to stoechiometric $NiPt_2Al$ is compared to the JCPDS (Joint Committee for Powder Diffraction Studies) database value, JCPDS #25-1220.

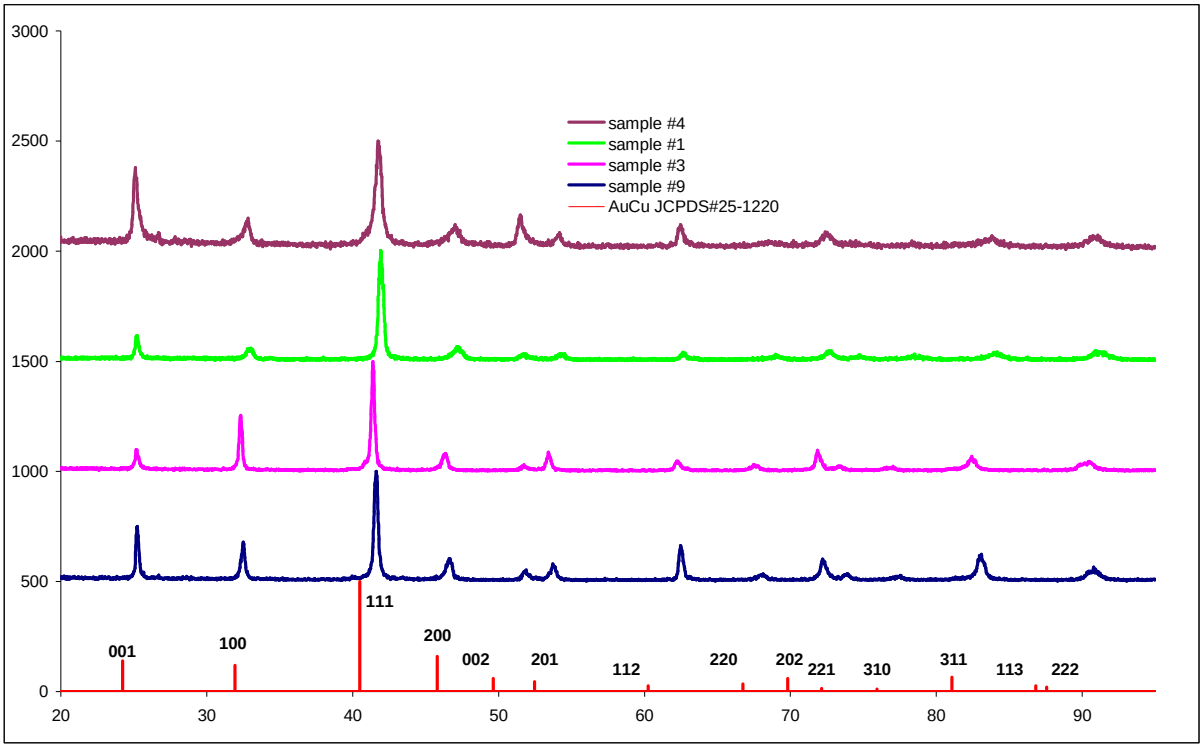

Figure 141 XRD spectra of powder #1, 3, 4, and #9 compared with AuCu JCPDS

Lattice parameters were calculated from the XRD spectra based on a primitive tetragonal cell; the distance *d* between two reticular plans *(hkl)* in a tetragonal cell whose lattice parameters are *a* and *c* is given by:

$$\frac{1}{d^2} = \frac{h^2 + k^2}{a^2} + \frac{l^2}{c^2}$$

Lattice parameters are gathered in Table 8, along with the expected composition for each sample, the experimental composition measured by EDS (average on 5 measurements), the current intensity crossing the alumina boat when the reaction occurred, and the relative brittleness of the sample. The brittleness is only subjective and relative, as milling the intermetallic into a powder was drastically varying with the composition. Samples having only the α-phase on their XRD spectrum are bolded. The other samples have mainly the α-phase pattern plus an other phase: β-(Ni,Pt)Al for data point #6, and Pt_3Al for data points #11bis, 12, 13, and 8.

Table 8 Cell parameters of the bulk intermetallic samples, reaction current and relative brittleness

Sample	*expected compostion (at%)*			*measured composition (at%)*			*lattice parameters*		*current*	*brittleness*
	Ni	Al	Pt	Ni	Al	Pt	a,b	c		
1	**33.3**	**33.3**	**33.3**	**32.8**	**29.8**	**37.5**	**3.85**	**3.53**	120A	**
2	**45**	**33**	**22**	**47.1**	**29.9**	**23.1**	**3.80**	**3.48**	70A	*
3	**22**	**33**	**45**	**22.4**	**28.5**	**49.2**	**3.92**	**3.53**	140A	***
4	**29**	**38**	**33**	**33.4**	**25.9**	**40.7**	**3.86**	**3.54**	90A	*
4bis	29	38	33	17.1	64.9	18.0			90A	
6	22	39	39	23.7	38.6	37.7	3.89	3.50	90A	**
8	13.5	33	53.5	11.7	25.6	62.7	3.91	3.65	100A	**
9	**24**	**36**	**40**	**25.0**	**30.4**	**44.6**	**3.89**	**3.52**	100A	***
11	**17**	**31**	**52**	**17.8**	**26.9**	**55.3**	**3.92**	**3.56**	120A	**
11bis	17	31	52	5.6	33.8	60.6	3.95	3.61	120A	*
12	10.5	41	48.5	8.6	29.3	62.1	3.94	3.62	130A	***
13	13.5	45	41.5	8.8	29.1	62.3	3.93	3.63	110A	*
14	13.5	45	41.5	13.1	19.37	67.53	3.85	3.49	110A	*

The structure proposed by Kamm et al[202] in 1994, and confirmed by Meinieger et al.[203] later in 2003 is a fully ordered $L1_0$ intermetallic with Ni atoms on the (001) faces, and Al at the corners. The shift to the stoechiometry was calculated in this study to be controlled by random distribution of Ni on the Pt lattice.

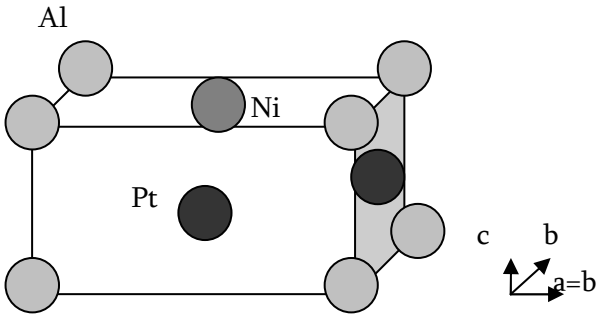

Figure 142 Structure for the $NiPt_2Al$ compound as proposed by Kamm et al.[202]

This structure is fully ordered, inducing the presence of superlattice peaks as a consequence[214]. These peaks are only due to the fact that this order at the lattice level (i.e. "surperlattice") reduces symmetries compared to a structure with random distribution on the lattice sites. None of these peaks can be observed for any of the experiment carried out at Cranfield. This means either the structure manufactured at Cranfield do not show the ordering proposed by the literature, either the sensitivity of the XRD spectrometer used is not sufficient. As one can notice in Table 10, all the superlattice peaks have a low intensity (this being a usual property of these peaks). The fully ordered structure ("Kamm cell", in Figure 142), and the non ordered P4/mmm cell ("Cranfield cell", similar to AuCu in Figure 148, with random distribution of Ni and Al on the Au lattice and Pt on the Cu lattice), where computed with a crystallography software, CaRIne[215], with the experimental cell parameters of sample#9, to give the diffraction peak list. Systematic peaks extinctions due to increase in symmetry in the non ordered cell are bolded.

Table 9 Calculated values for the "Cranfield cell"

h	*k*	*l*	*2θ*	*I/rel.*	*/F(hkl)/*
1	**0**	**0**	**22.842**	**0**	**0**
0	0	1	25.281	22.5	73.2
1	1	0	32.526	24.32	70.4
1	**0**	**1**	**34.33**	**0**	**0**
1	1	1	41.637	100	132.45
2	0	0	46.662	36.04	127.84
0	0	2	51.911	13.15	123.27
2	**1**	**0**	**52.564**	**0**	**0**
2	0	1	53.806	12.5	62.6
1	**0**	**2**	**57.421**	**0**	**0**
2	**1**	**1**	**59.196**	**0**	**0**
1	1	2	62.61	8.15	59.93
2	2	0	68.123	11.59	110.69
2	0	2	72.35	19.48	107.8
3	**0**	**0**	**72.891**	**0**	**0**
2	2	1	73.929	5.22	56.94
2	**1**	**2**	**77.011**	**0**	**0**
3	1	0	77.54	4.65	56.08
3	**0**	**1**	**78.556**	**0**	**0**
0	0	3	82.068	1.03	55.06
3	1	1	83.109	27.22	101.15
1	**0**	**3**	**86.584**	**0**	**0**
2	2	2	90.602	11.46	97.11
1	1	3	91.08	11.36	96.87
3	**2**	**0**	**91.118**	**0**	**0**
3	**0**	**2**	**95.102**	**0**	**0**
3	**2**	**1**	**96.62**	**0**	**0**
3	1	2	99.634	6.3	51.71
2	0	3	100.119	3.14	51.63
2	**1**	**3**	**104.721**	**0**	**0**
4	0	0	104.761	4.94	90.72
4	**1**	**0**	**109.464**	**0**	**0**
4	0	1	110.522	3.16	50.06
3	**2**	**2**	**113.742**	**0**	**0**
3	3	0	114.307	1.62	49.55
4	**1**	**1**	**115.403**	**0**	**0**
2	2	3	119.3	3.4	48.92

Table 10 Calculated XRD values for Kamm et al. cell

h	*k*	*l*	*2θ*	*I/rel.*	*/F(hkl)/*
1	**0**	**0**	**22.842**	**1.74**	**14.24**
0	0	1	25.281	30.97	94.36
1	1	0	32.526	33.42	90.68
1	**0**	**1**	**34.33**	**1.25**	**13.15**
1	1	1	41.637	100	145.53
2	0	0	46.662	36.09	140.56
0	0	2	51.911	13.19	135.63
2	**1**	**0**	**52.564**	**0.34**	**11.11**
2	0	1	53.806	17	80.2
1	**0**	**2**	**57.421**	**0.26**	**10.58**
2	**1**	**1**	**59.196**	**0.46**	**10.39**
1	1	2	62.61	11.01	76.55
2	2	0	68.123	11.69	122.12
2	0	2	72.35	19.67	119.01
3	**0**	**0**	**72.891**	**0.06**	**9.07**
2	2	1	73.929	7	72.46
2	**1**	**2**	**77.011**	**0.19**	**8.73**
3	1	0	77.54	6.22	71.29
3	**0**	**1**	**78.556**	**0.09**	**8.61**
0	0	3	82.068	1.37	69.91
3	1	1	83.109	27.59	111.88
1	**0**	**3**	**86.584**	**0.07**	**8.04**
2	2	2	90.602	11.64	107.55
1	1	3	91.08	11.54	107.29
3	**2**	**0**	**91.118**	**0.06**	**7.76**
3	**0**	**2**	**95.102**	**0.06**	**7.54**
3	**2**	**1**	**96.62**	**0.11**	**7.46**
3	1	2	99.634	8.35	65.4
2	0	3	100.119	4.16	65.29
2	**1**	**3**	**104.721**	**0.1**	**7.08**
4	0	0	104.761	5.04	100.67
4	**1**	**0**	**109.464**	**0.05**	**6.89**
4	0	1	110.522	4.17	63.19
3	**2**	**2**	**113.742**	**0.1**	**6.74**
3	3	0	114.307	2.14	62.52
4	**1**	**1**	**115.403**	**0.1**	**6.69**
2	2	3	119.3	4.49	61.7

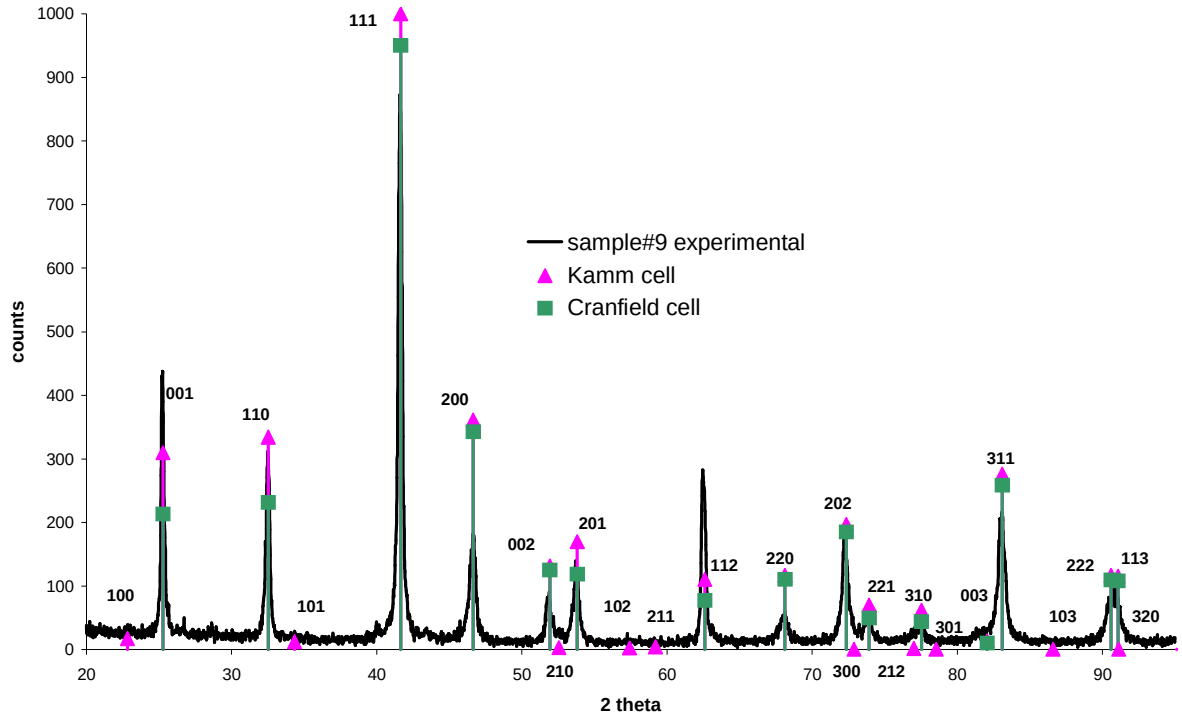

Figure 143 Experimental XRD spectrum of sample #9 compared to "Cranfield cell" and "Kamm cell" compiled spectra

The peaks intensities of experimental data do not entirely fit with compiled spectra, this being observed for all the compositions. The plans (001) and (110) diffraction peaks change intensity because of the Pt/Al ratio content: Al atoms substitution on Pt lattice results in a change in the structure factor, reducing the intensity of these peaks. For the same reason the (200) diffraction peak is always weaker than calculated.

The lattice parameters measured are relevant with the literature as shown in Figure 144, where sample #9 parameters are plotted on Kamm et al. plot across the 25at%Al pseudo binary system.

No trend can be concluded on the required current intensity to trigger the reaction within the reaction chamber. Nor on the relative brittleness of the bulk samples when reduced to powder, e.g. sample #4 was more difficult to mill than sample #9, though their composition is similar.

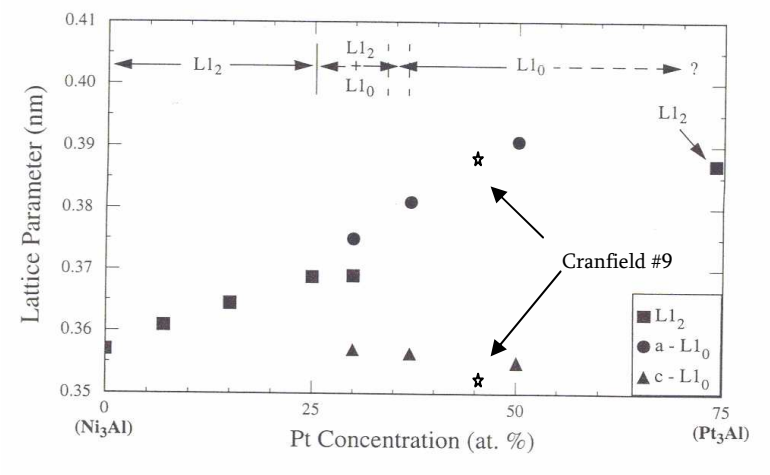

Figure 144 Added data on chart from Kamm[202]

Furthermore, in order to evaluate the composition effect on the cell parameter the a and c values were plotted as a function of the composition. Experimental points are roughly along a line parallel to the NiPt axis, so that the Pt content was chosen as the reference (Figure 145).

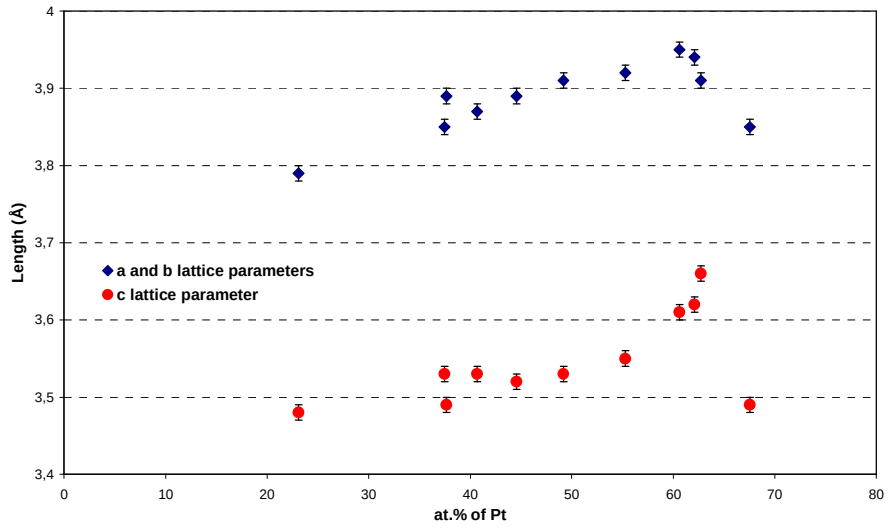

Figure 145 Variation of a and c lattice parameters as a function of Pt content

The variation is close to expected. When the proportion of platinum increases in the phase along pseudo binary parallel to the Ni-Pt axis, atoms of nickel are substituted by platinum, keeping the atomic percent of aluminium constant. These substitutions show the cell increases in size with increased Pt content, straining the lattice. The last two points at 67.5at%Pt correspond to sample #14 which does not contain α-phase, and where the XRD diagram is not very accurate.

The maximum recorded strain is only 5%, and other diffraction peaks are already observed for the points beyond 60% of Pt. However, a phase transformation is commonly observed for an

average of 15% strain; this contradicts the XRD results. Thus there is perhaps no phase transformation when compositions tend to the right of α-phase field.

Moreover, the strain caused by substitutions is relatively homothetic. Indeed the c/a ratio stays around 92%. The c/a ratio is plotted as a function of the Pt content in Figure 146

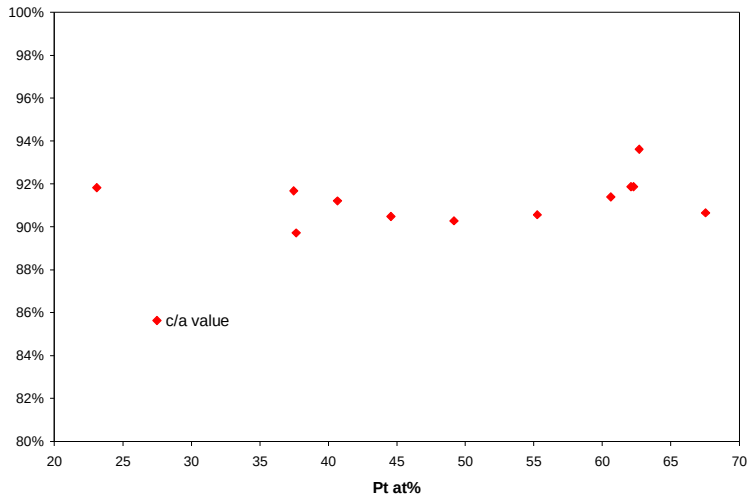

Figure 146 c/a ratio variation (mark size cover the error bar)

Moreover one can plot the rough cell size on the ternary diagram in order to evaluate the variation function of the global composition, only by plotting one of the parameters (in this case, "a" parameter is plotted in Figure 147). Data dots circled in black in Figure 147 corresponds to the samples showing other peaks than α-phase ones.

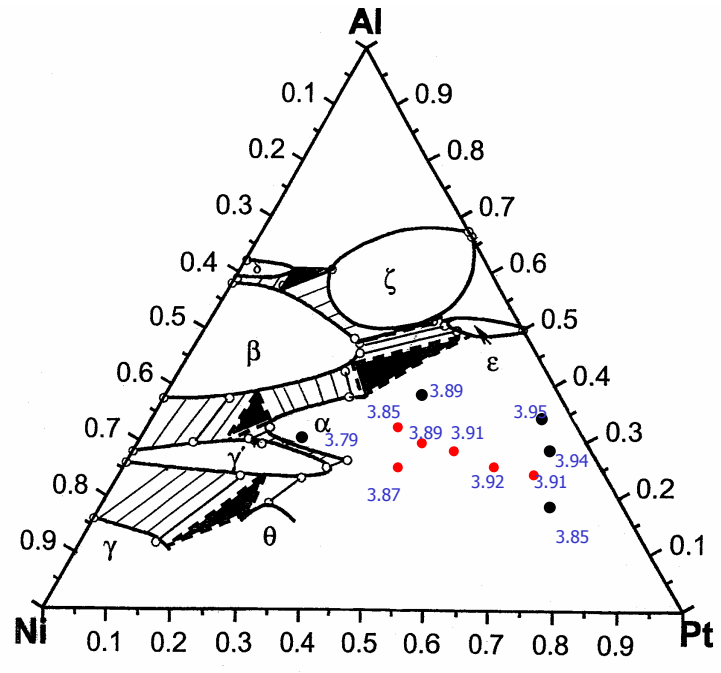

Figure 147 Global view of α-phase cell size variation with composition

This confirms the cell size is principally dependent on platinum content; a shift to the right side of the diagram corresponds to an increase of lattice parameters. On the contrary, aluminium proportions have less influence on the size.

IV.1.2.2 Discussion on the α- phase and other related compounds

The Ni-Pt binary diagram is not fully described in the literature[41], though it shows at solid state the presence of two structures α' and α'' within the large field of a α-(Pt.Ni) solid solution. The choice of Brian Gleeson to call α the phase spotted in the first ternary diagram comes from the Ni-Pt binary system. The α' and α'' are ordered structures of the solid solution: α'' is a AuCu type whilst α' is a $AuCu_3$ type. Ordering is a recurrent property of the $L1_0$ compounds[214], and the $NiPt_2Al$ is likely to display this behaviour.

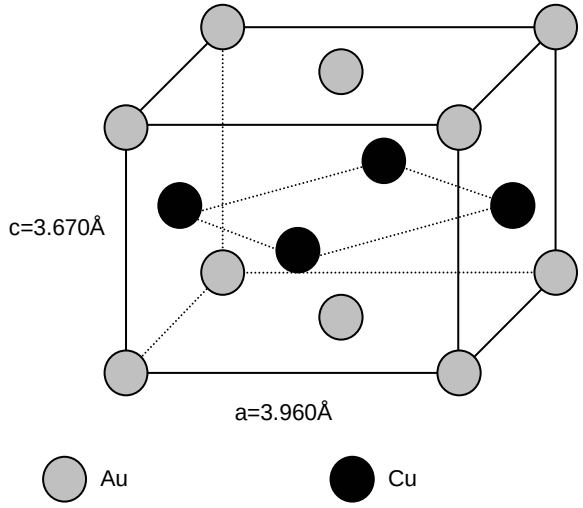

Figure 148 AuCu tetragonal P4/mmm cell

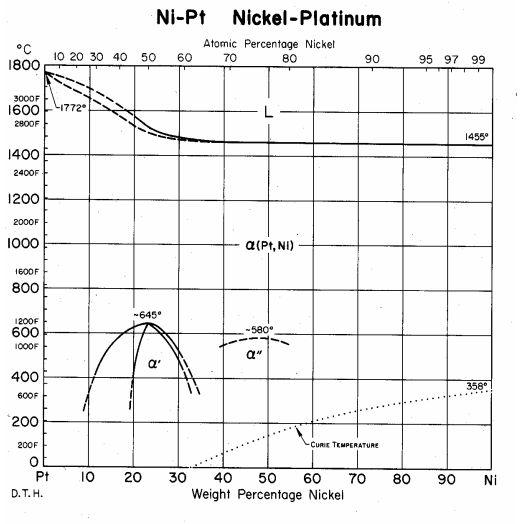

Figure 149 Nickel Platinum binary diagram[41]

Hayashi et al.[201] carried out high temperature XRD experiment on two compositions of the ternary α-phase: Ni-30at%Al-42at%Pt and Ni-30at%Al-35at%Pt (see Figure 150). They noticed an expected expansion of the *a* and *b* lattice parameter with temperature, but a rather odd behaviour on the *c* parameter: it increases with temperature up to 950°C-1000°C, and then drops drastically above a 1000°C .

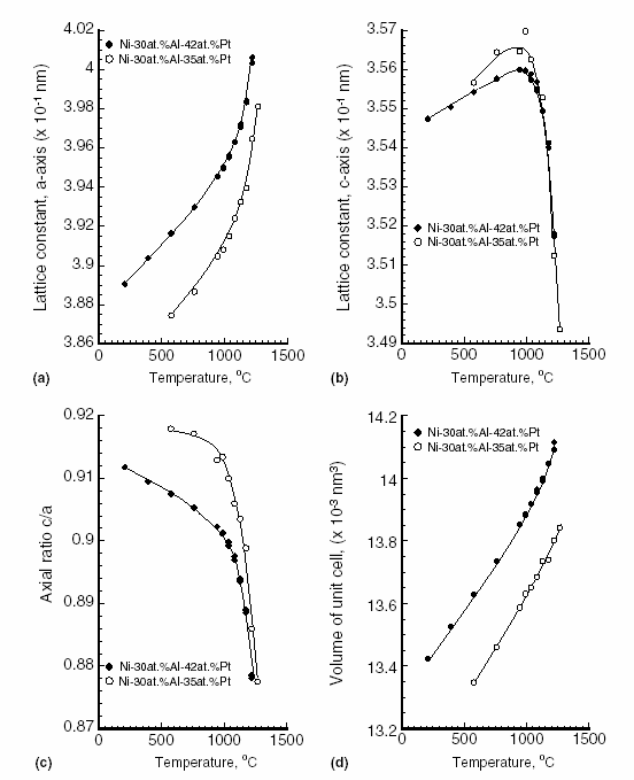

Figure 150 Temperature dependence on lattice parameters (a) *a* axis, (b) *c* axis, (c) *c*/*a* ratio, (d) volume of unit cell

The experimental data from this study are relevant with our tests (which were chronologically carried out before this publication). Although the *c* parameter behaves strangely, the overall volume of the unit cell increases with temperature: the expansion of the α-phase is not anisotropic, and the *tetragonality* of the phase increases with temperature.

Isotropic CTE's were not calculated in this study; this is carried out from Ni30Al42Pt data as it is the closest to the stoechiometric compound:

- ✓ For the *a* parameter: $1.9.10^{-5}K^{-1}$ for the 200°C-1000°C range, and 7.10^{-5} K^{-1} for the 1000°C-1200°C range
- ✓ For the *c* parameter: $3.9.\ 10^{-6}$ K^{-1} for the 200°C-1000°C range, $-5.8.10^{-5}K^{-1}$ for the 1000°C-1200°C range

The dramatic change in lattice size at 1000°C is likely to be linked to an order/disorder transition in the α-phase, with Pt atoms moving to the Ni sublattice, or local disorder at the corner sites as proposed by Hayashi et al[201].

An other specificity of the α-phase is its similarity with the two surrounding cubic $L1_2$ phases Ni_3Al and Pt_3Al. The system behaviour between these two phases at a fixed Al content of 25at% is actually the point of Kamm's work[202].

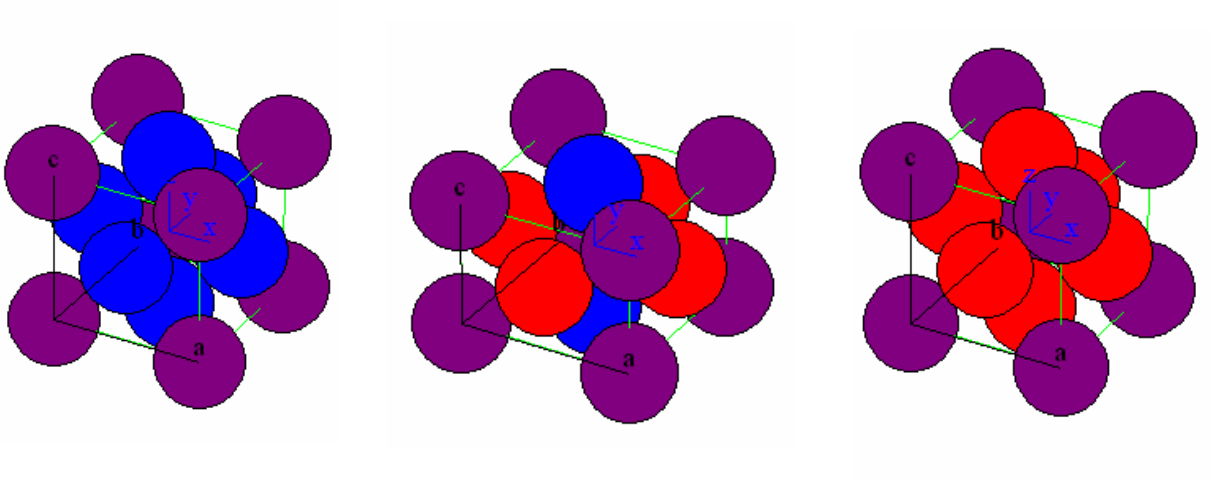

Figure 151 Compared structures of $L1_2$ Ni_3Al, $L1_0$ $NiPt_2Al$ and $L1_2$ Pt_3Al (Al atoms in purple, Ni in blue, Pt in red)

Pt_3Al has two structures, $L1_2$ is stable only over 400°C, the low temperature structure of Pt_3Al is the result of a martensitic transformation of the $L1_2$ structure, to a distorted $L1_2$ structure (D0'c type)[216].

The ordered structure of α-phase has a strong diffusion path along the <001> orientation. Diffusion of nickel which are closer from each other, easier jump of vacancies on this sublattice, with the corner of the cell[217].

Magnetic properties[218]: $L1_0$ compounds were discovered for their magnetic properties over 70 years ago. Since then this class of hard-magnetic materials has attracted continuing attention in various areas, including high-density magnetic recording. Scientific interest has been fueled by the specific features of $L1_0$ magnets, such as the layered crystal structure, the two-sublattice nature of the magnetism, and the simultaneous involvement of 3d and 4d/5d electrons.

Magnetic $L1_0$ or CuAu(I) compounds having the nominal structure MT consist of alternating layers of light or 3d transition-metal atoms (T) and heavy or 4d/5d transition-metal atoms (M), but the most general L10 composition is ABC2, where C planes are separated by A–B planes.

IV.2 Thermal analysis works

IV.2.1 Melting point measurement

The bulk samples of intermetallics, manufactured by heating wires of pure Pt, Ni and Al together in a protective atmosphere were analysed by quantitative differential scanning calorimetry (DSC). The experimental procedure and calibration are described in the chapter III of the thesis. These samples have already reacted into an intermetallic bulk compound. The aim of this experiment is to give the melting point of the bulk compound, and the enthalpy of melting. The peak corresponding to the melting is highlighted with an arrow. The blue line corresponds to the furnace temperature; the pink curve corresponds to the heat flow signal. The plot of bulk #9 is given at a greater scale because this sample corresponds to the middle of the α-phase field.

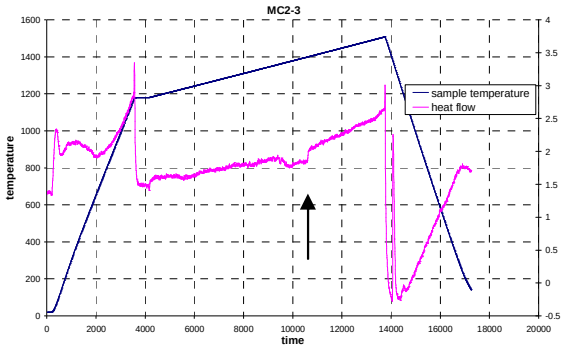

Figure 152 DSC of bulk sample #2

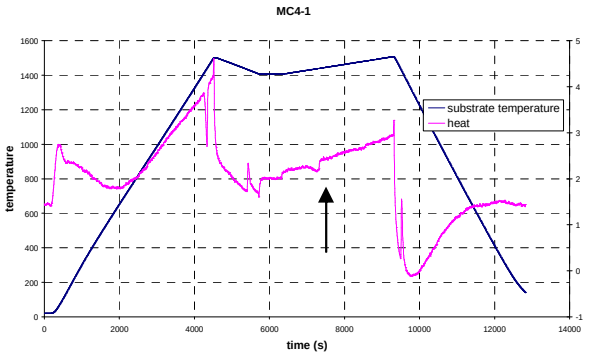

Figure 154 DSC of bulk sample #4

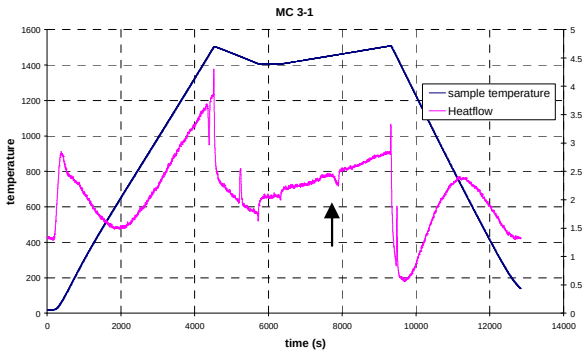

Figure 153 DSC of bulk sample #3

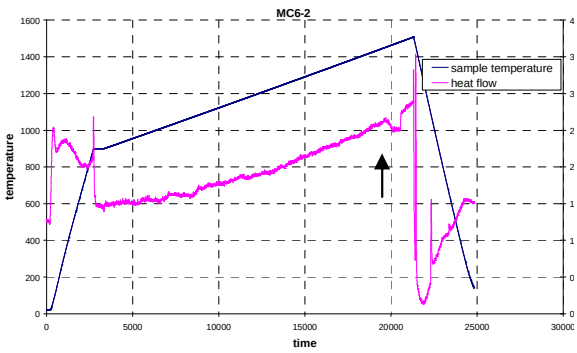

Figure 155 DSC of bulk sample #6

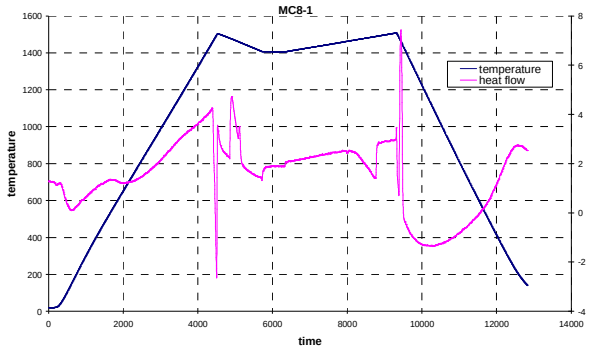

Figure 156 DSC of bulk sample #8

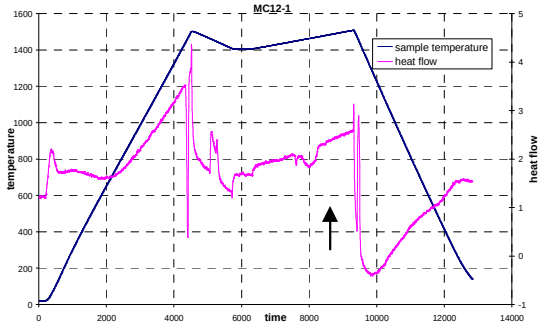

Figure 157 DSC of bulk sample #12

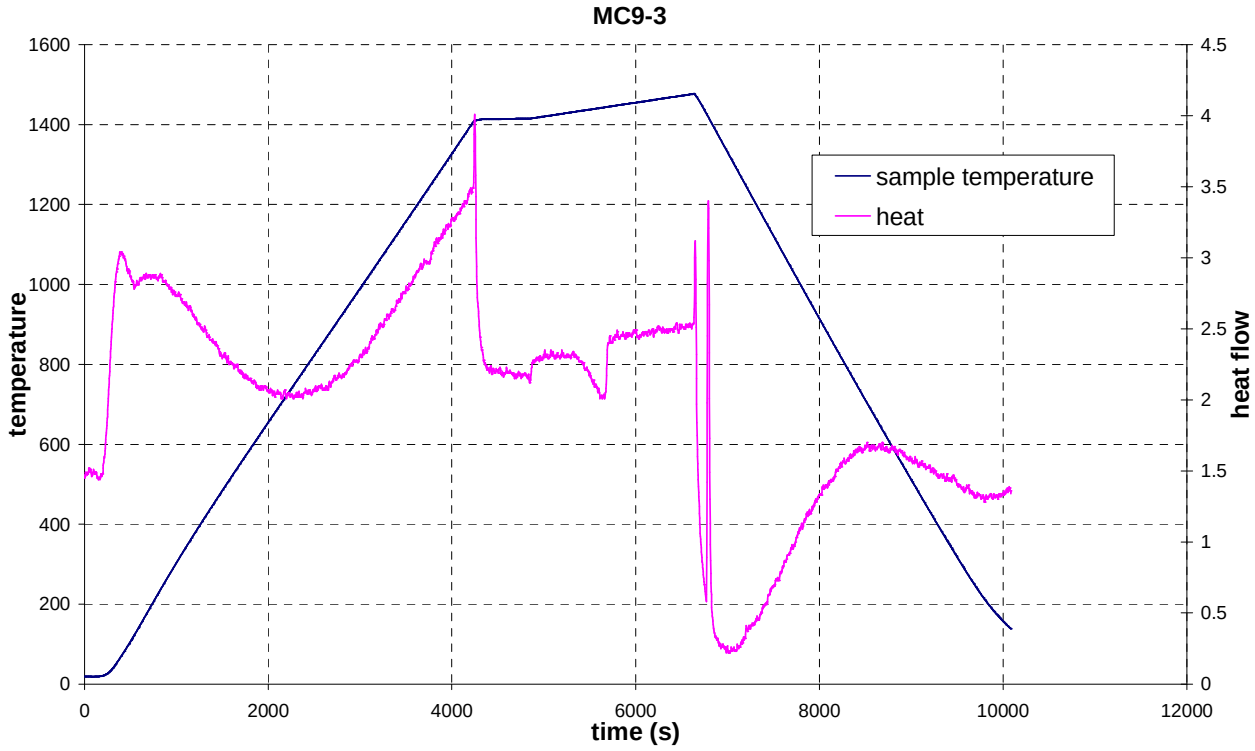

Figure 158 DSC of bulk sample #9

The results of the integration and melting point are given in Table 11. Due to the error on the reading of K (corrective coefficient obtained by calibrations), and due to uncertainty on the integration value (5% for both), the value of the enthalpy is given with an error of ±7% (confirmed by the manufacturer of the apparatus). The enthalpy of melting, ΔH, is calculated with the equation below (H is the integration value given by the software of the DSC facility, K is given by the calibrations and M is the molecular weight of the compound.

$$\Delta H = \frac{H}{K} \cdot M$$

Table 11 Results of the integration of bulk samples

sample	*Experimental data*				*Correlated with calibration curves*	
	T_{onset}	T_{peak}	H (μV.s/mg)	dT	K	ΔHfusion (kJ/mol) ±7%
#2	1359	1377	8.06	+2	0.03	16.3 (presence of 2 peaks)
#3	1454	1459	7.89	+4	0.03	30.7
#4	1430	1438	5.00	+3	0.03	17.7
#6	1456	1481	5.88	+4	0.035	16.4
#8	1474	1489	4.39	+2	0.035	17.1
#9	1435	1443	6.85	+3	0.03	25.2
#12	1448	1463	5.81	+4	0.035	22.3 (presence of 2 peaks)

Samples #2 and #12 do not show a clear and distinct peak: this may be due to the presence of two phases melting at a different temperature. The samples which are really in the middle of the α-phase field (for all the ternary diagram versions) are #4, #3 and #9 and have a nice peak of melting, which give more accuracy to the integration value. The melting point of α, corresponding to the onset temperature (it is a crystallographic material), is relatively low compared to other intermetallics. However, the melting of γ' is a peritectic at 1385°C -1395°C and Pt_3Al melting occurs at 1556°C with an eutectic melting at 1507°C. The α-phase is located between this two compounds (for the exact stoechiometries: $Ni_3Al+2Pt_3Al=3xNiAlPt_2$), therefore, a melting point of 1440°C seems logic.

Besides, this low temperature might be a problem regarding the applications at high temperature expected for α as a bondcoat. The melting point is not directly linked to the actual performances of an oxidation resistant coating, like other parameters such as the kinetic of the oxide growth, the volatility of the oxide or its chemical bonding. Nevertheless, it will definitely affect the mechanical properties of the system.

If the melting point of α is confirmed to be around 1440°C, it would imply the bondcoat works at more than 80% (in°K) of its fusion temperature (compared with 72% for NiAl or 58% for RuAl). However, the microstructure and the thickness of the low mass bondcoats might reduce the effect of a low melting point for the mechanical behaviour of the overall TBC system. Moreover, $PtAl_2$, which is partially present in low activity diffusion bondcoat, has a melting point of only 1406°C.

Table 12 Melting points and enthalpy of formation of some intermetallic compounds

Compound	*NiAl*	*Ni_3Al*	*$PtAl_2$*	*PtAl*	*Pt_3Al*	*RuAl*
T_m (°C)	1630	1390	1406	1554	1556	2080
ΔHf (kJ/mol)	-67	-42	-84	-100	-63.6	-110

IV.2.2 Pseudo enthalpy of formation

The energy released during the reaction of formation of the α-phase from the pure metal was measured by quantitative DSC. A system similar to the metal multilayer coating pattern was produced, it is a free standing coating in order to exempt the effect of the substrate.

A very thin foil of aluminium (1.5µm) was used as a substrate, Pt and Ni layers were deposited onto this foil by the usual sputtering process described in the coating manufacturing chapter of the thesis (with the rotation of the substrate because the pattern is symmetrical), see Figure 159. The global composition of the system is $Pt_{45}Al_{28}Ni_{27}$ and the thicknesses of each Pt and Ni layers are respectively 0.55µm and 0.48µm. Because the substrate is very delicate to handle (1.5 µm thick foil tends to fold itself by static electricity) it had to be framed between glass slides to keep it steady and give some weight to the sample hooked in the deposition chamber.

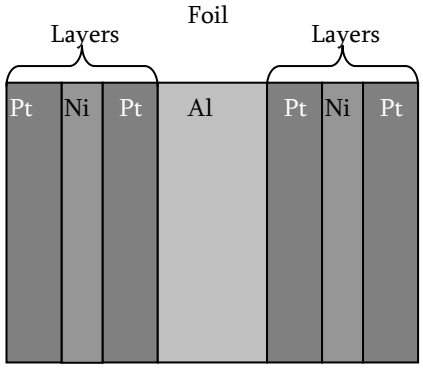

Figure 159 Layout of multilayers for DSC

Once manufactured the sample was cut with a scalpel and fold to fit inside the DSC crucible. Three experiments were carried out by heating at 2°C/min from room temperature to 1600°C in order to track the reaction triggered at low temperature. However, a consequent mass of material was needed in order to overcome the sensitivity of the DSC sensor. The successful experiment was carried out with 15mg of free standing coating, folded into the DSC crucible (previous tries at 0.4mg and 3.5mg were not sufficient enough).

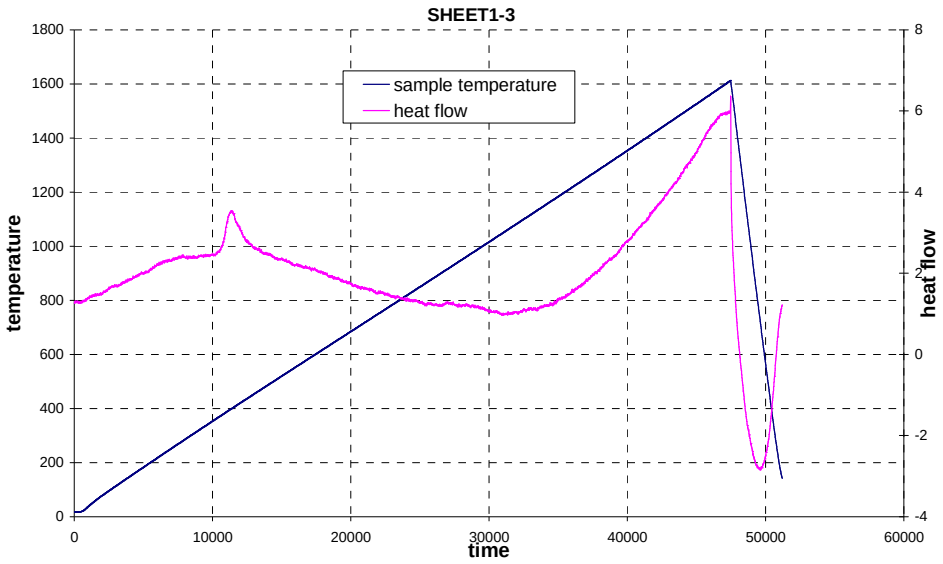

Figure 160 DSC result of free standing multilayer sample

The heat flow curve (in pink in Figure 160) displays an exothermic peak whose onset temperature is 376°C. The peak temperature is achieved at 399°C while the offset occurs at 431°C. This peak corresponds to the reaction of the metallic layers to form the intermetallic compound. One can notice that the curve slope differs before and after the peak. The slope of a DSC signal is directly related to the heat capacity of the analysed sample: the nature of the sample did change prior and after the reaction. Moreover, the slope changes again, at a temperature below the melting point of the compound. This change occurring around 1100°C is likely to be related to the high temperature behaviour of the α-phase: an order-disorder transition (with a smoother change in slope as this transition is gradual). The very last change in slope corresponds to the melting of the compound occurring at higher temperature than previously measured (around 1500°C, the melting peak is very smooth due to the low mass of the sample).

As expected the reaction is triggered at low temperature, below the melting point of the Al layer: it is a solid state reaction. The quantitative integration of the exothermic peak gives an enthalpy of -38.2kJ/mol. This value is globally lower than the enthalpies of formation of other intermetallics of the Ni-Pt-Al system (Table 12). However, the energy measured by this method can not be considered as an energy of formation as the reacting metals are not in thermodynamic standard state when the reaction occurs. The metals are on thin film state, with some internal stress growth and not fully dense. Moreover the presence of interfaces between the layers adds surface potential energy to the system. It can therefore be expected to obtain a lower value than expected.

IV.2.3 Conclusions and future works

During this project, some results were obtained, which improves the current knowledge on α-phase which is quite interesting regarding to the poor content of literature on this compound.

- ✓ The α-phase phase field at 1100°C was investigated, confirming the ternary diagram of B.Gleeson
- ✓ The crystallographic structure of α-phase was confirmed to be an ordered tetragonal $L1_0$ intermetallic centered on the Pt_2NiAl stoechiometry
- ✓ The variation of lattice parameters with composition was investigated: the Pt content influences the most the cell size
- ✓ The melting point of α-phase was experimentally measured and is relevant with the melting points of surrounding intermetallic, although it is not as high as β-(Ni,Pt)Al, suggesting α is not as stable.
- ✓ The energy released during the reaction of pure metals layers to form α-phase was measured: this reaction is triggered around 400°C, with an energy of -38.2kJ/mol, which, if compared to standard state enthalpy of formation of other intermetallic of the ternary system, is not very high in absolute. This confirms that α-phase may not be the most stable phase of the Pt-Ni-Al system.

In order to improve the understanding of the α-phase, some experiments would be interesting to carry out, which are possible with Cranfield University facilities:

- ✓ The coefficient of thermal expansion is a key property for high temperature intermetallic used as protective coatings. This can be measured by the mean of thermo mechanicial analysis (TMA), which measures the strain of a sample ingot when exposed to a given temperature profile
- ✓ The structure of α-phase is likely to encounter order-disorder transition. This would be measurable by carrying out a measurement of the Curie temperature of the compound. A change in the order of the structure leads to changes in electronic levels in the structure which may be possible to measure.
- ✓ At last the young modulus of α-phase can be measured by traditional mechanical testing (on bulk or on coatings by acoustic analysis).

Chapter V

Intermetallic coating manufacturing

V.1 Introduction and generalities

The intermetallic coatings manufactured during this project follow the principle of the Low Mass Bondcoat manufacturing process described earlier in this thesis. However, it has to be demonstrated that it can be switched to a 3 metals system with alternating layers of Nickel, Aluminium and Platinum. Moreover, it has never been proven before, in the literature nor at Cranfield University, that the α-$NiPt_2Al$ phase can be manufactured as a coating on metallic substrate.

Sequencing the layers of each metal deposited by sputtering offers the main advantage of controlling the overall resulting composition of the film, as it was proven by Colgan[47], Saint-Ramond[207] and Silva[208]. Thus, knowing the atomic weight (M) and the density of each element (ρ), it is possible to link the thickness ratio of the three elements, Ni, Pt and Al with the global composition.

Table 13 Al, Ni and Pt densities and atomic weight

	ρ (g.cm-3)	*M (g.mol-1)*
Al	2.702	26.98
Ni	8.90	58.71
Pt	21.45	195.09

For a given composition $Pt_xAl_yNi_z$, and a given total thickness of the multilayer coating a_{tot}, the thickness of each element layer, a_{Pt}, a_{Al}, a_{Ni} can be calculated by:

$$\begin{cases} \dfrac{a_{Al}}{a_{Pt}} = \dfrac{y \cdot M_{Al} \cdot \rho_{Pt}}{x \cdot M_{Pt} \cdot \rho_{Al}} \\ \dfrac{a_{Al}}{a_{Ni}} = \dfrac{y \cdot M_{Al} \cdot \rho_{Ni}}{z \cdot M_{Ni} \cdot \rho_{Al}} \\ a_{Al} + a_{Ni} + a_{Pt} = a_{tot} \end{cases}$$

Calibration is therefore needed to know the deposition rate for each metal at a given power and pressure. Many parameters would affect the resulting coating. No systematic study of the effect of each of these parameters was done, but they have to be listed.

Concerning the preliminaries of the process:

- ✓ *The substrate type*: Ni25Cr and Ni-based superalloy do not have the same mechanical properties at high temperature; therefore the interaction between the multilayer film and the substrate will differ during the annealing of the layers to form the intermetallic. The difference in chemistry will as well induce change in interdiffusion behaviour between the coating and the substrate: NiCr is γ based whereas superalloys are γ/γ' composites.
- ✓ *The substrate preparation*: Cleaning is a key step in surface engineering; removing organic pollutant from the surface, and removing any fine oxide or hydroxide scale that could formed during the storage or the machining of the substrate material, or other detrimental impurities such as sulphur. The surface finish as well changes a lot the adherence properties of the film, as the type of machining, grinding or grit-blasting.
- ✓ *The quality of the sputtering targets*: Chemical impurities within the target material will be deposited onto the substrate. Sputter cleaning of the targets prior to deposition has always been carried out in order not to coat the substrate with the unclean fist atomic layers of the targets. Platinum targets do not need as much cleaning as Aluminium for instance, as platinum is a noble metal whereas pure aluminium is very reactive and is likely to form oxide and hydroxide on its surface.
- ✓ *The cleanliness of the deposition chamber*: This point may seem obvious, however the sputtering facility used during this project were shared with other researcher, and needed regular cleaning. The inner walls of the chamber are fully dismountable and were regularly cleaned by grit blasting and IPA soaked fine cloth. All the elastomer seals of the chamber were regularly cleaned with IPA and re-lubricated with vacuum grease in order to ensure the best vacuum (seals from the sensor and rotating axes feedthroughs, targets insulating frames, chamber lid seal).
- ✓ *Samples handling and storing*: once machined and cleaned, the samples were held with powder free latex gloves to prevent any skin grease to get deposited on the

surface, and were stored in a dry atmosphere (desiccator with silica moisture absorbing granules).

During the deposition itself:

- ✓ *Position of the samples on the substrate holder:* the deposition rate for each metal depends on the working distance between the substrate and the target, it depends as well on the layout in x and y across the holder, as the vapour cloud is not symmetrical (magnetron effect and non homogeneity of the magnetic field)
- ✓ *Base pressure:* before injecting Ar in the chamber and starting the deposition, the chamber is pumped down to a high vacuum by a secondary pump, typically to 10^{-7} mbar. The lower the base pressure, the cleaner the gas environment, especially regarding to oxygen, nitrogen and water vapour that may react with metals to form respectively oxides, nitrides or hydroxides.
- ✓ *Sample temperature and Ar pressure:* As explained in the literature review chapter, the film microstructure depends on these two parameters, following Thornton's model. In this study the samples were not heated by an external heater (option offered by the coater, by infrared radiative heating of the back of the substrate holder); however, the plasmas created over the targets radiate some energy converted to thermal energy, it is often acknowledged that for the order of magnitude of power used in this study, the resulting temperature does not exceed 250°C.
- ✓ *Targets positions regarding to each other:* each target has a different magnetic field, due to the various paramagneticity of each material, the thickness of the target, the thickness of the copper backing plate (if there), the amount of power applied to each plasma, the type of applied power (DC, RF, pulsed) and the homogeneity of the magnets on the magnetron. As a consequence there is an "induced" effect of the other targets on the one being use for sputtering. This induced effect is as well strongly dependant on the chamber geometry i.e. for a single coater the substrate holder geometry (the size of the chamber and the distance between targets I soften kept constant)
- ✓ *Power and type of signal:* obviously the electrical power applied to the target is directly linked to the plasma density (the more bias the more Ar+ ions in the

plasma), hence to the number of ions impacting the target resulting in a denser metal vapour cloud and an increase of the deposition rate. Power is limited by the coater geometry (cooling efficiency of the magnetron to prevent any melting of the plastic frame), by the induced temperature on the film, and by the induced stress on the deposited film. The type of signal: DC, RF or pulsed is often imposed by the material to be deposited, but results in change in deposition rate for a same power value, and a change in coating microstructure.

- ✓ *Purity of the Argon:* the Argon used during the process is U type. However its purity regarding to oxygen is improved by the use of a getter furnace (pure Titanium chips heated at 700°C) on the inlet line, which traps oxygen by forming some Ti oxides.
- ✓ *The use of initial ion plating:* applying a negative bias to the substrates during the fist 15min of the deposition improves dramatically the adherence of the film (see later in this chapter).
- ✓ *Number of layer on the multilayer pattern:* For a given total thickness, the number of metallic layer, will change the homogeneity of the coating. Moreover, the more layer, the more sequential rotations of the substrate holder, inducing possible intrusion of impurities through the mechanical axes feedthrough of the chamber.
- ✓ *Mulilayer pattern:* With 3 metal targets instead of 2, the number of possible alternation pattern is multiplied. Depending on the alternation pattern, various behaviours during the annealing will be observed.

During the annealing of the metallic multilayers to the intermetallic:

- ✓ *The type of furnace:* the heat treatment is carried out under protective atmosphere, i.e. either vacuum or Ar. Various results were obtained depending on the method used. The Argon furnace is an alumina tube, with convective, and radiative heating whilst the vacuum furnace is mainly controlled by radiative heating from the graphite electrodes.
- ✓ *The heating and cooling rate*: Argon and vacuum furnace do not allow the same heating and cooling ramp. The Argon furnace has a lot of thermal inertia which improves the stress release in the film during its annealing.

This chapter is divided in three parts corresponding to chronological evolutions of the process. At first empirical tries were carried out on dummy metallic substrate Ni25Cr alloy, with

various results. The second part corresponds to the manufacturing of intermetallic coating on AM1 with and without rotation of the substrate. At last the final part of this chapter describes how the overall process procedure was changed for a better control of the resulting film.

During this project, 40 batches of coating were actually produced, corresponding to over 200 samples with various parameters (substrate type, surface finish, deposition power, deposition pressure, composition, number of layers, rotation of the substrate, annealing temperature, annealing atmosphere…)

V.2 Early experiments on NiCr substrates

These experiments correspond to the first approach with the sputter coater. Therefore dummy sample of Nimmonic 75 were used for these preliminary tests. The main results achieved with these experiments concern the detrimental role of ion plating on coatings adherence. The effect of the multilayer pattern was as well observed. At last calibrations issue were raised, regarding to the use of an automated rotation of the substrate holder in front of each target for a better control of high multilayer systems. At the end of these setting tests, a study of some parameters of the heat treatment parameters were controlled.

Overall this first experimental part of the project was rather disappointing as none of the coating were adherent after annealing the layers. But it proved that it was possible to manufacture α-$NiPt_2Al$ phase coating with this way, and raised key points for the following of the study such as calibration and quality control of the deposited layers.

V.2.1 Detrimental role of the ion plating: blz1-3,5, and 7

V.2.1.1 As deposited coatings

The 3 first batches produced in this study where relatively empirically produced. Samples are plainly hanged to a metallic mesh with NiCr wire, and the position of the substrate is rotated manually in front of each target. The three first batches are called blz1, blz2 and blz3. This batch terminology will be carried out throughout the thesis for more convenience as it was used throughout the project, and progress reports. Calibrations were carried out on step measurement on glass slides, by DEKTAK mechanical step.

Deposition power where chosen empirically from previous experience on the coater: 300W on the Pt target, with RF mode, 190W for Ni in DC mode and 160W on Al in DC mode. Later on DC power will be expressed in current intensity: the power supply is controlled in current mode, which is proportional to the quantity of electron passing through the system, hence proportional to the Ar bombarding of the target, hence to the deposition rate. At fixed current the

bias tends to reduce with deposition time due to heating and erosion of the target. The Argon pressure during sputtering was quite high, set at 28mTorr in order to increase deposition rates.

The metallic layer relative thicknesses were chosen for a total composition of $Pt_{46}Al_{37}Ni_{17}$, and a total thickness of 5µm. Blz1 has a total number of 9 layers whereas blz2 and blz3 have 5 layers in total in order to get a better view of the layers on SEM observation. Blz1 has 9 samples hanged on the mesh, from batch blz2, only 6 substrates where loaded, as it corresponds to the width of the plasmas, therefore giving a better homogeneity on deposited thicknesses. Substrates were ground with surface finish of 1200 grit or 4000 grit. Parameters are gathered in Table 14.

Moreover, the chosen alternation of layers is not trivial: the first layer has to be Pt to avoid diffusion of substrate elements as much as possible during heat treatment; the last layer has to be a Pt one too to avoid oxidation of the coated sample. At last, it was decided to deposit Al layers between each Pt and Ni ones, because it would diffuse more easily in its adjacent layer, to form the intermetallic. Thus the following structure is deposited: Pt/Al/Ni/Al/Pt (…/Pt for the 9layers)

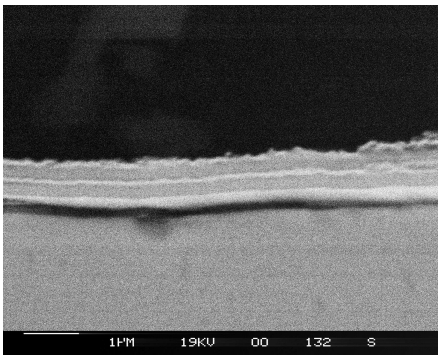

Figure 161 Secondary electrons picture of sample blz1A

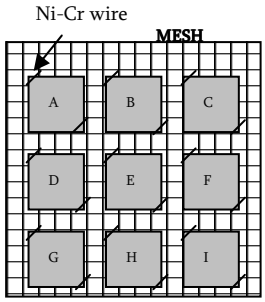

Figure 162 Configuration of samples in blz1 run

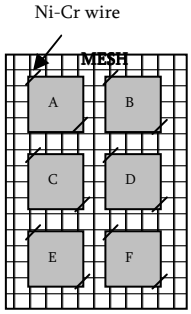

Figure 163 Samples configuration for 6-sample runs

The coatings produced with these 3 batches have a very poor adherence, and calibration had to be enhanced, as blz1 sample cross section shows thicknesses far from expected. 60% of the samples reacted during the deposition process forming disastrous delaminated coating. When reaction did not occur in situ, the coating delaminated while being cut for cross section observation (Figure 164).

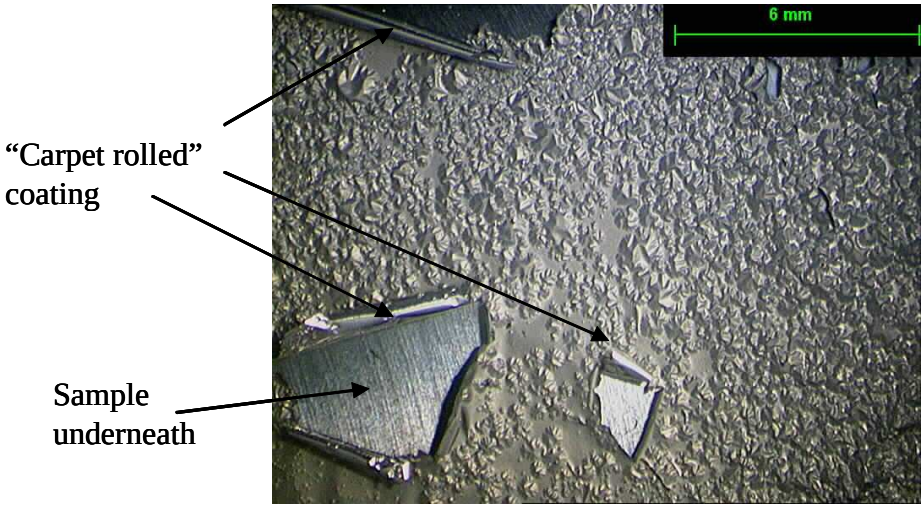

Figure 164 Optical micrograph of a delaminated stressed coating from blz2

The as deposited coating were extremely stressed (the rolled carpet shape of the detached film suggests a compressive stress), presenting a weak adhesion, and, most of all, some layers reacted in situ in the chamber during the run. Changing some process parameters could reduce the stress, increase the adherence and limit the triggering of the exothermic reaction in situ:

- ✓ The higher the power during deposition, the higher the coating stress is, but if reduced, the deposition rate falls and substrates have to be coated for a longer time in front of the target, and have to be longer exposed inside the plasma.
- ✓ The higher the substrate roughness is, the better the mechanical gripping of the coating will be.
- ✓ The higher the number of layers is, the better the stress repartition over the interfaces will be: global stress is thus reduced. Moreover, substrates are exposed for shorter time in the plasma, so they heat less, reducing the risk of triggering the reaction.
- ✓ If the pressure of Argon is reduced, the plasma will be weaker, and collisions softer. However, pressure has to be sufficient enough to obtain a stable and not pulsing plasma.
- ✓ The working distance can also play a role (the nearer the sample is to the target, the more it will be heated), but this parameter is difficult to modify on the sputtering facility.
- ✓ The most efficient solution is to apply a negative bias, during the first layer deposition, to increase the initial adhesion.

Therefore the three following batches where manufactured with the same deposition power but with applying a negative bias on the substrate prior to start the actual deposition. The first layer being Pt, the ion plating was carried out in front of the running Pt plasma as follow:

- ✓ 5 min:-300V on the substrate for a 100W plasma
- ✓ 5min:-250V on the substrate in front of a 200W RF plasma
- ✓ 5min:-200V on the substrates in front of a 300W RF plasma

Straight after 15min, the ion plating bias is switched off and the deposition of Pt starts with the plasma already set at 300W RF. This negative bias forces the Ar ions from the Pt target plasma to hit the substrate surface, therefore cleaning the first atomic layers of the substrate and enhancing the adhesion of the first deposited Pt atoms.

Three batches were manufactured this way: blz4, blz5 and blz7. As deposited coatings are very adherent and no reaction occurred during the deposition process. The beneficial effect of ion plating can be observed on cross sections, with a "pegging" of the first platinum layer in the substrate (highlighted by the BSE mode in Figure 165).

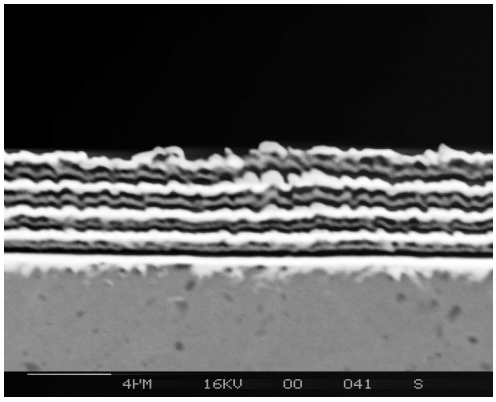

Figure 165 Blz7 sample as deposited (BSE mode)

Increasing the roughness (blz5 and blz7) to 600 grit gave as well adherent as deposited coatings. Changing the composition did not change the adherence of as deposited coating (blz5), nor a higher number of layer (blz7 has 17 layers for the same 5µm total thickness).

However, the high sputtering pressure (28mTorr), gives an important cauliflower surface finish to the Pt layer which can result in some local stress when overlapped by another layer. Moreover, this roughness of Pt layers induces some porosities within the multilayer stacking (Figure 167)

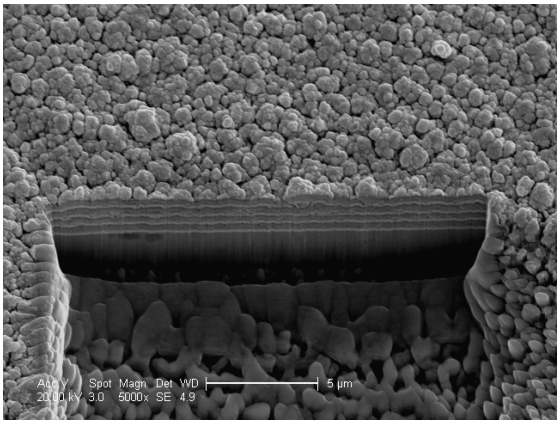

Figure 166 Secondary electron picture of blz7 sample FIB milled (tilt=20°)

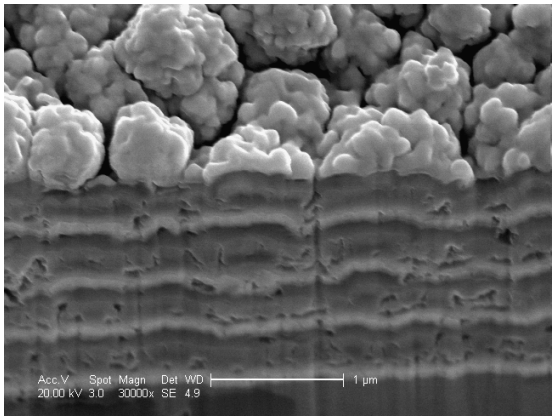

Figure 167 Secondary electron picture of blz7 sample FIB milled (zoom)

Table 14 Parameters for the batches blz1-blz7

# run	*blz1*	*blz2*	*blz3*	*blz4*	*blz5*	*blz7*
# sples	9	6	6	6	6	5
Surface finish (grit)	1200	1200 4000	1200 4000	1200	600	600
# layers	9	5	5	9	9	17
composition(Pt%Al%Ni%)						
Expected	46-37-17	46-37-17	46-37-17	46-37-17	43-32-25	43-32-25
layer thicknesses measured				35-46-19	52-27-21	41-33-26
Pt (µm/hr@W)	3.8@300	1.5@300	1.5@300	1.5@300	1.03@300	1.4@300
Ni (µm/hr@W)	1.83@190	1.83@190	1.83@190	1.83@190	1.89@190	1.89@190
Al (µm/hr@W)	3.5@160	0.8@1A	0.8@1A	0.8@1A	0.78@1A	0.78@1A
Ion plating Bias (V)	no	no	no	300	300	300

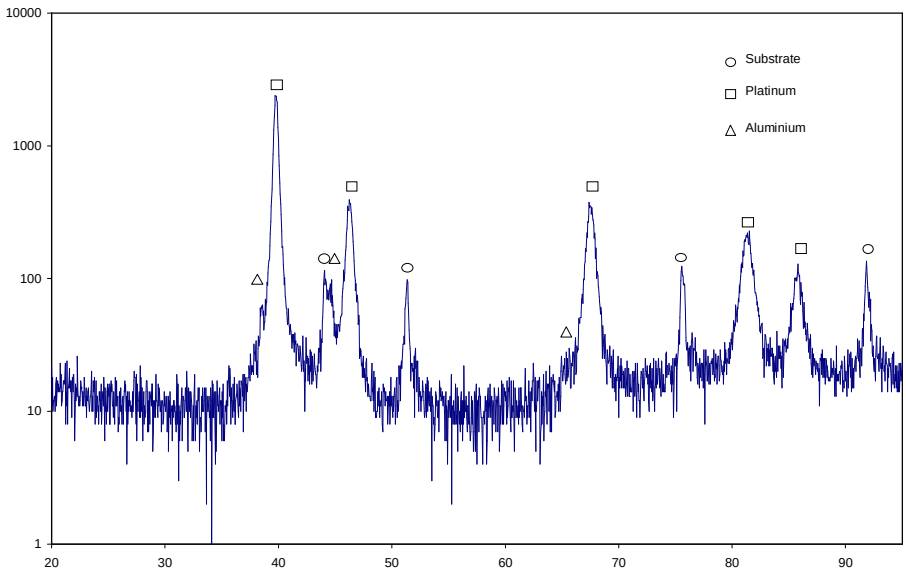

Figure 168 XRD spectrum of blz4 as deposited (log scale)

As deposited, XRD analysis of the films was carried out to check if any compound was formed: it shows only the peaks of the pure metals, as expected. Peaks of Nickel frome the coating are hidden by the peaks from the NiCr substrate (Figure 168).

V.2.1.2 Thermal annealing of the metallic layers

Thermal annealing was carried out on samples having had ion plating during the deposition of the first platinum layer, especially from blz5 and blz7 batches. Samples were cut in four parts with the precision saw prior to annealing in order to increase the number of possible experiment. After reaction, XRD analysis and cross section were carried out. Heat treatments are:

- ✓ Under vacuum at 700°C and 750°C for 2 hours
- ✓ Under vacuum at 800°C, 900°C and 1000°C for 500min.
- ✓ Under vacuum at 900°C for 24 hours
- ✓ Under Argon at 750°C for 2 hours and 800°C for 5 hours.

After these heat treatments, all the films buckled, except after 500min at 800°C and under Argon annealing. However, under Argon, some oxidation occurred on the surface due to a poor isolation of the furnace from the external environment.

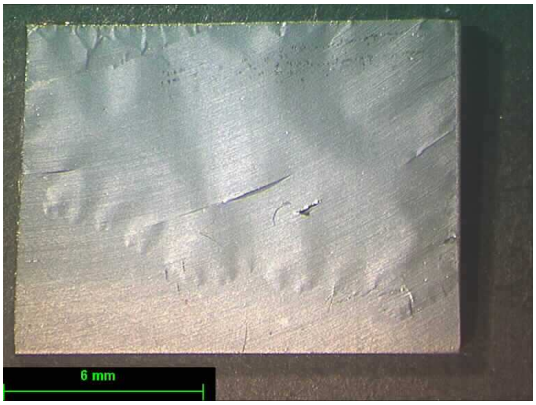

Figure 169 Typical buckling of the coating after heat treatment on NiCr sample

Figure 170 Reaction in Ar furnace: unexpected oxidation

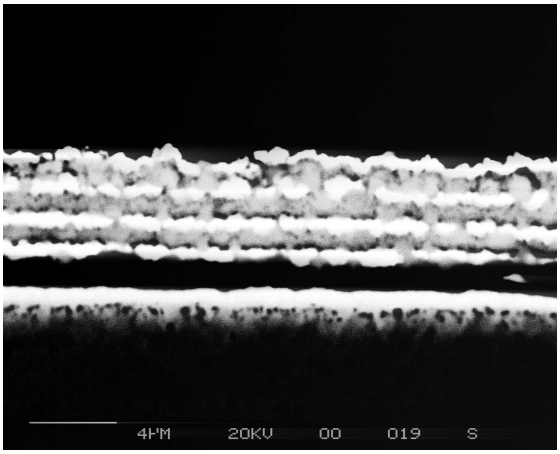

Figure 171 Blz7E sample heat treated 2 hrs@750°C

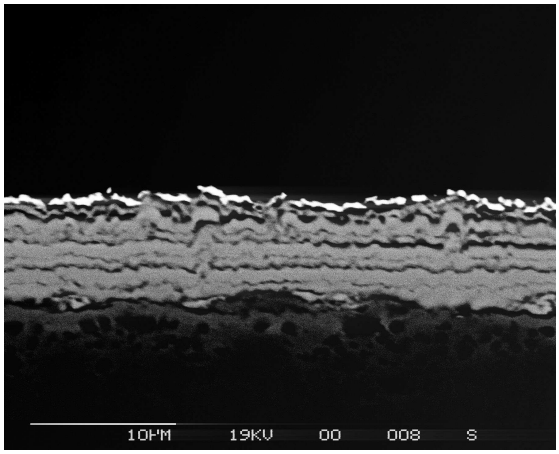

Figure 172 Blz7D sample heat treated 500min@900°C

XRD was carried out in order to determine the different phase obtained after different heat treatments. Samples are not always the same, but situated on the same line on the mesh in front of the target. It can so be assessed they are equivalent. The two heat treatments at 700°C and 750°C present a very complex XRD diagram (Figure 171), this signifies all the layers didn't react, some pure material are still present, and synthesised intermetallics are not the more thermodynamically stable (the major detected phases are PtAl, NiAl, and Al_3Pt_5) . The fact that the reaction did not occur entirely can be seen in Figure 171: the change in contrast between the layers of the coating confirms the presence of various phases with various Pt content (Pt rich zones are lighter in backscattered SEM micrograph, as Pt is heavier).

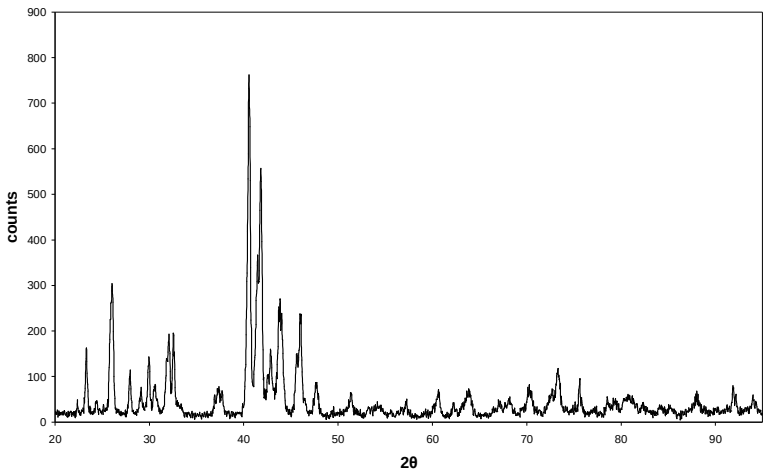

Figure 173 XRD spectrum of Blz7E after 2 hours under vacuum at 700°C

The longer and hotter treatments, at 800°C, 900°C and 1000°C give cleaner diagrams, suggesting the reaction occurred totally. These is confirmed by the homogeneity on the

backscattered cross section of these coatings (Figure 172). The 900°C heat treatment gives the clearest XRD diagram indeed, with PtAl and NiAl as the predominant phases.

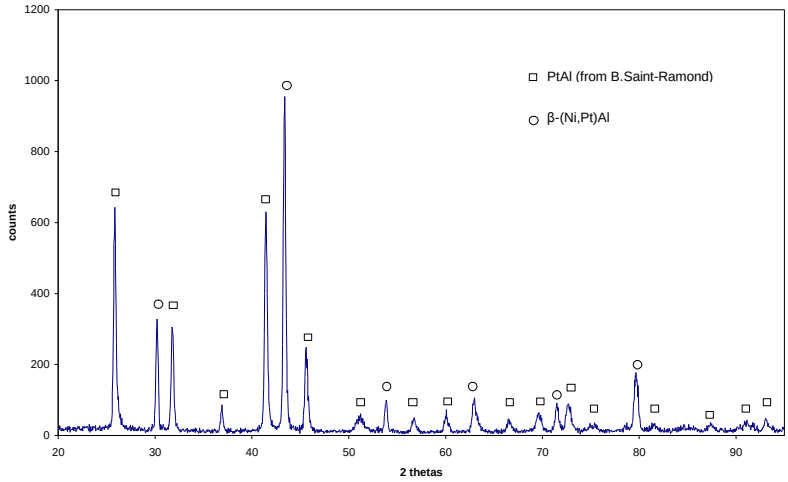

Figure 174 XRD diagram of Blz7 after 500min at 900°C

In conclusion, the adherence of the films after reaction is very poor; however, the reaction of the layers into intermetallics from the Pt-Ni-Al system was successful. The reaction is not complete below 800°C, possibly due to the fact that the coating delaminated from the substrate, therefore would not have the ideal thermal conductivity on the inner side. Below 800°C, transient platinum aluminide intermetallics are formed, however, at higher temperature, the chemistry of the films tends to a mixture of β(Ni,Pt)Al and PtAl. This fact can be explained by the pattern chosen for these experiments: β is a very stable compound, and will reacts at the Ni/Al interface; at the Al/Pt interface, transient platinum aluminide are formed, until they finally end to the PtAl compound. This mechanism is sketched in.

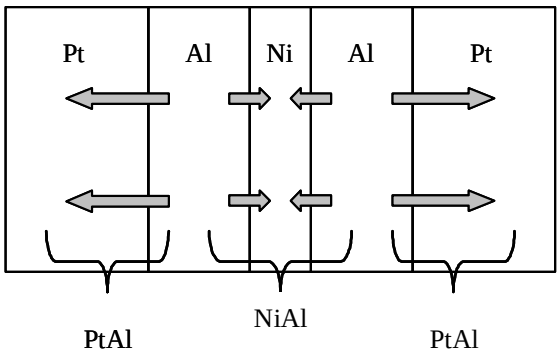

Figure 175 Diffusion and compounds formation during heat treatment of a Pt/Al/Ni/Al/Pt pattern

V.2.2 Effect of the alternation pattern : blz8 and blz9

Due to the previous result, it was decided to change the alternation pattern of the metallic layers. Nickel and Aluminium were deposited so they never stand next to each other in order not to form the β-NiAl compound. Platinum stays as the first and the last layer for the same reasons explained earlier. The alternation pattern thus becomes: Pt/Al/Pt/Ni/Pt….Ni/Pt. This way Aluminium and Nickel are always surrounded with Platinum.

Two batches were manufactured like so, called Blz8 and Blz9. The global composition for these batches is $Pt_{43}Al_{32}Ni_{25}$ for a total thickness of 5µm, and a sequence of 5 and 9 layers respectively. The Argon pressure was reduced to 18mTorr in order to reduce the cauliflower structure of the platinum layers. The powers were set to: 300W RF for the Pt target; 1.1A DC for the Al target (corresponding to ≈305W); 0.43A DC for the Ni target (corresponding to ≈185W).

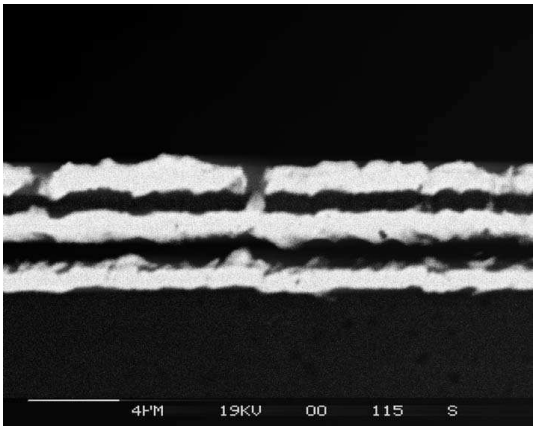

Figure 176 SEM micrograph of BLZ8

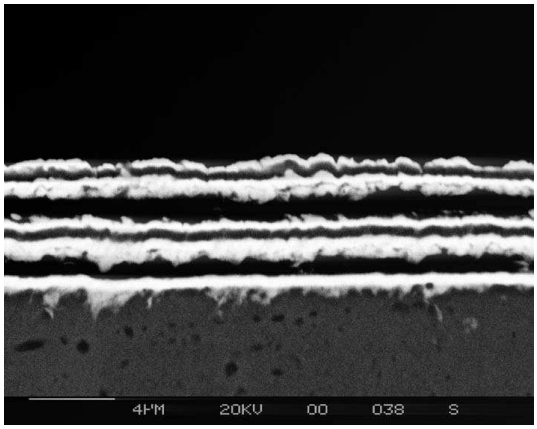

Figure 177 SEM micrograph of BLZ9

These samples were annealed under vacuum for 500 minutes at 700°C and 900°C. The XRD spectra of the reacted samples show that no β-(Ni,Pt)Al was formed. Instead, it appears clearly that the α-phase is formed, as it is shown in Figure 178 were the reacted coating are compared with the experimental XRD of the bulk α-phase experiment #9.

The new alternation pattern clearly plays its role as expected, and changes the compound formed during annealing; however at 700°C there are still transient binary platinum aluminides, which do not appear much after annealing at 900°C.

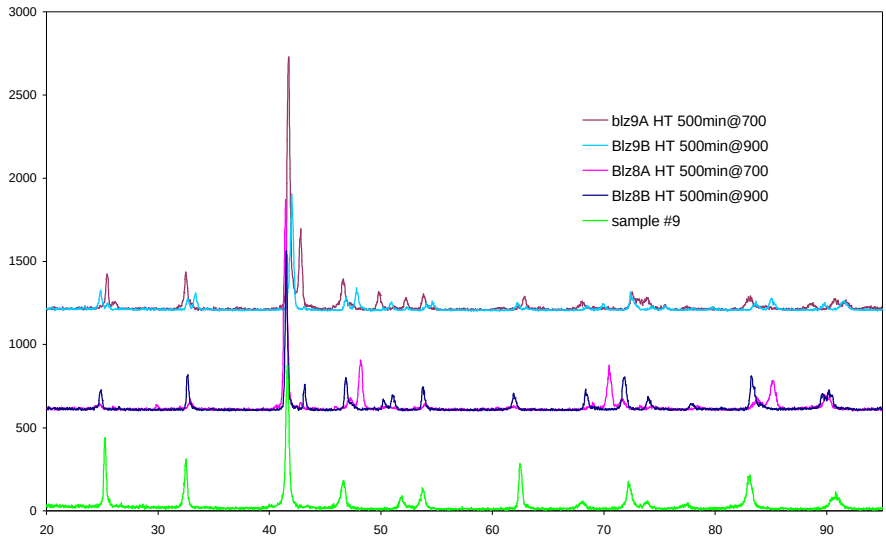

Figure 178 XRD spectra of Blz8 and Blz9 annealed compared to α-phase

In spite of these very promising results chemical wise, the adherence of the film remains a strong issue: all the film buckled when unloaded from the annealing furnace, revealing the recurrent issue of stress in the films, released during the heat treatment (Figure 179 and Figure 180).

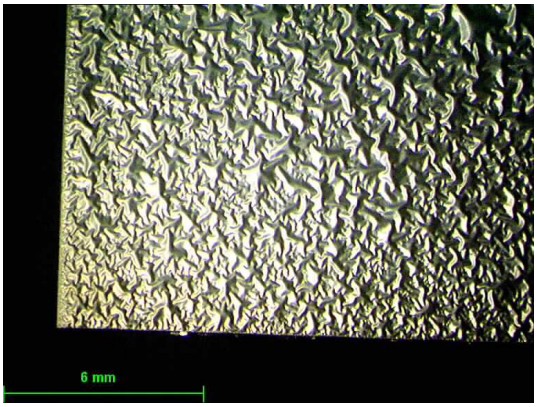

Figure 179 Surface of Blz8 after annealing at 900°C for 500min

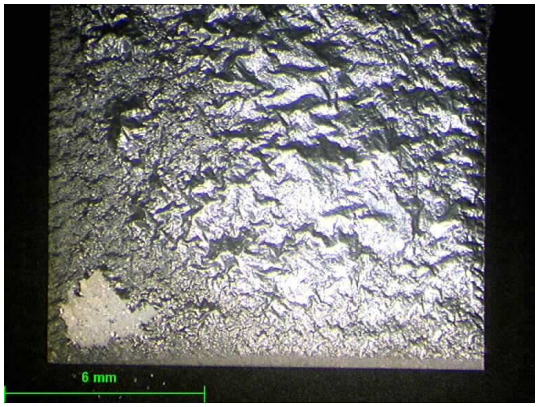

Figure 180 Surface of Blz9 after annealing at 900°C for 500min

V.2.3 Use of motor step drive and calibration: blz10-11

In order to improve the adhesion of the coatings, it was decided to increase the number of layers in the film, for the same fixed total thickness of 5µm. For this purpose, the automated

rotation of the substrate holder in front of each target was used. Calibrations and set up were carried out on two batches: blz10 and blz11.

Measuring the thickness of the deposited layers on SEM cross sections leads to major errors, probably due to the low resolution of the SEM used, and to the mechanical polishing of the cross section.

Blz10 run is a 9 layers system with the same expected composition as the previous ones, $Pt_{43}Al_{32}Ni_{25}$, and the deposition rates determined with the previous BLZ8 and BLZ9 runs as calibration. The difference of layers thicknesses between a traditional cross section and a FIB section is blatant:

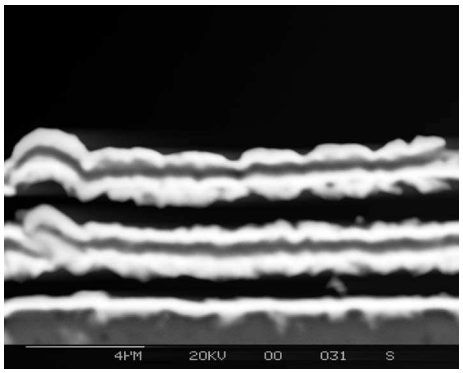

Figure 181 Blz10 SEM cross section

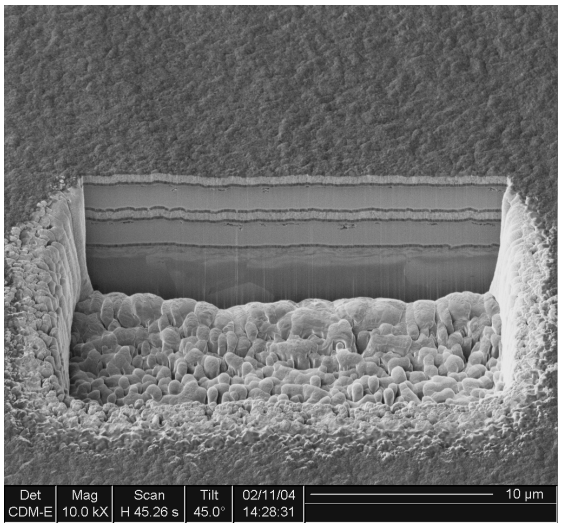

Figure 182 Blz10 FIB section

The deposition rate calculated for each metal changes dramatically depending on the type of cross section it is based on (SEM or FIB). A FIB section is more expensive than a traditional SEM cross section, but gives more accurate results, relevant with glass slides step measurements.

Table 15 Compared deposition rates between a traditional SEM cross section and a FIB section

	SEM cross section	*FIB cross section*
Pt	2.6 µm/hr	0.67 µm/hr
Al	1.2 µm/hr	2.5 µm/hr
Ni	2 µm/hr	2.7 µm/hr

BLZ11 was dedicated to the deposition run calibration by FIB observation. It is a 13 layers system, with variable thicknesses in order to draw the variation of the deposition rate with

thickness. Deposition times of BLZ10 were multiplied or divided by 2 or 4 and sputtering parameters are kept constant:

- ✓ Base pressure ≈10^{-7} mbar
- ✓ Sputtering Ar pressure : 0.018 Torr
- ✓ Aluminium: 1.1A (≈300W)
- ✓ Nickel: 0.43A (≈180W)
- ✓ Platinum: 300W RF
- ✓ Pt/Al/Pt/Ni/Pt… alternation pattern

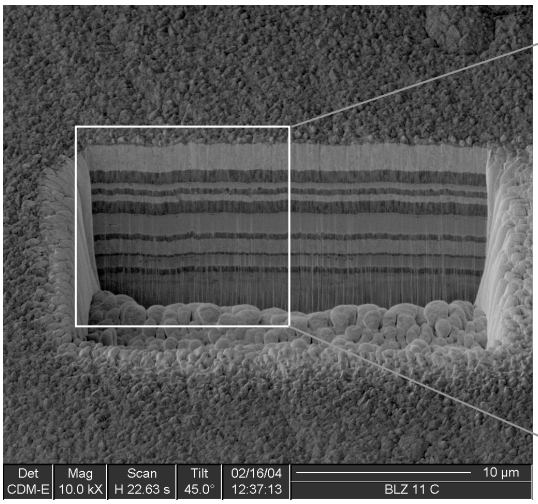

Figure 183 Blz11 FIB milled

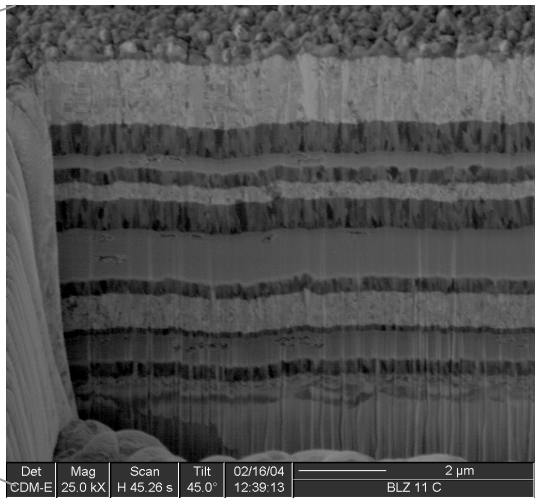

Figure 184 Blz11 FIB milled (zoom)

Image analysis is carried out on Figure 184 to determine deposition rates. The uncertainty is set to +/- 1 pixel, and is plot on the calibrations graphs.

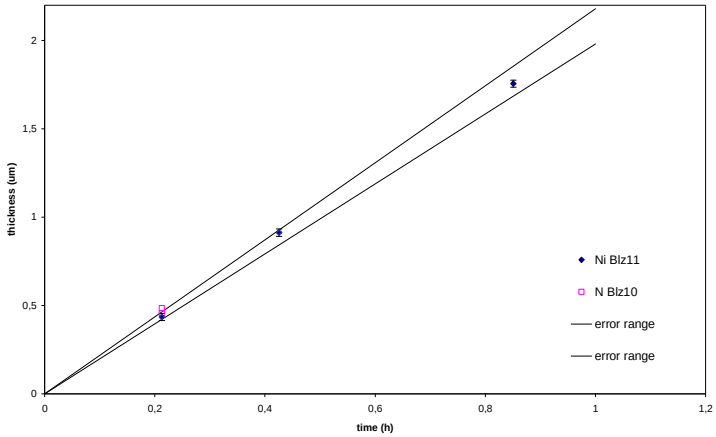

Figure 185 Calibration for Nickel deposition rate

Calibration for Nickel layers is excellent, the linear regression leads to a deposition rate of 2.08µm/h. The data points fit correctly within the uncertainty sector (Figure 185).

The alignment of the points on the Aluminium calibration chart is not acceptable; it was decided to take the slope of the two first points, the sputtering time in front of the Al target during the multilayer deposition being always inferior to 30 min. These two points are correctly aligned with the origin of the chart, with a slope of 2.18µm/h. The uncertainty sector fitting is acceptable (Figure 186).

Platinum data are more numerous as there is twice more platinum layer deposited with the chosen multilayer deposition pattern. However, the regression of the data points does not cross the origin of the chart (Figure 187). The origin being taken into account or not, the deposition rate of Pt is either 0.61 or 0.58µm/h.

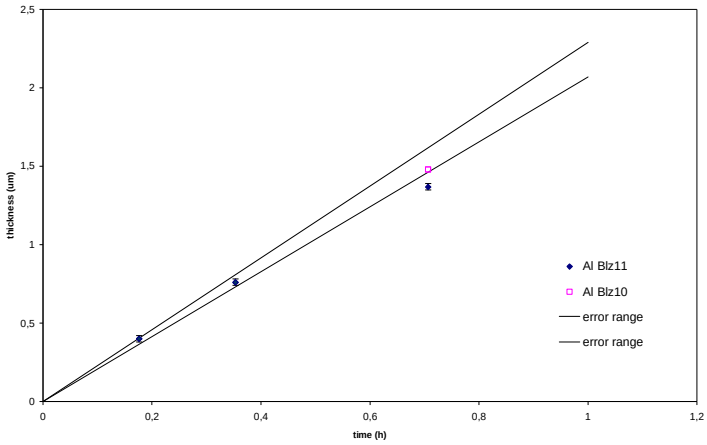

Figure 186 Calibration for Aluminium deposition rate

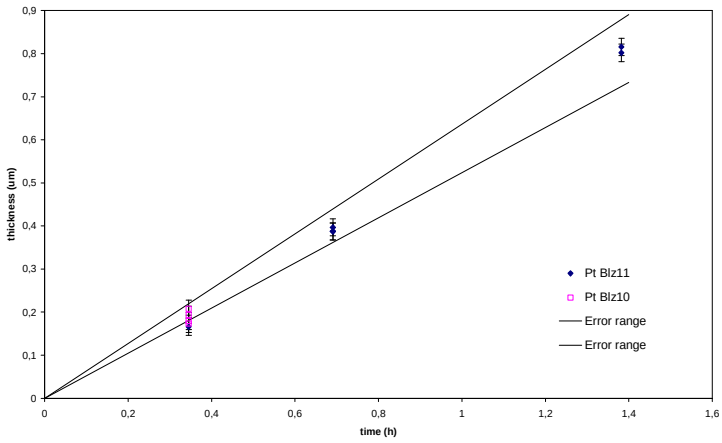

Figure 187 Calibration for Platinum deposition rate

The deposition rates calculated with the FIB sectioning will be used for the following batches on NiCr substrates.

V.2.4 Heat treatment effect: blz12-14

V.2.4.1 Deposition parameters and uncertainty considerations

Three batches were manufactured for the study of the effect of heat treatment on the formation of intermetallics. These coating were manufactured with the automated rotation stepper motor drive, differences between the samples of these batches are on the number of layers and deposition rate for Pt. The alternation pattern is kept, Pt/al/Pt/Ni/Pt…Ni/Pt, deposition power and pressure are kept constant and the total thickness is 5µm.

Table 16 Deposition parameters for batches blz12, Blz13 and Blz14

	Composition	*Layers*	*Ion implantation -300V for 15 min*	*Al rate 1.1 A*	*Ni rate 0.43A*	*Pt rate 300W*	*Process pressure*
BLZ12	$Pt_{45}Al_{28}Ni_{27}$	**25**	Yes	2.18	2.08	**0.61**	0.018 Torr
BLZ13	$Pt_{45}Al_{28}Ni_{27}$	**73**	Yes	2.18	2.08	**0.61**	0.018 Torr
BLZ14	$Pt_{45}Al_{28}Ni_{27}$	**25**	Yes	2.18	2.08	**0.58**	0.018 Torr

In conclusion from the previous part, the error appreciation is a key issue which has to be solved. Lot of parameters imply errors, and the way to measure them is not always so easy:

- ✓ *Constant deposition rate*

The deposition of a layer by PVD is not at a constant rate. The substrate plays its role for the first atomic layers, thereafter the actual substrate becomes the deposited materials itself. Ideally, the deposition rate run should be as long as they are during the process and done on the actual substrate (eg. Al or Ni for the platinum, and Pt for the aluminium and the nickel).

The fact that Pt FIB calibration data does not match with the origin is a proof: It is obvious that with a null time of deposition, the layer thickness is null.

- ✓ *Thickness measurement precision*

The error bands for the deposition rates give a variation on the total composition. This was plotted in Figure 188 over the Ni-Pt-Al ternary diagram. The resulting error is acceptable regarding to the width of the stability field of the α-phase.

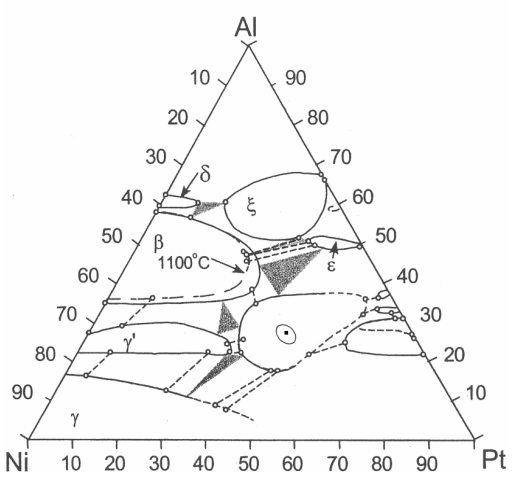

Figure 188 Error due to deposition rate uncertainty

- ✓ *Situation on the substrate holder*

Last but not least, this parameter changes with position on the substrate holder. B. Saint-Ramond measured a difference of 14% in thickness along 10cm on the substrate holder. Therefore it was decided to place the samples always on the same position so that four are exactly symmetric to the centre of the magnetron (i.e. C, D, E, F):

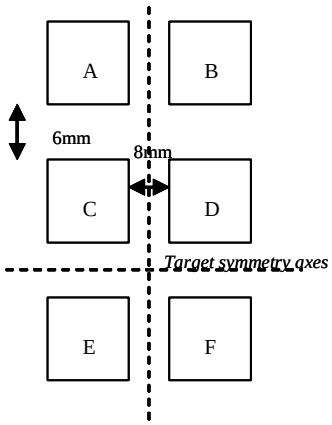

Figure 189 Samples layout toward the magnetron

All the calibrations were done on one of this our samples. Moreover it may be noticed that the denser the plasma, the more thickness variation. Thus, Ni layers are strongly affected by this phenomenon (Ni plasma is very dense close to the electron path on the target, due to enhanced magnetic confinement, giving an important density variation across the nickel target). On the contrary, Pt plasma is more homogeneous and less dense because the platinum is mounted onto a mild steel backing plate aimed at reducing the magnetic field at the target surface, giving a good repartition of the deposition (on the other hand this gives extremely slow deposition rates).

V.2.4.2 Heat treatments experiment plan and results

Systematic heat treatment tests were carried out on blz12 batch samples. Blz13 and Blz14 batches samples were used for specific further investigations. Blz12 batch as deposited samples were cut in four with a precision saw in order to increase the quantity of experiment. L and R stands for L and right, and U and B for upper and bottom.

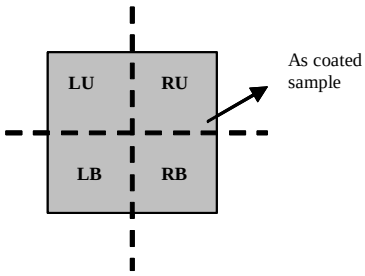

Figure 190 Sample cutting identification

Three facilities were used for heat treatment: a vacuum furnace, a sealed tube furnace linked with an argon line and a box furnace in air. The vacuum furnace is based on electrode heating, resulting mainly in radiation and conduction heating. On the contrary the tube and the box furnaces are elements heated facilities, heating mainly by convection.

The vacuum furnace need a first dwell before the heat treatment to burn off organic particles, and also to allow the pumps to evacuate the pressure that raises because of the temperature. The argon furnace has slow heating and cooling ramps due to its element configuration. The box furnace was used in order to have the fastest heating and cooling rate as possible whereas oxidation obviously occurred in the air.

Four parameters were varied: the temperature, the dwelling time, the heating ramp and the cooling ramp.

Results of these tests proved disappointing. Although the as-coated coatings are very adherent, none of them remain adherent after any heat treatment. All the coatings show a compressive stress induced spallation. Two samples are given in example in Figure 191 and Figure 192.

Table 17 Heat treatment parameters on blz12 batch

Samples	*furnace*	*temperature*	*Time minutes*	*heating °C/min*	*cooling °C/min*	*remarks*
BLZ12A LU	Vac	700	500	10	max	first dwell 10min@400
BLZ12E LU	Vac	700	500	10	max	first dwell 10min@400
BLZ12A RU	Ar	700	500	10	max	
BLZ12E RU	Ar	700	500	10	max	
BLZ12A RB	Vac	500	500	10	max	first dwell 10min@300
BLZ12E RB	Vac	500	500	10	max	first dwell 10min@300
BLZ12A LB	Vac	700	120	10	max	first dwell 10min@400
BLZ12E LB	Vac	700	120	10	max	first dwell 10min@400
BLZ12B LB	Vac	700	60	10	max	first dwell 10min@400
BLZ12F LB	Vac	700	60	10	max	first dwell 10min@400
BLZ12B RB	Vac	500	60	10	10	first dwell 10min@300
BLZ12F RB	Vac	600	60	10	10	first dwell 10min@350
BLZ12B LU	Ar	700	120	10	10	
BLZ12F LU	Air	700	30	max	max	
BLZ12FRU	Vac	700	120	10	1	

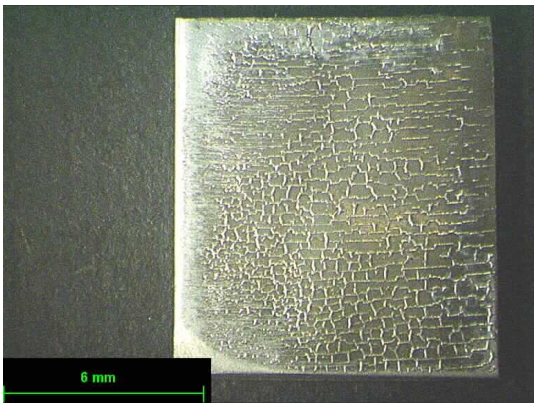

Figure 191 BLZ12ERU after 500min@700°C in Argon

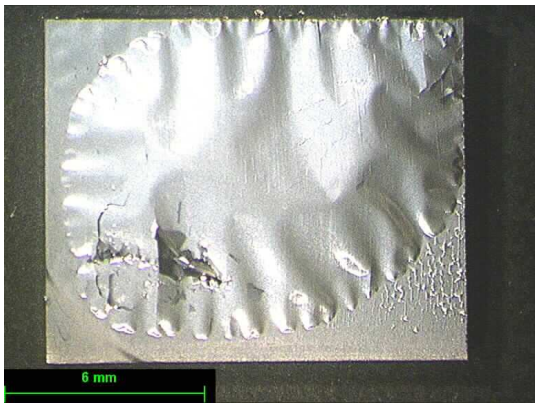

Figure 192 BLZ12E RB after 500min@500° under Vacuum

Two different aspects of de-bonding were observed. First a plain and smooth surface simply detached from the surface (e.g. Figure 192). For others, some samples display a pattern of ridges oriented at 90° from each other associated with the final machining marks on the component surface as shown in Figure 191. This pattern is thought to be due to the grinding of the substrate surface before deposition. The polishing was carried out on #240 grit paper in one direction, and then on #600 on the perpendicular direction. The stress induced by polishing may explain that the coating spalled preferentially along these weak lines, alternatively, spallation may

result from out-of-plane stress generated at the top of ridges if the film stress is highly compressive.

The Argon furnace provided poorer protection against oxidation than the vacuum furnace. The coatings lost there grey colour and turned brownish. The XRD diagrams of the reacted samples are less clear that the vacuum reacted however no oxide peaks were detected.

As the spallation seems to start from the cut edges of the sample, a heat treatment of 120min@700°C in vacuum was carried out on a whole sample. Unfortunately spallation also occurred. Another test was also carried out on a whole sample of the Blz14 batch in order to evaluate the effect of multilayering. After 120 minutes at 700°C in vacuum, the coating buckled, with an XRD diagram comparable to the one of the BLZ12 run.

The observation of cross sections gives two main indications: the effectiveness of the reaction between the layers, and the spallation mechanism.

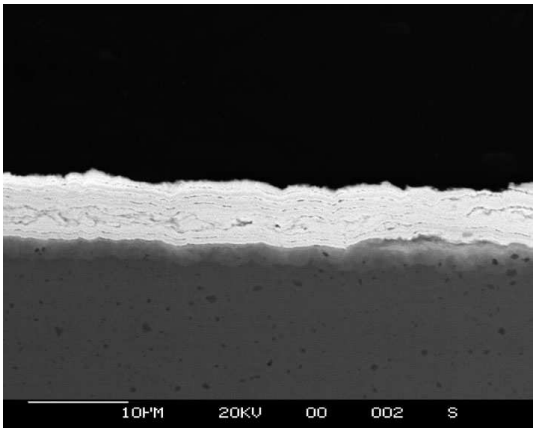

Figure 193 After 500min@700℃ in vacuum

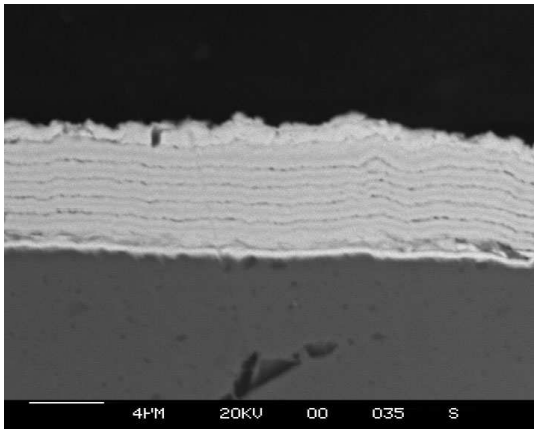

Figure 194 After 500min@500°C in vacuum

As shown in the two previous SEM micrographs, the layers are denser, and the contrast had to be increased at its maximum to be able to see the grey nickel layer. Aluminium is the darker in backscattered observation, but the question is to know if the black lines corresponds to the remnant aluminium layer or voids.

The failure was observed by FIB cross section on the sample heat treated 500min at 500°C under vacuum (Figure 195 to Figure 197). The debonding always occurs at the aluminium layer. The first one cracks because it is the most stressed, but voids are observed at each of the six aluminium interlayers. The FIB milling shows also the presence of dark zones within the nickel interlayer: these may correspond to precipitates, but also to voids.

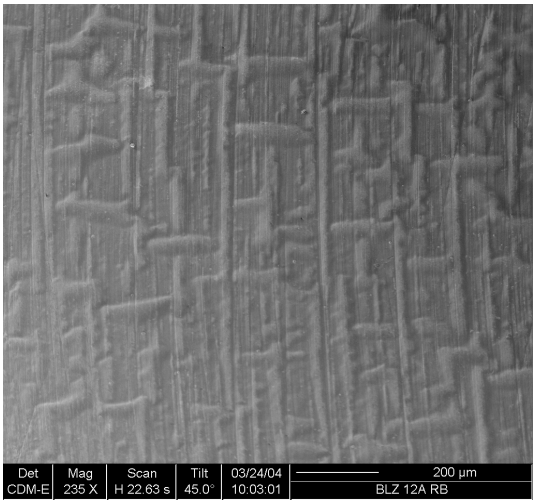

Figure 195 BLZ12ARB: surface ridges after reaction

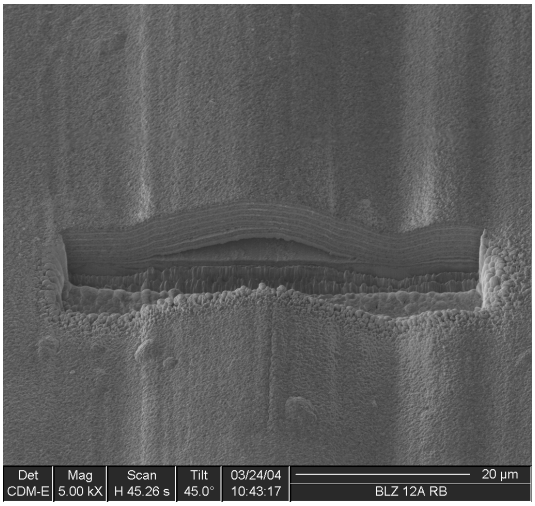

Figure 196 FIB section layout on Blz12ARB after annealing

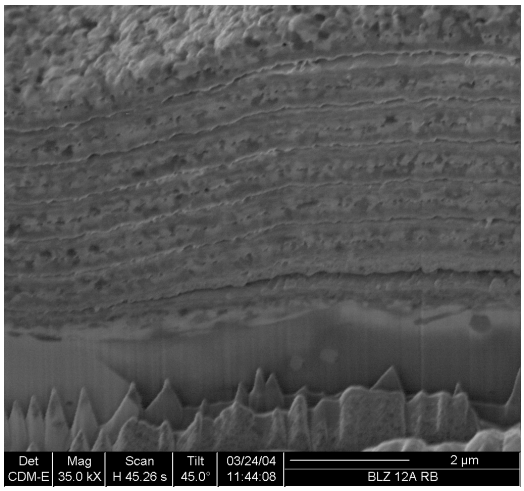

Figure 197 Zoom on the FIB cross section on Blz12ARB after annealing

V.2.4.3 XRD analyses

Beyond the adherence of the coatings, XRD were performed in order to evaluate if the reaction of the layers occurred well and entirely. It may be interesting to notice that the substrate peaks are no longer present on the reacted samples XRD diagrams. This may be due to the densification of the coating after reaction (intermetallics based on platinum are denser than pure metals), and high atomic mass atom absorbs X-ray more easily.

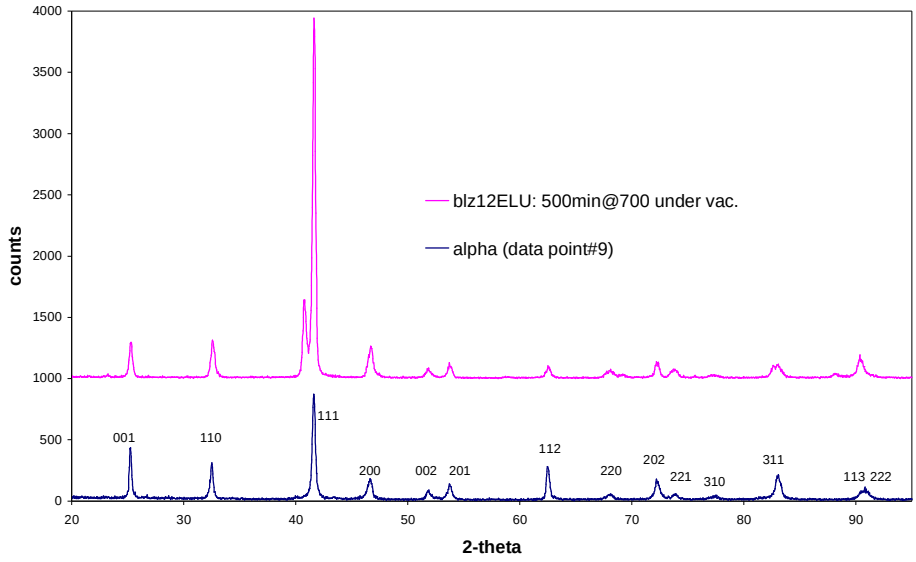

Figure 198 Comparison between blz12ELU heat treated 500min@700°C in vacuum and alpha

The heat treatment for the longest dwell and at the highest temperature theoretically gives the ultimate reaction and diffusion. When compared with an experimental data of alpha obtained in the previous chapter, the fitting is excellent (Figure 198), with a 111 preferential orientation of the coated alpha compared to the bulk.

The non expected peak at 2θ=41° corresponds only to the Pt rich aluminide Pt_3Al. The presence of this compound is confirmed by the presence of smooth peaks around 2θ=23°, by the shoulder of the (200) peak, and the presence of the low intensity peak at 2θ=87°.

The effect of temperature was analysed with the four experiments which were carried out for 60min at 700, 600 and 500°C. The first dwell step of the vacuum furnace (see earlier) had to be lower for the lower reaction temperatures (respectively 400, 350 and 300°C).

The comparison of the XRD diagrams (Figure 199), and in particular the comparison of the relative intensity of the (111) peaks (at 40.55° for Pt_3Al and 41.64° for alpha) of each compound clearly establishes that the hotter, the more (Ni,Pt) lattice is present compared to the Pt_3Al lattice. At 500°C, the two peaks have almost the same intensity, whereas the (Ni.Pt) lattice becomes four times more intense at 700°C. The same deductions are obtained when comparing the intensity of the (001) peaks (at 22.84° for Pt_3Al and 25.28° for alpha).

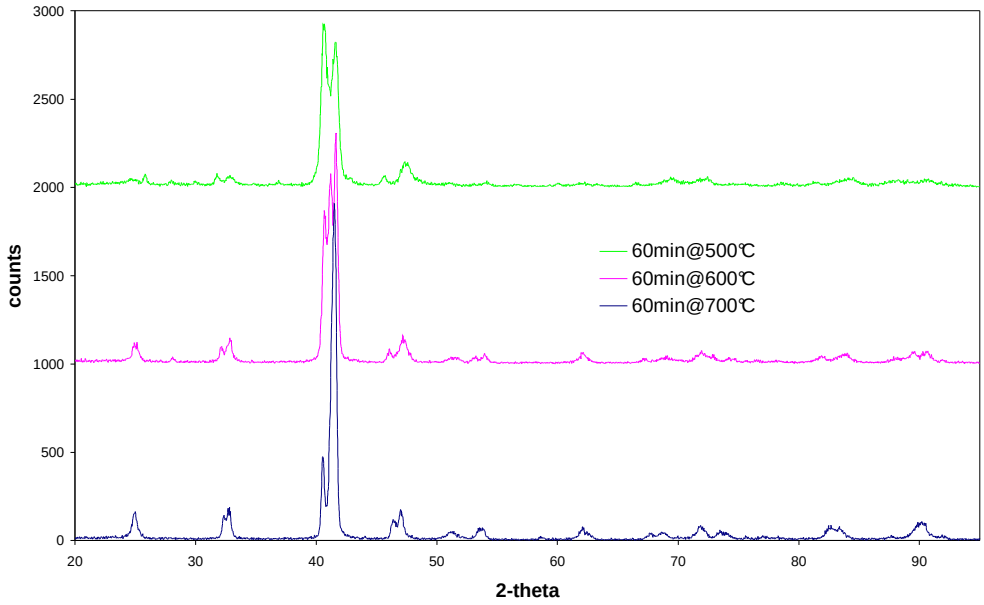

Figure 199 Effect of the temperature on the relative content of α-phase

Surprisingly, the effect of heat treatment time is different from the temperature: the longer the more Pt_3Al is present (Figure 200). It is usually acknowledged that multiplying the heat treatment dwelling time by two is equivalent to increase the temperature by 100°C (for a single compound formation), therefore, time should act in the same direction as temperature, which is obviously not the case. This implies that the Pt_3Al compound must be as stable if not more stable than α-phase.

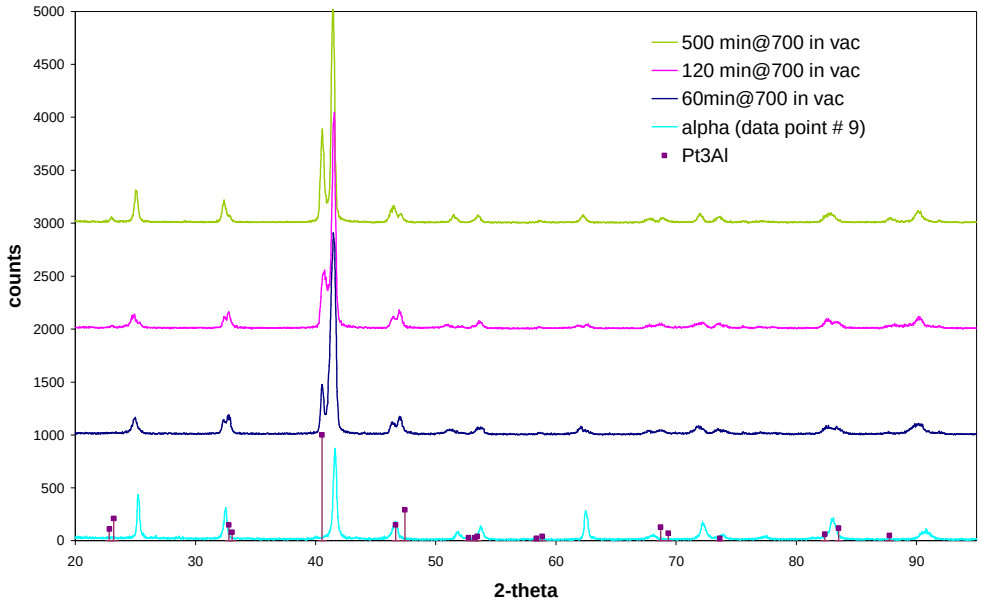

Figure 200 Effect of the dwell time on the relative content of α-phase

V.2.5 Conclusions: preliminary batches

Although the adherence of coatings produced on NiCr samples was poor, it improved the knowledge on the manufacturing route developed during this project. These results were important when shifting to deposition on superalloy substrates.

- ✓ The critical effect of the negative bias prior to start the deposition: this manufacturing tip is in fact a key parameter to improve adhesion of the multilayer film.
- ✓ The alternation pattern of the Al, Pt and Ni layers drives directly the resulting compound after annealing.
- ✓ Calibration by FIB image analysis proved to be functional, although expensive. This made the automated run possible.
- ✓ The manufacturing of α-phase coatings was proven to work by this manufacturing route.
- ✓ The type of annealing did not improve the adherence of the multilayer system after reaction
- ✓ Delamination after heat treatment seems to occur at the former Al layers.

V.3 Manufacturing on AM1 coupons

V.3.1 Use of superalloy substrate and rotating substrate holder

V.3.1.1 Samples manufacturing

After the experiments on NiCr substrate, multilayer coatings were produced on commercial grade superalloy used for single crystal turbine blades at Snecma: AM1 low sulphur. Sample preparation is the same as previous: manual grinding at grit#600 for most of them, ultrasonic cleaning in Acetone and IPA and ultra pure IPA cleaning.

For the single face coating, disks were clipped onto a steel mesh by NiCr wires. The rotating substrate holder has been installed as well in order to coat both faces of the disks. In order to avoid drilling the superalloy, it has been decided to hook the substrates by the edge with a NiCr wire; the disks were lied and arranged in a set of three (see Figure 201 and Figure 202).

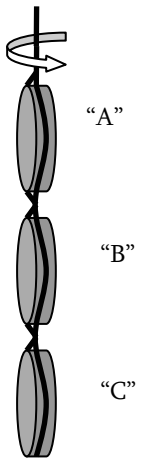

Figure 201 Fixing of the disk substrates

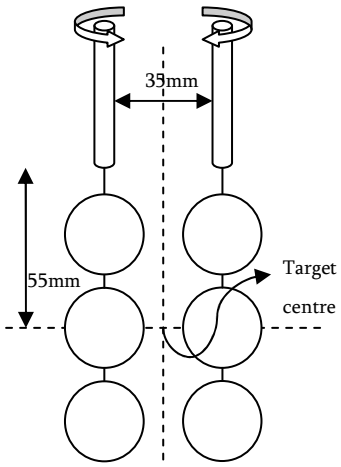

Figure 202 Layout facing the magnetron target

With this layout, the uncoated surface is negligible; there is no stress and edge effects as with a drilled hole or chemical modification as with a welded stick. The sputtering chamber is the same as previously, mounted with three targets, Ni, Al, and Pt, with another rotating system that allows alternating each deposited layer. Double side coating were manufactured in order to carry

out oxidation experiments with weight gain measurement for the determination of the oxide scale growth kinetic.

Another type of power supply was tried for Pt deposition instead of radio frequency (RF), in order to improve the deposition rate, and maybe improve the coating performances by changing its microstructure. The pulsed DC bias is a non symmetric square signal (Figure 203). The parameters of this signal are the frequency (between 50 and 250kHz), the pulse width (τ, with $\tau/\lambda<0.4$) and the power (up to 5kW). The deposition last while the bias is negative (during $\lambda-\tau$), when the bias is positive, the charge build-up on the target surface is reduced. This type of signal is usually used for ceramic targets, or for reactive sputtering in order to avoid the target poisoning (re-deposition of the reacted sputtered compound onto the target).

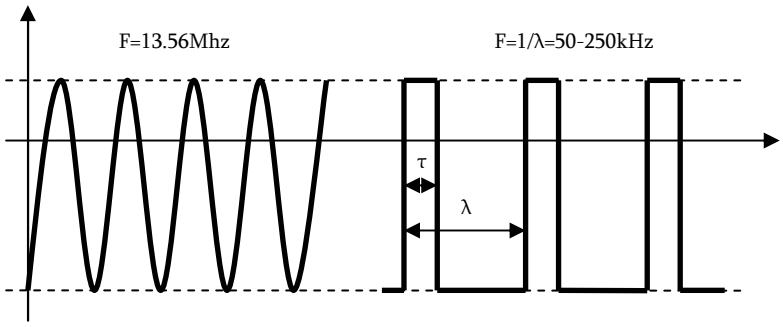

Figure 203 Comparison between RF signal and pulsed DC

Deposition considerations are the following:

- ✓ The batch terminology follows previous experiments
- ✓ All the experiments have 25 layers on 5µm total thickness, except for Blz21 batch, which is a 49 layers system, 2.5µm thick.
- ✓ All the experiments have the Pt/Al/Pt/Ni/Pt alternation pattern, except Blz16 which is Pt/Ni/Pt/Al/Pt.
- ✓ All the experiments have the expected total composition of $Pt_{45}Al_{28}Ni_{27}$.
- ✓ All the substrates are gritted at #600 except for Blz16 where they are #600, #600 without preferential direction, and #1200.
- ✓ All the experiment were carried out with DC supplies for Ni and Al, respectively set at 0.43A (≈140W) and 1.10A (≈352W).
- ✓ The ion plating facility was not used for blz17 and Blz19 batches.
- ✓ Two small drilled AM1 samples (14mm diameter, 1mm thick) where added to Blz20 and Blz21, hooked at the bottom of the third large AM1 disk.
- ✓ Once coated, all the samples are stored in a dried dessicator.

Table 18 Deposition parameters and deposition rates for batches blz15-blz21

Batch	*Number and substrate type*	*Negative Bias*	*Double side*	*Pressure (Torr)*	*Pt power*	*Pt µm/h*	*Al µm/h*	*Ni µm/h*
Blz15	3AM1/3NiCr	Yes	No	0.010	RF 300W	0.52	3.92	2.8
Blz16	3AM1/3NiCr	Yes	No	0.010	RF 300W	0.50	3.90	2.20
Blz17	4AM1	No	Yes	0.013	RF 300W	0.25	2.45	1.46
Blz18	6AM1	Yes	Yes	0.013	RF 300W	0.24	2.48	1.38
Blz19	6AM1	No	Yes	0.023	RF 300W	0.37	1.88	1.19
Blz20	6AM1/2smalls	Yes	Yes	0.013	Pulsed 350W 250kHz/1616ns	0.33	2.70	2.00
Blz21	6AM1/2smalls	Yes	Yes	0.013	Pulsed 340W 250kHz/496ns	0.22	2.80	1.70

Precise calibration was still difficult to be carried out. Step measurement accuracy on glass slides is not acceptable, and the reading of the deposition rate is subjective (see Figure 204), especially for Pt, whose thickness deposited in one hour is quite low (250nm in one hour…). Calibrations were performed with a mechanical stepper drive, on glass slides, the measured step being located at the middle of the 2nd hooked AM1 disk.

The low deposition rate of Pt (nearly as slow as 10 atoms a minute) is clearly a problem, leading to experiments that can last more than 8 hours. This will be a problem when depositing 10 or 15µm thick bondcoats. This is the main driving reason for increasing the sputtering pressure or using pulsed DC power supply.

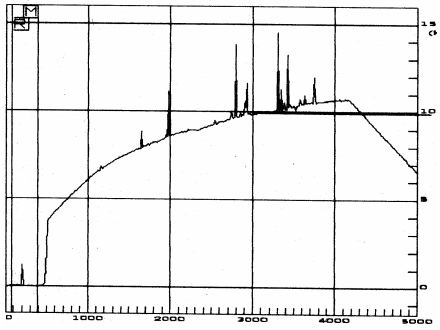

Figure 204 Step profile of Ni (x in µm and y in kÅ)

V.3.1.2 Thermal annealing

Adherence of the film as deposited is excellent for all batches. No dramatic debonding was observed either after heat treatment on Blz15 batch samples. This batch was analysed for microstructure observation after annealing and XRD analysis. Heat treatments were performed under vacuum for 2hrs at 600°C, 700°C, and 800°C. XRD spectra for the various temperature are gathered in Figure 205, SEM cross sections on reacted samples were carried out (Figure 206 and Figure 207), as FIB sectioning of a reacted sample (Figure 208 and Figure 209).

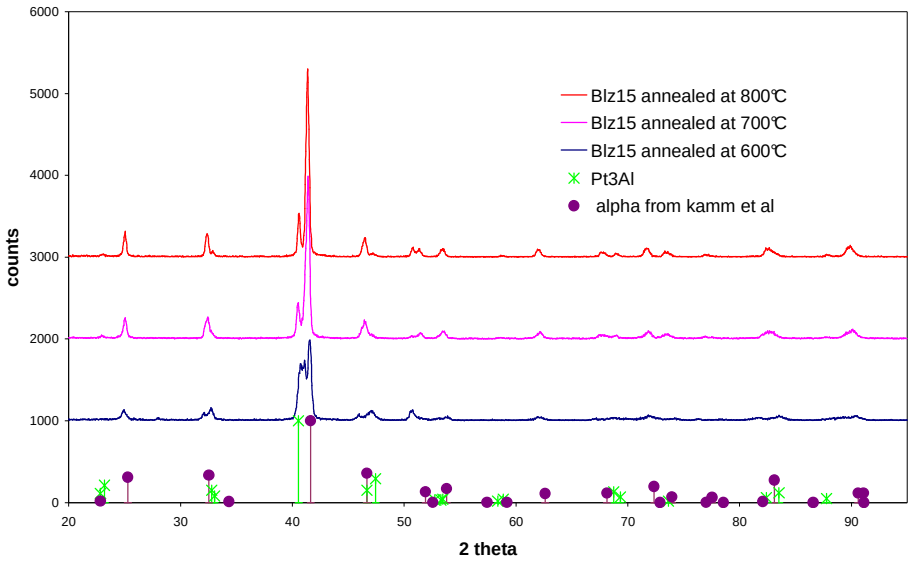

Figure 205 Blz15 after thermal annealing under vacuum at 600, 700 and 800°C compared with α and Pt_3Al

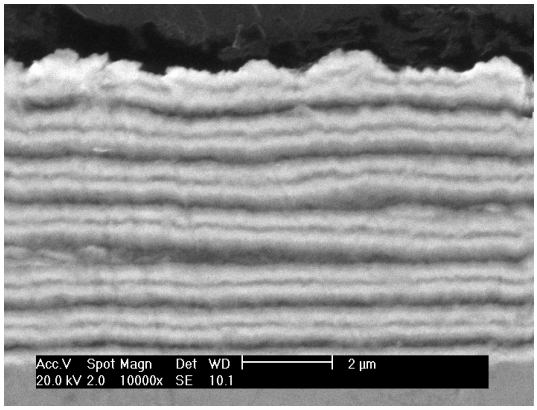

Figure 206 Blz15C as coated (SEM cross section)

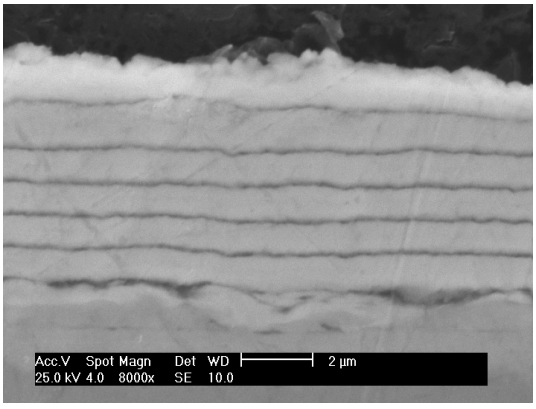

Figure 207 Blz15C HT@800 for 2h in vacuum

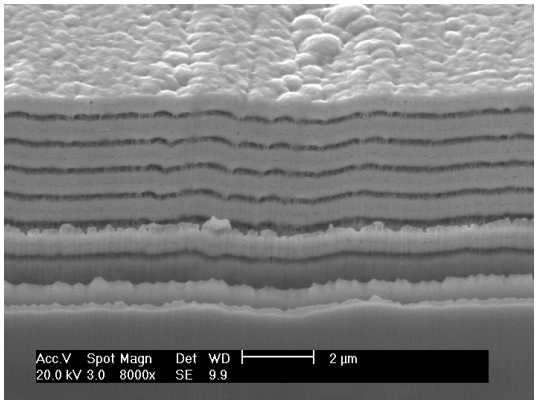

Figure 208 FIB cross section of Blz15 after 2h at 700°C

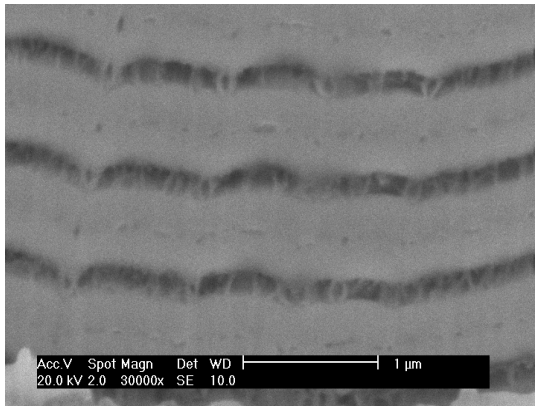

Figure 209 Zoom of Figure 208

The XRD diagrams are equivalent to the one obtained on Ni20Cr substrates, pointing out the presence of two $L1_0$ phases: α and Pt_3Al. The proportion of α is greater with a heat treatment in vacuum at 700°C than at 600°C (the differences between 800°C and 700°C are low). After reaction of the layers, the multilayer pattern is still clear, with 6 "dark interfaces" and a seventh shiny and racked layer (called "interlayer" at the substrate interface). On the FIB micrograph, some porosities seem to stand out within these "dark interfaces". Thus, these "dark interfaces" are not cracks, but an Al rich phase (elemental contrast from the Scanning Electron Microscope), with some porosities in this phase.

It can therefore be argued that Al diffused into its neighboured layers during the heat treatments leaving some vacancies at the "dark interfaces". Moreover, the position of these "dark interfaces" clearly corresponds to the former Al layer (see Figure 206°. All these results lead to the diffusion layout described in Figure 210. The "interlayer" would be a pure Pt_3Al layer, and the shiny ones, a succession of Pt_3Al, alpha, Pt_3Al. The enrichment of Ni in Pt_3Al moves the composition of the compound parallel to the Ni-Pt axis of the ternary diagram, into the α-phase field, by substitution of Pt by Ni on the Pt sites of the lattice.

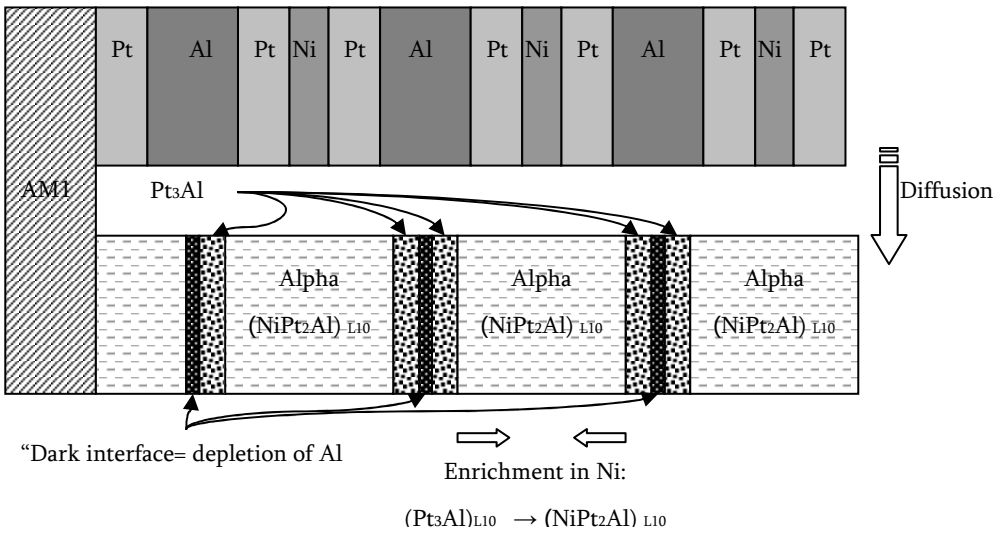

Figure 210 Possible Diffusion-Reaction mechanism during the annealing

However, samples from Blz16, blz17 and blz19 batches failed after heat treatment. For blz17 and blz19 samples, the failure can be attributed to the absence of ion plating during the deposition of the first platinum layer, confirming the dramatic need for this first step during the manufacturing of the multilayer coatings.

The fact that Al is the predominant moving species in the multilayer systems is confirmed by the literature. Some works on platinum aluminide and nickel aluminide thin films, manufactured by similar method have the same conclusions. In these works, pure layers of nickel or aluminium are deposited onto platinum and SiO_2, followed by an annealing in the range of 500°C. Al was found to be the main diffusing species, leading to the formation of voids by the nucleation of the excess of Al vacancies.[47;219-222]

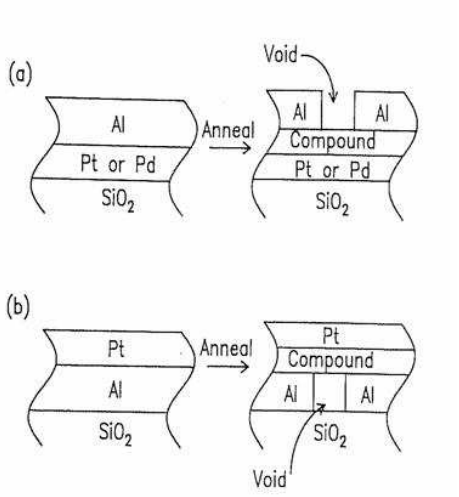

Figure 211 Formation of voids by excess of Al vacancies on the formation of platinum aluminides[47]

V.3.2 Change in composition

The next series of batches was focused on the shift of the overall composition to higher content of Aluminium and Platinum in order to retard the dramatic interdiffusion with the nickel from the substrate during ageing experiment (see next chapter).

Sample preparation is the same as previous, the only change being the overall expected composition. Only six AM1 samples were loaded per batch for a single side deposition (labelled A, B and C and vertically centred in front of the targets).

Blz22 batch corresponds to a close to stoichiometry alpha phase, blz23 and blz24 are poorer in Nickel, while Blz25 corresponds to a duplex system with 2.5µm of $PtAl_2$ followed by 2.5µm of stoichiometric α, manufactured during the same deposition process. All the samples from these batches have a total thickness of 5µm and 25 layers. The alternation of the layers was carried out with the automated stepper motor drive and the calibration realised by glass slide step measurement.

Table 19 Deposition parameters for batches blz22-25

Name	*Composition*	*Pt deposited by*	*Remarks*
Blz22	$Pt_{43}Al_{34}Ni_{23}$	Pulsed DC (340W/250kHz/1016ns)	
Blz23	$Pt_{55}Al_{32}Ni_{13}$	Pulsed DC (“)	Poorer in Ni but still in α phase field
Blz24	$Pt_{57}Al_{35}Ni_{8}$	RF(400W)	Poorer in Ni, only in the Gleeson diagram (not the HIPERCOAT version)
Blz25	$PtAl_2$+Pt_2AlNi	RF(400W)	2.5 µm of each, 25layers in total

The difference of composition between Blz23 and Blz24 corresponds to crossing the hypothetic boundary of the α-phase field in B. Gleeson ternary diagram (Figure 212).

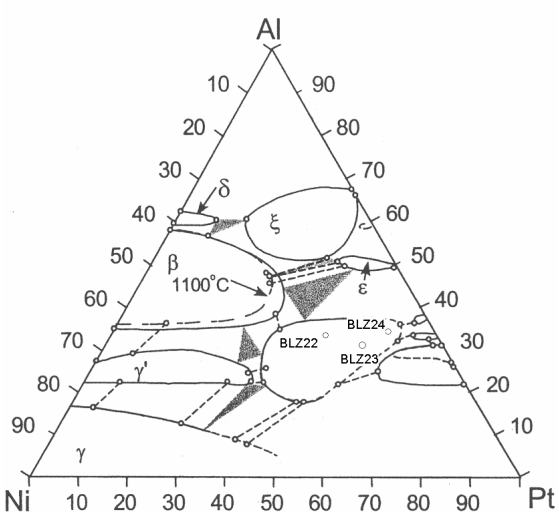

Figure 212 Blz22, Blz23 and Blz24 compositions plotted on the Pt-Al-Ni ternary diagram

Heat treatments were carried out in Vacuum and Argon as detailed in Table 20. Heat treatment temperature was set at 700°C for both types of annealing.

Table 20 Heat treatments carried out on Blz22-Blz25 samples

	A	*B*	*C*
Blz22	HT700 in Vac	HT700 in Vac	HT700 in Ar
Blz23	HT700 in Vac	HT700 in Vac	HT700 in Vac
Blz24	HT700 in Vac	HT700 in Vac	HT700 in Ar
Blz25	HT700 in Vac	HT700 in Vac	HT700 in Ar

XRD analysis of the reacted samples is relevant with the expected peak distribution: Blz22 and Blz25 have an excellent match with the α-phase; the lattice parameter being close to the stoechimoetric value. Blz23 and Blz24 show a distorted lattice due to the increase in Pt content and the decrease in Ni content. Blz25 Displays as well the pattern of $PtAl_2$ free of lattice distortion. Blz24 samples stand in the stability field of both α and Pt_3Al as the peaks from the high Pt content binary aluminide appear.

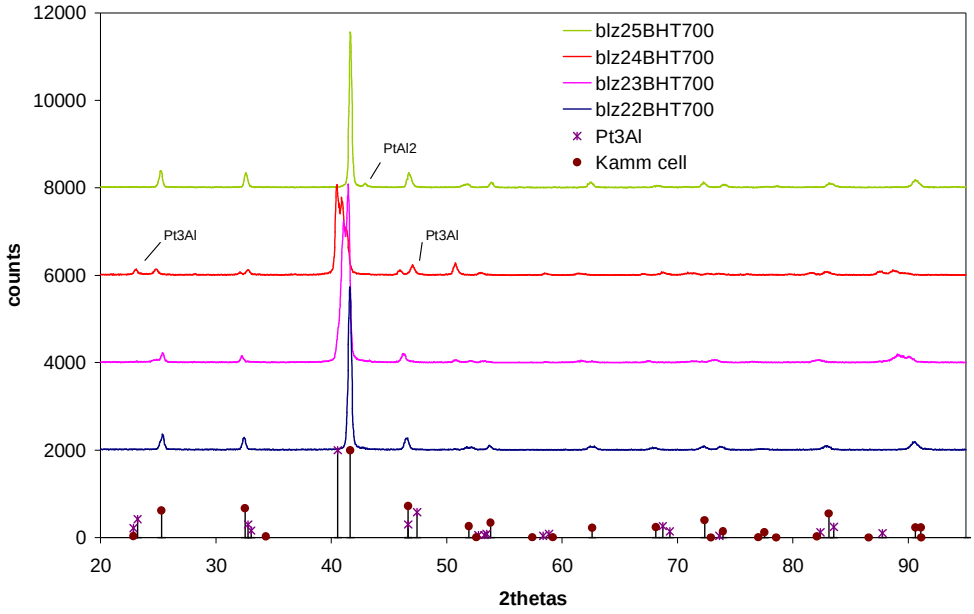

Figure 213 XRD spectra of Blz22-Blz25 heat treated samples

Although the control of the synthesis of the intermetallic compound is excellent, adherence of the coating is very poor once annealed. All the sample failed cohesively, within the overlay.

Figure 214 Example of cohesive failure on Blz24

The failure clearly occurred at the former Al layer on all the sample as SEM section on failed free standing coating show (Figure 215 and Figure 216).

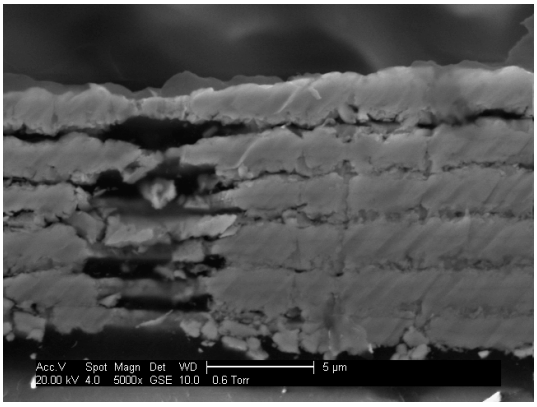

Figure 215 Failure of the coating after annealing on Blz24

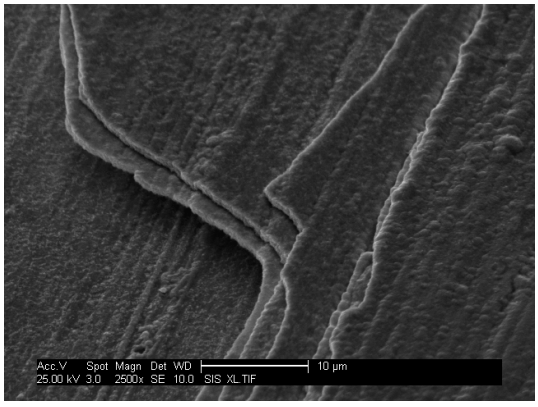

Figure 216 Step like failure at each former Al interlayer

For each of the sample, XRD was carried out on each interface i.e.: remains on AM1 after coating peel off, failed interface on the free standing coating side, and top side of the free standing coating.

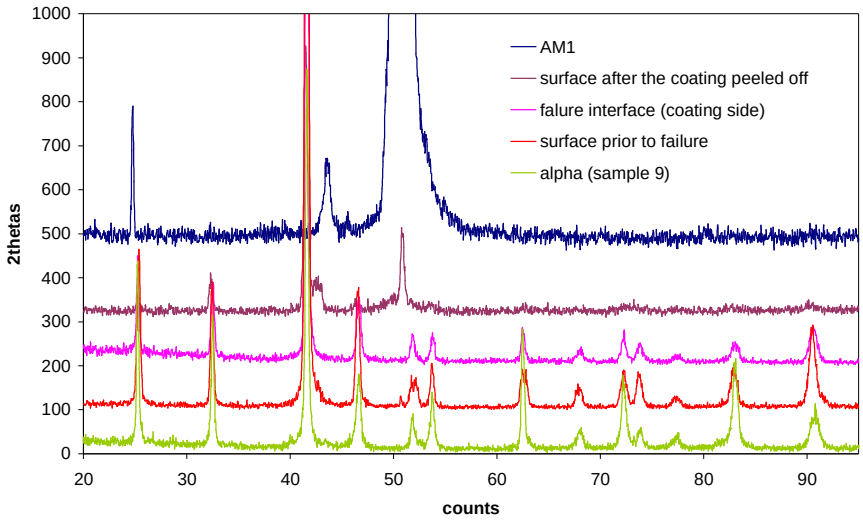

Figure 217 Blz22 after peel off

As described earlier, Blz22 after reaction matches perfectly with the pattern of the α-phase. However, α peaks are very weak on the remains of the disc after failure, suggesting that the majority of the coating peeled off.

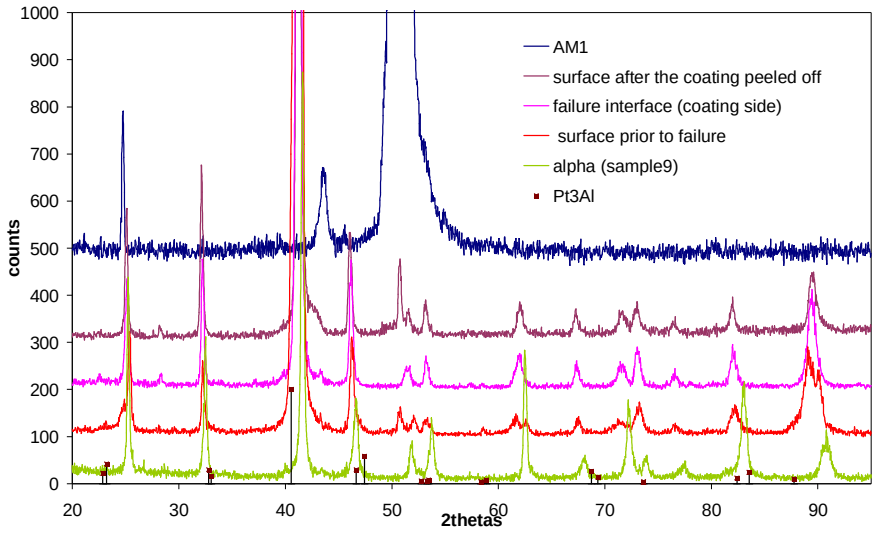

Figure 218 Blz23 after peel off

Failure analysis of Blz23 shows that the Pt_3Al peaks observed on the reacted surface ar no longer present over the surface of the disc, while α phase peak are still present. This suggests that failure occurred at a α-Pt_3Al interface, with some of α staying adherent to the substrate.

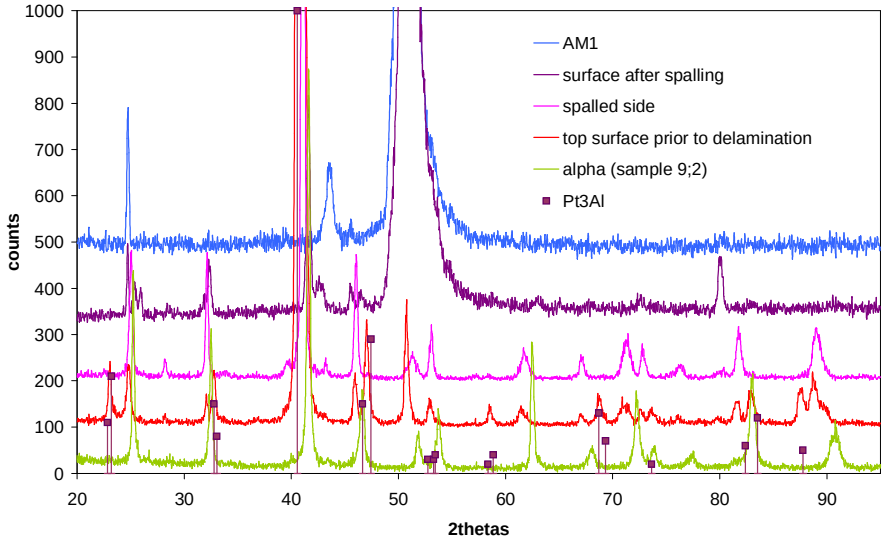

Figure 219 Bkz24 after peel off

Blz24 sample which contains even more Pt_3Al as it is richer in Al and Pt shows the same behaviour as Blz23: the Pt_3Al phase is only present on the delaminated part of the coating suggesting the failure occurred at the first Al depleted layer of the reacted system described earlier in Figure 210.

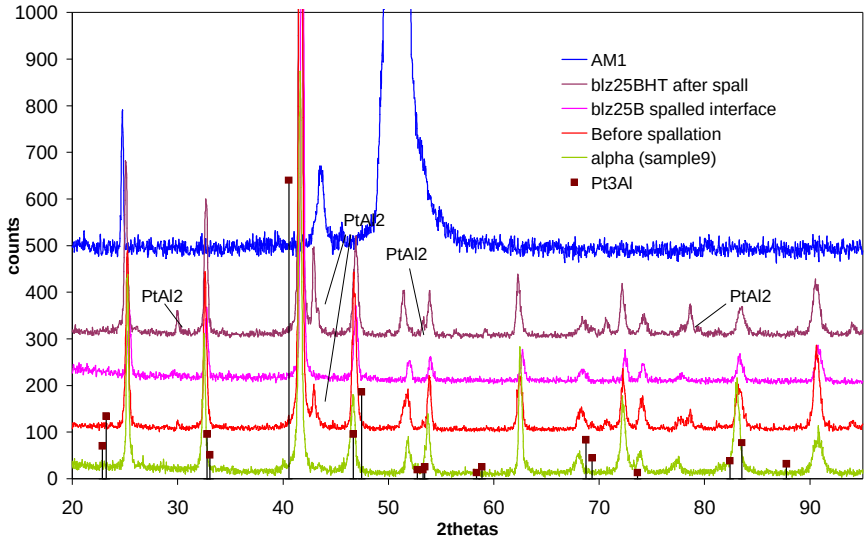

Figure 220 Blz25 after peel off

Blz25 failure analysis clearly shows that the failure occurred within the α phase part of its duplex structure as no peak is observed on the failed interface of the free standing coating. This fact confirms that the weakness at the former Al interlayer is characteristic of the α phase coating.

V.3.3 Conclusions

In conclusion the dramatic results of these experiment outline two points:

- ✓ The coatings made this way have a defined weak point: the former Al interlayers. These zones correspond to the depletion of Aluminium that diffused to the neighbour Pt layer to form the desired aluminide. If the densities of the sputtered metal layers is supposed to be ideal (i.e. equal to bulk metals), then the reaction of (Al+Ni+2Pt) to α-$NiPt_2Al$ leads to a volume shrinkage of 10%. This shrinkage is concentrated at these Al depleted layers as Al is the fastsest diffusing species. Failure occurs at the first of these depleted layers as it is the point in the coating were the induced stress is maximum.
- ✓ These weak points would not be such a problem if the films were stress free. The deposition process has to be modified to reduce the stress build up. Either changing the sputtering parameters (pressure, temperature, deposition power), or increasing the number of layers. This last point is promising as Blz21 coatings, which were 2.5μm thick in total for 50 layers, stood very adherent after annealing.

V.4 New deposition process procedure

V.4.1 Procedure description

Regarding to the disappointing results of previous batches, and to the lack of composition control, the Low Mass Bondcoat process procedure had to be rethought. Some objectives and proposed solutions are explained below.

First a better *calibration* is needed in order to control the variation in composition across the substrate table. The deposition rates were previously done by the measurement of the thickness of a step on a single glass slide. This method had three disadvantages:

- ✓ It relies on the use of a mechanical step measurement device whose accuracy was good, but the measure was done on a single point
- ✓ This method does not give the value across the total surface of the substrate holder, or it would be time consuming and resulting in a thickness mapping which hardly exploitable on a 6 coupons per run display.
- ✓ Last but not least, the thickness is used to determine thereafter the quantity of deposited material, hence making a strong hypothesis on the density of the film (which was so far considered equal to the bulk material which is known to be incorrect)

It has therefore been decided to use *weight gain* to make the calibration of the deposition rate for each metal. Each sample is weighted before and after deposition on a precision balance (+/-0.01mg), giving a similar accuracy, and an average on each single coupon. Each coupon is weighted 6 times to improve the precision. Each run needs therefore 5*6*6=*180 weightings* (3 runs for each targets, plus samples before and after the actual deposition run).

For this purpose, samples have to be fitted at the exact same position for each run (calibrations and proper deposition run). *A sample holder* had therefore been manufactured. It can stand 6 AM1 coupons. Moreover, this samples holder is designed so there is no shadowing on the main side of the sample. The substrate holder consists in a NiCr plate drilled with grooved holes fitting the samples and the samples edges. Each sample is kept in place by a couple of reusable wire.

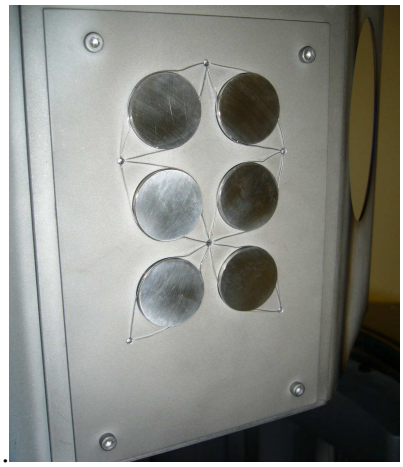

Figure 221 Picture of the new substrate holder

The terminology used to name the samples on the planar substrate holder is: R and L for right and left, and A,B, C for the vertical positioning. Then for instance, the sample called Blz27RC corresponds to the disc which was 3rd from the top, on the right hand side when facing the holder.

Failures of the previous samples were likely to be due either to a low layering, or to an excessive internal stress within the films. It has therefore been decided *to reduce the deposition power* for Al and Ni. The difference in deposition rate is not critical (Pt low deposition rate is the one that mainly affects the total deposition time). Moreover, these low powers have been selected so the deposition rate for Ni and Al fit with the slow Pt deposition rate i.e. the *sample stays roughly the same time in front of each target* to achieve a Pt_2NiAl composition. This feature will be as well very important when the number of layer will be increased, so the samples don't stay for instance 5 sec in front of Ni and Al, and 1 min in front of Pt. This reduces the error on the total time spent in front of each target (the more layers, the more steps in the stepper motor program, the more errors are added).

The *calibration of the stepper motor drive* was as well improved to reduce this error as much as possible. The step time entry in the program is an arbitrary unit, U, and it has to take in account the time for the substrate holder to move from a target to another.

1s=1003U

Movement of 90°=t_{90}=1505U

Movement of 180°=t_{180}=2357U

($t_{180} \neq 2 * t_{90}$ because the motor speed is not linear)

For instance, blz28 calibration lead to 75 cycles with 1'09 per Al layer; 1'10 pet Ni layer and 1'29 per Pt layer (2 layers per cycles). In order to get the Pt/Al/Pt/Ni/Pt/Al…alternation, the samples move following the sequence:

$$Pt \xrightarrow{+180°} Al \xrightarrow{-180°} Pt \xrightarrow{-90°} Ni \xrightarrow{+90°} Pt \xrightarrow{+180°} Al....$$

Therefore, the times spent in front of each target are calculated, and entered into the program loop:

$$t_{Al} = 69 \times 1003 + 2357 = 71{,}564U$$
$$t_{Ni} = 70 \times 1003 + 1505 = 71{,}715U$$
$$t_{Pt\_from\_Al} = 89 \times 1003 + 2357 = 91{,}624U$$
$$t_{Pt\_from\_Ni} = 89 \times 1003 + 1505 = 90{,}772U$$

The process has to run with *the 3 plasmas constantly on:* The frequency of rotation is too important to let the operator switch on and off the unused plasmas. This will reduce the target lifetime, but can hardly be avoided.

The *working pressure* was chosen to be 0.015 Torr.

After several tries, the selected powers for each target are:

- ✓ 100W for Al (instead of 352W previously), using a last generation pulsed DC supply, set in constant current mode
- ✓ 50W for Ni (instead of 140W previously), using a second last generation pulsed DC supply set in constant current mode
- ✓ 350W for Pt in RF mode: this power is the upper limit the system can sustain (thermal issue), during such long times. The deposition rate is still very poor (less than 0.7μm/h)

The *substrate preparation* is the same: 600 grit paper finish, clean in Acetone and IPA under ultrasounds, and in ultra pure IPA under a Soxhlet.

A 15min long ion plating of Pt is always carried out before actually starting the process:

- ✓ 5min@-300V for 100W (RF)
- ✓ 5min@-250V for 200W (RF)
- ✓ 5min@-200V for 350W (RF)

In order to manufacture 3D coated sample, a rotating substrate holder was set up. Samples are hooked to two revolving sticks loaded on the substrate table, which rotates in front of each target position. Calibration procedure is the same as for planar samples, by weight gain. Substrates

used for these runs are mechanical testing cylindrical sample. Two AM1 discs of 17mm diameter were loaded under the cylindrical samples. The system is centred so the cylinders face the middle of the targets.

Figure 222 3D samples: cylindrical sample for mechanical test and small AM1disc

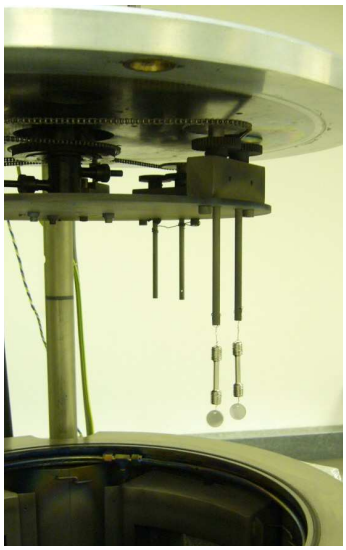

Figure 223 Samples layout with the rotating substrate holder

For all the batches manufactured with this procedure, the thermal annealing of the substrate was carried out in the Argon furnace, for 2 hours at 700°C.

V.4.2 Experiment Plan

Fifteen batches were manufactured with this deposition process, corresponding to a total of 86 samples (6 samples per batches and 4 samples per batches with rotating holder). Parameters which were changed are:

- ✓ *Expected composition*: This composition was calculated with the 3 calibration runs which were carried out prior to each deposition batch. $NiPt_2Al$ was targeted, as an Al richer alpha. Binary intermetallics were manufactured: $PtAl_2$ and Pt_2Al_3 platinum aluminides in order to compare their behaviour with M Silva work; β-(Ni,Pt)Al with 10at%Pt in order to compare their behaviour with β based commercial systems
- ✓ *Rotation*: 2 batches were realised with the setup described previously, loaded with two cylindrical samples and two small AM1 discs
- ✓ *Total thickness*: it was kept constant at 5 µm except for Blz32, set at 15µm and Blz30, Blz31 and Blz41 in order to match M Silva samples.

- ✓ *Layer density*: was mainly varied from 100 to 300 layers per 5 µm, except for blz36 that stands with only 5 thick layers over the 5 µm.
- ✓ *Surface finish*: the majority of the samples were ground with SiC paper (grit#600), some samples were grit blasted (grit #220)

These parameters are gathered in Table 21.

Table 21 Parameters for Blz26-Blz40 batches

Sample ref	*Composition*	*Rotation*	*Total thickness*	*Layers/5µm*	*Grit blasted*
Blz26	**Alpha**	No	5	100	-
Blz27	**Alpha**	No	5	200	-
Blz28	**Alpha**	No	5	300	-
Blz29	$Ni_{40}Pt_{10}Al_{50}$	No	5	200	-
Blz30	$PtAl_2$	No	**2.5**	100	-
Blz31	Pt_2Al_3	No	**8**	100	-
Blz32	**Alpha**	No	**15**	300	-
Blz33	**Alpha**	**Yes**	5	300	-
Blz34	Al rich Alpha	**Yes**	5	300	-
Blz35	Al rich Alpha	No	5	300	**2**
Blz36	**Alpha**	No	5	**5**	**2**
Blz37	$Ni_{40}Pt_{10}Al_{50}$	No	5	100	**3**
Blz38	**Alpha**	No	5	300	**4**
Blz39	**Alpha**	No	5	100	**4**
Blz40	Pt_2Al_3	No	**8**	100	**4**

V.4.3 Effect of high multilayering

For samples from batches blz26 to blz28, no reaction of the layer was triggered during the deposition process, though it was proven that reducing the layers thicknesses was decreasing the triggering temperature for the formation of the intermetallic[209]. The XRD of as deposited samples was checked, only the peaks from Ni, Pt and Al are present, as shown in example on Figure 224. The most intense peaks correspond to the Pt in the film, which is the most present. Al main peak is hidden by the (111) peak of Pt at 39.763°. The most intense Ni peak is at 44.507°. A strange result is the presence, or not, of the substrate peak: no relevant explanation was found to explain its disappearance for some samples from the same deposition batch. The samples have a very

similar coating structure, and this is not depending of the orientation of the grinding marks on the surface.

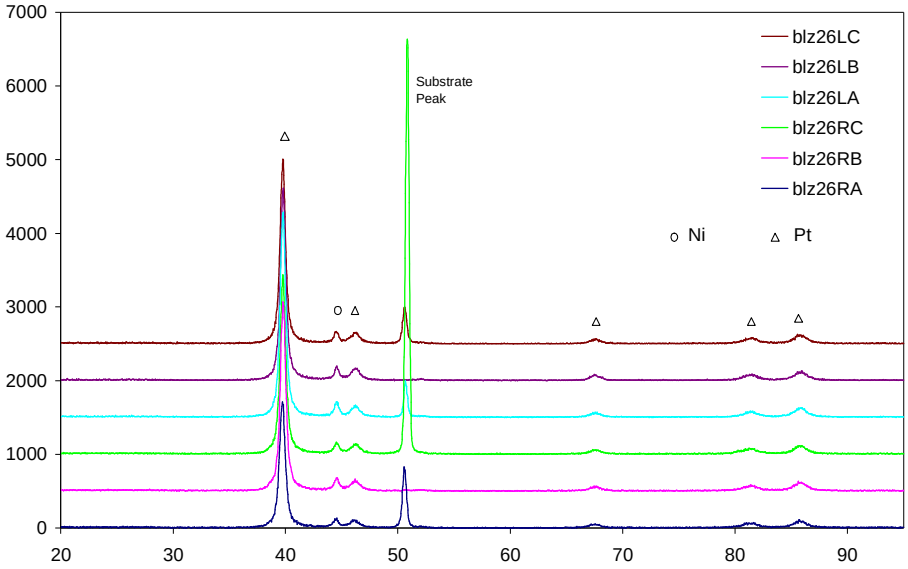

Figure 224 XRD diagrams of Blz26 samples as coated

No significant difference was found due to the number of layers in the film, as the XRD of Blz27 as coated samples shows in Figure 225.

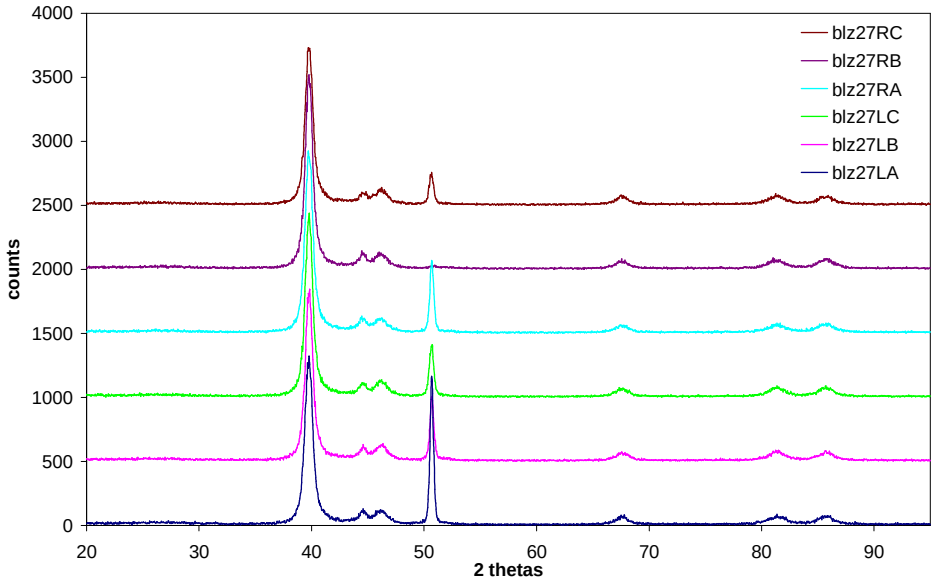

Figure 225 XRD diagrams of Blz27 samples as coated

The microstructure of the as deposited films is very homogeneous, and adherent as none of the film spalled after deposition. The structures are defect free thanks to the cleanliness of PVD deposition process, up to 300 layers over 5µm(Figure 226,Figure 227, and Figure 228).

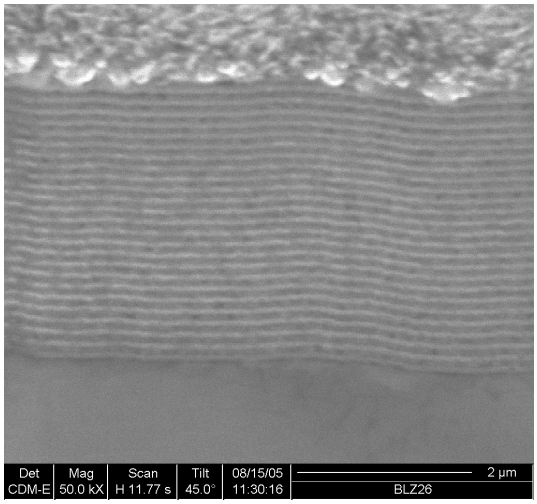

Figure 226 FIB section of Blz26 as coated

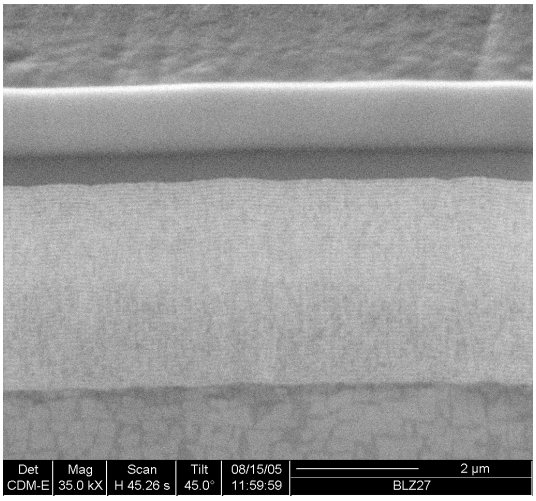

Figure 227 FIB section of Blz27 as coated

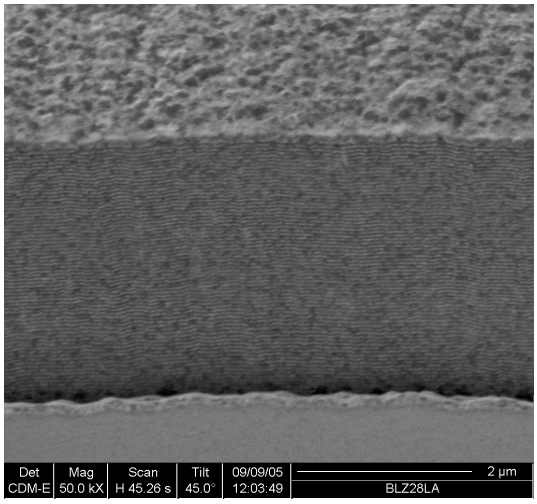

Figure 228 FIB section of Blz28 as coated

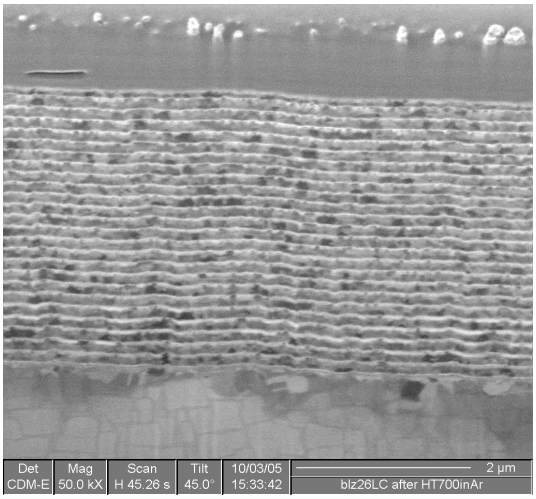

Figure 229 FIB section of Blz26 after reaction

Unlike the previous batches, all the annealed coatings remain adherent after heat treatment. The observation of a reacted sample (Figure 229) shows the grains reprecipitation in the coating. The scars from the multilayer pattern are still present, and some interdiffusion with the substrate occurred during the thermal annealing.

The XRD analysis of reacted samples of Blz26, blz27 and blz28 batches shows the films are α-phase based. All the samples show an important texture on the (111) diffraction peak, which is quite typical as this is the close pack plan of the intermetallic structure.

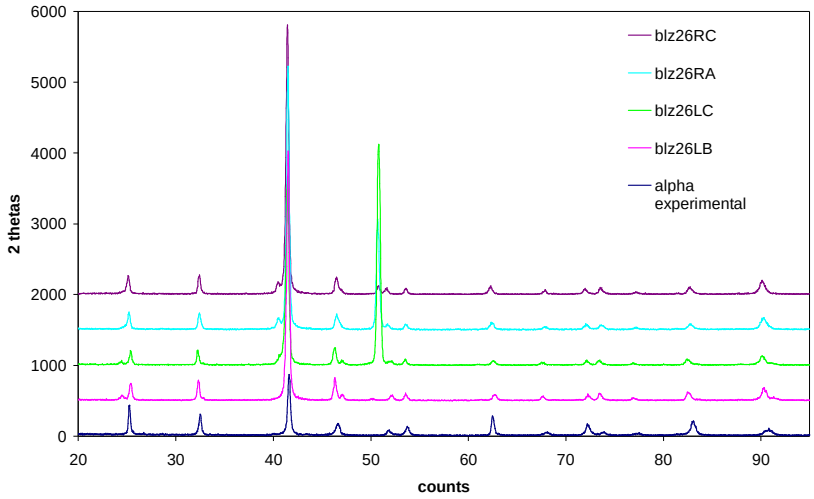

Figure 230 XRD spectra of Blz26 samples after heat treatment compared to experimental alpha

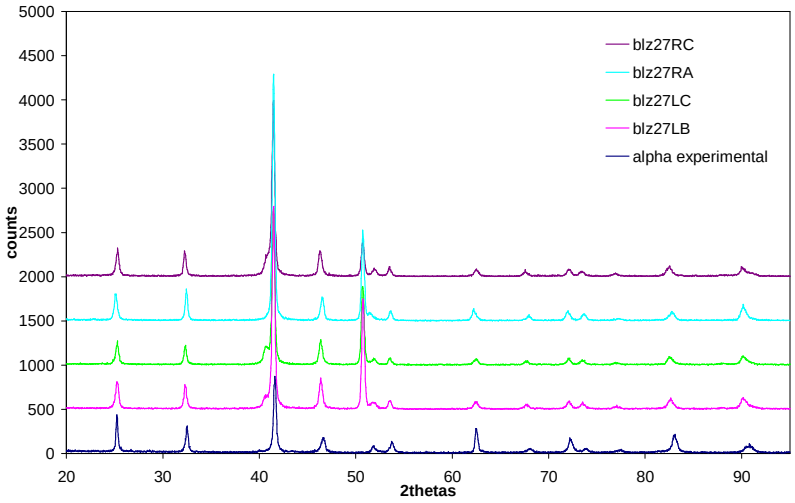

Figure 231 XRD spectra of Blz27 samples after heat treatment compared to experimental alpha

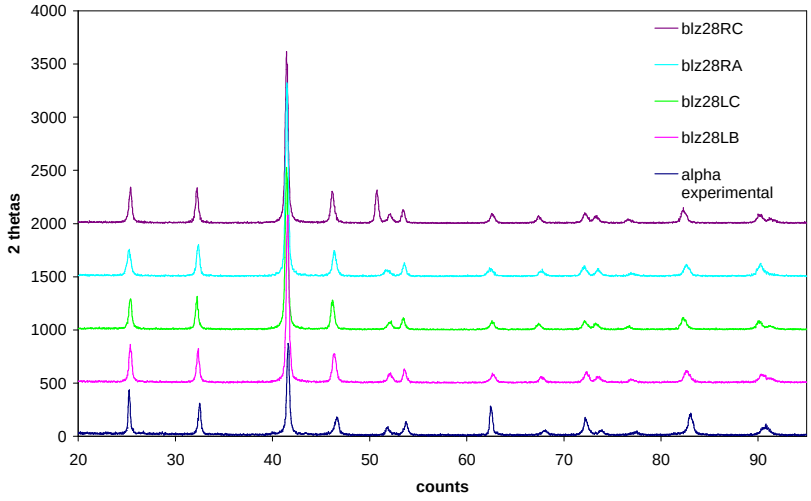

Figure 232 XRD spectra of Blz28 samples after heat treatment compared to experimental alpha

Some trace of another compound is found for blz26LC and blz26LB: these two samples are quite poor in Al (≈14at%), which could explain the formation of a low Al content intermetallic, which was not found on the JCPDS database. With 100 and 200 layers samples, one can still detect the presence of the Pt_3Al phase, with the peak around 40.6° shouldering the main α-phase peak at 41.6°. However, samples from Blz28 have clear spectra of the α-phase.

Another effect of multilayering which is noticeable is the texture of the reacted film: the fewer layers, the stronger the (111) peak relatively to the rest of the pattern. This point will be outlined as well on the study of extremely low multayering later on in this chapter.

V.4.4 TEM analysis of an as reacted sample

In order to investigate the microstructure of the reacted sample at lower scale, transmission electron microscopy (TEM) was carried out on a reacted sample of blz26 batch. The TEM section was manufactured with the FIB as describe in the experimental procedure chapter of this thesis. One can see on Figure 233 that this sample preparation resulted in a partial milling of the top surface of the coating, and an non homogenous thickness in depth of the section. Only the edge of the section was exploitable for TEM observation (typically below 100nm of thickness). Some back-sputtering can as well be expected: the atoms milled by the FIB are redeposited onto the section surface.

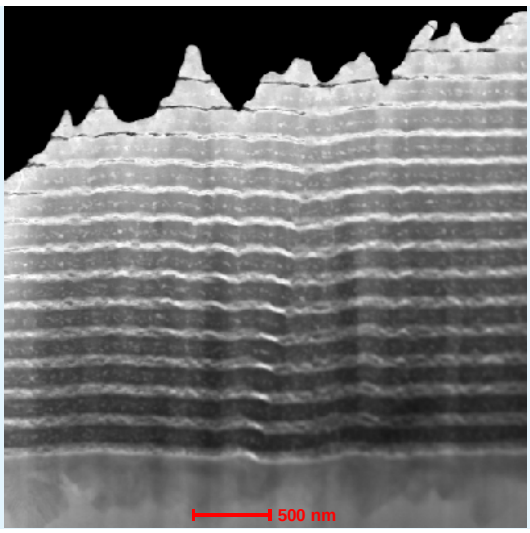

Figure 233 TEM dark field micrograph of blz26 as reacted (global picture)

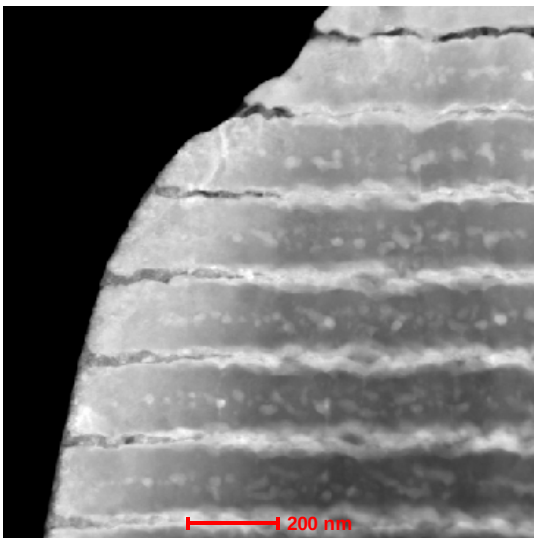

Figure 234 TEM dark field micrograph of blz26 as reacted (zoom on the edge)

However, the internal microstructure of a reacted film is clearly outlined in dark field mode (Figure 234). Two kinds of defects are observed: planar voids along the former Al layers, and nodules precipitates at the former Ni layers. The planar voids confirm the previous observation of reacted multilayers with the FIB: aluminium is the fastest diffusing species and leaves kirkendall voids when diffusing and reacted with the surrounding layers. These defects were analysed with nano EDS in situ of the TEM.

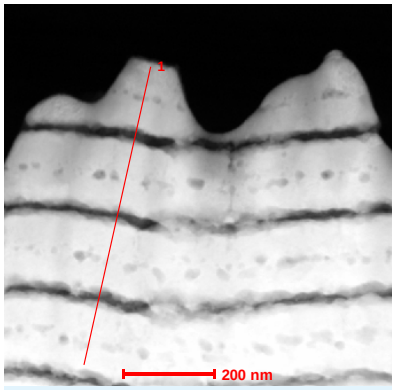

Figure 235 HAADF picture of blz26HT

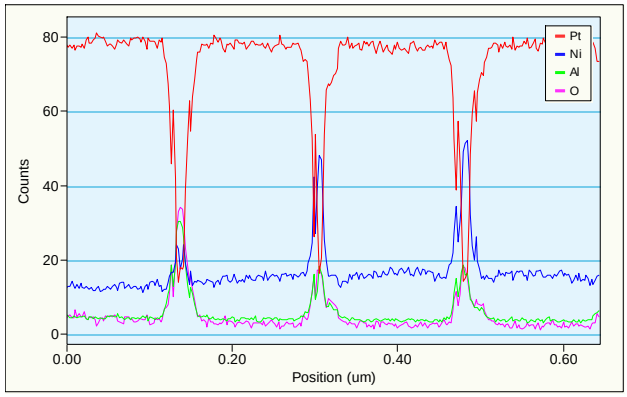

Figure 236 Global concentration profile

Global composition profile was measured across three linear void defects from the top of the section (Figure 235 and Figure 236). There is no Platinum left from the protective Pt strip at the top of the section. One can notice than the Al level in the profile is very low, not comparable to the EDS carried out in EDS (which is between 15 and 20at%). This is likely to be due to the spreading effect of the FIB, or due to a higher sputter etching yield of Al with the FIB. This profile shows a very constant concentration within the intermetallic layers, and a peak in Al and O within the planar voids. The drop in Pt and increase in Ni is likely to be an effect of the absence of material within the void. These dark lines seem therefore to correspond to voids and oxide.

A closer analysis of this region (Figure 237and Figure 238) confirms this interpretation. At the defect point there is an increase in Al and O; Ni seems rather to be a consequence of the drop in Pt concentration as Al and O concentration increase more in relative to Ni. This confirms these defects are voids; the lack of Pt rich bulk is measured, with some aluminium oxide. However one can notice a slight Ni enrichment at the edge of the defect that could correspond to a Ni richer intermetallic region.

The oxygen observed within the reacted coating comes from the sputtering deposition process as the reaction was carried out in a protective atmosphere, its presence deep in the coating can not be explained otherwise. The pollution by the oxygen is typical when sputtering Al, as Al

atoms are highly reactive with the oxygen impurities of the deposition gas, there is some oxygen in the film. This was outlined by XPS experiment by M. Silva[208] on other sputtered coatings systems.

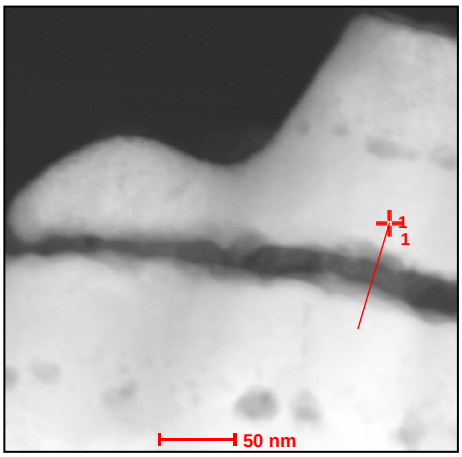

Figure 237 HAADF micrograph of a planar void defect

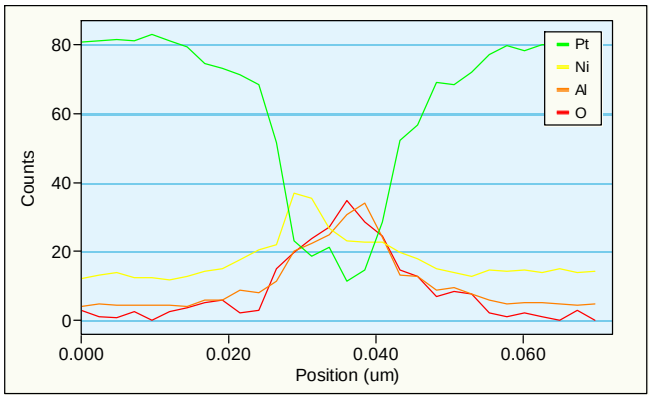

Figure 238 Profile of a planar void defect

The chemical analysis of the nodule like defect standing at the former Nickel layers shows that these defects are only topographic, as no sensible difference was measured (Figure 239). These defects are therefore likely to be trace of a reprecipitation of the intermetallic compound at these layers.

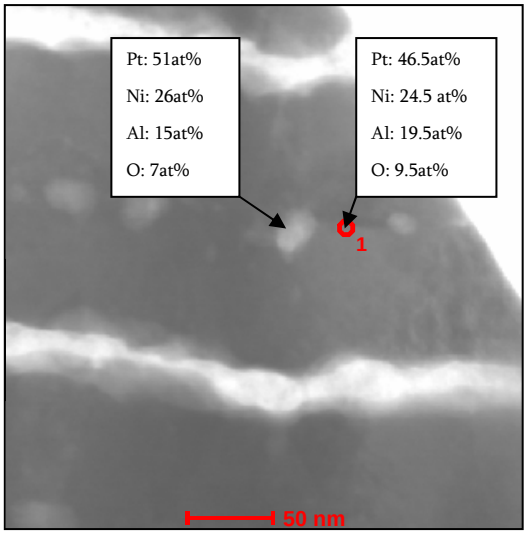

Figure 239 Chemical analysis on a nodule precipitate

V.4.5 Effect of low multilayering and of substrate grit blasting

In order to have a better understanding of the mechanism occurring during the reaction of the layer, samples from Blz36 batch were manufactured only with 5 "thick" sputtered metallic layers, and the same total thickness of 5µm. This system was deposited on both ground surface and grit blasted, in order to study the effect of the surface finish as well. XRD analysis of the film and FIB sectioning were carried out.

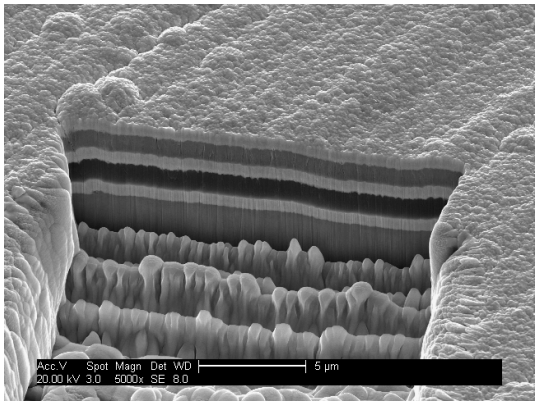

Figure 240 Ground Blz36 as coated

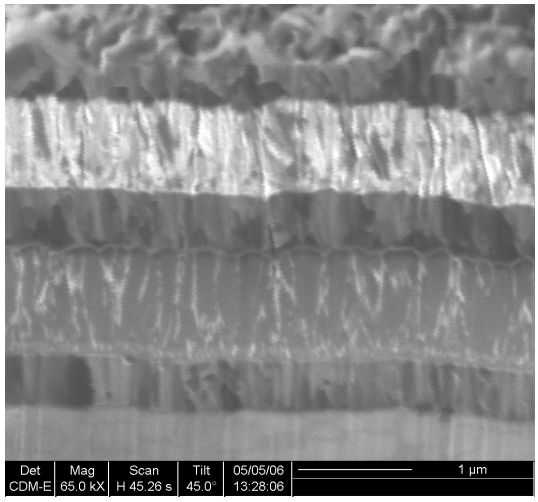

Figure 241 Ground Blz36 as coated (zoom)

The as deposited structure of the thick Pt/Al/Pt/Ni/Pt system (Figure 240) shows the homogeneity of the sputtered metallic layers. Furthermore, the difference in microstructure between each layer is outlined in Figure 241. The platinum layers are quite dense, whereas Nickel and even more Aluminium tend to have a columnar structure, with a rough interface. This is clearly due to the great difference in melting point between Pt, Al and Ni. Aluminium clearly stands in the zone II of Thornton's PVD thin film model, and Platinum in the more stable zone T (Figure 242).

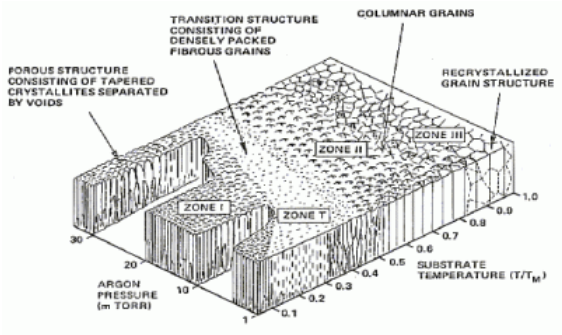

Figure 242 Thornton's model

This difference in structure is likely to lead to important surface stress at the interfaces, especially the Pt/Al interfaces, which will be more reactive than Pt/Ni interfaces, due to the greater surface contact area.

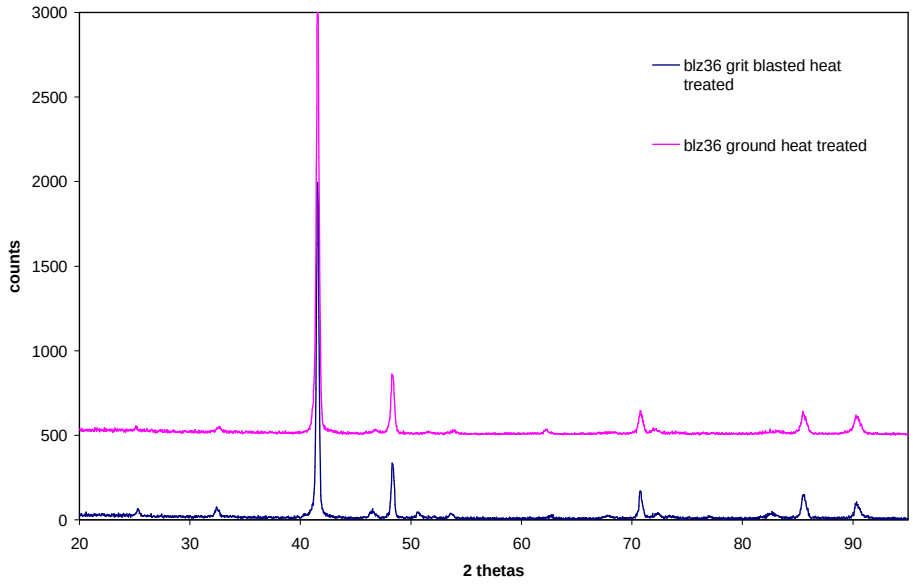

Figure 243 XRD spectra of Blz36 samples after reaction with ground and grit blasted surface

The presence of only five metallic layers does not affect the capacity of the film to react into the expected α-phase intermetallic compound. The only point of the high multilayering is to reduce the stress within the coating: on the ground surface finish, the film buckled after reaction. However, the secondary effect of multilayering regarding to the texture of the film is confirmed: as shown on Figure 243, outlining the dramatic texture of the film on the (111) diffracting plane.

Although the surface of the grit blasted superalloy is relatively rough compared to the thickness of the overall coating, the covering of the substrate is excellent, as shown in Figure 244. The difference in microstructure between the 3 type of metallic film is outlined as well on the rougher surface. The bumpy interface between the first platinum layer and the aluminium layer is maybe more developed due to the roughness (Figure 245).

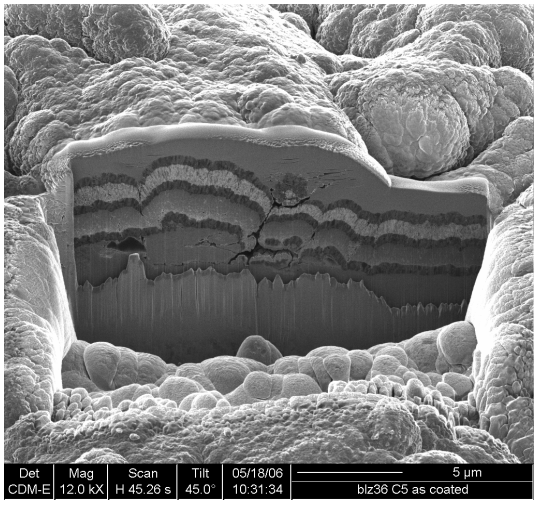

Figure 244 FIB section of blz36 on grit blasted surface

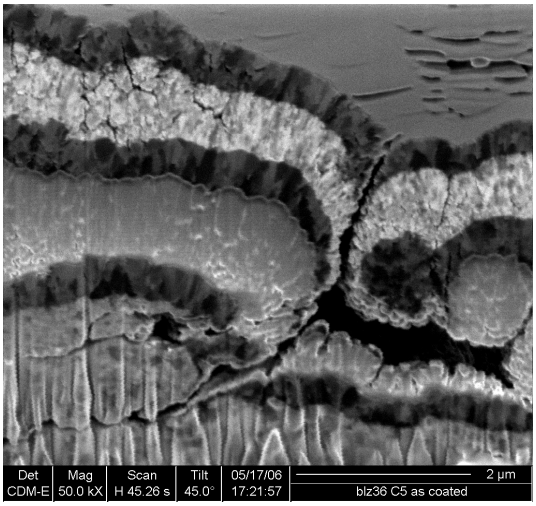

Figure 245 FIB section of blz36 on grit blasted surface (zoom)

On the crystallography of the reacted coating, the roughness does not seem to play any role as the XRD spectra in Figure 243 are very similar, with the same (111) texture. However, the adherence changes a lot between the two surface roughnesses. As said before, the ground sample at grit #600 failed after heat treatment, and after deposition of a ceramic topcoat without prior heat treatment. On the contrary, the grit blasted sample was still adherent after heat treatment. However its structure showed impressive defects, as shown on FIB sections in Figure 246 and Figure 247.

The relative thickness of the layers dramatises the microstructure transformation occurring during the formation of the intermetallic. The voids at the former Ni and Al layers is clearly pictured on these micrograph. As interpreted from the previous TEM sample, the Al and Ni atoms have a faster diffusion towards the platinum layers, and leave kirkendall voids behind. The only reason for the coating not to fail is the mechanical locking provided by the roughness. The re-precipitation into the intermetallic compound is noticeable on these micrographs, showing the grains at the former Pt layer. The middle compound layer even shows an in plane symmetry, proving the reaction grows from the former middle of the Pt layer.

The volume shrinkage between a (2Pt + Al + Ni) and the α-$NiPt_2Al$ compound is 9% when considering crystallographic cells, hence ideally dense systems. The Figure 247 clearly shows a greater shrinkage, proving the original metallic layer were not fully dense, as it is often the case in PVD deposited films.

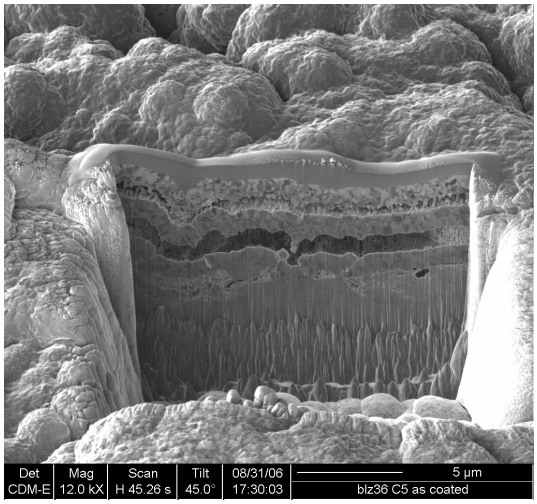

Figure 246 FIB section of blz36 on grit blasted surface after reaction

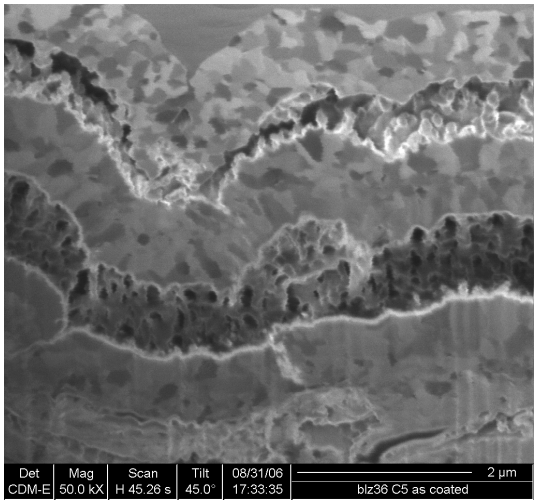

Figure 247 FIB section of blz36 on grit blasted surface after reaction (zoom)

Grit blasting does not have any influence on the crystallography of highly multilayered system after reaction, as shown on the comparative XRD analysis of blz38 and blz39 in Figure 248. The presence or absence of the AM1 peak at 50.9° is not linked to the surface finish either. It is noticeable that these analyses still confirm the fact that lower multilayering increases the proportion of Pt_3Al compound, and the (111) preferential orientation of the α-phase film.

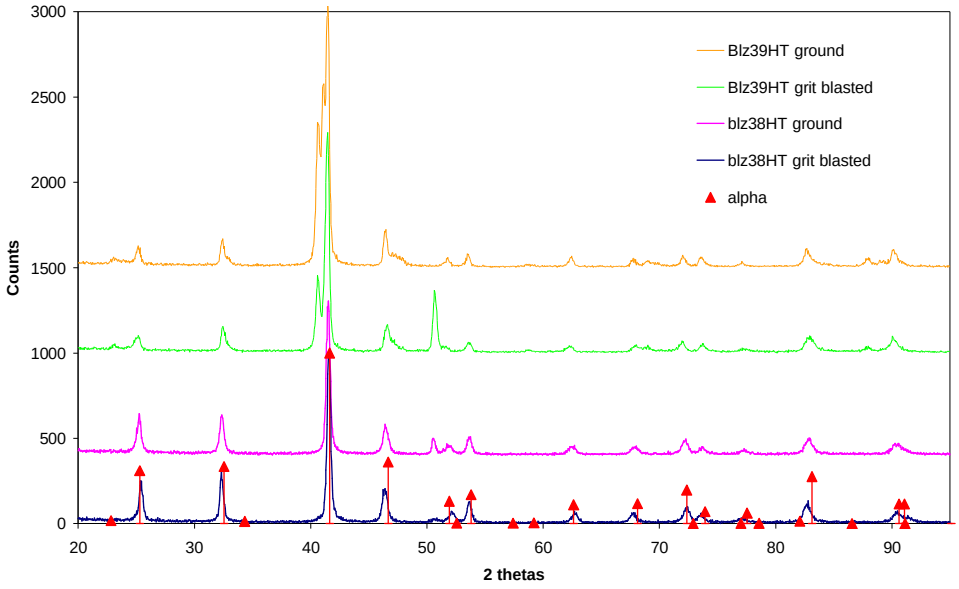

Figure 248 Comparison of XRD of ground and grit blasted surface finish on blz38 an blz39 batches

However, there is a slight difference between the crystallography of grit blasted and ground samples prior to the reaction of the metallic layers. Ground samples have a stronger 200 orientation, observable for both Pt and Ni layers. This is relevant with a columnar growth of the film, as (111) is the closest packed crystallographic plan for fcc systems, the facets of the columns tips grow along this plan, which corresponds to a <100> growth direction for the column, hence the relative increase for the (100) and (200) diffracting plans. Hence the metallic layers have a greater tendency to columnar growth on ground samples thin grit blasted. This relevant to the fact that columnar growth is facilitated on defect free and smoother surfaces.

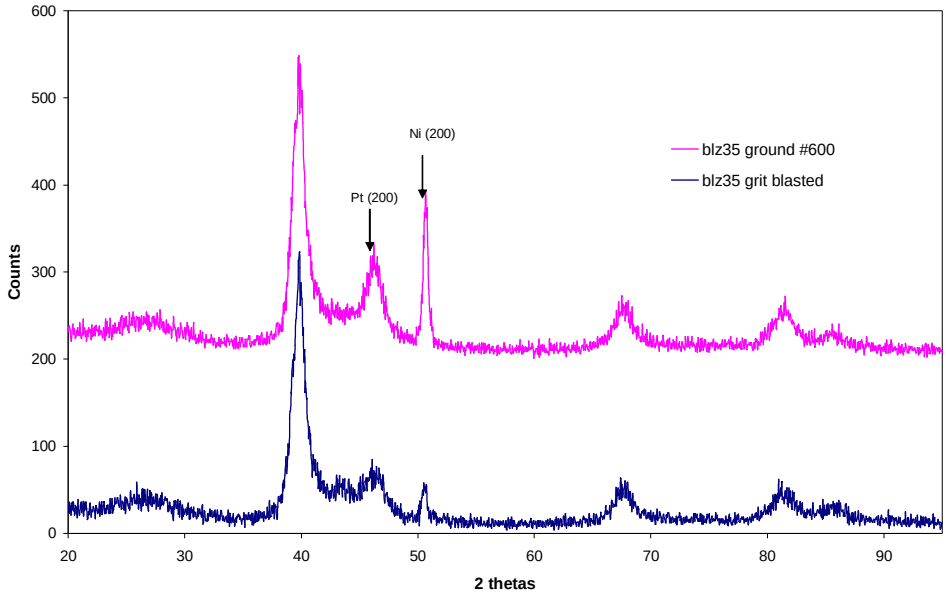

Figure 249 Effect of grit blasting on as coated samples (XRD spectra of blz35)

V.4.6 Effect of the total thickness

Samples from the batch blz32 have a coating of 15µm total thickness for a total of 900 layers. This configuration corresponds to an "ultimate" α-phase based oxidation resistant coating, as it corresponds to a total content of Pt of 7.84µm which is the same order of magnitude as Pt electroplated in commercial β-(Ni,Pt)Al coatings. The observation of the surface of the coating in SEM shows the presence of consequent grooves. These grooves are following the grinding marks, and were not as obvious on thinner coatings. The total thickness enhances this phenomenon. After reaction of the layers in the argon furnace, these grooves are expanded, due to the shrinkage of the film when reacting into the intermetallic.

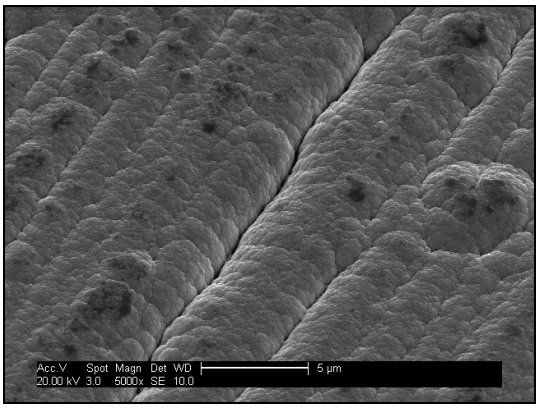

Figure 250 Blz32 surface groove before reaction

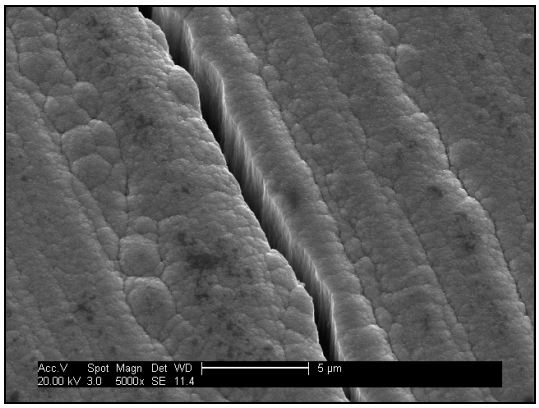

Figure 251 Blz32 surface groove after reaction

The presence of such grooves is likely to be problematic when considering the high temperature oxidation protection of these coatings, as they cross the overall coating as proven by a FIB section. The V shape of the groove goes down to the superalloy substrate.

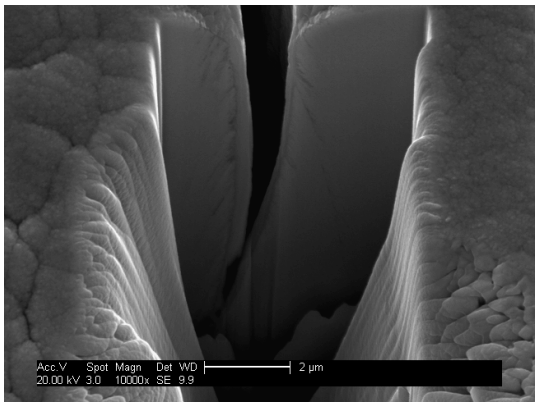

Figure 252 FIB section of a groove on Blz32 after heat treatment

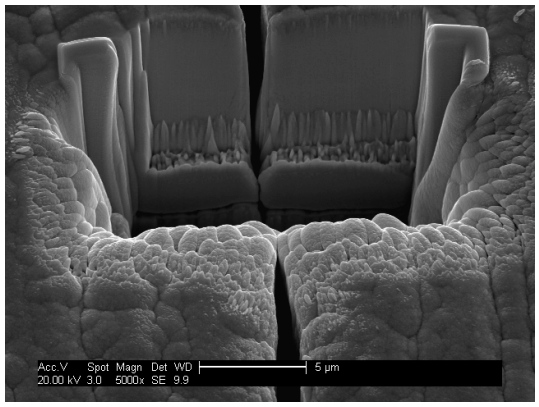

Figure 253 FIB section of a groove on Blz32 after heat treatment (2)

These defects can be solved by changing the surface preparation and roughness, by grit blasting as it will be explained earlier in this chapter. Like the previous tests, the XRD of reacted samples is excellent, showing the presence of the sole α-phase.

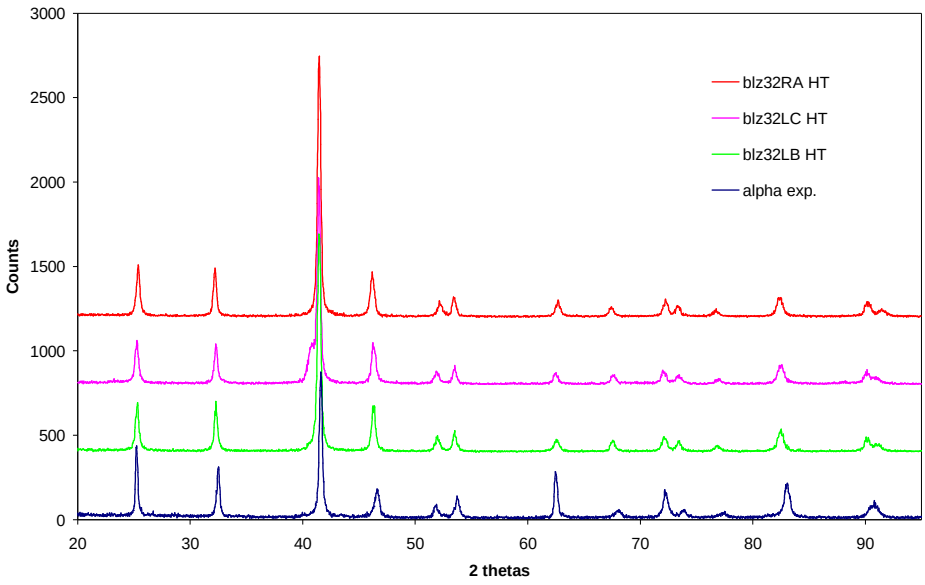

Figure 254 XRD spectra of Blz32 samples after reaction compared with experimental α

V.4.7 Manufacturing of binary intermetallics

Three binary intermetallics were chosen to be manufactured with the low mass bondcoat process, in order to compare ht behaviour of α-phase based system with some references. Two platinum aluminides: $PtAl_2$ and Pt_2Al_3 were manufactured. These compounds were studied by M.Silva and B. Saint-Ramond at Cranfield[209]. The chosen systems are the same as in M. Silva thesis: $PtAl_2$, with a total thickness of 2.5µm and Pt_2Al_3 with a total thickness of 8µm; both systems with the same layer density of 100 layers for 5 µm (hence a total number of layer of respectively 51 and 163). The first and last metallic layers are platinum, the first layer being deposited with the same ion plating process. These systems were manufactured in the batches labelled blz30 for $PtAl_2$ and blz31 and blz40 for Pt_2Al_3, blz40 batch includes grit blasted samples unlike the two others.

Figure 255 Optic pictures of Blz30RC, Blz30LB, Blz31RC and Blz31LB after annealing

As one can see in Figure 255, the reacted coating surface colour is not homogeneous, which can be explained by the non-homogeneity of the formed intermetallic on the surface. Blz30 samples show a grading of grey and amber colours, while Blz31 samples have a grading of grey and pink (as a reminder, α-phase based coating are simply light grey).

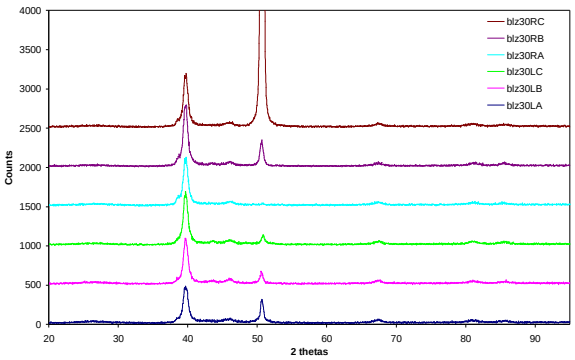

Figure 256 XRD spectra of Blz30 as coated

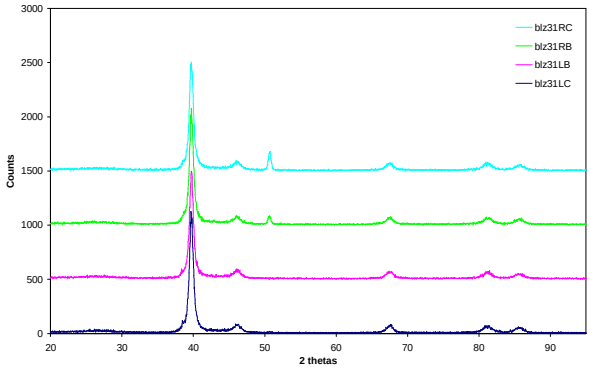

Figure 257 XRD spectra of Blz31 as coated

The XRD spectra of as deposited samples from these batches show that no reaction was triggered during the deposition of the metallic layers during sputtering (Figure 256 and Figure 257). Results are similar for samples from Blz40 batch, and are not shown here, with solely the peaks from the Pt and the Al layers plus the substrate peak, especially for the samples from Blz30 as the coating is only 2.5µm thick.

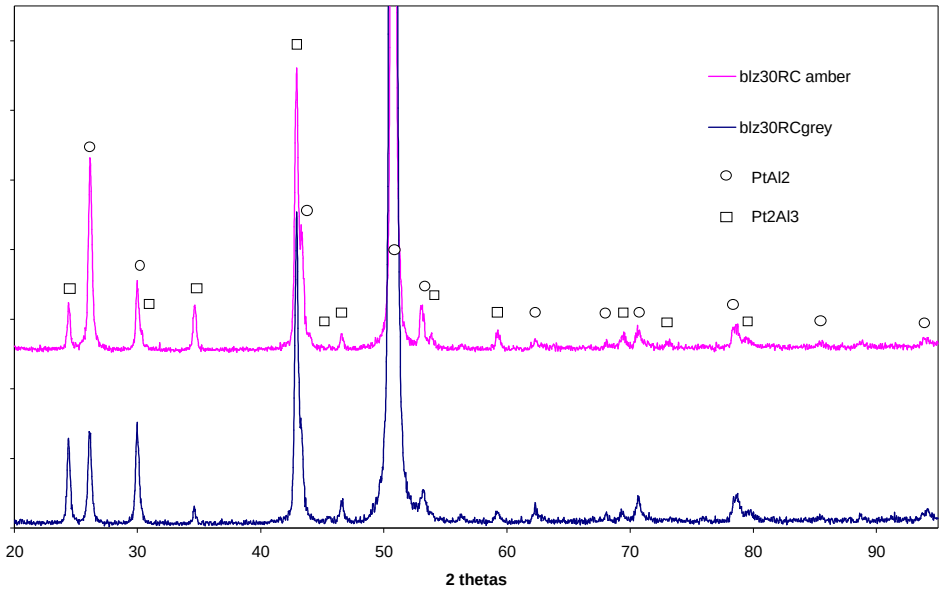

Figure 258 XRD spectra of Blz30RC after reaction on the two area, amber and grey

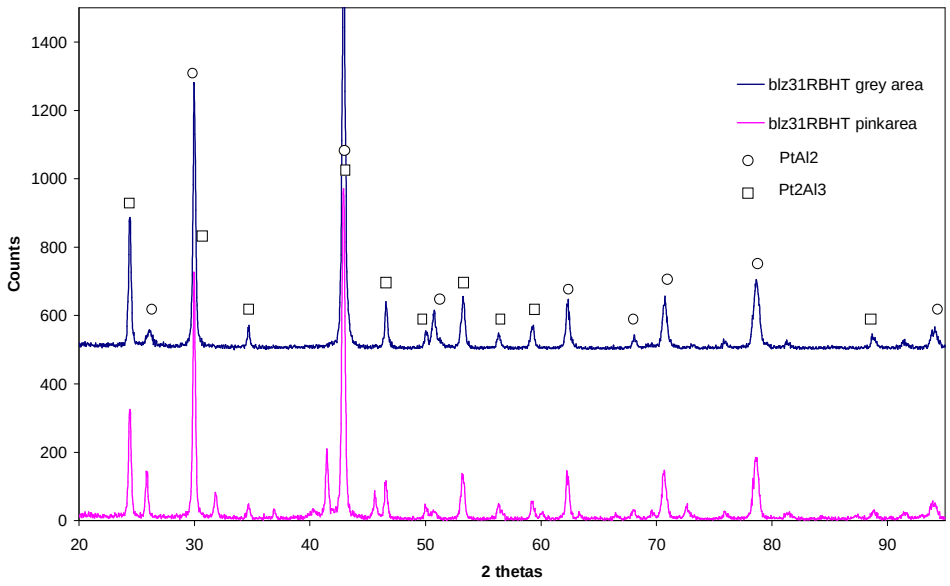

Figure 259 XRD spectra of Blz31 samples after reaction

After reaction the amber and grey area of the samples from Blz30 batch do not seem to correspond to the formation of any different compound. Both spectra show that the coating contains both $PtAl_2$ and Pt_2Al_3 compounds. The XRD analysis of samples from Blz31 batch shows that the pink

area corresponds to a $PtAl_2$ rich area, and that again the coating is biphasic with both $PtAl_2$ and Pt_2Al_3 intermetallics. These results are relevant with the EDS analysis of the surface of Blz31 samples which shows that pink area are richer in Pt.

Table 22 EDS analysis of the surface of Blz31 sample after reaction

Sample	*Blz31RB HT1h@700*		*Blz31LC HT1h@700*		*Blz31RC HT2h@700*		*Blz31LB HT1h@700*	
expected	$Pt_{38.6}Al_{61.4}$		$Pt_{33.3}Al_{66.7}$		$Pt_{32.3}Al_{67.7}$		$Pt_{33.6}Al_{66.5}$	
area	Grey	Pink	Grey	Pink	Grey	Pink	Grey	Pink
Ni[at%]	0.2	0.4	0.3	0.4	0.3	0.4	0.5	0.2
Al[at%]	59	54.6	58.4	51.9	58.7	52.8	51.4	52.3
Pt[at%]	40.8	45.1	41.3	47.7	41.0	46.8	48.1	47.5

This lack of control to form a single intermetallic is likely to be due to the narrow domain of stability of Pt_2Al_3 phase field, as it can be seen on the Al-Pt binary diagram. The EDS analysis of the surface of Blz30 shows that the resulting coating is too rich in Pt hence the presence of the more complex Pt_2Al_3 compound.

The third binary reference binary intermetallic is β-(Ni,Pt)Al; which was fixed on the stoechiometry of $Ni_{40}Pt_{10}Al_{50}$. The alternation is chosen so the first and last layer is Pt, with the pattern: Pt/Al/Ni/Al/Pt/…Ion plating procedure was applied to the first Pt layer. Blz29 and blz37 batches samples were manufactured this way, with a layer density of respectively 200 and 100 layers for 5µm, and grit blasted surface finish in blz37batch. The accuracy of the process on the manufacturing of these samples is much better than binary platinum aluminide, as shown in Figure 260, where the experimental spectrum perfectly match with the NiAl pattern.

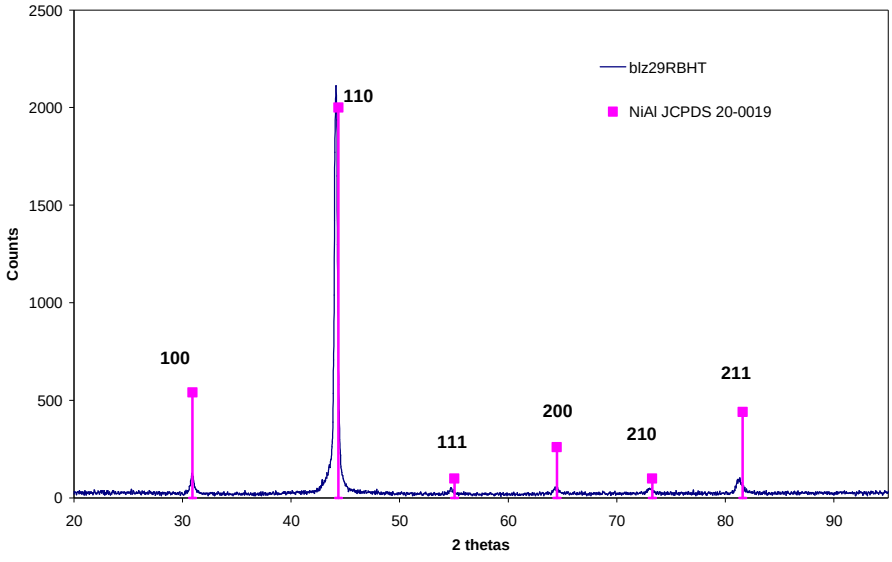

Figure 260 XRD spectrum of Blz29RB after reaction compared with NiAl pattern

V.4.8 Effect of substrate rotation

The manufacturing of coatings on 3D samples generates three main changes on the properties of the coating, due to the rotation itself, or due to the use of another layout inside the chamber with the rotating substrate holder:

- ✓ PVD deposition on a rotating substrate changes its intrinsic microstructure.
- ✓ The rotating substrate holder is fully open, hence the possible pollution from the 2 other plasma during the deposition of a single layer.
- ✓ The movement of rotation is transmitted through a rotating axis feedthrough into the vacuum chamber, increasing the leaks in the deposition atmosphere.

PVD films grown on rotating substrate enhances the columnar growth, as the vapour tends to deposit on the facets of a column when it rotates. This phenomenon is the one used during the deposition of the ceramic topcoat of a TBC by EB-PVD. Three SEM micrographs of the metallic films surface were taken with the same magnification of 50,000X (Figure 261). The columnar growth of Aluminium is clearly enhanced, and will change the activity of an interface with the denser and fibrous microstructure of the platinum film. This difference is not that obvious between the nickel and the platinum films. Calibrations on mono-elemental layers were carried out on NiCr cylinders of 5mm diameter, similar to the AM1 mechanical testing samples.

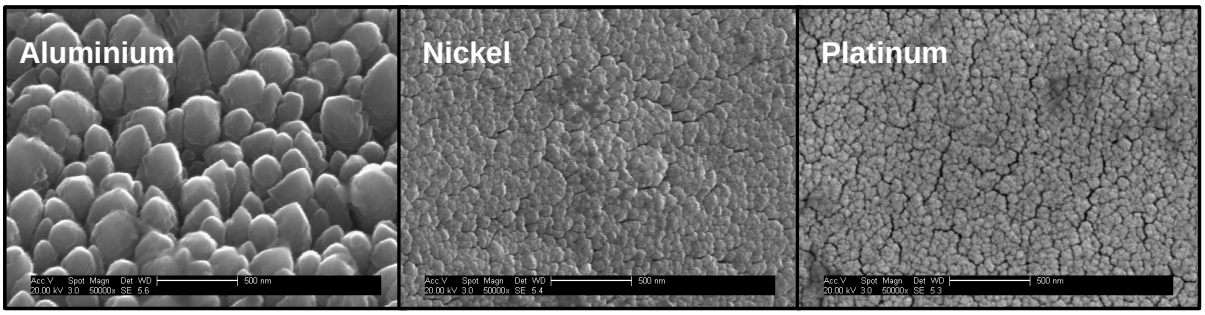

Figure 261 Three SEM secondary electron micrographs at 50,000X of Al, Ni and Pt films surfaces on a rotating substrate

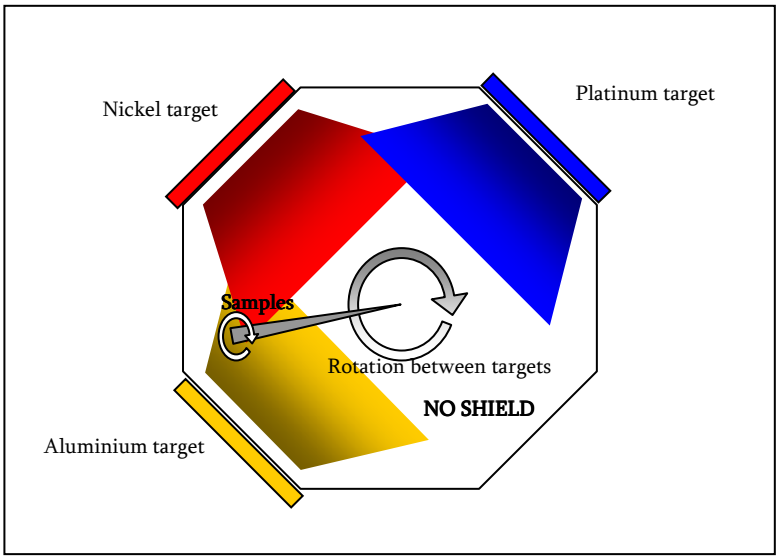

Figure 262 Sketch of the sputtering chamber when fitted with the rotating substrate holder

The layout of the deposition chamber when loaded with the rotating substrate holder does not provide any shield or shutter to prevent codeposition of the two other materials during a deposition. This was measured on calibration runs on dummy cylinder samples, and compared with the an earthing of the substrate holder. Indeed the substrate holder is connected to the DC power supply for ion plating, which, is not connected to the earth when switched off. Therefore a floating bias is induced on the substrate holder by the RF field of the Pt plasma. This induced bias does change the electrical field geometry within the chamber and would influence the codeposition phenomenon.

Table 23 Co-deposition pollution comparison

Target used	*Floating bias substrates*	*Earthed substrates*
Al	No pollution from others	No pollution from others
Pt	Ni: 7at%	Ni: 2at%
Ni	Pt: 4at%	Pt: 1.5at%

There are strong differences in deposition rates between planar and 3D deposition. However, results are rather unexpected, as gathered in Table 24. Deposition rates are compared with the same unit: mass gain per surface per time unit. One would expect the rotation to reduce the resulting deposition rate as the considered surface is not facing the vapour cloud all the time. The drop of Pt deposition rate of 72% is consistent with the usually acknowledged rotation effect. However, Al and Ni deposition rate increase with rotation of the substrate. This can not be explained physically: the amount of pollution form the other target is not consequent enough (it is even nil for Aluminium as proven before), and the increase in surface reactivity due to the curvature of the surface is negligible (and would improve as well

the Pt rate). Moreover, the working distance between the substrate and the target is slightly high when using the rotating substrate holder.

The only rational explanation is that oxygen is co-deposited with Al and Ni during the sputtering of the metal. This fact is confirmed by the pink colour of the plasma during the deposition. This colour is known to be a proof of oxygen presence inside the gas mixture. This colour is triggered when the rotation of the substrate is switched on: the rotating axis feedthrough is a source of leaks, maybe due to an insufficient amount of lubricant. This effect could not be solved by increasing the amount of grease in the rotating parts in contact.

The presence of oxygen was found in the chemical analysis of the as deposited samples of blz33 and blz34 batches.

Table 24 Comparison of deposition rates between planr and rotating substrates

Element	*Pt*	*Ni*	*Al*
Deposition power	350W RF	50W DC	100W DC
Rotating deposition rate compared to planar	72%	130%	146%

V.4.9 Conclusions

- ✓ The developed process does work to make adherent and controlled α-phase coatings on superalloy substrates: this process is "on shelf"
- ✓ Calibration by weight gain proved to be the most relevant for these types of coatings, despite this is not the common use for thin films.
- ✓ This process route was able to produce reproductible α-phase, β-(Ni,Pt)Al, or platinum aluminide coatings, controlled by XRD.
- ✓ High multilayering was successfully used: up to 300 layers were deposited for a coating of 5µm total thickness
- ✓ Grit blasting proved to enhance drastically the adherence of the coating, as a 5 thick layers system did not spall dispite the important interfacial voids at the former Al layers.
- ✓ The weakness of former Al layer after annealing is confirmed by TEM analysis: there is presence of voids and alumina, the oxygen being imported from the sputtering process.
- ✓ The presence of oxygen is more important during 3D deposition as the rotating shaft feedthrough being a source of leaks. This phenomenon plus the codeposition of other metals due to the absence of shutter made the double side coatings difficult, but only inherent to the deposition chamber.

Chapter VI

Isothermal Oxidation

VI.1 Preliminary isothermal oxidation tests

In order to understand the behaviour of an α-phase low mass bondcoat systems at high temperature, isothermal oxidation experiments were carried out. These mainly consisted in exposing the coated samples to an oxidant atmosphere at 1100°C as explained in the experimental procedure chapter. Some TGA experiments were carried out in addition. The first part of this chapter corresponds to experiments carried out on samples produced before the change in deposition procedure described in the previous chapter. It corresponds therefore to low multilayer systems, deposited with relatively high sputtering power, and without ideal composition control.

VI.1.1 Isothermal tests on Blz15 batch

Samples from Blz15 batch have deposition parameters are recalled:

- ✓ Composition is aimed at $Pt_{45}Al_{28}Ni_{27}$ obtained from glass slides/Dektak calibrations
- ✓ 5µm total thickness for 25 layers with the Pt/Al/Pt/Ni/Pt…Ni/Pt alternation pattern
- ✓ Ion plating was used during the deposition of the first Pt layer
- ✓ Deposition power are: Pt=300W[RF]; Ni=140W[DC];Al=350W[DC]
- ✓ Deposition working pressure of Argon is 10mTorr

VI.1.1.1 Analysis of the surface

The samples are cut from the Blz15E sample. This was cut in four parts. All parts were previously heat treated for 2 hours at 700°C in vacuum. The oxidation tests last 1h, 5h, 20h and 50h in a box furnace in laboratory air at 1100°C.

VI.1.1.1.1 Observation

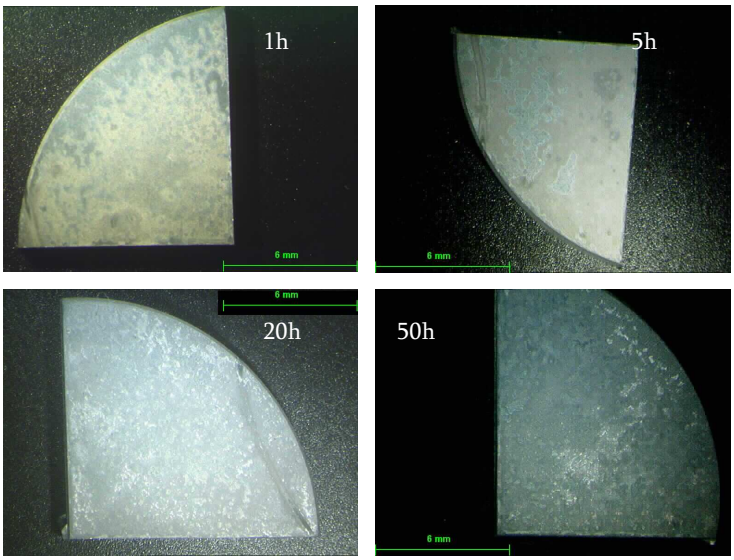

Figure 263 Optical micrograph of Blz15 after 1h, 5h, 20h and 50h of oxidation exposure

The surface is not homogenous for any of the test. The observation with optical microscopy shows islands that looks more oxidised than others (Figure 263). Moreover, some shiny areas suggest some of the oxides had spalled or the coating failed, and that re-oxidation of the spalled area occurred, leading to a thinner newly formed oxide scale (Figure 264 and Figure 265).

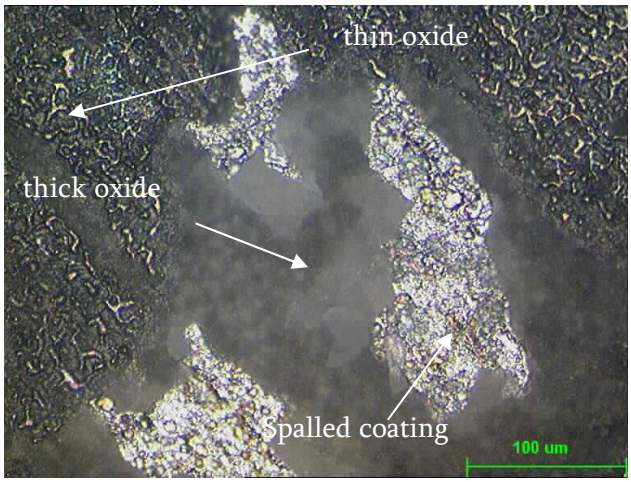

Figure 264 Optical microscope micrograph of BLZ15E oxidised for 50h at 1100°C.

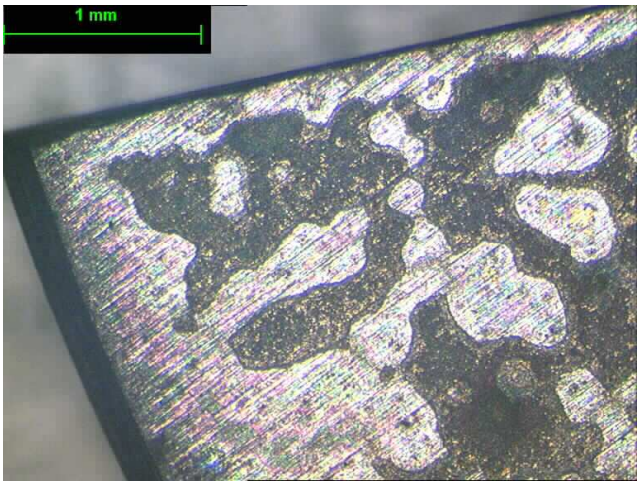

Figure 265 Surface of Blz15Eoxidised for 1h at 1100°C (optical micrograph with grazing light)

The observation of the surface at higher magnification in the SEM confirms this heterogeneity (Figure 266). The dense oxide zone has a cauliflower-like shape that still follows the ridges of the substrate roughness (Figure 267, Figure 269). On the contrary, the other area shows spots, or little mounds, that look like emerging oxide which is likely to spread to a dense layer (see interface between the two area in Figure 268). The microstructure of this dual oxide scale suggests the growth of α-alumina on the bondcoat. Failure of this bondcoats leads to the formation of less protective oxide with the less dense structure observed on the right side of Figure 268.

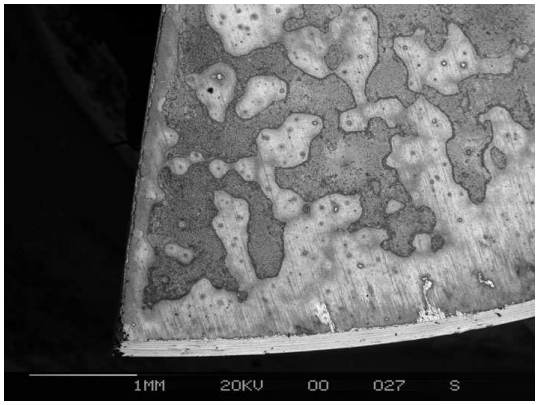

Figure 266 Micrograph of Blz15E oxidised for 1h (general view)

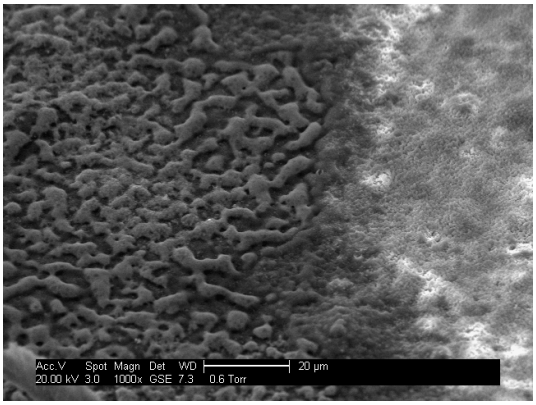

Figure 268 Micrograph of Blz15E oxidised for 20h (zoom2)

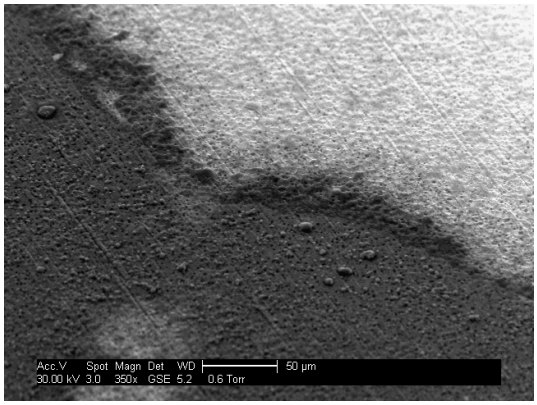

Figure 267 Micrograph of Blz15E oxidised for 1h (zoom1)

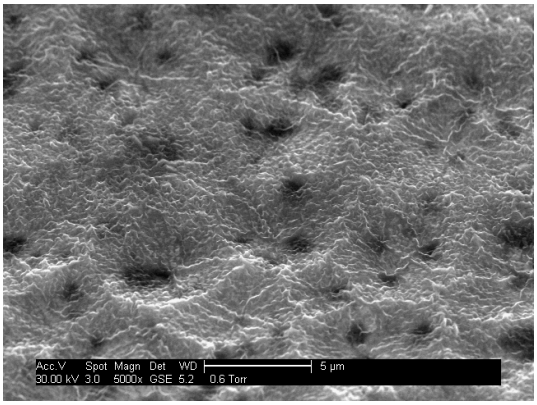

Figure 269 Micrograph of Blz15E oxidised for 1h (zoom3)

VI.1.1.1.2 XRD analysis

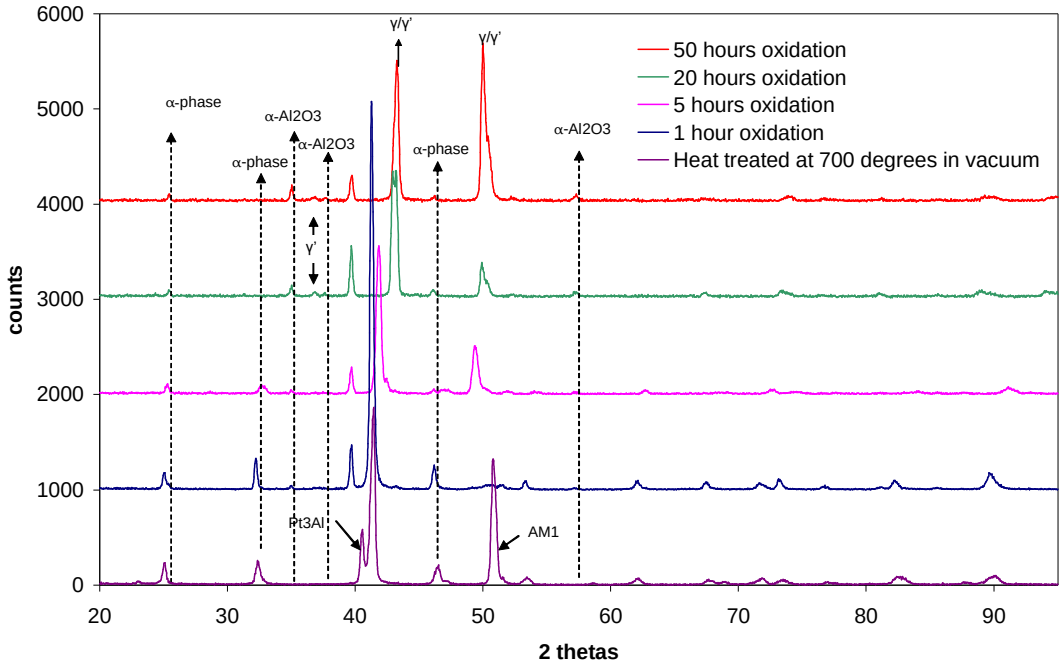

Figure 270 XRD of Blz15E sample as reacted and after isothermal oxidation (1, 5, 20,50h)

The XRD diagrams of the oxidised samples in Figure 270 show an increase of α-Al_2O_3 content with oxidation time, the peaks of alumina appearing already after 1 hour of exposition in air. The α-phase and Pt_3Al content reduce dramatically during ageing, while the peaks of γ and γ' Ni based phases appear after 5hours of oxidation only.

VI.1.1.2 Diffusion profiles and cross sections

VI.1.1.2.1 Cross section

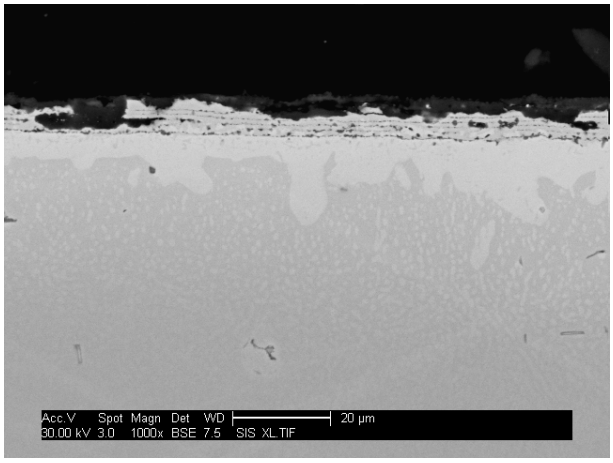

Figure 271 BSE micrograph of Blz15 ox.50h cross section

The observation of the cross section of oxidised samples confirms the partial failure of the multilayer coating. The failure of the coating seems to occur at the former Al layers, which were already identified as weak points of the produced coatings after reaction. The oxide layer is quite thick: between 1 and 2µm after 50h oxidation on the non-spalled zones. The microstructure of the underlying superalloy changes drastically with exposure at 1100°C. A clearer phase seems to form under the coating up to a depth of 25µm into the substrate (see Figure 271). This phase is continuous during the first micrometers, and penetrates preferentially deeper in the substrate thickness (lighter regims). The longer the oxidation time, the deeper the penetration depth of this phase.

EDS was carried out at single points in the substrate. The points are situated at the same depth but in the light or the dark area of the two phases microstructure, highlighted by the BSE mode. This was carried out for sample oxidised for 5h and 50h. These values are compared to the composition of the AM1 substrate. The clear phase, just under the coating, that split into small regions is richer in Al, Pt, Ti, and Ta. On the contrary, the dark phase (which looks more like the deeper substrate) is richer in Cr, Co, Mo and W. This can be interpreted as a Pt modified γ/γ' structure. The γ' phase being rather Ti rich whilst the γ phase is richer in Chromium. This is relevant with the XRD analysis.

Table 25 Comparative EDS analyses of the binary structure in the superalloy after oxidation

Sample	area	Al	Ni	Pt	Cr	Co	Ti	Ta	Mo	W
5h oxidation	clear	8.5	61.7	11.2	3.3	4.2	2.2	7.5	0.0	1.5
	Dark	4.0	61.4	6.5	3.0	8.7	0.3	3.7	0.8	3.4
50h oxidation	Clear	8.9	67.5	7.1	3.0	4.4	1.3	6.4	0	1.6
	Dark	5.1	60.2	6.6	13.0	8.0	0.3	3.5	0.4	3.0
AM1		7.0	67.0	0.0	9.0	7.4	1.5	4.1	1.2	2.9

VI.1.1.2.2 FIB section

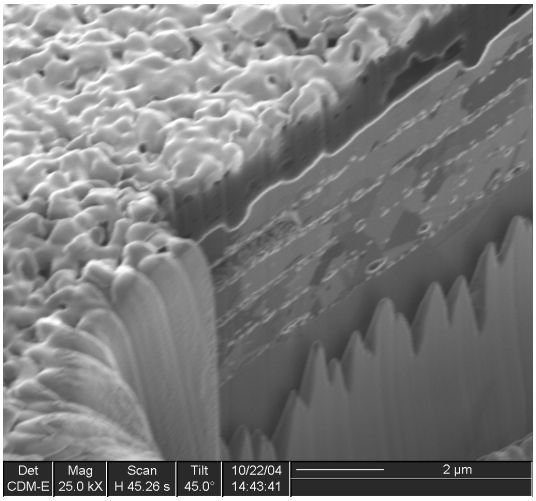

Figure 272 FIB section of blz15 after 20h oxidation

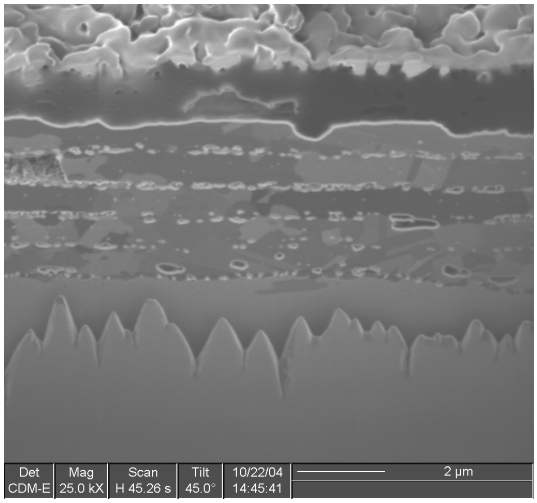

Figure 273 FIB section of blz15 after 20h oxidation (front view)

FIB sections were carried out in the area corresponding to the thick oxide where the integrity of the coating remains after 20h of exposure. The presence of porosities after the oxidation at the "dark interfaces", corresponding to the former Al layer, is clear in these micrographs. The intermetallic coating clearly has re-crystallised: the grain structure of the coating is equiaxial. Although the oxide surface is quite rough and cauliflower like, the oxide is dense in its thickness and doesn't show porosities.

VI.1.1.2.3 Diffusion profile

Diffusion profiles were carried out on the simply annealed coating, and were compared with oxidised samples for each time of exposure. The step between each point is set to 0.5µm, so two consecutive points cover twice the volume of the pear of interaction. The value for the oxygen content is not plotted.

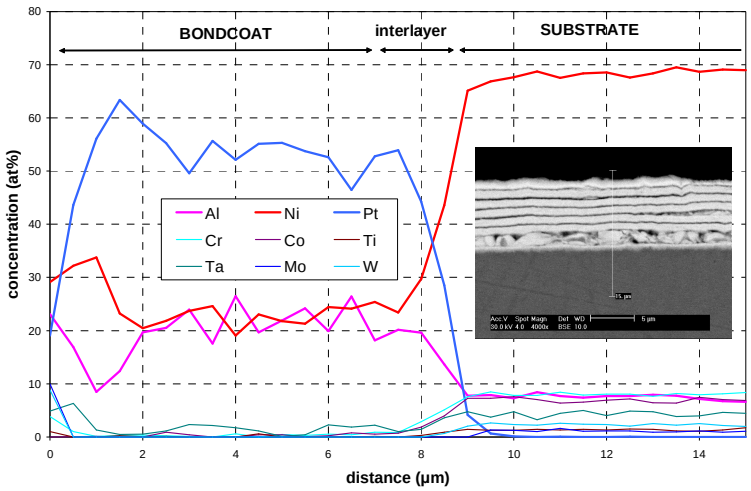

Figure 274 Composition profile of Blz15 after annealing in the vacuum furnace

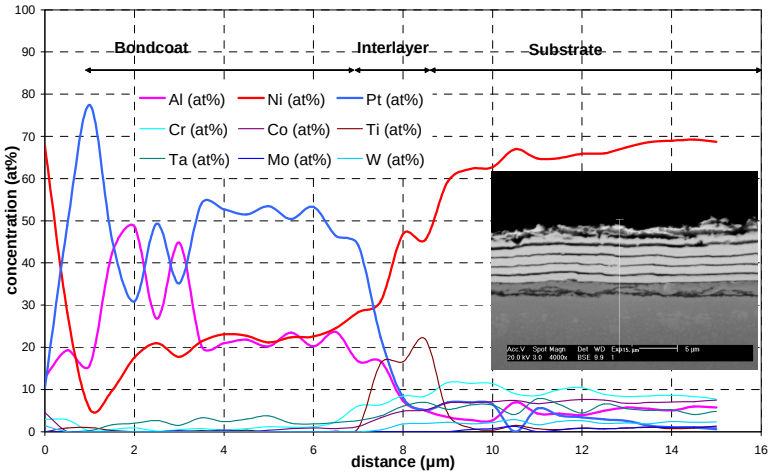

Figure 275 Composition profile of Blz15 after 1h oxidation

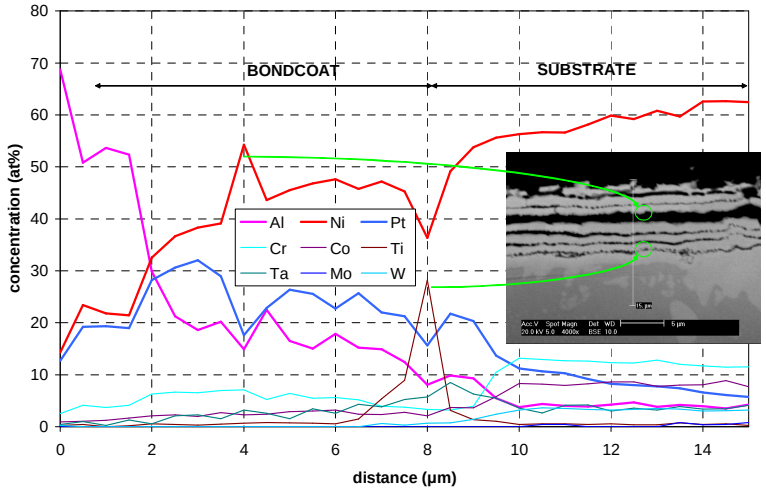

Figure 276 Composition profile of Blz15 after 5h oxidation

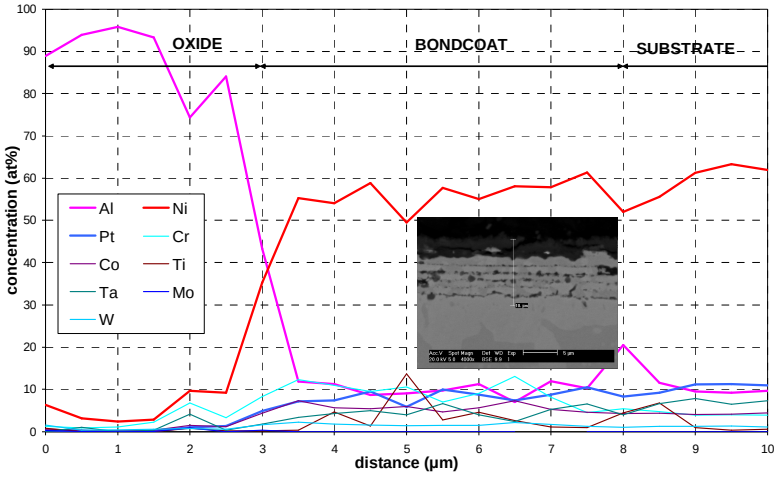

Figure 277 Composition profile of Blz15 after 50h oxidation

- ✓ The interlayer that appears after heat treatment of the multilayers disappeared between the 1hour and the 5 hours oxidation tests.
- ✓ The alternation of dark/light areas at 1µm in the bondcoat can be seen on the digipoint of the 1 hour oxidised sample: the darker region corresponds to an aluminium rich zone (Ni/Pt/Al ratio of 18/32/50 which might corresponds to the presence of β-(Ni,Pt)Al), the light areas being richer in Pt(at 2.5µm the proportion is $Pt_{50}Ni_{22}Al_{27}$, which is roughly corresponding to α).
- ✓ Between 3.5 and 6µm from the surface of the 1 hour oxidised sample, the composition is quite steady, at Pt55Ni23Al22 which correspond to the bottom end of α phase field on the ternary diagram.
- ✓ After 5 hours of oxidation, the proportion of Ni in the coating increased massively, while Pt goes far deeper into the substrate (more than 5 at% at 15µm from the surface, compared with less than 1at% after only 1 hour of oxidation)
- ✓ After 50 hours of oxidation, the loss of Pt and Al is dramatic, the bondcoat having a homogeneous composition with more than 55at% of Ni.
- ✓ The digipoint of the sample oxidised for 5 hours shows a high concentration of Ti at the interface between the overlay bondcoat and the substrate.
- ✓ The interdiffusion of other elements from the substrate is quite significant, in particular Ta that appear even before starting the oxidation. Only the proportion of Mo is nil within the bondcoat after 50 hours oxidation.

VI.1.1.3 Discussion

The exposition at 1100°C of the reacted layers on AM1 did not give the expected behaviour at all. The alpha phase was expected to act as a diffusion barrier towards the elements from the substrate, but both refractory elements and nickel diffused rapidly into this bondcoat. Moreover, the platinum diffused rapidly into the substrate. This interdiffusion, and the depletion of aluminium to form the oxide layer resulted in a rapid shift of the Pt_3Al/α system to a γ/γ' structure under the oxide. The light phase in the substrate is likely to be γ': the EDS analysis confirms the Ni_3Al stoechiometry, and the solubility of chromium into Ni_3Al is known to be poor.

During Manuel Silva's work, the ageing of a $PtAl_2$ Low Mass Bondcoat lead to a stable alpha composition. These results suggested that the manufactured system was to "far into" the $PtAl_2 \rightarrow \alpha$ ageing, shifting very rapidly to a γ/γ' system. It would therefore be very interesting to work at lower nickel content in the multilayer system. This suggestion lead to the manufacturing of samples Blz22 to Blz25, which resulted in a very poor adhesion as was described in the previous chapter.

VI.1.2 Thermogravimetry experiments

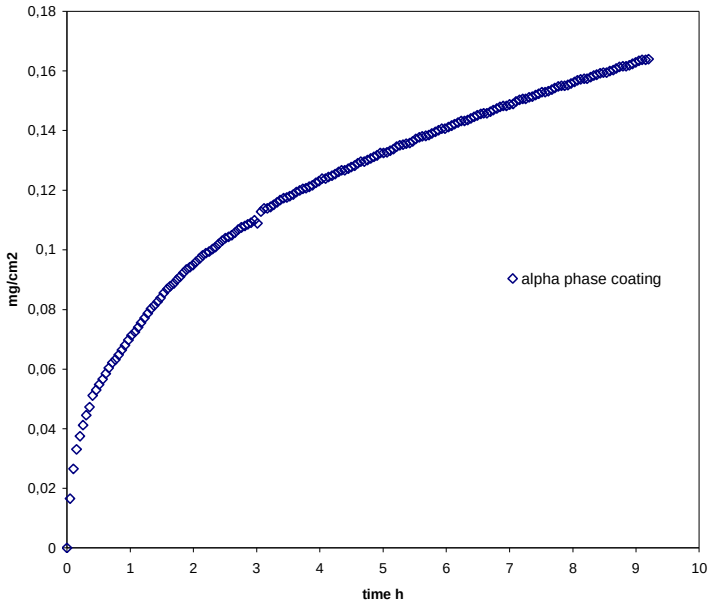

Figure 278 TGA curve of Blz 20 sample at 1100°C in air

As explained in the chapter 5, only few samples with rotating substrates were manufactured. However, some TGA was carried out on alpha phase coated samples were carried out in order to evaluate the isothermal kinetic of oxidation. Small discs of AM1 were loaded in Blz20 batch (25 layers and 5µm total thickness). These were then heat treated under vacuum for 2 hours at 700°C and loaded in the TGA for isothemral oxidation in air at 1100°C (Figure 278). Morevover, some difficulties in control of the TGA facility were encountered, especially due to the temperature varations in the room.

The weight gain curve shows a typical parabolic growth mode. The constant of parabolic growth, Kp, was calculated by two methods: an apparentl Kp corresponding to the overall weight gain and a local Kp corresponding to the kinetic during the steady state growth. Local Kp is $2.68.10^{-7}$ $mg^2cm^{-4}s^{-1}$ and apparent Kp is $1.34.10^{-7}$ $mg^2cm^{-4}s^{-1}$.

These values are to be taken precautiously as only few samples were measured. Kinetic values are quite high compared to other bondcoat systems, such as β-(Ni,Pt)Al, whose typical growth rate is approximately 8.10^{-8} $mg^2cm^{-4}s^{-1}$.[100]

VI.2 High multilayered systems

Isothermal oxidation tests were carried out on samples from batches Blz26, Blz27 and Blz28. These batches consist of α-phase composition, with high multilayering (respectively 100, 200 and 300 layers for 5µm total thickness), and a better control of the adhesion and the deposition process. The surface finish of all these samples is ground to 600 grit.

As previously, one sample of each batch is cut in 5 parts, each exposed in a box furnace at 1100°C in air to study the oxidation.

VI.2.1 Surface analysis

VI.2.1.1 Observation

The oxidised surface is very similar for each sample of the three batches. It was observed under ESEM after 1h and 50h of isothermal oxidation. The four pictures below show the microstructure of the surface of the scale of Blz28 sample at 1000x and 5000x magnification for both times of exposure.

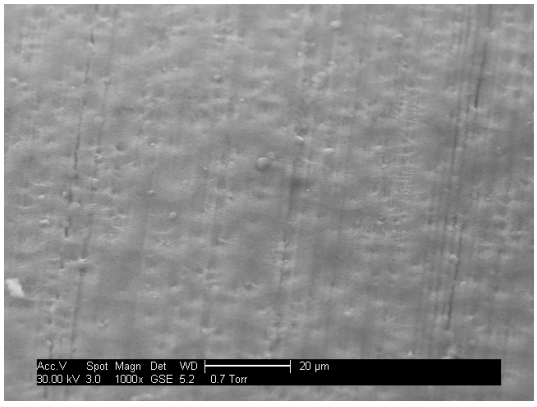

Figure 279 Blz28 surface after 1hour oxidation (x1000)

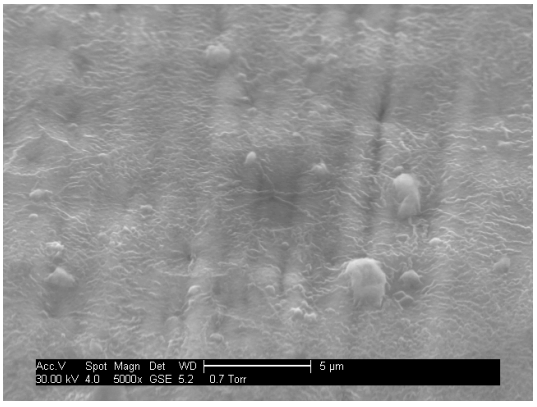

Figure 280 Blz28 surface after 1hour oxidation (x5000)

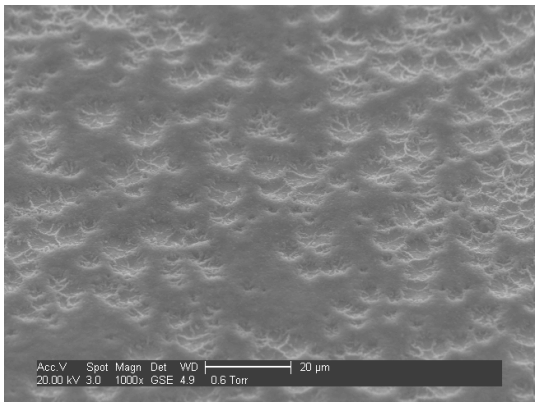

Figure 281 Blz28 surface after 50hours oxidation (x1000)

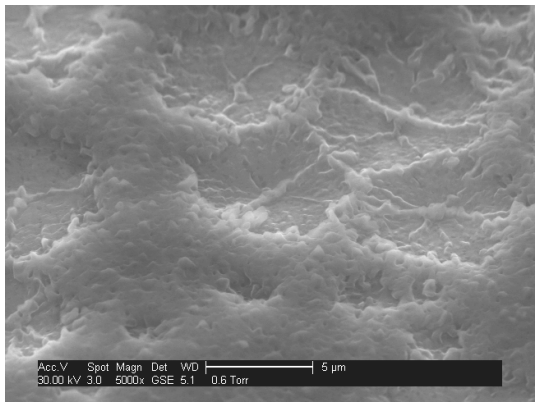

Figure 282 Blz28 surface after 50hours oxidation (x5000)

After 1 hour of oxidation only, no needle shape growth is observed. This growth mode is usually associated with the presence of fast growing transitional alumina. On the contrary, the scale is rather dense, except for the presence of periodic star shaped indents. These indents have already been observed on some oxidation tests of NiAl samples[81;91;121], and correspond to the transformation θ->α alumina. The remarkable result of these observations is that the transformation has already occurred after 1 hour at 1100°C; it usually takes between 5 to 10 hours at this temperature to get this transformation on platinum aluminide coatings. This effect is either due to the intrinsic properties of the intermetallic α-phase, or due to the surface finish, which is rougher than usual for oxide growth studies.

After 50 hours of isothermal oxidation, the number of these indents per surface area stays constant, but these indents are more marked. This shows that the creation of these indents occurs at the very beginning of the oxidation stage. The increase in contrast between these marks and the dense scale are likely to be due to a thickening of this denser part of the scale.

VI.2.1.2 XRD analysis

Analysis of the oxidised samples with XRD confirms the observation of the surface of the scale. The behaviour of the three types of samples is similar (Figure 283), with the presence of α-Al_2O_3 after 1 hour of oxidation only. The α-Al_2O_3 peaks get more intense after 50 hours of oxidation due to the thickening of the scale. No trace of θ-Al_2O_3 could be found in these analyses, even when a logarithmic scale is used.

The most impressive result is the total loss of signal from the intermetallic α-phase after 1 hour of oxidation only. This occurs whatever the properties of the film: number of layers, texture (stronger for low number of layer) or presence of some Pt_3Al in the film (for lower multilayers).

Instead of the pattern of the α-$NiPt_2Al$ $L1_0$ lattice, the pattern of the $L1_2$ lattice corresponding to γ'-Ni_3Al is observed (Figure 284). However, the diffraction pattern of Ni_3Al is slightly shifted towards lower angles, implying an increase of cell size, likely to be due to the substitution of Pt on the Ni sites of the lattice. For instance, for Blz28, after the first hour of oxidation, the cubic Ni_3Al lattice has a parameter of 3.635Å instead of 3.572Å.

After 50 hours of isothermal oxidation (Figure 285), the α-Al_2O_3 peaks are more intense, and the Ni_3Al lattice reduces in size, probably due to the decrease in Pt concentration in this lattice. No trace of other oxides nor intermetallic compound was found (peaks of γ-Ni, might be present but hidden by other peaks).

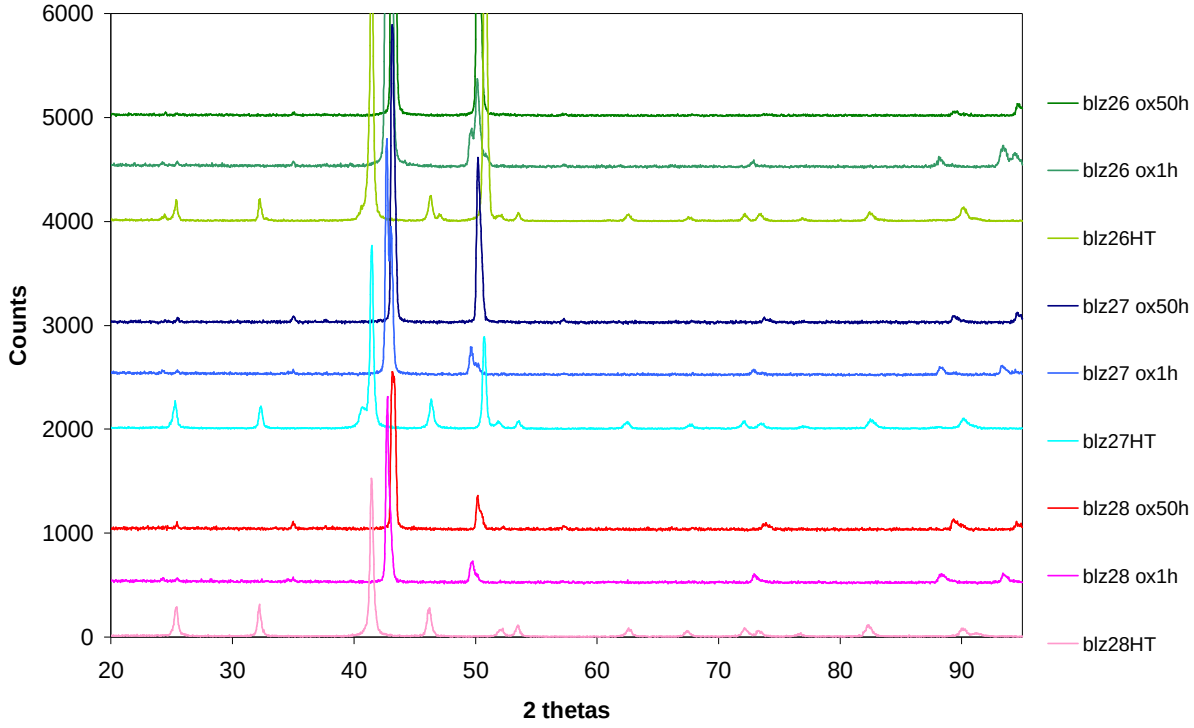

Figure 283 XRD spectra of blz26, blz27 and blz28 samples after isothermal oxidation

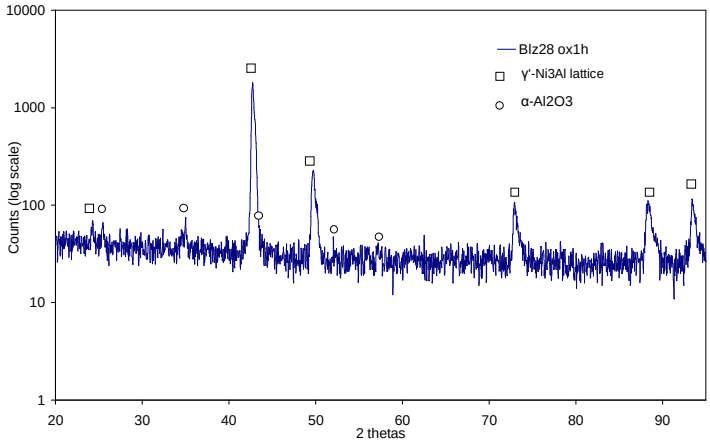

Figure 284 XRD using a log scale of Blz28 after 1 hour isothermal oxidation at 1100°C in air

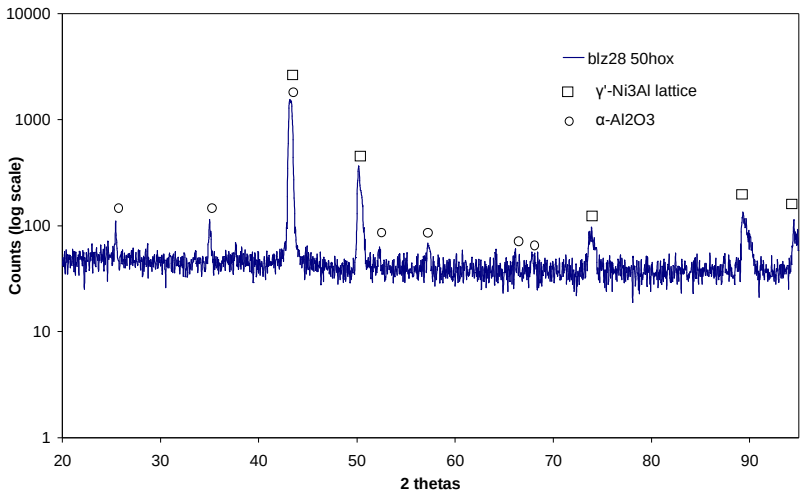

Figure 285 XRD using a log scale of Blz28 after 50 hours isothermal oxidation at 1100°C in air

VI.2.2 Cross section and diffusion profiles

VI.2.2.1 FIB cross sections

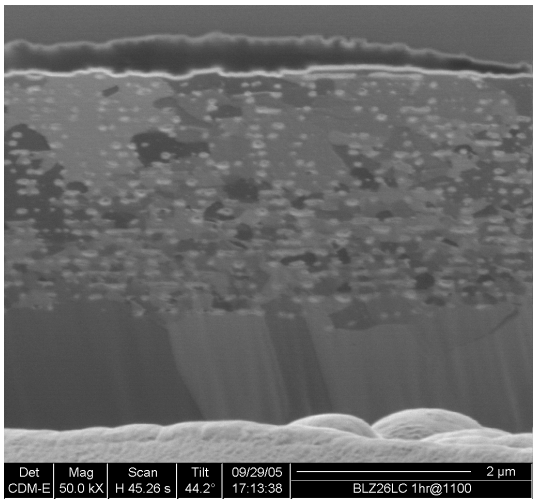

Figure 286 FIB section of blz26 oxidised 1hour (100 layers system)

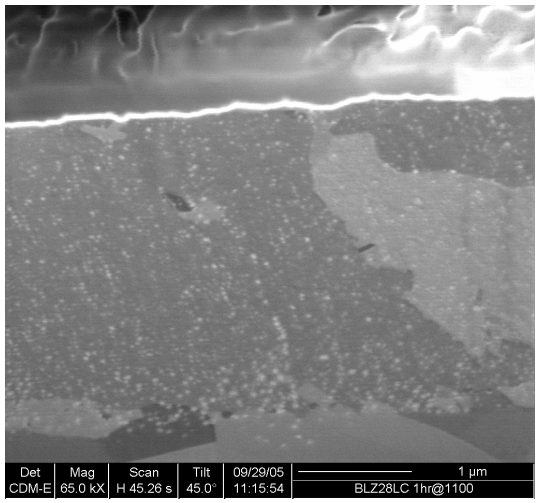

Figure 287 FIB section of blz28 oxidised 1hour (300 layers system)

The observation with the FIB of oxidised higher multilayer systems is relevant with the previous experiments on low multilayer systems. Very regular voids are observed within the coating after 1 hour of oxidation only (Figure 286). These voids occur at the former Al layer interface. The size of the void is proportional to the actual thickness of the original metal layer. The dispersion is therefore very fine on a 300 layer system (Figure 287).

Analysing these micrographs with image analysis software results in void size of 200nm for blz15, 60nm for blz26 and 20nm for blz28. These sizes correspond very closely to the original thickness of the Al layer in the as deposited systems: in order to obtain 5µm of α-$NiPt_2Al$ phase, the total thickness of deposited Al is 1.437µm respectively divided by 5, 25 and 75 which are respectively the number of alternation pattern for blz15, blz26 and blz28.

Increasing the oxidation exposure time does not change the size nor the distribution of these voids (Figure 288 and Figure 289). Only the thickness of the oxide scale changes. The equiaxed re-precipitation of grains within the overlay coating was already observed after 1 hour of oxidation only.

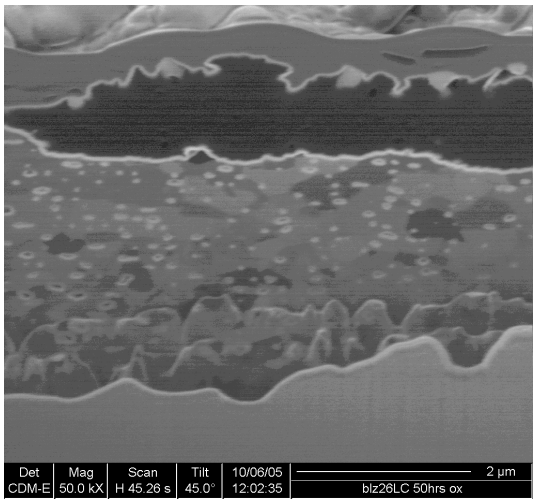

Figure 288 FIB section of blz26 oxidised 50hours

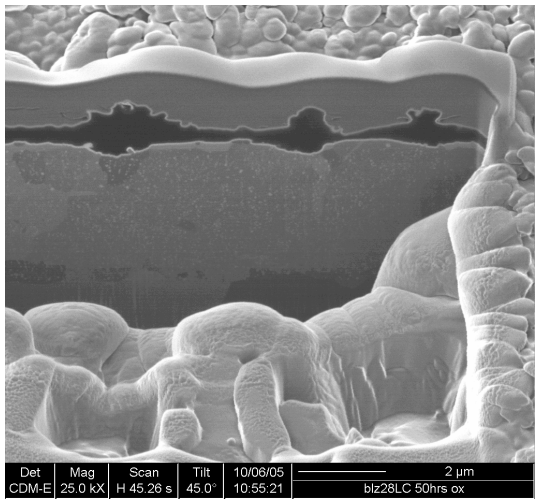

Figure 289 FIB section of blz28 oxidised 50hoursComposition profiles

As for Blz15 samples, the evolution of the chemistry of the coating+superalloy system was measured by EDS. The diffusion profiles were carried out for each sample with a 0.5µm step for the as reacted samples and after 1hour and 50hours of isothermal oxidation at 1100°C. Only composition profiles of Blz28 are shown, as Blz27 and Blz26 behave exactly the same.

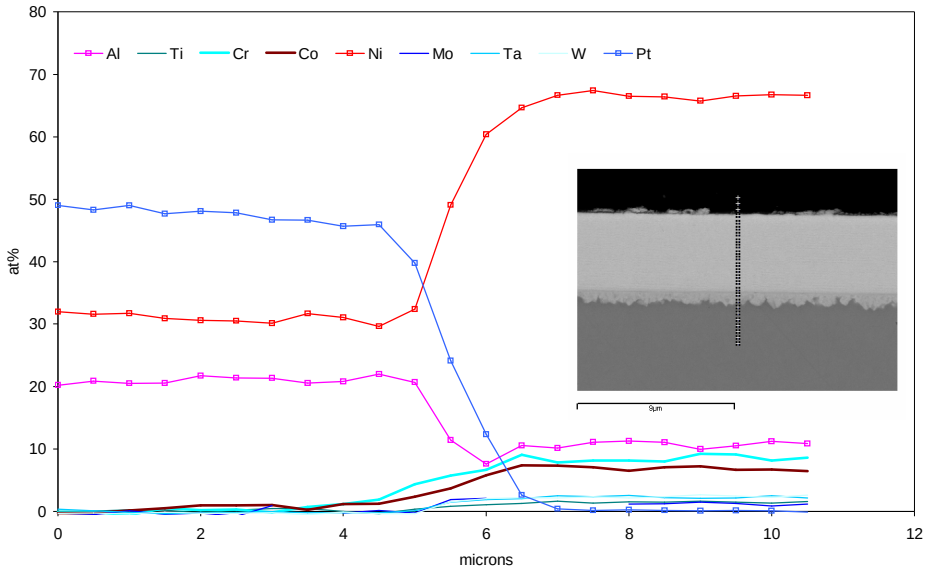

Figure 290 Blz28 as reacted composition profile

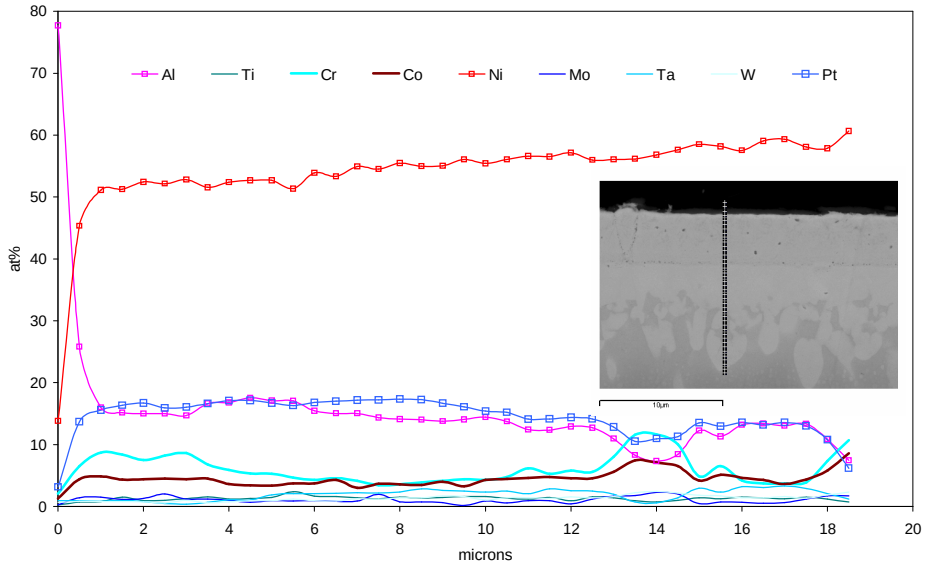

Figure 291 Blz28 composition profile after 1h of oxidation at 1100°C

As one can see on the samples after heat treatment only, the internal profile of concentration are quite steady, respecting the α-phase stoechiometry. However, the Al content is always below the expected 25at%, which confirms the chemical analysis of the surface of these samples.

Here again, after 1 hour of exposure, the composition changes dramatically, with a "flattening" of the Pt and Al curves. Platinum diffuses extremely rapidly into the substrate. Aluminium diffuses to the substrate too (slight enrichment of the superalloy), and is as well pumped to the surface for the formation of the alumina scale. The number of layers does not make any difference, except maybe less scattering on the data when the layer density is higher. Refractory elements diffused as well into the coating, after 1 hour of oxidation only.

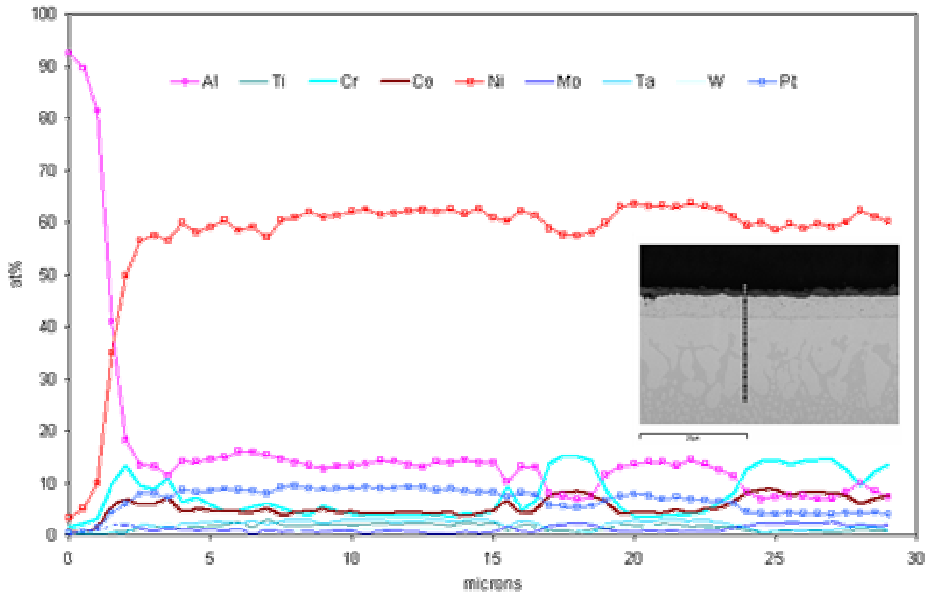

Figure 292 Blz28 composition profile after 50h of oxidation at 1100°C

The composition shifts to a Pt modified γ' intermetallic. Some Pt modified γ-Ni is observed in the coating after 50hours of oxidation. The higher concentration of Cr is typical from the γ-Ni phase. This α→γ'→γ transformation can be outlined by plotting the Ni/Pt/Al ratio across the section on the ternary diagram at 1100°C.

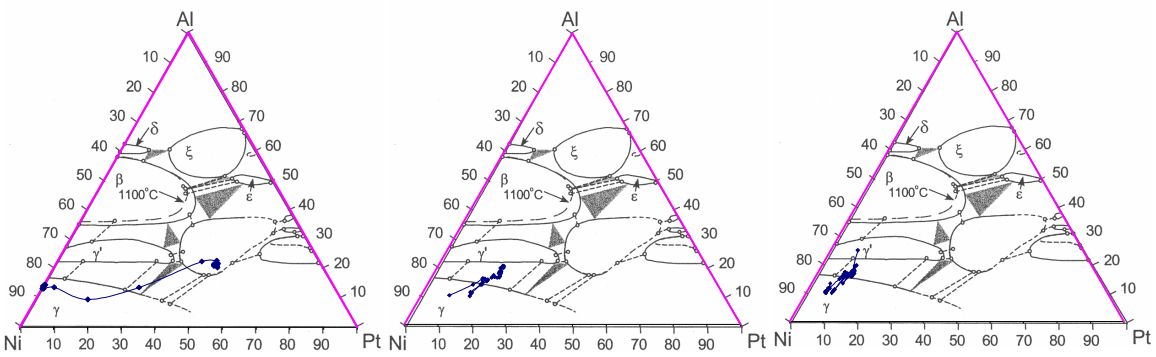

Figure 293 Plot of Pt/Al/Ni concentration profiles on the ternary diagram as reacted and after 1h and 50h of isothermal oxidation on Blz28

VI.2.3 TEM analysis

VI.2.3.1 Microstructures observation

Observation and analysis of a TEM section of Blz28 after 50h of oxidation was performed in order to have a better understanding of the system evolution during isothermal oxidation exposure.

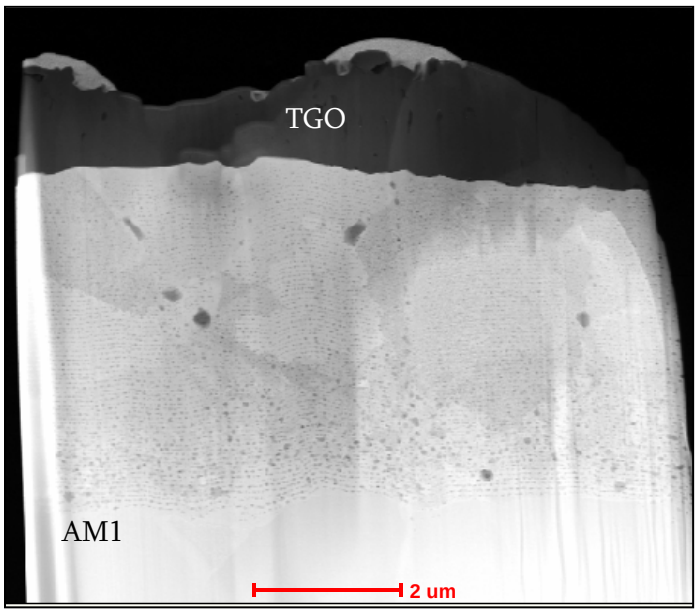

Figure 294 Global microstructure of Blz28 after 50h oxidation (HAADF)

A global view of the section shows the system: superalloy+coating+oxide scale+Pt protective strip. One can notice the columnar growth of the oxide to a thickness of roughly 1.5µm. The coating exhibits interlayer defects following the original multilayer pattern. The coating shows a grain reprecipitation which corresponds to the $\alpha \rightarrow \gamma' \rightarrow \gamma$ degradation. The presence of large defects (≈200nm diameter) is as well observed inside the intermetallics grains. The superalloy/coating interface seems to be defect free.

The observation of the coating in TEM mode gives a better topographic view of the degraded coating than scanning TEM. The regular defects have a significant volume and display a cauliflower like strucure. These defects have an ellipsoidal shape in the micrograph, which could correspond in 3D to a "pancake" shape, with two long spreading directions and a short direction, normal to the sample surface. The measured size of these defects is typically 20 to 34nm in the normal direction of the sample surface. The spacing between these defects is very constant: between 37 and 44nm. These measurements were carried out by image analysis.

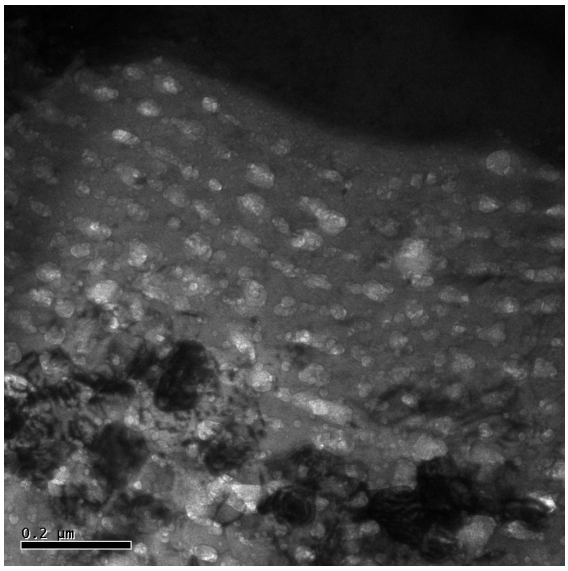

Figure 295 Interstitial defects (TEM mode)

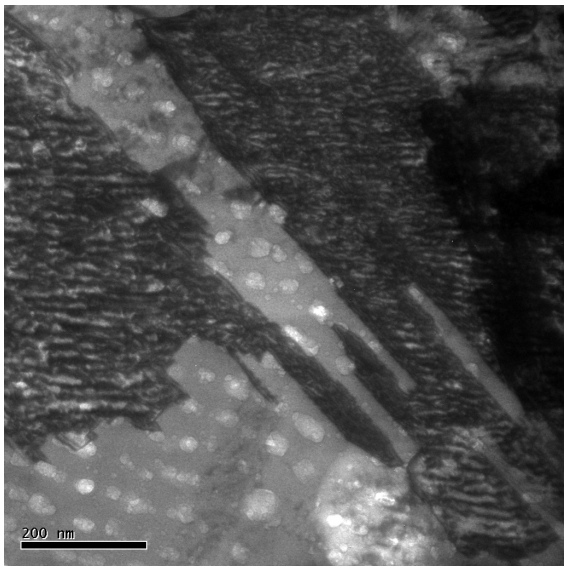

Figure 296 Grain boundary artefacts (TEM mode)

The measured size for these defects is consistant with the original alternation pattern of the metallic multilayers (Figure 297). The measured distance between the middle of two defects (between 57and 76nm) fits perfectly with the distance between the middle of two consecutive Al layers. On the other hand, the thickness of the intermetallic (comprised between 37 and 44nm) corresponds to the thickness of the layers between two consecutive Al layers minus the 10% of volume shrinkage due to the transformation into α.

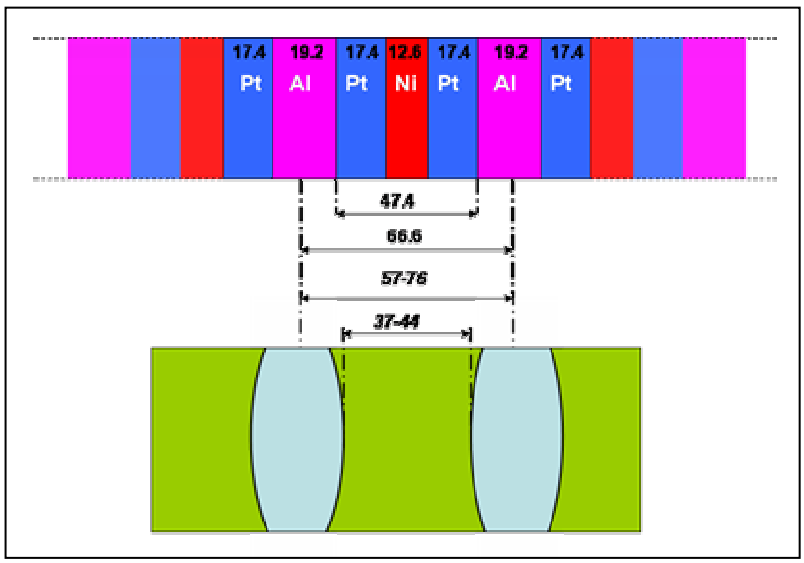

Figure 297 Defects size compared with deposited multilayer (values are in nm, values in italic are experimentally measured while normal ones are calculated from deposition calibration)

The Figure 296 from the TEM shows some Moiré fringe artefacts. These are only due to the fact that the section is not perfectly flat, inducing the electron to cross two grains with various orientations, creating this interference effect. These zones move when the orientation of the sample is changed.

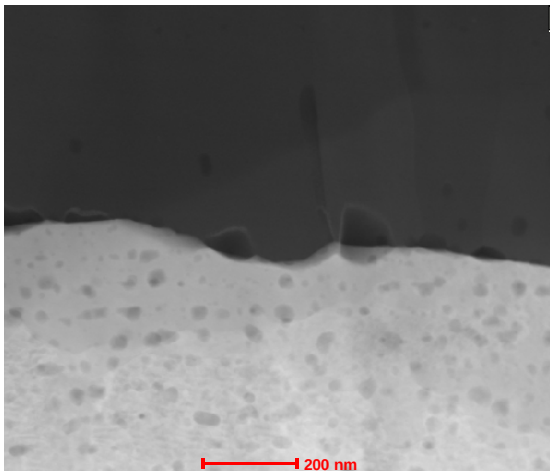

Figure 298 Metal oxide interface (STEM HAADF)

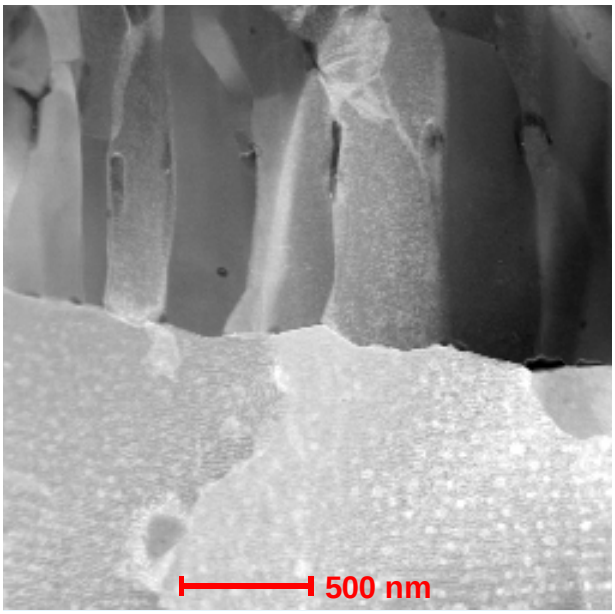

Figure 299 Alumina scale (Dark field)

The oxide scale exhibits a columnar structure (Figure 299), with grain width between 100 and 400nm. Porosities between these columns are observed, as well as porosities between the scale and the coating (Figure 298). The interface porosities is associated with some oxide pegs. These porosities likely come from the early transformation of the alumina from transient alumina to α alumina. The volume shrinkage associated with these transformations typically leads to pores at the metal/oxide interface. The small size of these porosities (below 100nm in height) confirms the rapid shift from the system to a stable α-alumina growth mode, consistent with previous XRD observations.

VI.2.3.2 Concentration profiles

Chemical analysis of the interlayer defects clearly shows the presence of alumina with an increase of both Al and oxygen content (Figure 300 and Figure 301). With regard to previous observations of the FIB sections of the coating after reaction and oxidation, these defects are voids (created by the volume shrinkage during the intermetallic formation), which are therefore internally coated with alumina. The oxygen is suspected to come from the sputtering stage as this high level of oxygen was already observed prior to exposure to air at high temperature.

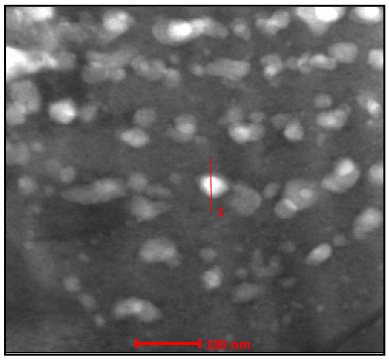

Figure 300 Profile on interlayer defect (bright field)

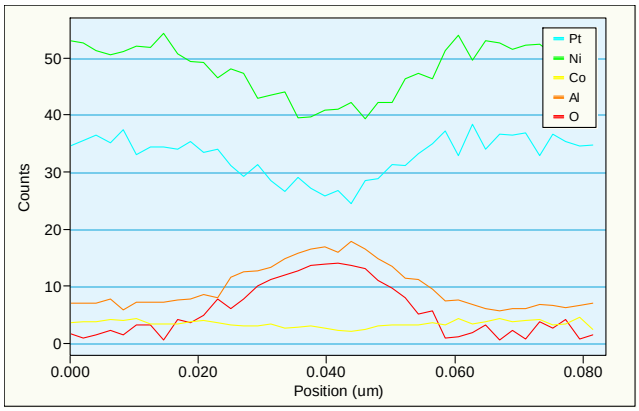

Figure 301 Profile on interlayer defect

The coating/superalloy interface is clear from microstructural defects (Figure 302). Moreover, no specific chemical segregation was observed (Figure 303) confirming the excellent bonding between the coating and the superalloy. The first nanometres of this composition profile confirm the presence of alumina in the interlayer defects.

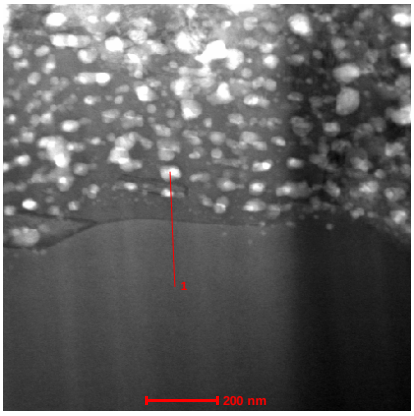

Figure 302 Coating/AM1 interface (bright field)

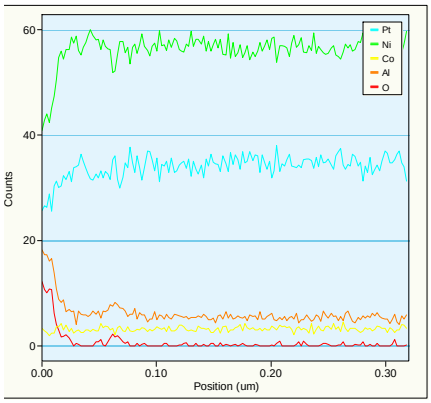

Figure 303 Coating/AM1 concentration profile

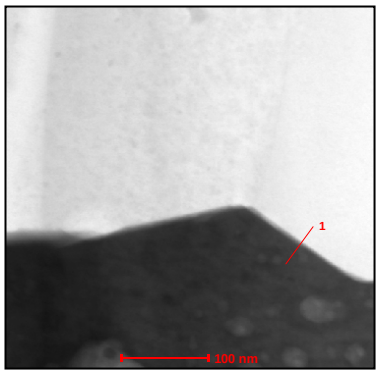

Figure 304 Metal/oxide interface (bright field)

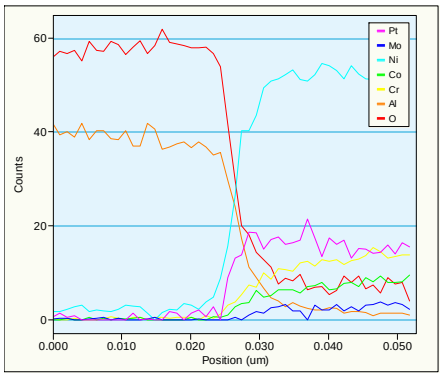

Figure 305 Profile at the metal oxide interface

The analysis of the coating/oxide interface shows no specific segregation (Figure 304 and Figure 305). Sulphur for instance was not observed at the interface. One can notice that elements from the substrate reached this interface, such as Cr, Co or Mo. The concentrations of Co, Mo and Cr are compatible with the presence of a γ type alloy at this interface (see next analysis on γ/γ' interface within the coating). Oxygen is also observed dissolved in this layer.

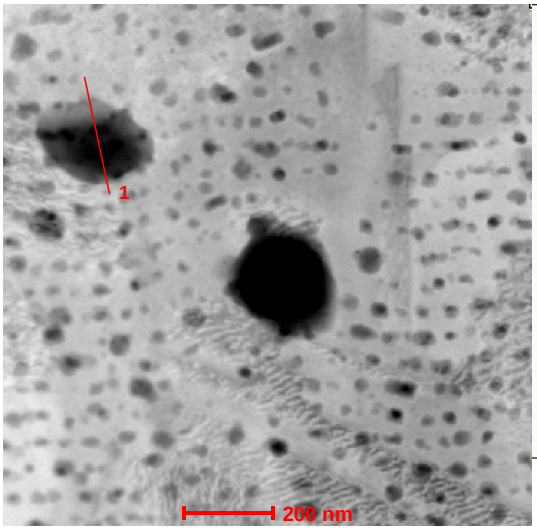

Figure 306 HAADF picture of the large defects

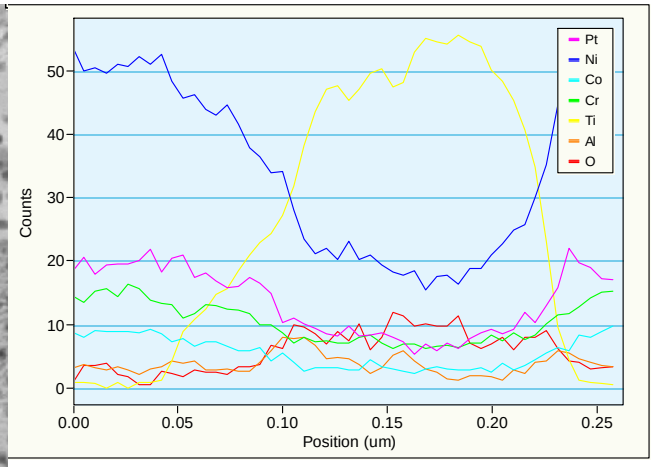

Figure 307 Profile over a large defect

Some large intra-granular defects (150 to 200nm) are observed within the degraded coating (Figure 306). The Moiré fringes on the edge of these defects suggests they partly overlap the γ/γ' grains. The chemical analysis of these defect shows they are Ti rich particles, but not exclusively Ti oxide particles, possibly partially oxidised TiN particles. The AM1 superalloy is very rich in Ti compared to other superalloys. TiN can form at high temperatures due to solution of N_2 into the alloy. These oxidise and Ti oxides are observed on the surface of oxidised samples after 200h of cyclic oxidation.

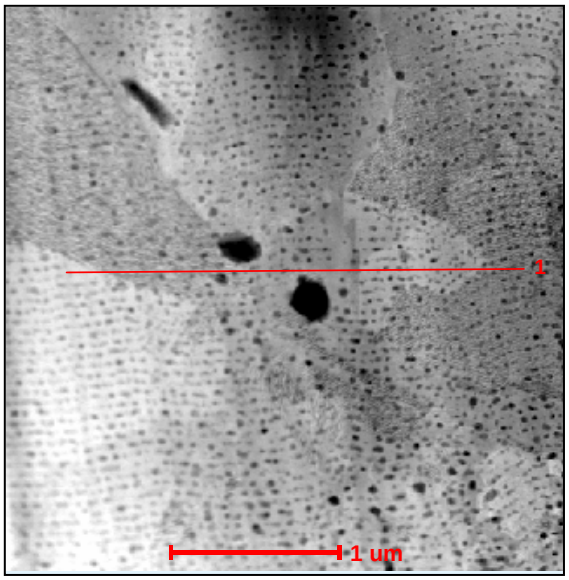

Figure 308 Trans-grain profile (HAADF)

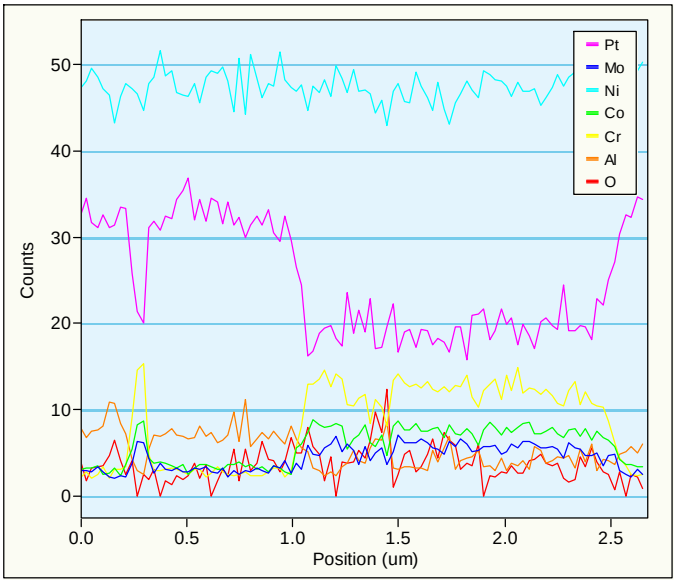

Figure 309 Concentration profile across various grains

The last composition profile was carried out across an intermetallic grain within the degraded coating (Figure 308 and Figure 309). In HAADF mode, the atomic contrast is equivalent to backscattered mode in the SEM: the clearer the heavier the element (this profile was taken from the right to the left). The degraded coating exhibits a typical Pt modified γ/γ' structure: Cr has a poor solubility in γ', whereas platinum can dissolve in γ' up to 35at% at 1100°C (Gleeson ternary diagram), which is consistent with the concentration profile. This is as well confirmed by the Mo profile: Molybdenum is a typical solid solution strengthener of the γ matrix in superalloys. It is found in here alongside Cr. The Moiré fringes effect is proven to be an artefact on this profile again, as no change can be seen on the γ phase zone.

VI.2.4 Conclusions and discussion

The analysis of Blz26, Blz27 and Blz28 behaviour under isothermal oxidation leads to important results. First, for these highly multilayered systems, the number of layer does not seem to play an important role regarding to their decomposition mechanism. Secondly, this study shows that although α phase coatings were successfully produced, with a good covering of the superalloy and a very homogeneous composition of the coating after manufacturing (i.e after annealing), this phase is not stable in contact with AM1, a nickel based single crystal superalloy, at high temperature. This fact is due to the important difference in chemical activities at the

coating/superalloy system. The Ni based superalloy act as a pump for Pt, leading to an extremely fast shift towards a Pt modified γ/γ' system and to a flattening of the composition profile. The diffusion of Al into the substrate and its consumption to form the alumina scale increases this phenomenon. This raises an issue of interest related to the manufacturing of such a complex system when electrodepositing Pt followed by a diffusion treatment is enough to form such a system (the low cost bondcoat). Does the new manufacturing method permit modifications to the γ+γ' bondcoat system or is the interest only economical, as it avoids the patent which protect this process?

Nonetheless, the α-phase low mass bondcoat has intriguing and unique properties, which could modify the lifetime of these systems for high temperature oxidation protection. First, during the early stage of the oxidation: no transient alumina was ever found, when observed by XRD (even at grazing angles): only the stable and dense α-alumina was characterised after 1h of exposure. However, the microstructure of the scale, with the star shaped scars, would indicate that transient alumina had formed, most likely during the very early stage of oxidation much earlier than 1h. This very fast formation of α-alumina is expected to be very beneficial, reducing the stress induced by the volume shrinkage associated with the θ to α transformation, while giving a similar global rate of oxidation, as shown by TGA analyses.

A second unique behaviour is the formation of the periodic network of inclusions following the former Al layers in the coating. These inclusions, correspond to kirkendall voids covered with alumina, are observed following the annealing stage (see previous chapter), due to the presence of dissolved oxygen during the sputtering of the Al layers. This network is likely to play a role: diffusion paths are reduced compared to a dense α-phase coating, and mechanical properties of the coated are likely to be changed as a result of forming this nano-composite.

A noticeable point is that although elements from the superalloy diffuse rapidly to the metal oxide interface, no specific precipitation of secondary phases was observed, nor sulphur segregation. The only observed precipitation is Ti rich particles within the coating, thought to be due to nitridation of titanium that has diffused into the coating from the AM1 substrate.

VI.3 Influence of deposition parameters

Isothermal oxidation tests were carried out on the produced batches following Blz28. This allowed the study of the effect of various parameters used in the manufacture of the low mass bondcoat systems on the isothermal oxidation behaviour. Effect of composition have been studied (composition within the α-phase range, or other intermetallics such as β-(Ni,Pt)Al, Pt_2Al_3 or $PtAl_2$). The effect of the total thickness is studied for Blz32 batch, which correspond to a 15µm thick α-phase based system. And finally, the effect of surface preparation, on samples which were grit blasted prior to the deposition instead of being ground.

VI.3.1 Effect of the composition

VI.3.1.1 Isothermal oxidation of β-(Ni,Pt)Al

This was carried out on both Blz29 and Blz37 samples, which correspond to a β-(Ni,Pt)Al intermetallic, formed by the low mass bondcoat manufacturing process, by alternating Pt, Al and Ni sputtered layers but with an expected composition of $Ni_{40}Pt_{10}Al_{50}$, and with an alternation pattern of Pt/Al/Ni/Al/Pt… The difference between Blz29 and Blz37 is in the deposition power used during the sputtering process: Blz29 was deposited at a high level of deposition power, whereas Blz37 was deposited with low powers, and following the new manufacturing procedure described in the third part of the previous chapter. Moreover Blz29 samples had 200 metallic layers whereas Blz37 samples had only 100 layers, for the same total thickness of 5µm.

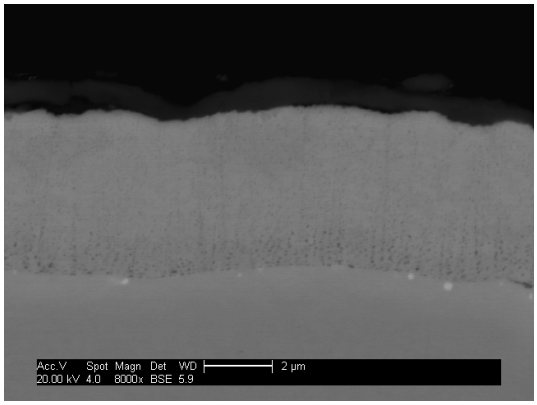

Figure 310 Blz29 sample after 1hr oxidation

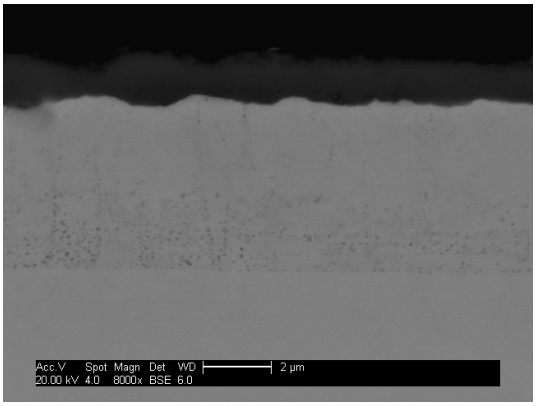

Figure 311 Blz29 after 50hr oxidation

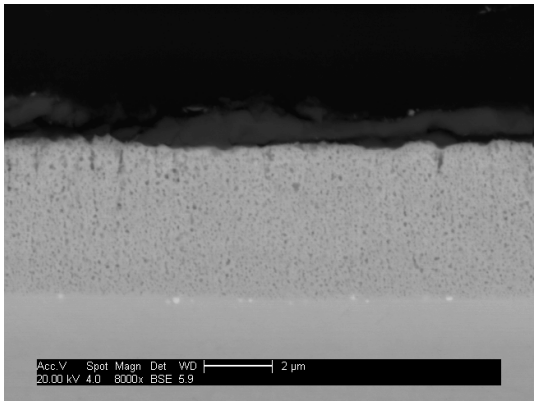

Figure 312 Blz37 sample after 1h oxidation

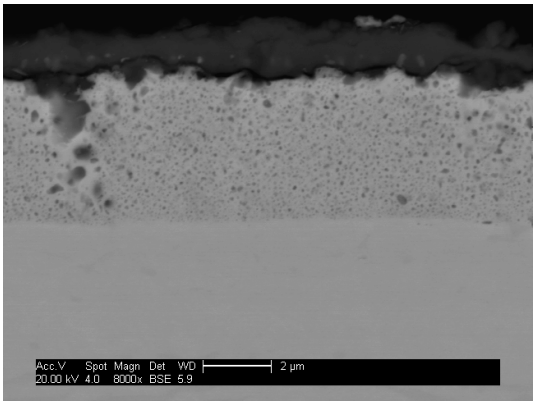

Figure 313 Blz37 after 50h oxidation

From observation of cross sections of Blz29 and Blz37 after 1h and 50 hrs of oxidations shows a similar microstructural degradation mode to that of the α-phase based low mass bondcoat systems (Figure 310 to Figure 313). The interlayer defects following the multilayering appear, meaning this ageing behaviour is characteristic of the manufacturing route rather than the type of synthesised intermetallic. Some differences occured though. First, the Blz29 section showed that the defects are larger in the bottom half of the coating than on the top. This does not appear in Blz37 and could be due to higher original deposition power which would have induced a greater stress gradient in the film.

Moreover, defects are larger in Blz37, simply due to the fact that the original metal layers are twice as thick in this system (100 layers in total instead of 200). After 50hrs these defects tend locally to coalesce: this behaviour was never observed for the α-phase based 100 layer system, Blz26. This coalescence may lead to a shorter life of the coating by loss of mechanical properties.

The re-precipitation of grains in the coating is not as obvious as in α-phase based system: this may be simply due to the lower content of Pt reducing the contrast in back scattered imaging mode. However, the typical vertical γ/γ' reprecipitation within the underlying superalloy which

was observed for the α-phase based system is not observed for these systems. Instead, some reprecipitation parallel to the coating/substrate interface is observed (Figure 314): this behaviour is similar to rafting observed for γ/γ' superalloys under high temperature creep mechanical loading.

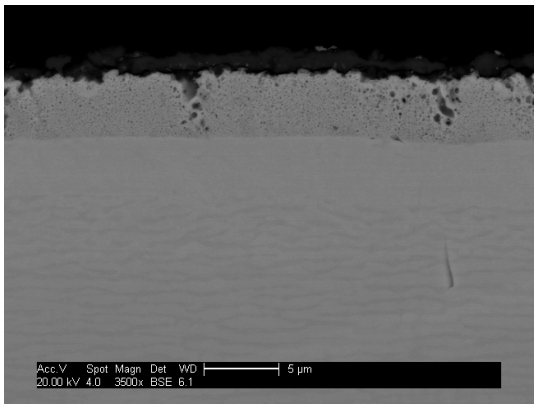

Figure 314 Blz37 after 50h oxidation (phase re-precipitation in the superalloy)

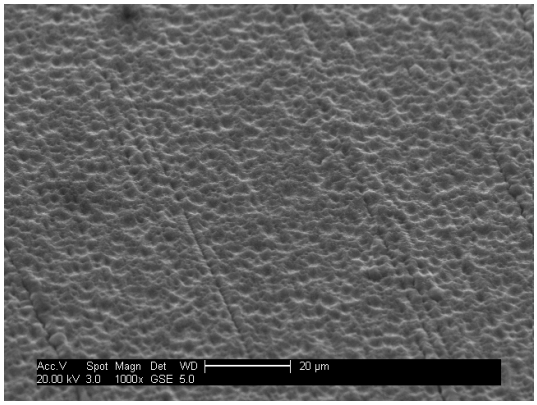

Figure 315 Blz37 sample after 1h of isothermal oxidation (1000x)

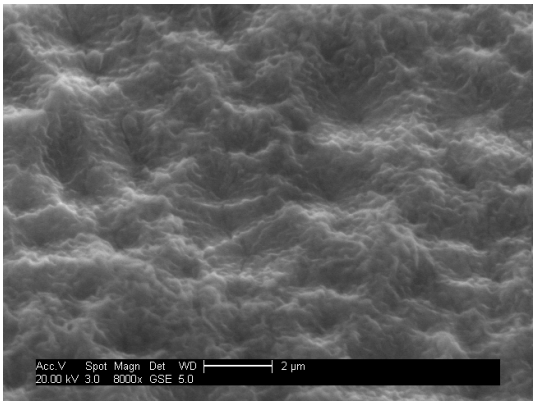

Figure 316 Blz37 sample after 1h of isothermal oxidation (8000x)

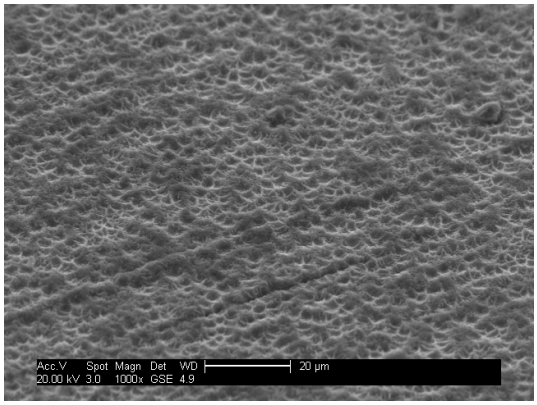

Figure 317 Blz37 sample after 50h of isothermal oxidation (1000x)

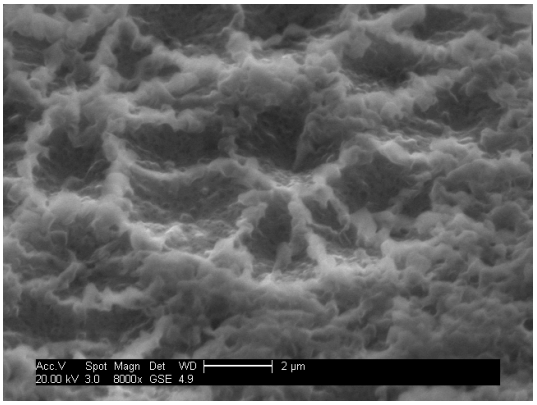

Figure 318 Blz37 sample after 50h of isothermal oxidation (8000x)

The surface of the oxide of Blz37 exhibits a dramatic star shape periodic pattern as was previously observed on α-phase based systems (Figure 315 to Figure 318). However, for the same surface finish, the frequency of these scars was increased, which would suggest that the formation of transient alumina is more likely early in the oxidation on these systems. Moreover, between 1h and 50hrs of exposure, the size of these scars increases, as previously observed, but for the β-NiAl bondcoat their frequency increases as well: this would mean that the θ-Al_2O_3→α- Al_2O_3 transition carries on after 1h of oxidation for this system.

This point is demonstrated by the analysis of the coating and its oxide scale by XRD (Figure 319). The XRD spectrum of Blz37 shows some slight traces of θ-Al_2O_3, which could not be observed for the α-phase based systems. Whilst as reacted the system exhibits a clear β-(Ni,Pt)Al pattern, the intensity of the peaks corresponding to this phase reduce drastically after 1 hour of oxidation. Peaks from γ'-$(Ni,Pt)_3Al$ are clearly observed instead. Peaks from α alumina are clearly present after 1 h of oxidation.

After 50 hours of oxidation, the peaks from γ'-$(Ni,Pt)_3Al$ have slightly shifted to higher 2θ values, due to the reduction in size of the lattice due to the reduction in Pt content. No peaks from θ-Al_2O_3 are now observed, nor peaks from the original β-(Ni,Pt)Al phase. The system, like α-phase based systems, has turned into a simple γ'-$(Ni,Pt)_3Al$ phase coating topped with a layer of α- Al_2O_3.

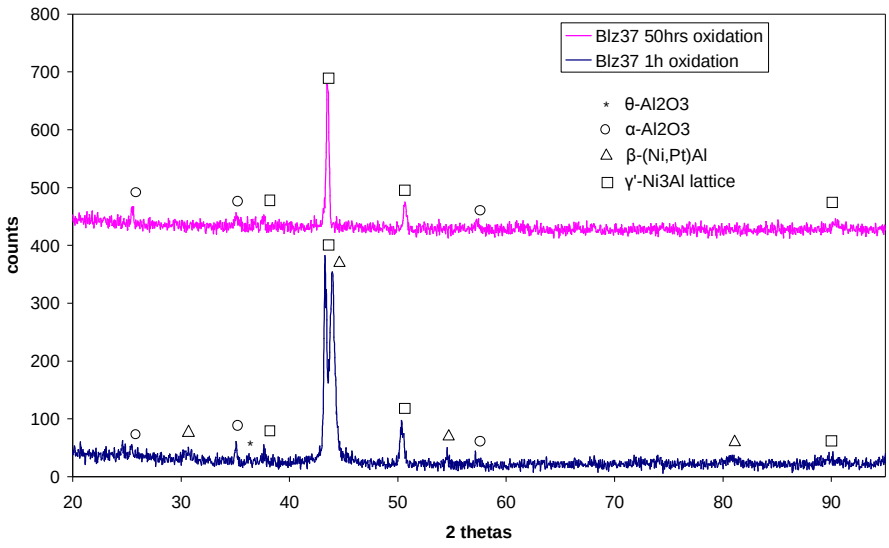

Figure 319 XRD diagrams of BLZ37 after 1h and 50hrs of isothermal oxidation

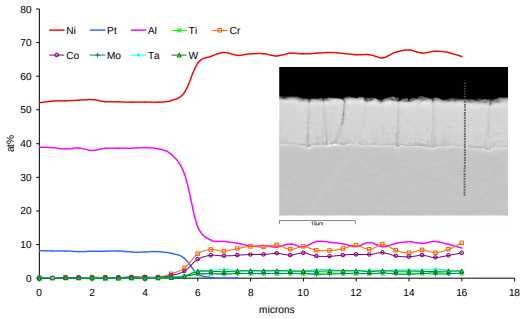

Figure 320 Composition profile of Blz29 as annealed

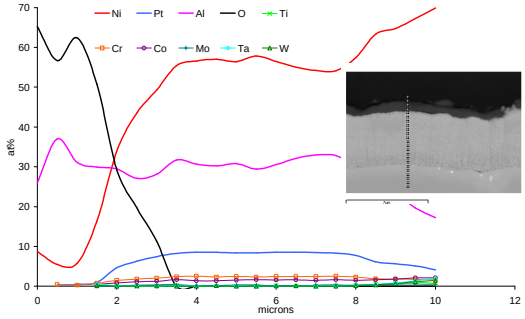

Figure 321 Composition profile of Blz29 after 1h oxidation at 1100°C

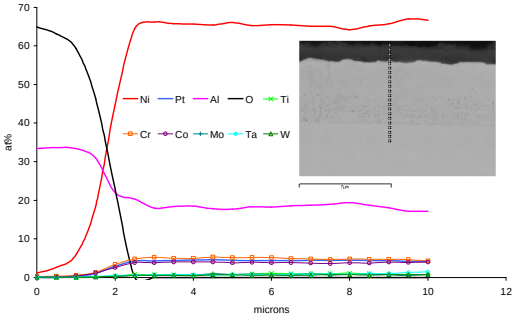

Figure 322 Composition profile of Blz29 after 50hrs oxidation at 1100°C

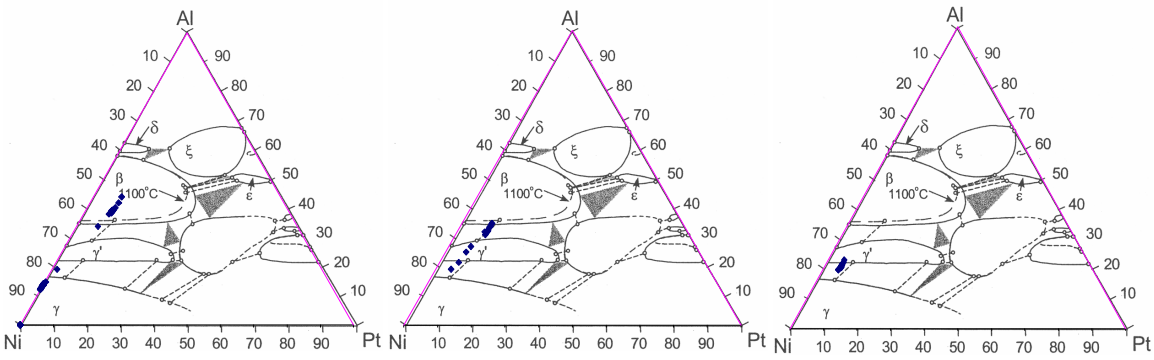

Figure 323 Plot of Pt/Al/Ni concentration profiles on the ternary diagram as reacted and after 1h and 50h of isothermal oxidation at 1100°C on Blz29

The analysis of the chemical profile of Blz29 as annealed and after oxidation gives some interesting results. First, the precision of the as annealed profile of the coating: the composition is very steady at the expected $Ni_{40}Pt_{10}Al_{50}$ composition. As observed in previous systems, interdiffusion is very fast, and after 1h of ageing at 1100°C only the coating composition has left the stability domain of the β phase. However, as noticed from the contrast in back scattered mode of the cross section, the formation of Pt modified γ does not occur: this is proven by the plot on

the ternary diagram, and by the level of Cr within the coating. The coating is now Pt modified β+γ'. After 50h at 1100°C it totally transformed into Pt-modified γ'.

VI.3.1.2 *Isothermal oxidation of $PtAl_2$ and Pt_2Al_3*

Although Blz30 and Blz31 batches were at first designed to form respectively $PtAl_2$ and Pt_2Al_3, the reacted coating resulted in a biphase mix of both $PtAl_2$ and Pt_2Al_3 phases as explained in the previous chapter. Blz30 is richer in $PtAl_2$ whereas Blz31 is richer in Pt_2Al_3. The behaviour of these two samples is similar, except Blz30 is only 2.5µm thick: only Blz31 behaviour will be presented and discussed further.

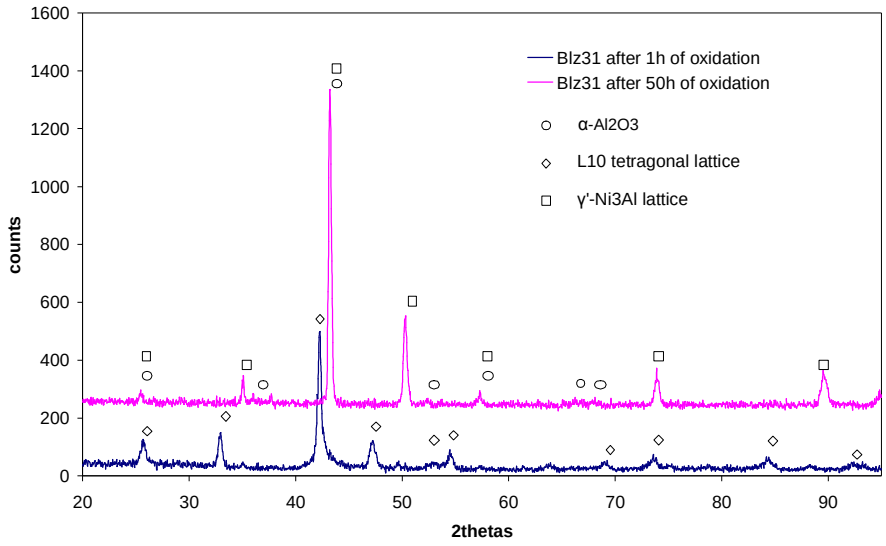

Figure 324 XRD spectra of Blz31 after 1h and 50h of isothermal oxidation at 1100°C in air

Analysing the decomposition of Blz31 is slightly more complex. Actually, the XRD spectrum of Blz31 after 1h of oxidation shows multiple peaks. The diversity of this pattern can not be explained by the presence of a simple $L1_2$ cubic lattice (γ' type): peaks at 32.88°, 47.40°, 54.44° and 84.56° would not fit. These peaks are present because of a compound with a loss of symmetry compared to cfc, with different cell parameters. In fact, one can notice that this multiplication of peaks corresponds to differences in diffraction planes but with equivalence in (h,k) miller indices (i.e. (100) and (010) plane diffract for the same 2θ value). In fact this compound fit perfectly with a tetragonal $L1_0$ phase (a=b=3.83Å c=3.49 Å) giving an intermetallic similar to the α phase.

Actually, this result is relevant to the analysis of the composition profile of Blz31 after 1hour oxidation (Figure 325). In the upper part of the coating, the relative ratio Ni/Pt/Al

corresponds to a composition between β and α phase field on the ternary diagram. This fact was observed by M.Silva[208] in his work on Pt/Al coating (one of the reason leading to the current study focused on the α phase).

Some traces of γ' phase are also observed on the XRD spectrum after 1h oxidation, but no peaks from a B2 type compound. (β(Ni,Pt)Al is a compound B2 with a body centred cubic lattice). This would imply that the stability field of the region between β, α, and γ' might be slightly different than the ternary diagram, with a smaller stability field for β, and larger for γ' and α.

After 50 hours of oxidation the Blz31 XRD spectrum suggest a similar behaviour to α phase based coatings, with a shift to a Pt modified γ/γ' structure topped by α-alumina surface layer.

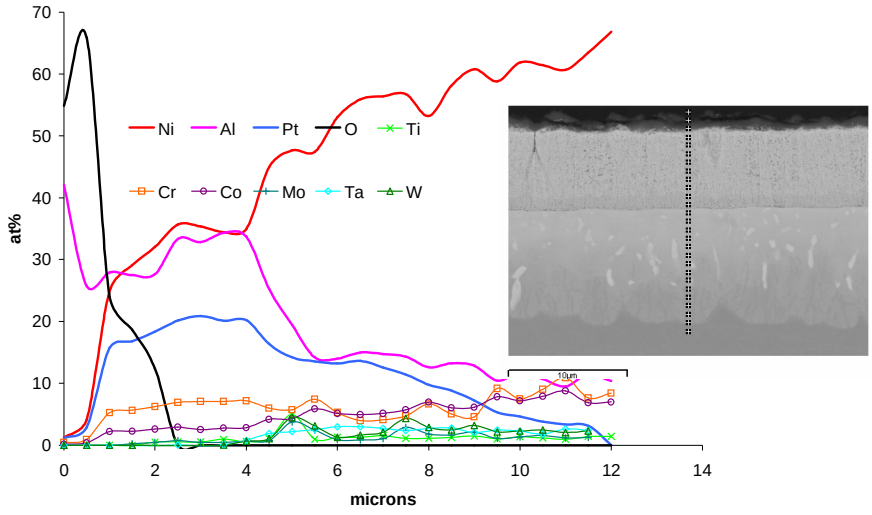

Figure 325 Composition profile of Blz31 oxidised for 1h

VI.3.2 Effect of the total thickness

Samples from the Blz32 batch of manufacturing parameters include the α-phase based intermetallic, 900 layers, 15µm total thickness. This batch was manufactured in order to compare performance between a 5 and a 15µm thick system, this thickness corresponds to the same amount of Pt as in a commercial β-(Ni, Pt)Al based systems.

A cross section of the as annealed coating shows a very dense and homogeneous system (Figure 326). Some vertical cracks are observed, and correspond to the grooves previously observed on the surface of the coating in the previous chapter, when only 5µm thick. These

grooves are likely to be due to volume shrinkage during the reaction to the intermetallic compounds, and triggered on the grinding scars on the superalloy surface. Slight interdiffusion has occurred with the substrate during the annealing treatment: a 1µm thick Pt richer layer stands at the coating/superalloy interface.

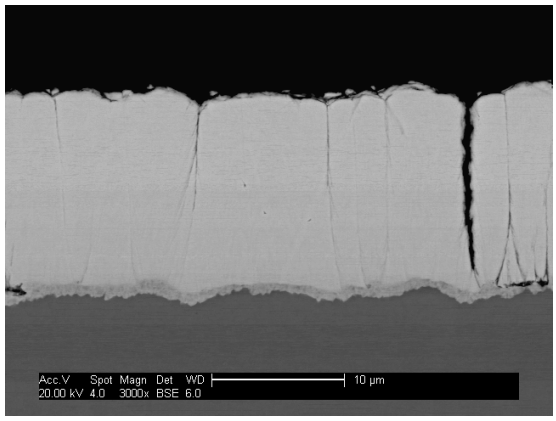

Figure 326 Blz32 cross section, as annealed

After 1h of isothermal oxidation (Figure 327), the coating exhibits a clear diffusion front, with a biphase structure. Interdiffusion occurs into the superalloy to a depth of 12µm. After 50hours (Figure 328), the entire coating has recrystallised, and oxidation went though the large scars down to the surface of the substrate. An homogeneous diffusion front goes down to 15 µm into the substrate. From 15 to 45µm, the superalloy exhibits a typical Pt modified γ/γ' like morphology.

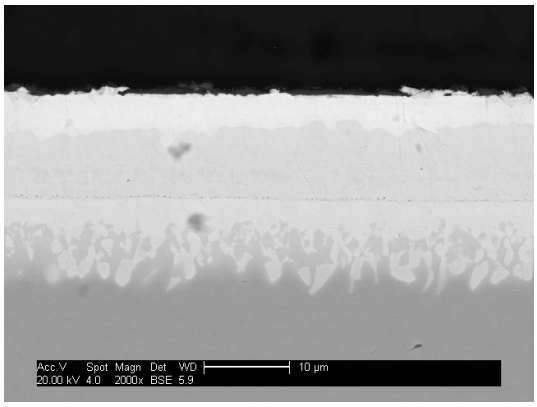

Figure 327 Blz32 cross section, after 1h oxidation

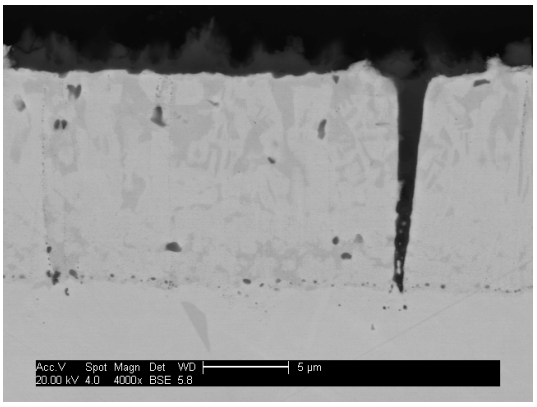

Figure 328 Blz32 cross section, after 50h oxidation

The XRD analysis of the oxidised samples can be compared to the cross section observation (Figure 329). After 1h of oxidation, the coating still exhibits the peaks of the $L1_0$ crystallographic structure of the α-phase. However, these peaks are slightly shifted compared to the as annealed

pattern, suggesting a reduction of the compound cell size due to the reduction in Pt content. Small peaks of α-alumina are observed after 1h of oxidation only, but no trace of θ-alumina. After 50hours of oxidation, the typical pattern of the tetragonal α phase has disappeared, to be replaced by fcc γ'-Ni_3Al structure, with a slightly greater cell size due to Pt substitution on the Ni sublattice. The γ peaks do not appear, but the observed pattern might be isostructural γ+γ' phase as suggest the cross section picture. Peaks from the α alumina are clearly observed.

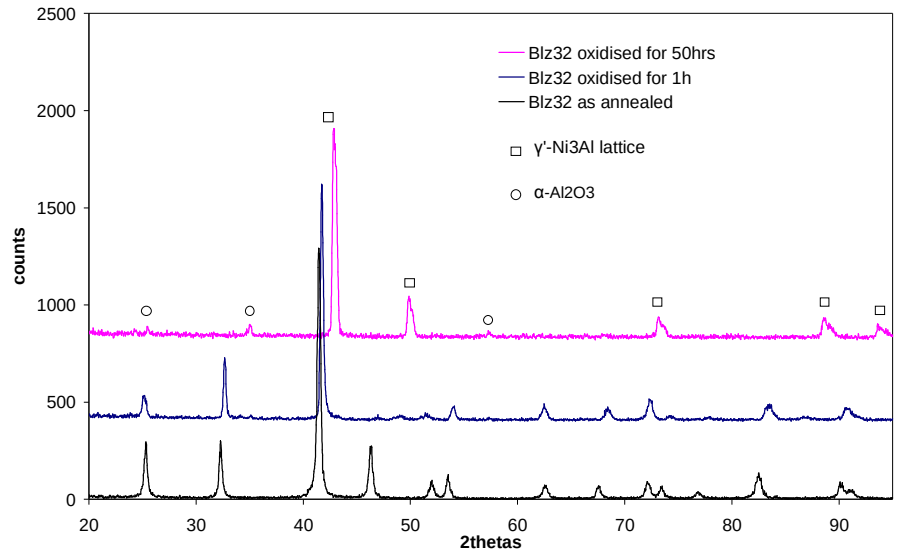

Figure 329 XRD spectra of Blz32 surface as annealed, after 1h and 50hrs of oxidation

The analysis of the evolution of the composition across the coating+substrate system with time, from the as annealed state to 50hours of oxidation is relevant to cross section observation and XRD analysis. The as reacted sample exhibits a very homogeneous α-phase composition across the coating (Figure 330), with a slight diffusion profile across the last 5 µm due to interdiffusion with the substrate, occurring during the heat treatment in the Argon furnace. But overall, this profile demonstrates the precision of the deposition process to manufacture α phase based coating.

After 1hour of oxidation (Figure 331), the dual structure system within the coating is clearly observed: the first 3µm are still in the phase field of the α-phase, until Ni and Pt signal cross each other on a typical interdiffusion profile. After this reaction front, the system is in a Pt modified γ' system, and no difference can be made between the coating and the substrate, as the Pt diffuses deeply into the superalloy to form Pt modified γ'.

After 50 hours of oxidation (Figure 332), the coating is made solely of Pt modified γ' (15at%Pt), and the composition profile is flattened. The presence of Pt modified γ is observed even deeper in the substrate, from a depth of 35µm roughly.

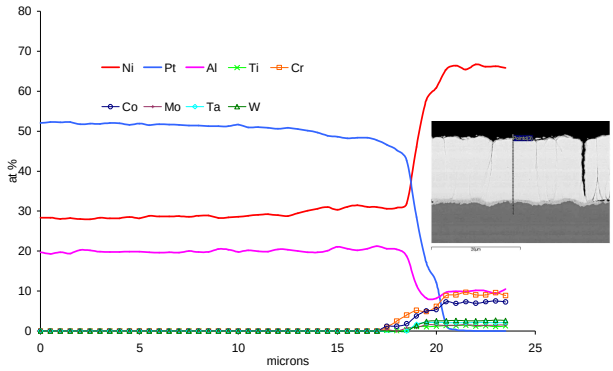

Figure 330 Blz32 composition profile, as annealed

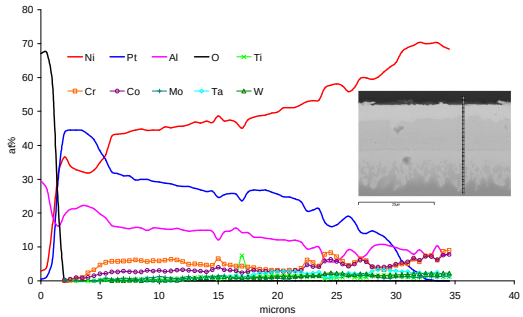

Figure 331 Blz32 composition profile after 1h oxidation

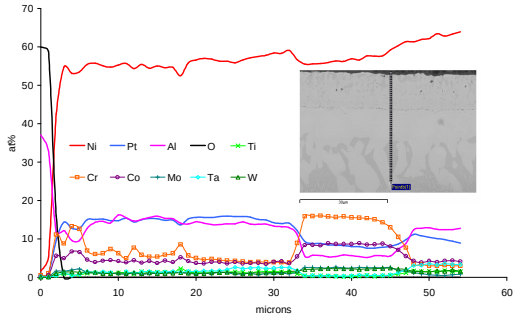

Figure 332 Blz32 composition profile after 50hrs oxidation

Overall the high temperature behaviour of this 3 times thicker coating conforms to the mechanism for the ageing behaviour of α phase based coatings. Due to the dramatic difference in Pt between the coating and the superalloy, interdiffusion occurs very rapidly, Pt rushes into the substrate, which as an opposite effect increases the Ni content in the coating. The decrease in Al content is due to both diffusion into the substrate, and alumina formation. The increase in Pt and Al content stabilises the γ'-$(Ni,Pt)_3Al$ phase in the system. The Pt enriches as well the γ phase, where it appears deeper in the substrate, when Pt and Al activities are now low enough to allow its formation. The α→γ'→γ+γ' transformation is retarded for this thicker coating due to the higher content of Pt atom added to the system. After 50hours of oxidation, the front of the γ'/γ+γ' reaction with the substrate occurs at 11μm from the substrate surface instead of 5.5μm on the thinner Blz28 sample. This difference is due to the higher available Pt content in Blz32 system. If the oxidation was carried on, this front would move upwards, following the impoverishment of the system in Pt and Al. For both thicknesses, some γ phase islands are observed within the coating, due to the depletion in Al to form the alumina scale.

VI.3.3 Effect of the surface finish

Grit blasting of the superalloy substrate was investigated as part of the manufacturing process from batch Blz35, but was introduced to isothermal oxidation tests on Blz38, Blz39, and Blz40 only (four grit blasted samples per batches, two for thermal cycling of the TBC, one for the TBC with sputter etching and at last one for isothermal oxidation).

The quantity of data is not as great as on ground substrates, however, the dramatic changes in thermal cycling lifetimes (see next chapter) add a lot of interest to the study,differing from the isothermal oxidation behaviour of these systems. Where Blz39 (100 layers) and Blz38 (300 layers) exhibit similar behaviours, only Blz39 will be detailed.

Cross sections of as reacted Blz39 and Blz40 show a similar homogenous coating than to that observed on a ground surface (Figure 333 and Figure 334). The artifacts at the former Al layers are still observable on Blz39 sample as they were on ground systems. The total surface of the substrate is covered by the coating despite its original roughness.

After 1 hour of isothermal oxidation at 1100°C, the Blz39 coating has a similar behaviour to that of Blz26, with the nucleation of regular array of interlayer defects at the former Al layer positions (Figure 335). However there is an important difference in the oxide scale thickness: whereas the oxide scale was roughly 0.8µm thick on Blz26 after 1h of exposure, it is twice as thick on Blz39. Unfortunately, no weight gain experiments was carried out on grit blasted samples to confirm this apparent increase in the rate of oxidation. The microstructure of the underlying superalloy is closely similar to the one observed on ground samples, with a diffusion front forming the γ+γ' structure. However, a difference is most noticable after 50hours of oxidation: the overlay coating is severely consumed, and no trace of the original multilayer is observable. Strong internal oxidation has also occurred.

Although they have different chemical composition, the Blz40 microstructural behaviour is similar to Blz39. After 1h of oxidation, the original layered coating/superalloy interface is very heterogeneous, and after 50 hours, the coating is largely consumed by preferential attack.

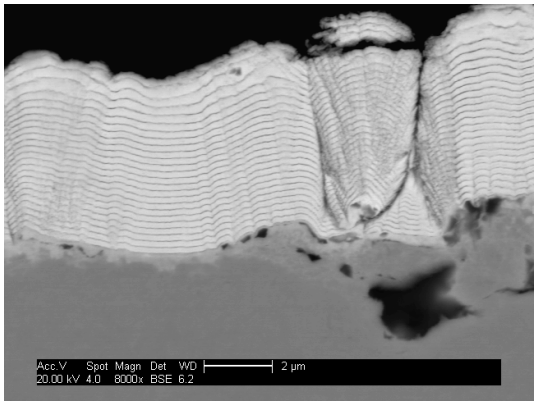

Figure 333 Cross section of Blz39 as annealed

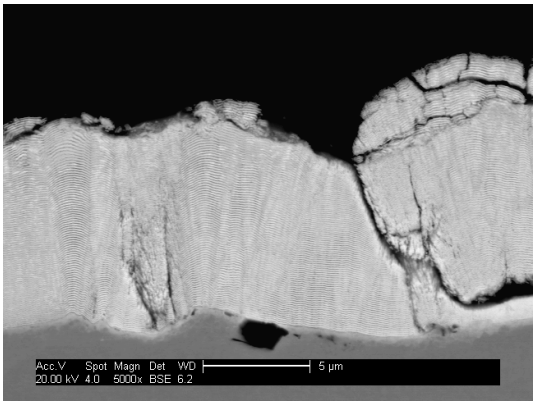

Figure 334 Cross section of Blz40 as annealed

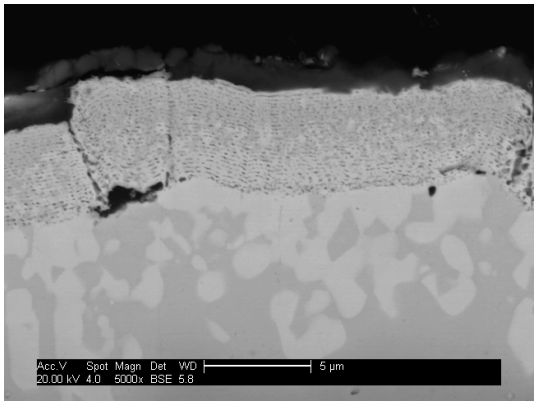

Figure 335 Cross section of Blz39 after 1h oxidation

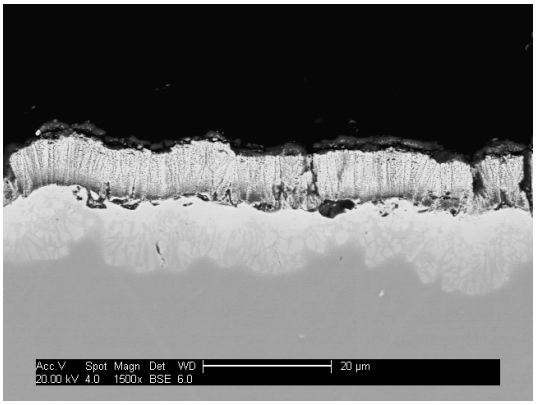

Figure 336 Cross section of Blz40 after 1h oxidation

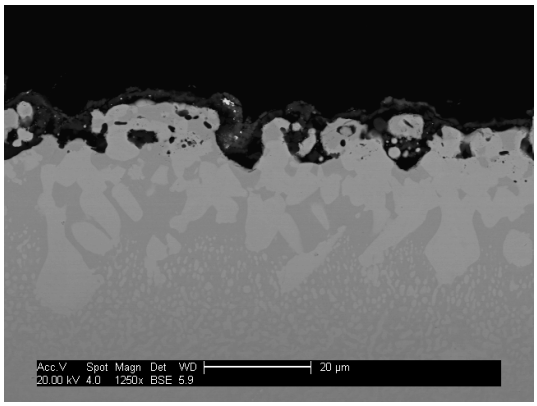

Figure 337 Cross section of Blz39 after 50h oxidation

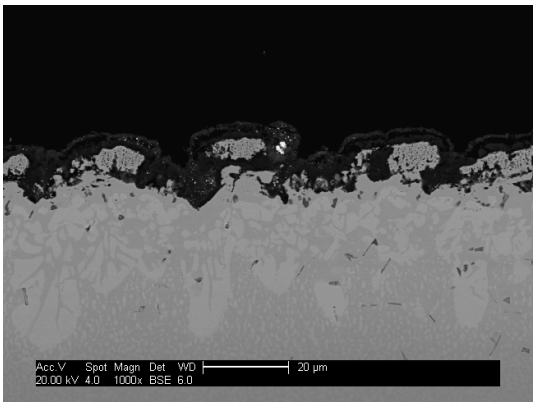

Figure 338 Cross section of Blz40 after 50h oxidation

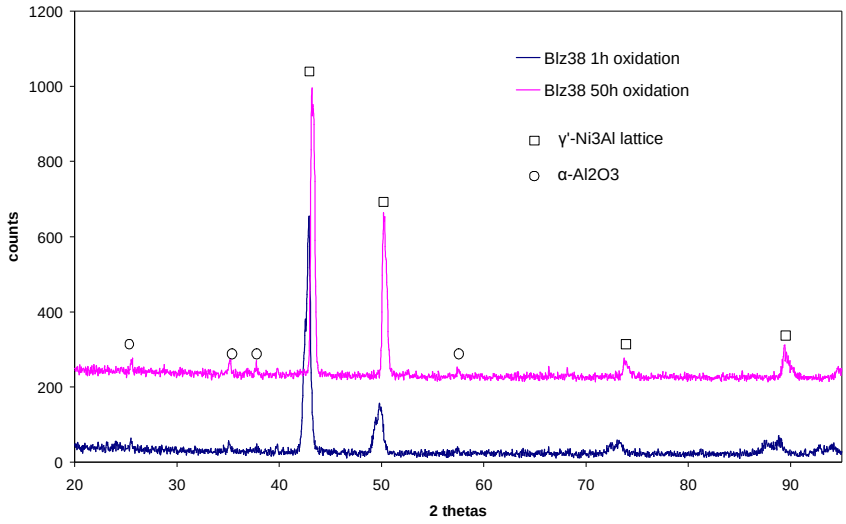

Figure 339 XRD spectra of Blz38 after 1h and 50h of isothermal oxidation

XRD analysis of Blz38 sample confirms the similar behaviour on a grit blasted sample to that on a ground sample (Figure 339). After 1 hour of oxidation only, no trace of α phase remain, but only α-alumina on a fcc type γ' lattice. After 50hours, the XRD spectrum remains the same, but with a reduction in size of the γ' cell.

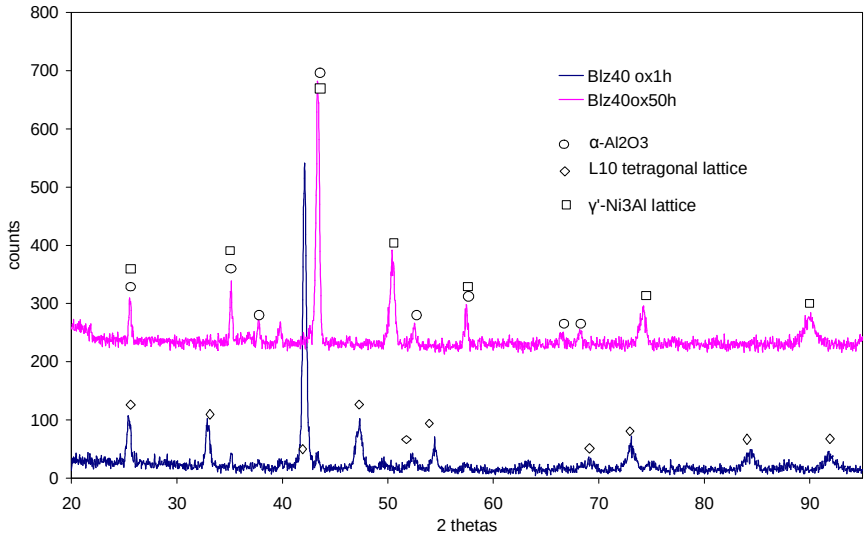

Figure 340 XRD spectra of Blz40 after oxidation exposure

After 1h of oxidation, the same XRD spectrum is observed on Blz40 to that on Blz31: with the presence of the tetragonal $L1_0$ lattice, which is consistent with the α phase (see previous discussion).

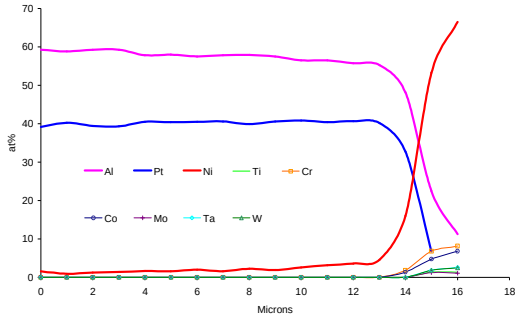

Figure 341 Blz40 profile after heat treatment only

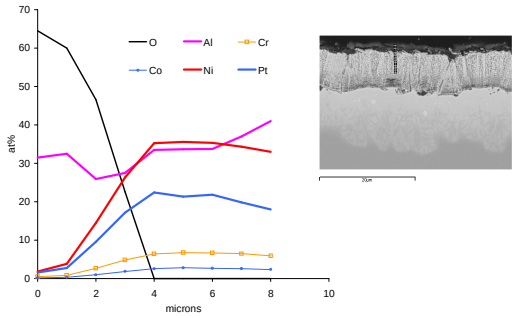

Figure 342 Blz40 composition profile of the upper part of the coating after 1h oxidation

After 50 hours of oxidation, the consumption of the coating is dramatic, with strong preferential attack, and large voids within the structure. Chemical analysis was carried out on BLz40 and Blz39 cross sections. As there are only a few remain area of the coating (there are even no trace of the typical interlayer defects for Blz39), single point analysis was chosen to study the degradation of the coating.

Figure 343 outlines the dramatic changes in microstructure that occurred for Blz40 after 50 hours of exposure. The coating thickness is severely reduced, and internal oxidation penetrated and locally consumed the overlay down to the surface of the substrate. The cracks in the oxide are caused as part of metallographic preparation. The overlay still exhibits the periodic interlayer defects, but as well some large vertical voids are observed. EDS analysis (results are gathered in Table 26, interesting figures are in bold) shows that the superalloy still has a biphase structure γ/γ' (*EDS 1* and *EDS 2*), however, γ (Cr rich) is stable and continues over the first 3 microns in the superalloy (*EDS 3*), due to the Al depletion to form the oxide. Ti rich phases defects precipitate within the superalloy (*EDS 4*): this is quite typical of the oxidation mode of coated AM1 (a Ti rich superalloy), but was rather observed for longer exposure times than 50 hours (see next chapter on cyclic oxidation). The coating exhibits a strong internal oxidation with high levels of oxygen within the overlay (*EDS 5*). The voids within the coating are areas of internal oxidation (*EDS 6*): and it corresponds to the first steps leading to the dramatic consumption of the scale observed along the cross section (*EDS 7*).

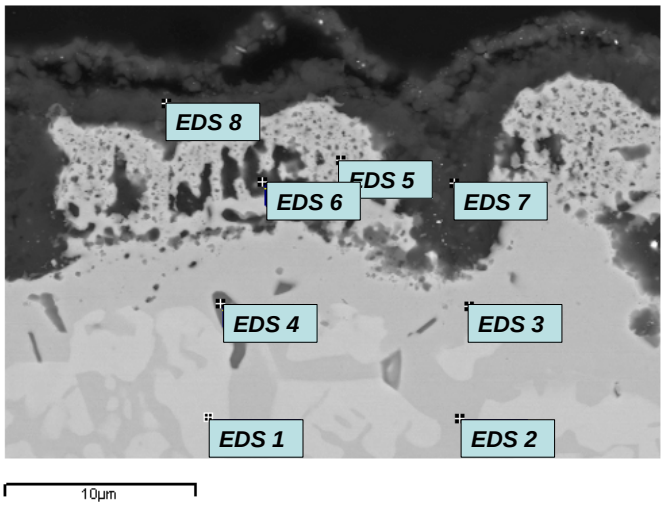

Figure 343 EDS point analyses on Blz40 oxidised for 50h

Table 26 EDS results on Blz40 after 50 hours of oxidation

	O	*Al*	*Ti*	*Cr*	*Co*	*Ni*	*Mo*	*Ta*	*W*	*Pt*
EDS 1	4.5	**12**	0.3	**3.3**	4.3	63	**0.7**	**3.9**	**1.5**	6.4
EDS 2	5.4	**5.5**	0.1	**13**	7.9	59.1	**1.6**	**1.1**	**2.4**	3.8
EDS 3	6.9	**5.4**	0.2	**13**	7.6	57.7	**1.8**	**1.1**	**2.4**	3.9
EDS 4	**0**	3.3	**45.3**	8.0	4.0	**32.6**	1.0	2.1	1.4	2.2
EDS 5	**18.1**	12.0	0.7	10.4	6.0	45.2	1.4	1.0	1.9	3.2
EDS 6	**10.0**	**41.3**	0.4	7.3	4.6	33.1	0.6	0.6	0.7	1.4
EDS 7	**65.2**	**33.2**	0.7	0.2	0.1	0.4	0	0.1	0	0.1
EDS 8	**61.3**	**35.2**	0.4	0.5	0.3	**2.1**	0	0.1	0.1	0

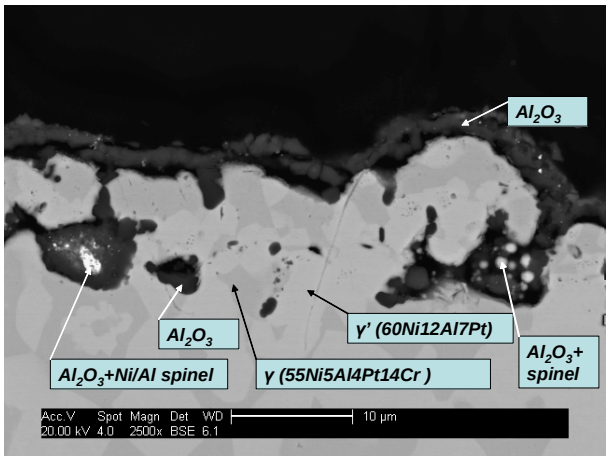

Figure 344 Cross section of Blz39 with EDS results

The observation and analysis of Blz39 shows the same strong internal oxidation of the system, with some spinels that formed, due to the low level of aluminium remaining within the Pt

modified γ phase. No trace of the typical interlayer defects can be seen: which would suggest the coating was completely consumed by the oxidation, after 50 hours of exposure only.

Overall, the behaviour of the coating on a previously grit blasted sample is very different from that on ground samples. This fact could be due to the consequent roughness of the surface of the substrate compared to the low thickness of the coating. Although the coverage of the substrate appeared satisfactory on pictures of the as annealed system, local breach may have formed, leading to this dramatic internal oxidation. Another consequence of this roughness is a possible easier inter-connection between the interlayer defects, which facilitated the coalescence of this small and periodic internal oxidation. Thus, this periodic interlayer porosity appears to be more stable on flatter coatings.

VI.4 Conclusions on isothermal oxidation tests

Samples with α-phase based low mass bondcoat were oxidised in a box furnace at 1100°C in air for fixed exposure times (1 to 50h). The main conclusions of this work are as follow:

- ✓ For all coatings, the crystallographic structures shift extremely rapidly to a Pt modified γ/γ' microstructure, typically after 1h of exposure only.
- ✓ This fact is independent from the number of layer, the original composition of the coating, or the surface finish. A thicker coating will only delay this phase transformation which is mainly driven by the diffusion of platinum into the substrate.
- ✓ Presence of Al_2O_3 at the former Al layers is detected for low or high multilayering. This alumina stands where voids were already formed after annealing due to the specific volume shrinkage associated to the formation of the intermetallic. This array of defect is thought to be alumina coated voids, the oxygen being suspected to come from the sputtering process.
- ✓ Unlike β-(Ni,Pt)Al coatings, no transient alumina could be detected on α-phase based coatings, even after short time exposure.
- ✓ Samples with grit blasted substrates have a faster oxidation rate, and a non uniform consumtion of the coating is observed, due to the original roughness.
- ✓ No TCP phases were detected after oxidation, suggesting the impact of such coatings on the mechanical properties of the superalloy is lower than conventional diffusion coatings.
- ✓ Oxidation rate of α-phase coatings seems higher than conventional diffusion β-(Ni,Pt)Al coating, although further TGA experiments need to be carried out on double sided coated samples.

Chapter VII

Thermal Cycling and TBC

VII.1 Bare intermetallic coatings: cyclic oxidation

VII.1.1 Weight gain results and discussion

Cyclic oxidation tests of bare bondcoats were carried out on two samples from the Blz21 batch. These samples are coated on both sides: Blz21RA and Blz21RB. These samples were heat treated under vacuum at respectively 700°C and 800°C for 2 hours (see chapter 5). These coatings are 2.5µm thick only, with 50 layers. A reference coupon, CN91 type coating was added to the experiment. This reference coupon was grit blasted as it is prior to TBC deposition: 3.5bars, 200mm distance from the nozzle, 10sec/faces.

Cyclic oxidation was carried out on the PYROX rig at 1100°C, but without forced air, and with a cold dwell of 15min and a hot dwell of 60min, in order to compare results with data from B. Saint Ramond[207]. The samples were removed for observation and XRD every 5 cycles first (until 20cycles), and then every 15 or 20 cycles. Blz21RA and CN91 cycling was stopped after 380 cycles, whereas Blz21RB was removed for observation after 200 cycles. Weighing was carried out on a Sartorius balance, +/-10µg, auto-calibrated and checked with a standard mass before each weighing. Six weighings were done for each sample to reduce the average error (error bars displayed on the. Weight gain charts).

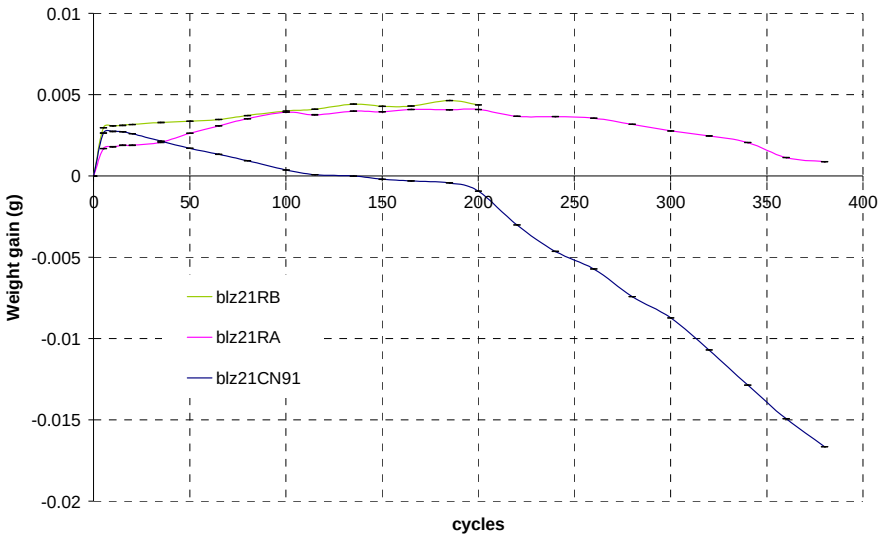

Figure 345 Weight gain curve for the cyclic oxidation of the bondcoats (and error bars)

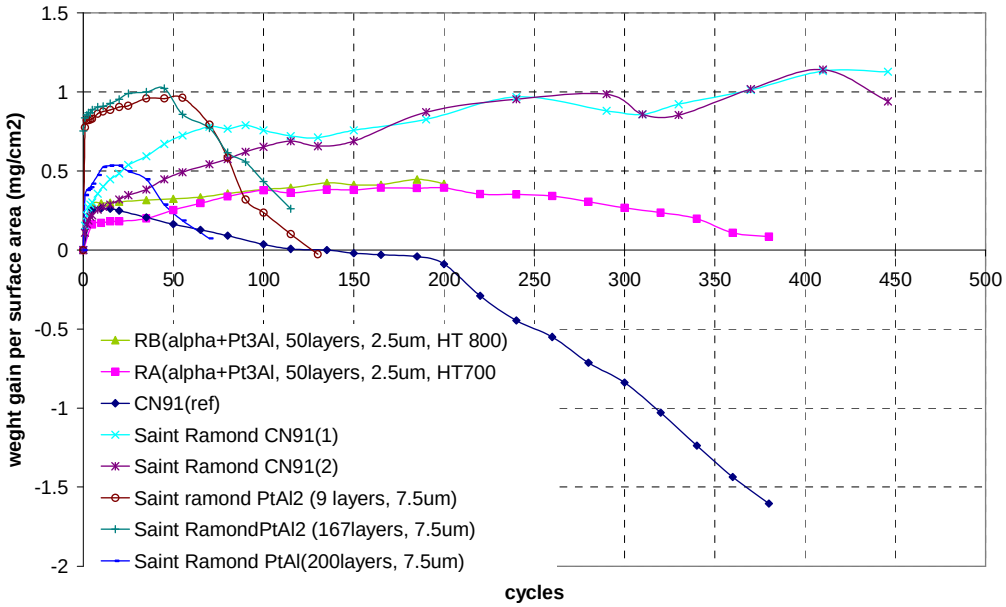

Figure 346 Weight gain per surface area curve of the cyclic oxidation experiment (large markers) and B. Saint-Ramond experiments (light markers)

The low mass α-phase bondcoats have rather good oxidation behaviour: the weight gain shows no spalling and near constant mass gain until rougly 100-200 cycles, where the first loss of oxide occurs. Saint Ramond's low mass $PtAl_2$ coatings showed similar behaviour but with higher initial mass gains and spallation that starts at approximately 50-70 cycles. But even after 380 cycles, the total gross weight gain is still positive (Figure 345). The behaviour of the reference sample is quite intriguing in comparison: the first oxide loss occurs very early, and the oxidation becomes dramatic after 200 cycles. The cycling conditions are the same as for B. Saint-Ramond experiments, meaning that this behaviour is not link to the test procedure itself. This behaviour could be due to the grit blasting of the CN91 sample prior to the start of the test (this was done in order to simulate the exact surface state of the bondcoat before the deposition of the zirconia). Another explanation could be the higher oxidation rate for remains of the holding stick used for the CN91 bondcoat deposition process (lollypop like) that could mask the actual oxidation of the surface of the sample. CN91 clearly shows 3 steps of almost linear weight loss: t=5-120cycles, t=120-180; t=180-380 cycles.

When compared with B. Saint Ramond's data, done on the same rig with the same cycle, α-phase bondcoat systems appear very competitive. The first weight loss occurs at 100 cycles instead of 50 for B Saint-Ramond's sample. Further, the α-phase coatings are 3 times thinner, and

has far fewer multilayers. The weight drop is not as dramatic as may be expected from the B. Saint-Ramond's systems either. The behaviour of the CN91 reference varied between these two tests. It is expected to oxidise in a manner similar to the previous measure behaviour of Saint Ramond, than the behaviour currently observed. The first mass loss of his CN91 experiments occurs at the same time as for our α-based low mass bondcoats. At last, the initial growth rate of the oxide on an α-phase low mass bondcoat system is slower (roughly 2 times); that implies that less transient alumina is formed during the early stages of the oxidation.

VII.1.2 XRD analysis

Although it is difficult to detect transient oxides using the XRD method, this method was used to monitor the formation of the thermodynamically stable oxides that form the scale. The intermetallic peaks disappear very rapidly. CN91 develops mainly alpha alumina, with slow amounts of $NiAl_2O_4$ after 380 cycles. The two XRD diagrams for the bondcoat are quite similar:

- ✓ Early stage: only alpha alumina is formed
- ✓ From 100cycles, the peaks of $NiAl_2O_4$ appear, and TiO_2 rutile peaks as well
- ✓ Cr_2O_3 peaks appear quite lately, only in the final XRD trace.

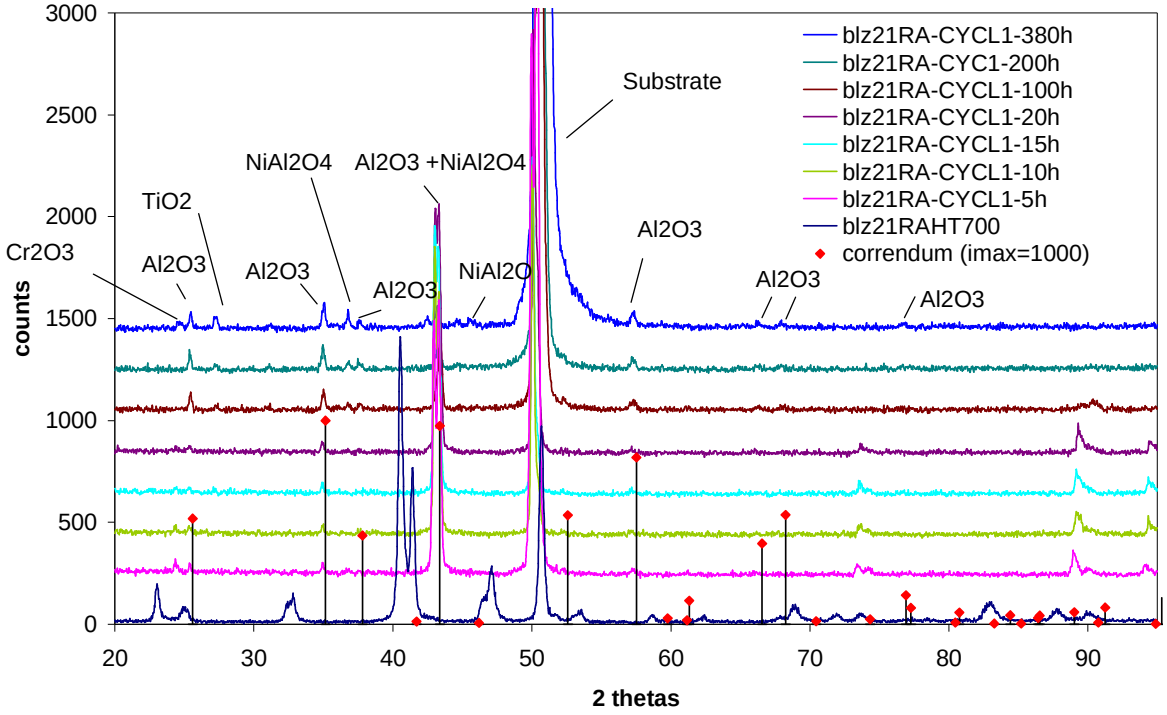

Figure 347 XRD diagram of blz21RA at different stages of cyclic oxidation

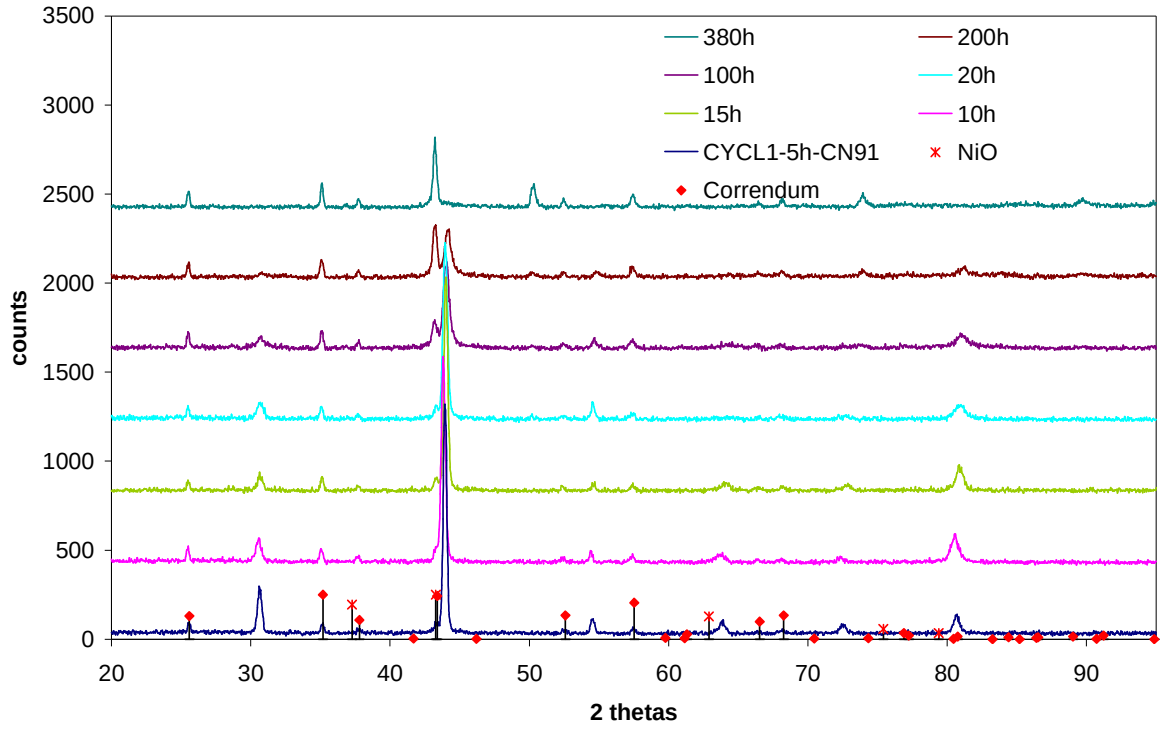

Figure 348 XRD diagram of CN91 at different stages of cyclic oxidation

VII.1.3 Early stage oxide scale observation

Until 100 cycles, the macroscopic aspects of the oxidised coating are similar between the low mass bondcoat systems and the CN91 reference, growing a typical grey scale. From 100 cycles, corresponding to the first oxide loss, green spots were observed on the surface of the scale of both low mass bondcoat samples, typical from Ni/Al spinels.

Figure 349 CN91, blz21RA, blz21RB after 20 cycles

Figure 350 CN91, blz21RA, blz21RB after 200 cycles

SEM micrographs of the surfaces of blz21RB and CN91 during the early stage of oxidation were taken in the E-SEM. The microstructure of the oxide scale helps understanding the beginning of the oxidation process, together with XRD analyses (see previous paragraph).

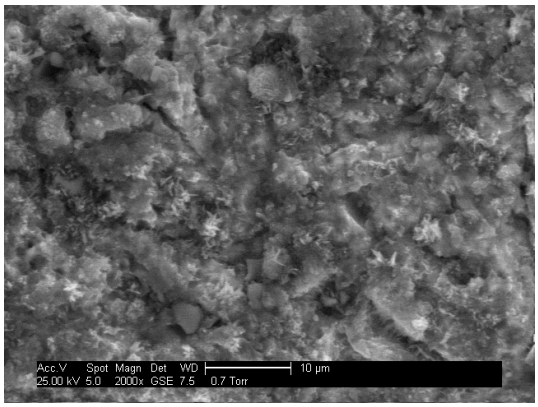

Figure 351 CN91 after 5cycles

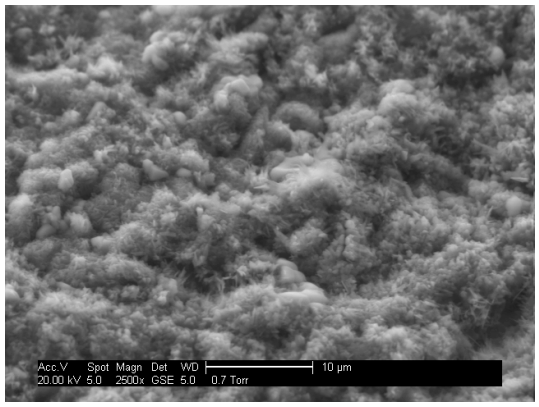

Figure 353 CN91 after 10cycles

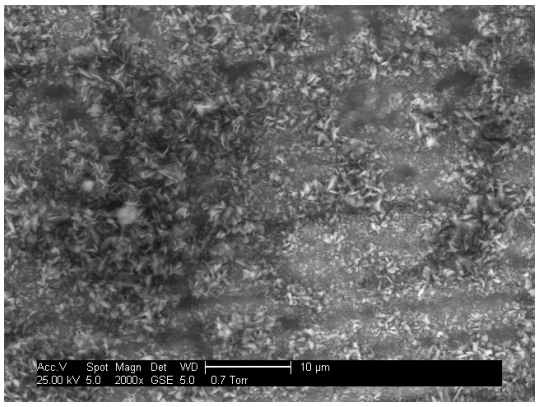

Figure 352 Blz21RB after 5cycles

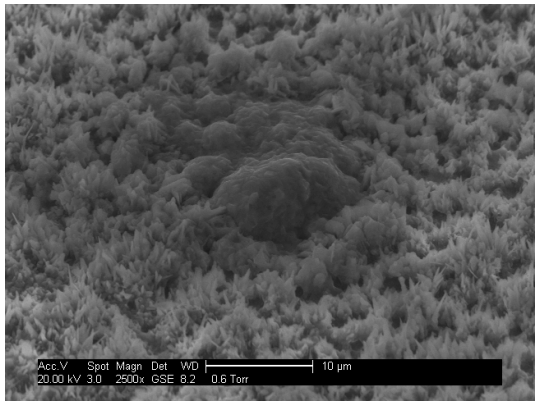

Figure 354 Blz21RB after 10cycles

Needle like growth is obvious in these micrographs for both types of systems. After 5 and 10 cycles, the oxide scale on CN91 appears denser than on the Blz21 sample, but still showing some needle like growth, typical from transient θ-alumina.

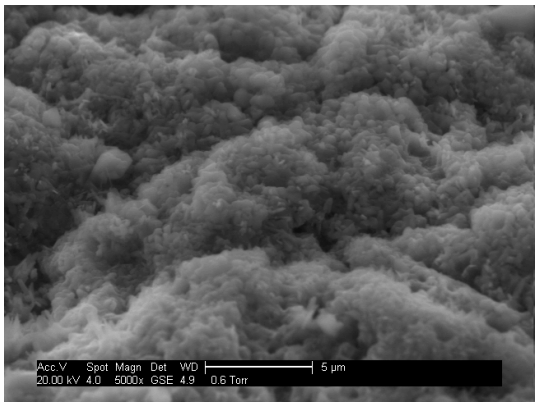

Figure 355 CN91 after 15cycles

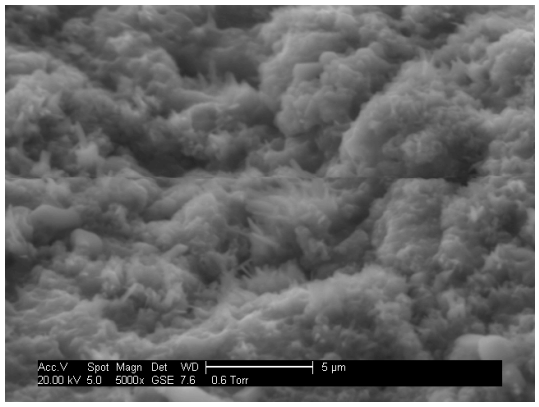

Figure 357 CN91 after 20cycles

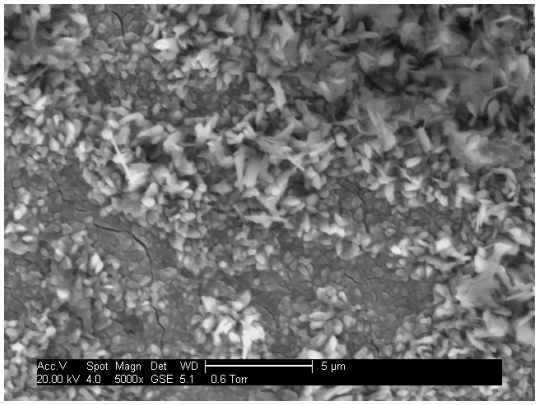

Figure 356 Blz21RB after 15cycles

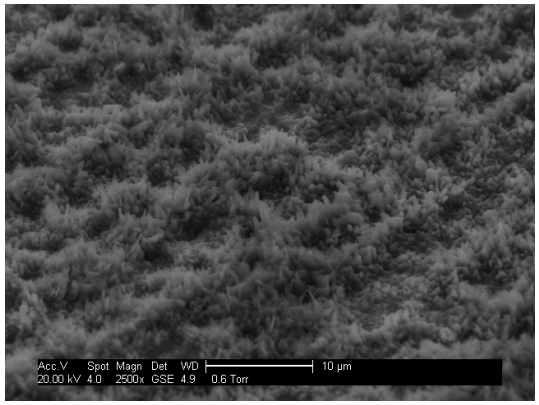

Figure 358 Blz21RB after 20cycles

Whereas oxide growth kinetic is drastically reduced after 10 cycles, needles are still present on both surfaces: these remains from the early formation of the transient oxide, the stable α-alumina growing underneath the structure of θ-alumina, with an anionic growth.

One can notice the difference in surface roughness between the 2 systems: this can not be interpreted as a rumpling yet, as one must remember the surface of CN91 was grit blasted prior to cyclic oxidation exposure.

However the microstructure of the oxide scale growing on the low mass bondcoat system is radically different from that observed after isothermal behaviour. Under isothermal exposure, no needle like growth was observed after a short time of exposure. This can be explained by the formation of microcracks in the scale initiated during the cooling of the substrate+coating system, leading to an increase of cationic growth because of the non continuous scale that would result.

VII.1.4 Analysis low mass bondcoat after 200 x 1h cycles at 1100°C

The surface and the cross section of sample blz21RB were observed after 200 cycles (200 hot hours). The surface is greyish (especially near the border of the coupon) with green granular dots. These green parts look like failed scale with another type of oxide growing.

On the greyish parts, the multilayers of the bondcoat are still in evidence, but with some porosities within the pattern (these could be internal oxidation but these could not be confirmed at this stage). On the greenish part, no remain of the overlay coating can be seen. The oxide that is formed is 5 to 6 µm thick on parts that have no boondcoat, and only 2-3µm over the remaining bondcoat. The overall aspect of the cross section is like "pitting", giving some surface undulations (Figure 361).

The same interdiffusion system is observed within the superalloy: a dark interdiffusion phase that has some internal oxidation, and then the lighter γ' phase, which penetrates deeper into the substrate (Figure 359).

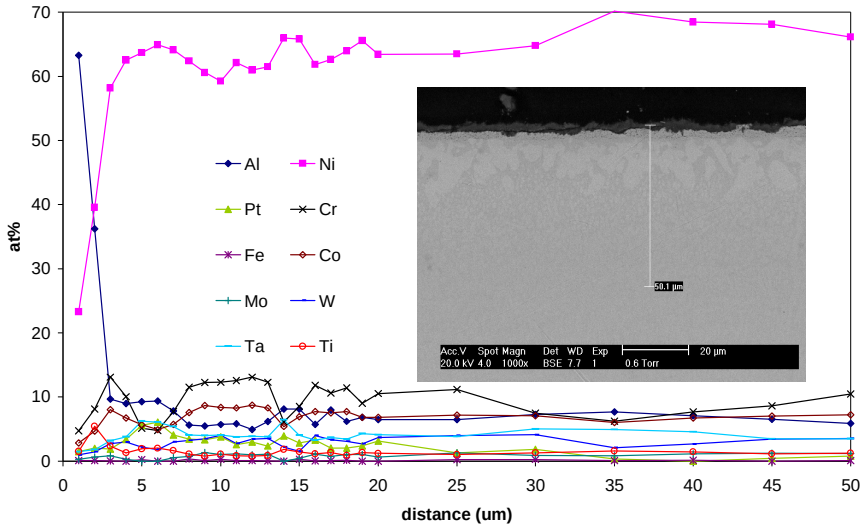

Figure 359 Digipoint of Blz21RB after 200 cycles (200 hot hours exposure at 1100°C)

From the macroscopic point of view, the bondcoat oxide is still adherent in the outer zone of the sample surface, and not in the middle of it (Figure 350): the cooling is supposed to be faster on the edges, i.e. buckling stresses will be greater in the middle of the disk.

As a last observation, the oxide tends to fail horizontally in two parts (Figure 360) that is likely to be due to the formation of other oxide that alumina that would induce a stress in the scale.

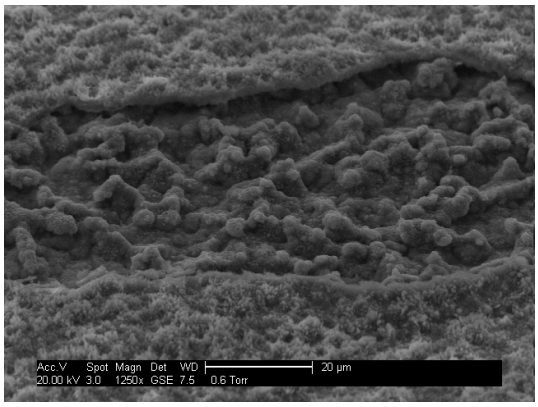

Figure 360 Blz21RB after200cycles: failed part, tilted view

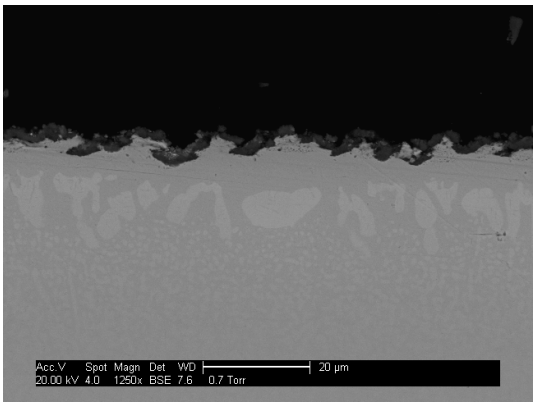

Figure 361 Blz21RB after200cycles, cross section: of the deteriorated bondcoat

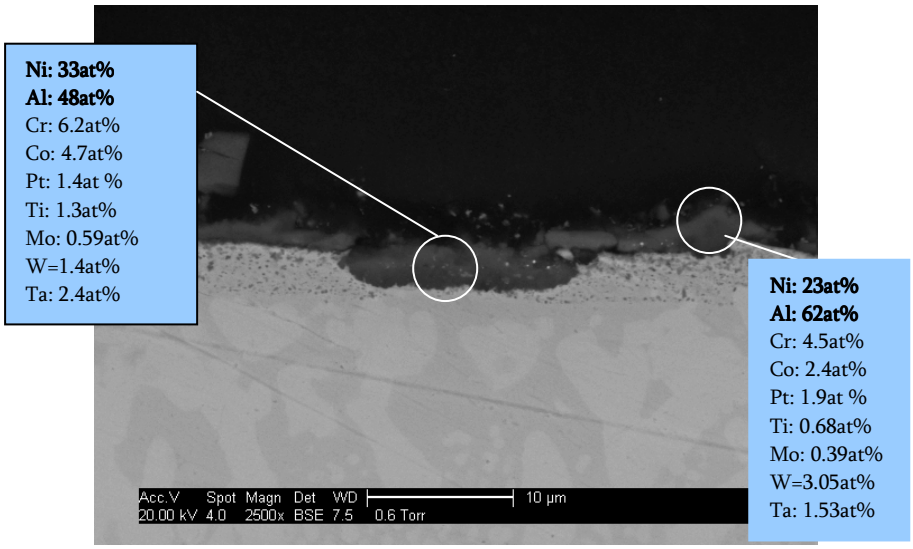

Figure 362 EDS on cross section of CYCL1Blz21RB after200 cycles

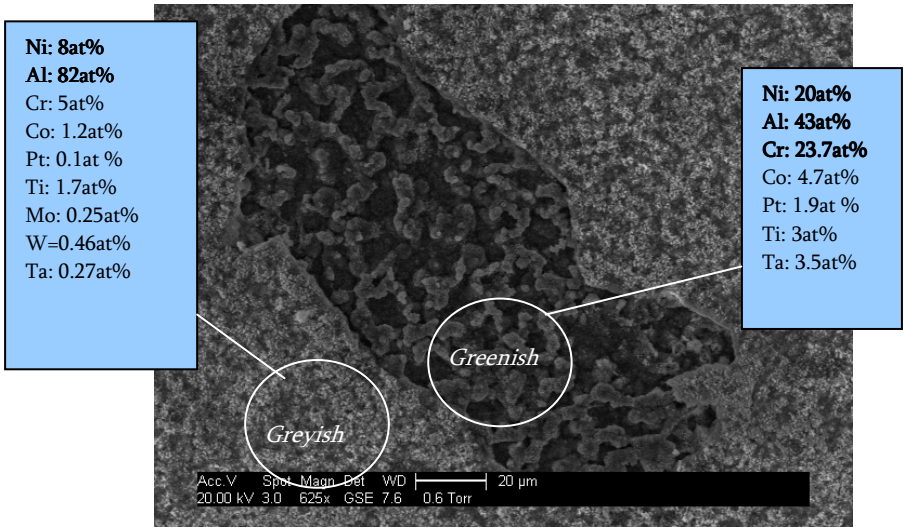

Figure 363 EDS on the surface of CYCL1Blz21RB after200 cycles

VII.1.5 Analysis of Blz21 and CN91 after 380 x 1h cycles at 1100°C

The surface of Blz21RA after 380 cycles(380 hot hours exposure) is very heterogeneous, with platelet of oxides above an underlying scale. The cross sectional observation shows that no bondcoat is left. And the oxide scale is sometimes clear under backscattered electron observation in SEM, meaning clearly that nickel oxide is formed: it has to be the Al_2NiO_4 spinel observed in XRD analysis.

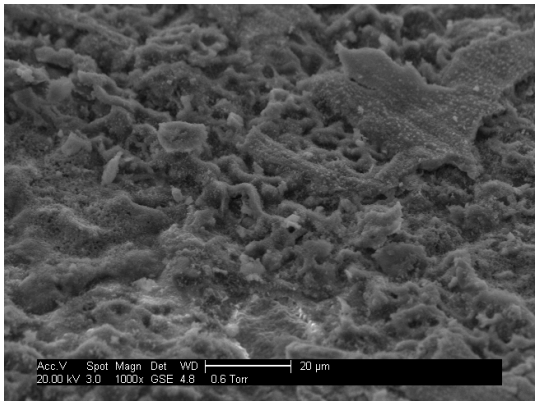

Figure 364 Blz21RA surface after 380 cycles

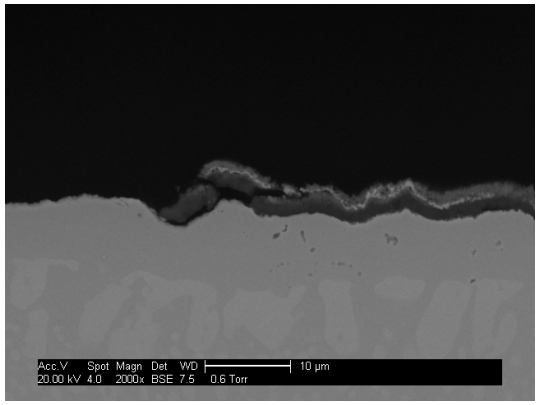

Figure 365 Blz21RA cross section after 380 cycles

By way of comparison, the oxide scale formed on CN91 after 380 cycles is quite dense, but very undulating (see Figure 366). The amplitude of the undulation is such that cracks are formed on the top of the hills due to the tensile stress generated (Figure 367), and in the valleys due to the compressive stress.

As explained before, a question was raised concerning the oxidation behaviour of the small remnant of the holding stick, on the edge of the sample. Figure 369 shows that oxidation is extensive at this place, with numerous voids formed in the substrate.

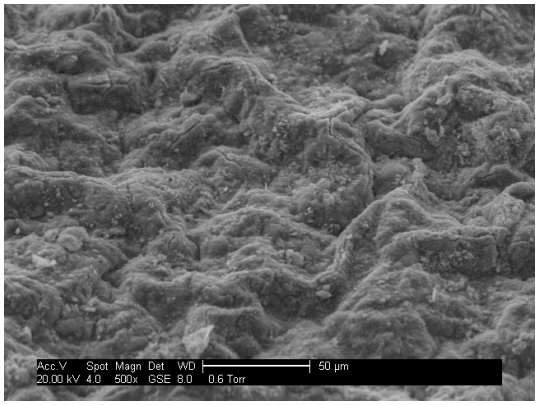

Figure 366 Surface of CN91 after 380 cycles

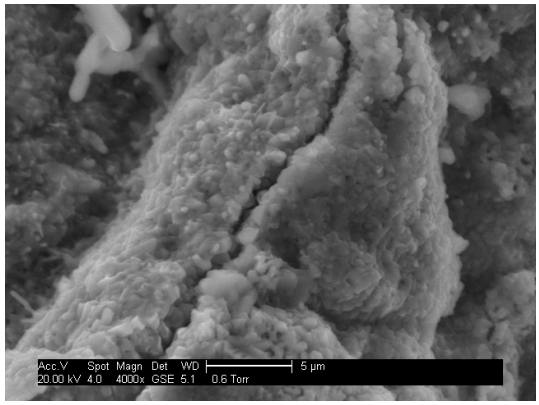

Figure 367 Crack on the top of the hills of the surface of CN91 after 380 cycles

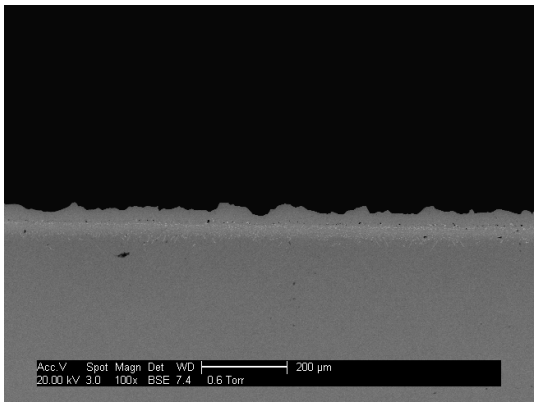

Figure 368 Cross section of CN91 after 380 cycles: general view, undulations

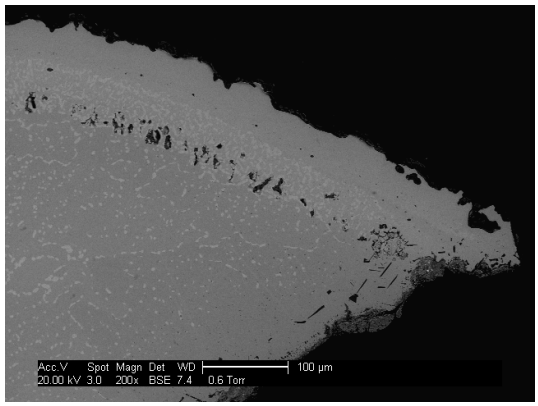

Figure 369 Internal oxidation on the rest of CN91 sample holding stick

Table 27 EDS on CN91 surface and blz21RA after 380 cycles of 1h at 1100°C

At%	Al	Ni	Pt	Cr	Fe	Co	Mo	W	Ta	Ti
CN91-surface	**81**	10	**0.4**	4.6	0.8	1.6	0	0.5	0	1.6
CN91-welding spot	**77**	14	**0.5**	3.4	1.3	1.3	0.4	0.7	0.2	0.8
Blz21RA-general	**67**	16	**0.9**	6.5	0.3	2.2	0	0.6	**1.7**	**4.6**
Blz21RA-platelet	**71**	13	**0.3**	5	0.2	1.9	0	0.1	0.2	**7.8**
Blz21RA-underlying scale	**76**	11	**0.5**	5.4	0	1.7	0	0.5	**0.9**	**3.2**

The EDS analysis of the surfaces is very interesting: there are not so much differences between the two samples (Blz21RA and CN91). The Al level is only 10% lower, and the Cr is 2 % greater on the low mass bondcoat system. The must interesting figure is the Ti content on the surface: an average of 5at%. This is a lot, compared to the 1-1.4at% original content of AM1, and confirms the TiO_2 peak that the XRD gives. It is known that Ti has a good solubility in the Ni_3Al phase of the superalloy. The alpha phase bondcoat has a similar crystallographic cell (tetragonal L10 instead of cubic L12), that could explain the affinity for Ti in the α-phase bondcoat. Moreover, after this time of exposure at high temperature, the structure changed into Pt-modified γ'.

EDS analysis was carried out on the cross sections as well. The two pictures have the same magnification, so one can really see the difference in the microstructure of the 2 oxidised systems (Figure 370 and Figure 371). The compositions of the phases were compared with the composition

in the Ni matrix, at the same depth (same chemical potential, or activity, for diffusion mechanism). Analysis spots are indicated on the following micrograph, and quantitative values are gathered in Table 28, with interest features being highlighted in bold.

The undulation of the surface of CN91 compared to the low mass bondcoat is obvious in these figures as these micrographs are at the same magnification.

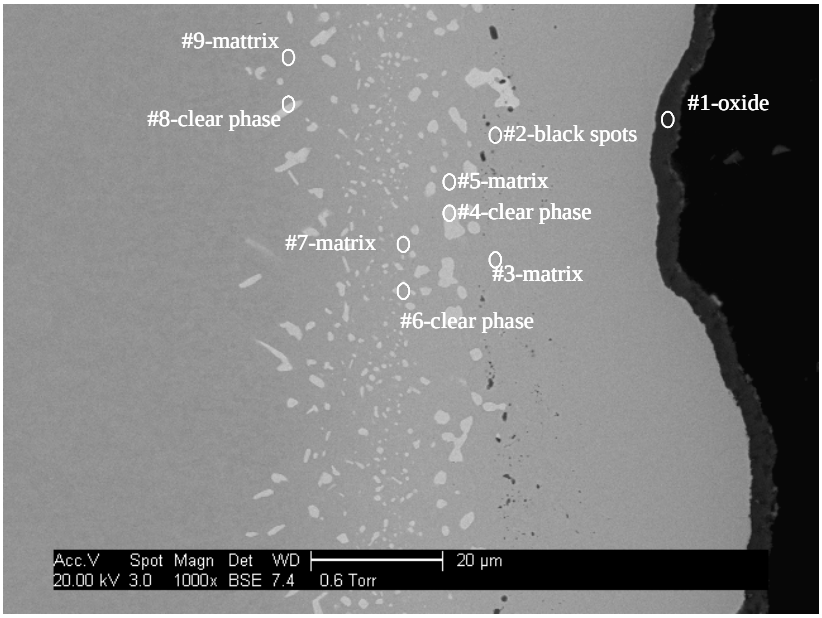

Figure 370 CN91 after 380 cycles at 1100°C magnification x1000

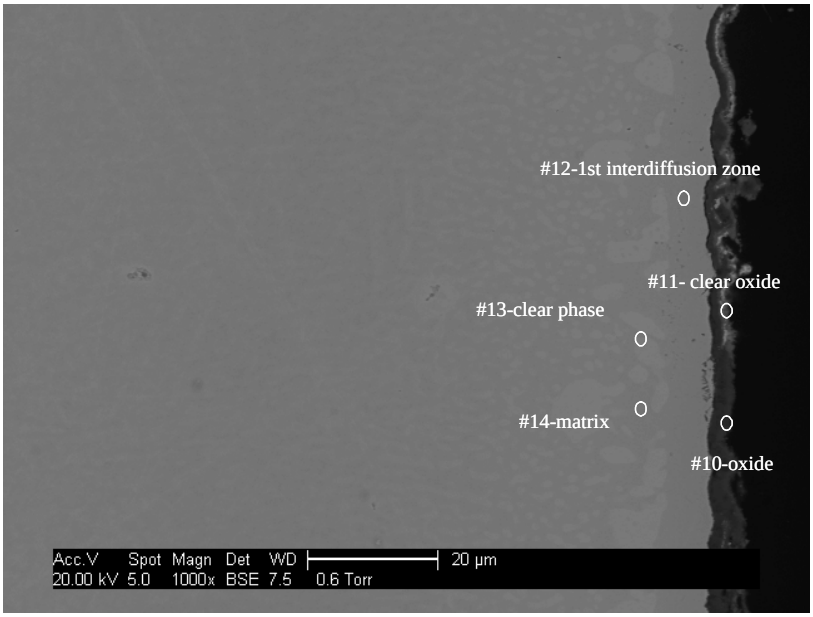

Figure 371 Blz21RA after 380 cycles at 1100°C magnification x1000

Noticable phases were compared with matrix composition at the same depth. On CN91 sample, the Al and Ta rich spot#2 corresponds to the grit line of the sample preparation, whereas spot#4 and #6 is Mo and W rich and corresponds to the μ phases. The typical σ phase (spot#8) precipitates have a misorientation and are W and Mo rich as well.

The analysis spots on Blz21RA show that the clear oxide is richer in Ni and probably contains $NiAl_2O_4$ spinels, and some traces of Ti oxide. Spot#12 and #14 are richer in Cr and lower in Al, Ti and Ta, and therefore correspond to the γ matrix, while it is confirmed that the clear phase is γ', higher in Al, Pt, Ti and Ta. The overall Pt content is rather low, lower than in the CN91 sample underneath the oxide, with an atomic percentage of 2 to 4% whereas it is over 10% in the reference sample (CN91). However, the absence of rumpling of the system is confirmed for the originally α-phase based bondcoat.

Table 28 EDS analysis in at% on CN91 and Blz21RA cross sections, after 380 cycles at 1100°C

sample	Spot	Content	Al	Ni	Pt	Cr	Co	Mo	W	Ta	Ti
CN91	#1	Oxide	62	22	1.7	4.3	2.6	1.6	2.5	1.3	1.8
	#2	Grit line	61	27	**11**	4.0	2.7	0	2.1	**6.2**	0.4
	#3	Matrix	21	52	**11**	6.9	4.8	0	0.8	2.7	0.7
	#4	μ phase	4.6	37	3.3	15	11	**7.2**	**18**	3.2	0.5
	#5	Matrix	13	60	7.8	5.2	5.7	0	1.7	5.1	1.2
	#6	μ phase	8.8	50	3.5	10	8.3	**3.1**	**11**	4.3	1
	#7	Matrix	12	62	5.6	5.1	5.8	0	2.1	6.2	1.3
	#8	σ-phase	5.6	48	1.3	12.5	9.3	**5.2**	**16.5**	3.2	1
	#9	Matrix	9.3	60	2.4	12	8.1	1.4	2.9	6.4	1
Blz21RA	#10	Oxide	**78**	15	0.1	3.1	1.7	0.4	0.3	1.2	0.9
	#11	Spinel	44	**34**	0.2	7.2	5.2	0.3	1.8	3.9	**3.1**
	#12	Matrix	7	61	**2.0**	**12.3**	7.9	1.2	3.3	4.3	1.1
	#13	γ'-phase	8.6	66	**4**	4.9	5.2	0	2.4	6.8	2.2
	#14	γ-phase	5.8	63	**2.4**	**11**	8.1	1.4	3.5	3.3	1.2

VII.1.6 Conclusions of the cyclic oxidation experiment

- ✓ Weight gain curves of the 2.5μm thick α-phase based low mass bondcoats have a better behaviour than B. Saint Ramond 7.5μm thick $PtAl_2$ or PtAl systems.

- ✓ First loss of oxide occurs at 100 1 hour cycles of cyclic oxidationat 1100°C for the α-phase low mass bondcoat developed in this study, 100 cycles for CN91, 20 cycles for PtAl and 50 cycles for $PtAl_2$ in B.Saint Ramond's study[207]
- ✓ The initial growth rate is slower for the α-phase low mass bondcoat.
- ✓ There is a strong needle like growth in the early stages, but the oxide scale is less undulated than on CN91
- ✓ The rapid oxidation weight curve of the CN91 sample tested in this study is likely to be due to the remains of the holding stick which showed a higher oxide scale growth.
- ✓ After 100 1hour cycles at 1100°C: $NiAl_2O_4$ and TiO_2 start to grow. Cr_2O_3 starts after 300 cycles
- ✓ After 200 cycles at 1100°C: there is still some overlay left, but with internal porosity and "pitting" that gives a wavy profile, and voids in the oxide scale. The scale above the overlay is mainly alumina whereas less protective oxides grew where the overlay failed
- ✓ After 300 cycles at 1100°C: there is no bondcoat left, and the oxide shows some clear parts corresponding to a Ni rich oxide. The superalloy substrate has a Pt modified γ/γ' structure. CN91 follows the classical degradation mode[129].

VII.2 Thermal cycling lifetimes of TBC systems

VII.2.1 Lifetimes discussion

Rather than discussing the results as they were gathered chronologically, it has been decided to discuss all the thermal cycling lifetimes together. The bar chart in Figure 372 gives all the data from blz26 to blz40 samples that were TBC coated and then thermal cycled on Pyrox rig at 1100°C. This chart highlights one of the main conclusions of this study: the effect of surface roughness on TBC systems lifetime. Chronologically, experiments were roughly produced from the bottom of the chart to the top.

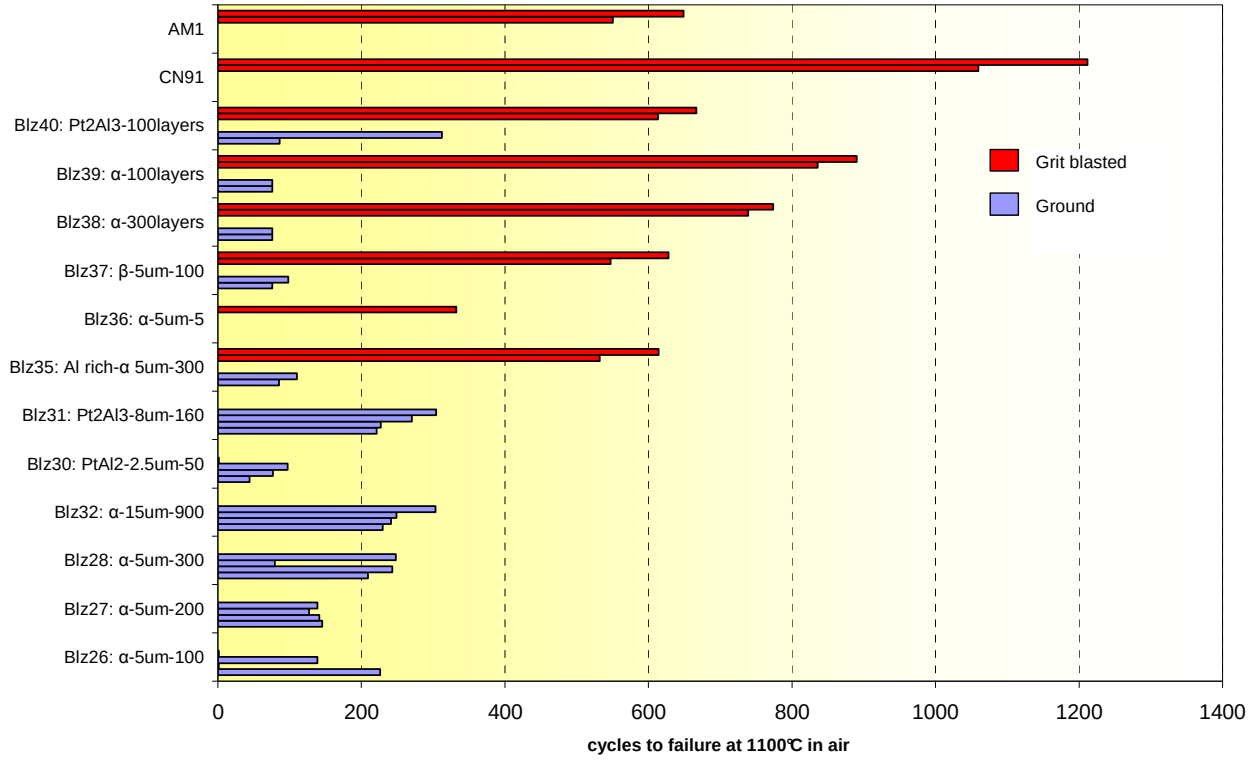

Figure 372 Thermal cycling lifetimes at 1100°C in air, 1h hot dwell on Pyrox rig

One can see at first that the number of multilayers used to manufacture this new bondcoat system does not influence the TBC lifetime. The ground 100 layer system behaves better than the 200 layer, while the 300layer system is the best of these three batches. The benefits of multilayering reaches its limit at 100 layer for 5µm total thickness. The difference in lifetime

between ground and grit blasted samples suggest that neither the multilayering nor composition are the causes of failure of the blue experiments: these are early failures triggered by interfacial mechanical failure (see next part of this chapter).

The batch Blz35 illustrates perfectly this assumption: although samples have the same composition, the same multilayering pattern and the same deposition parameters, those grit blasted prior to bondcoat deposition have lifetimes four to five times greater than those with a ground surface finish. This is confirmed with following batches (blz37 to blz40) where two ground samples were added for reference, with factors 5 to 8 increase in lifetime. The ground sample from batch blz40, which lasted over 300 cycles had a slightly higher lifetime, very likely due to the fact that this sample had a thinner substrate (2mm thick instead of 3mm, due to the lack of substrates at the end of the experimental plan which may reduce the thermal stress in the TBC due to greater creep of the thinner disc).

Batch Blz37 is very interesting as the coating contains only 10at% of Pt like the commercial coating CN91, but it is over 10 times thinner (only 5µm thick), yet it lasts only half the cycles of reference CN91 (around 600 compared to 1150cycles). This is a most promising result regarding to the lifetime/Pt content ratio when making platinum modified bondcoats.

Batch Blz30 however proved to be very disappointing as it contains as much Pt as CN91, spread over 15µm. None of the samples were grit blasted however prior to bondcoat deposition. Lifetimes are not much better than a 5µm low mass bondcoat systems This is likely to be a short life triggered by the surface state, as samples with ground surfaces consistently had lower lives than the grit blasted samples.

Finally, samples from batch Blz36 were also quite interesting. These have only 5 thick layers. The ground sample did not survive the heat treatment in Argon due to the lack of mechanical keying of the coatings. However the grit blasted did survive the heat treatment (see pictures in sample manufacturing chapter), and when topped with a ceramic coating, lifetimes were acceptable, but lower than 100layers systems. The ideal number of layers for manufacturing a low mass α-phase bondcoat therefore lies stands between 5 and 100 layers for 5µm thick coating.

All these results must however be compared and related to the lifetimes achieved using bondcoat free AM1. These were outstanding at circa 600 cycles at 1100°C. These substrates were only grit blasted following the same procedure as samples from other batches. This highlights the outstanding effect of surface preparation. Having no bondcoat reduces as well the “sandwich”

effect of having a very brittle intermetallic above the superalloy but below the TBC. However, the oxidation resistance, after ceramic spalling, of a such system is extremely poor. One can already predict the AM1 samples will have a very oxidised interface once ceramic spallation has occurred at this interface as no alumina forming coating is present at this interface.

VII.2.2 Microstructure analyses and discussions

VII.2.2.1 Samples with a ground substrate prior to bondcoat deposition

VII.2.2.1.1 Cross sections observation

All early failing samples shows the same typical microstructure. This microstructure is very specific and has never been observed in any paper from the literature on oxidation of bondcoats. It is very likely to be induced by the specific deposition process used to manufacture low mass bondcoats, coupled with to the relative smoothness of the substrate.

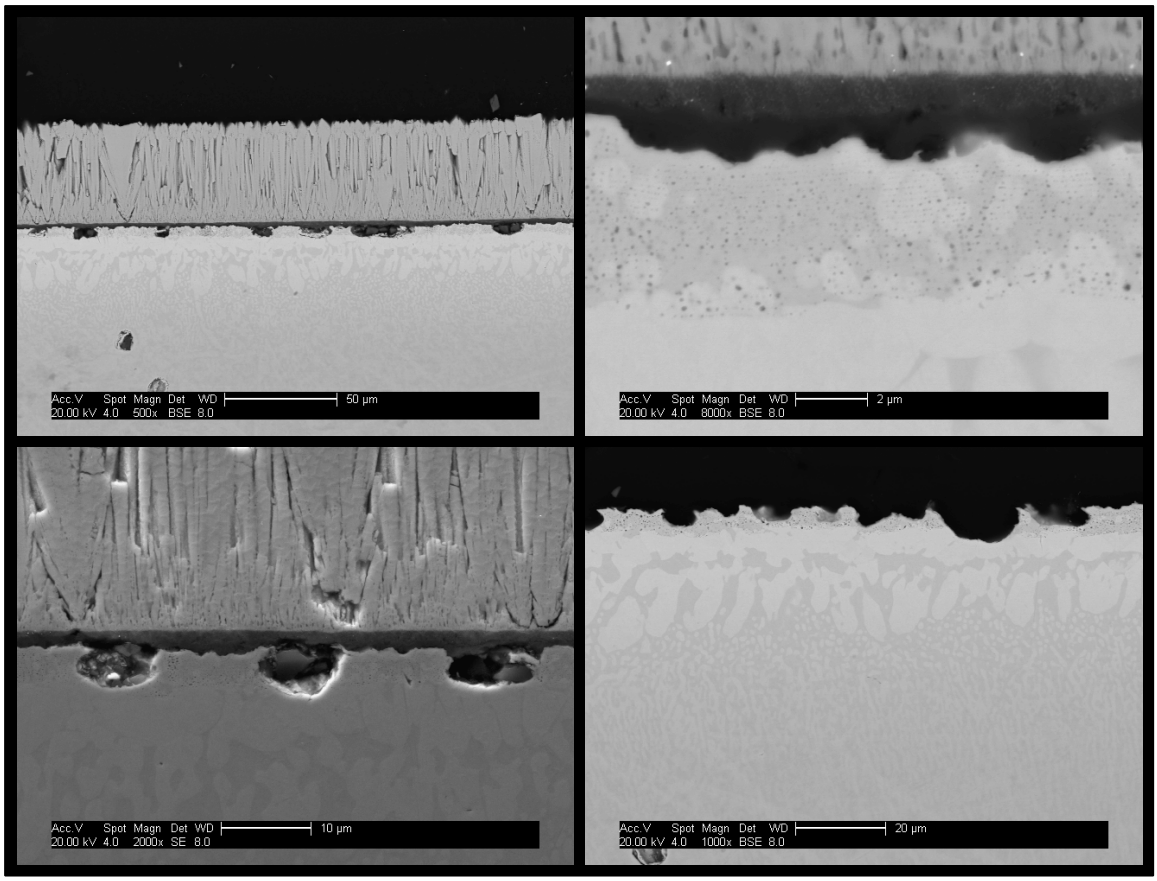

Figure 373 Blz26 after failure following 160 1h cycles at 1100°C at various positions along the cross section

Figure 373 shows various microstructures of the 100 layers system after failure when cycled (typically 150 cycles). As one can see, the overlay bondcoat is very locally consumed, whereas the nanoscale alumina dispersion is still present. The local consumption of the bondcoat leads to the formation of some spinel oxides, and therefore to a reduction of the scale adhesion. These periodic defects are likely to be the cause of the early overall failure of the coating system.

One may notice the metallic phase microstructure degrade to, and then keep the same γ/ γ' biphasic pattern, within the superalloy and the remains of the boncdcoat. At the very top of the overlay , there is zone depleted in Al, emphasised by the appearance of γ phase. This appear darker on these backscattered electron pictures.

For all these systems, with a former ground superalloy, failure of the TBC occurs at the metal/oxide interface, with fracture propagating above the regions of local pits containing spinel oxide phases.

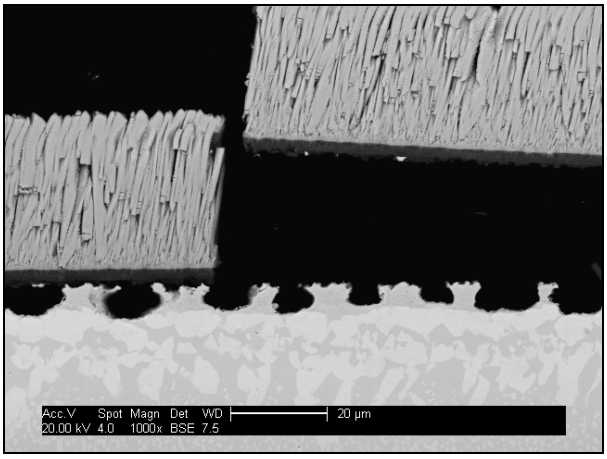

Figure 374 Blz27 after failure; 160 cycles at 1100°C

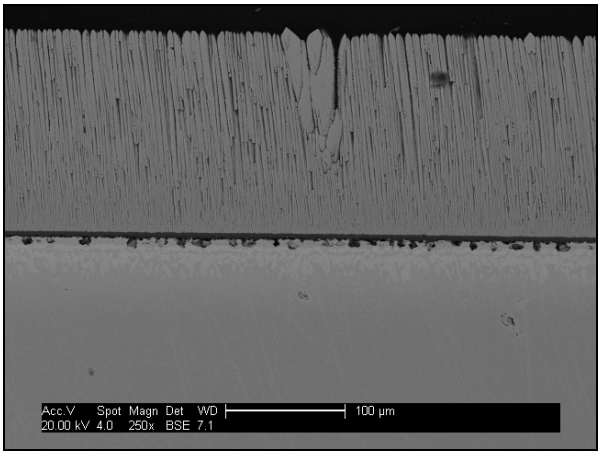

Figure 375 Blz28 after failure; 220 cycles at 1100°C

Figure 374 and Figure 375 show there is no effect from the layer density on the behaviour of these system, Blz27 was a 200 layers system while Blz28 had 300 layers. As discussed in the previous paragraph, differences in lifetime are low between the different coating manufactured, which implies the failure mechanism to be similar in all this family of samples. The TGO is held in place only by remains of bondcoat, until the surface is no longer able to maintain adherence of the scale. The uniformity of the TGO thickness confirms the consistency of this failure mechanism: it is steady at 2.5µm for all the analysed samples.

VII.2.2.1.2 Model of failure of low mass bondcoat on ground substrate due to cyclic oxidation

This very specific behaviour may be explained by the model in Figure 377 with a sketch of the ageing of the bondcoat at various steps. The periodicity of the voids in the aged coating approximately corresponds to the periodicity of the polishing marks of the ground surface. The valleys formed during the grinding induce defects in the coating, as outlined in Figure 378. At these defects , one can expect cracks in the TGO, implying an important local oxygen activity at the bondcoat interface, increasing the oxidation kinetics. Another possible source for the periodicity of these defect is that the diffusion path are following the mud flat cracks of the as deposited low mass bondcoat. These cracks are induced by the in-plane volume shrinkage during the intermetallic formation, as is evident for the 15µm thick sample (Figure 376).

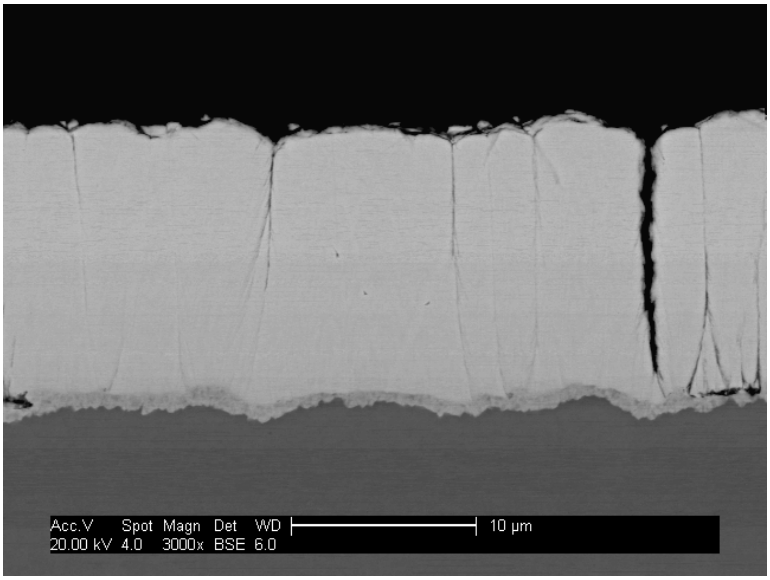

Figure 376 Mud flat cracks periodic network on blz32 sample

The diffusion of oxygen is greater through these short paths, with a greater aluminium consumption. At the bottom of these defects, there is a possible formation of less dense and weak oxides due to lower Al content, as observed on cross sections (e.g. bottom left picture of Figure 373). The typical “pear shape” of the recurrent defects (e.g. in Figure 374) could be explained by a local in plane diffusion of metallic species, favouring the former linear pattern of the coating, formed by the original layer deposition, prior to reaction heat treatment.

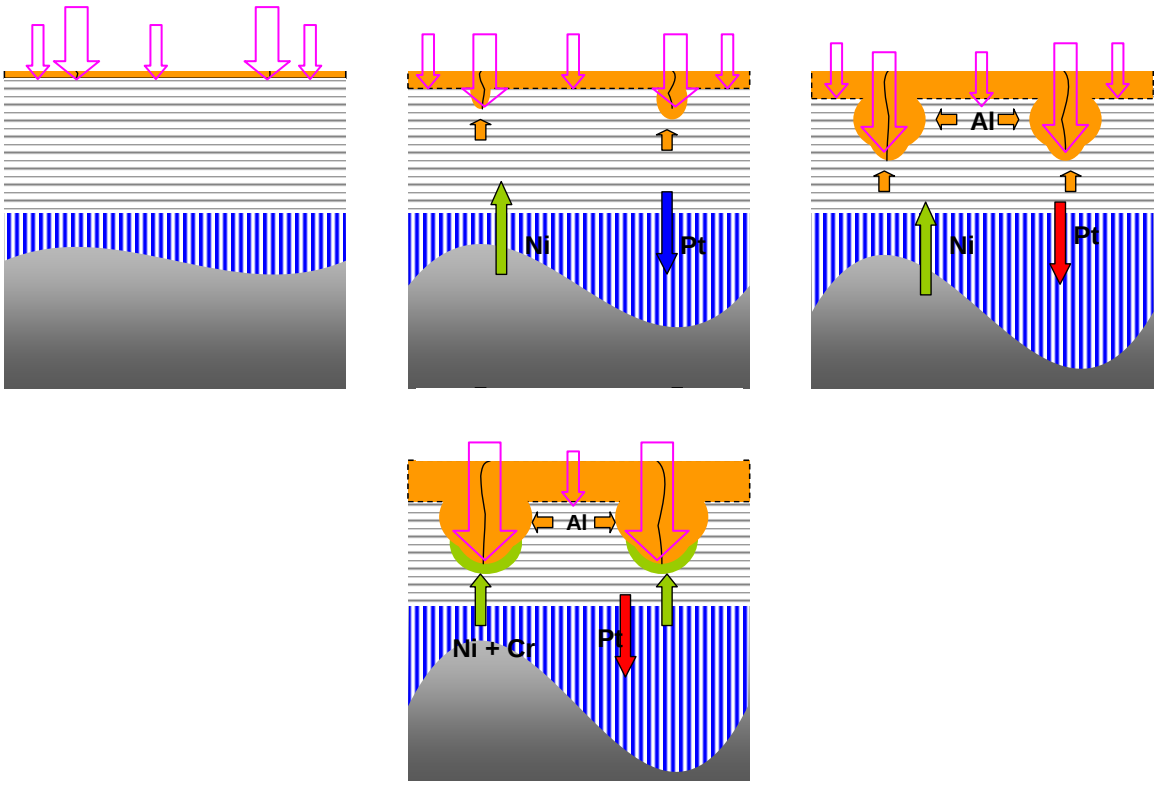

Figure 377 Possible failure model for low mass bondcoat on ground surfaces

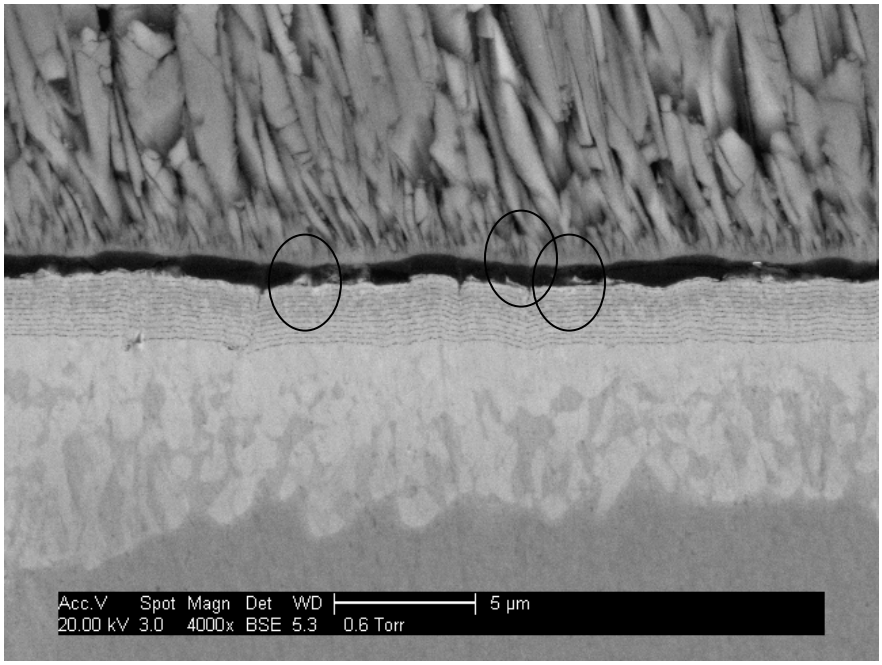

Figure 378 As deposited system (25 layers): presence of grinding defects

The ageing behaviour is not influenced by the original composition of the coating being the α-$NiPt_2Al$ phase. Actually, it has already been shown the α-phase coating is not stable over one hour at 1100°C (See chapter on Isothermal Oxidation). Moreover, Figure 379 and Figure 380 were taken from the ground sample of Blz37 batch, which was based on β-(Ni,Pt)Al compound: where behaviour is the same as previous systems containing originally α-phase.

On this sample, the γ/γ' structure is observed under the TGO, whereas it was not observed under isothermal oxidation after 50h (see previous chapter). This sample was cycled for over 100cycles at 1100°C: the degradation of β-(Ni,Pt)Al into Pt modified γ' occurs also when it is deposited with low mass bondcoat route, as has been observed in the literature for CVD diffusion bondcoats[129].

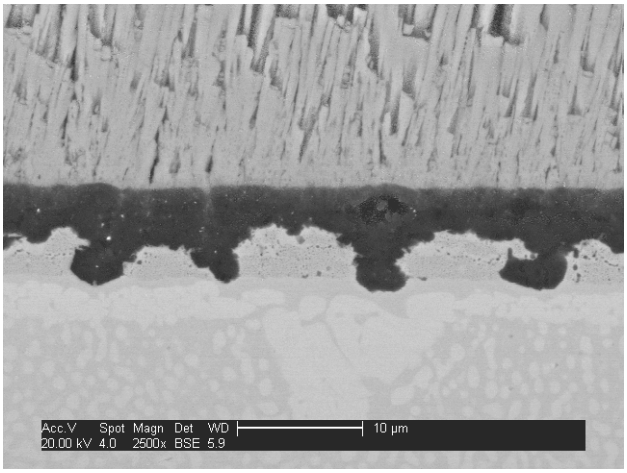

Figure 379 Ground sample from Blz37 failure

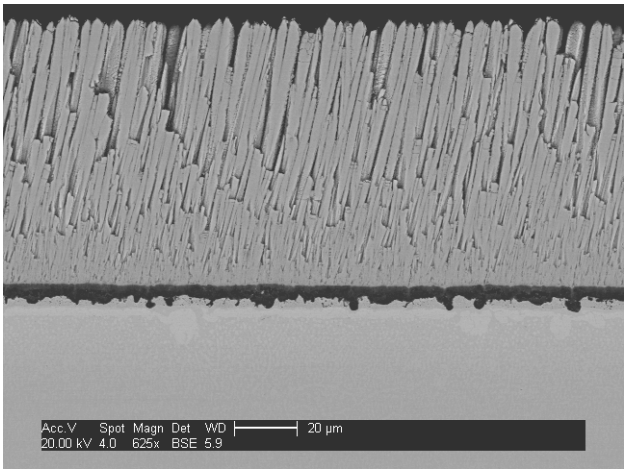

Figure 380 Ground sample from Blz37 failure (general view)

VII.2.2.2 Samples with grit blasted substrate

When the substrate is grit blasted prior to deposition of the low mass bondcoat, it was seen that the lifetime before spalling of the ceramic is highly enhanced.

Cross sections of Blz38 after cycling are shown hereafter: this sample had 300 layers deposited over 5µm total thickness, and the ceramic failed after 780 cycles at 1100°C. Sections of as deposited and cycled system are shown in Figure 381, with two magnifications (the bottom left picture is taken in BSE mode).

The oxide that is found at failure is thicker than for ground systems. It appears to be constituted of two parts: one corresponding to the former overlay, and one corresponding to the

interdiffusion zone. In between, one can see voids forming, as some less protective oxides such as Ni/Al or Ti/Al spinel occur. The aluminium activity in the first microns of metal is very low ([Al]=4at% and [Cr]=8at%) which is at the limit of the formation of an alumina scale. This two stage oxide growth is confirmed to be important in the failure when focusing on the spalling interface (Figure 382), with a two parts oxide.

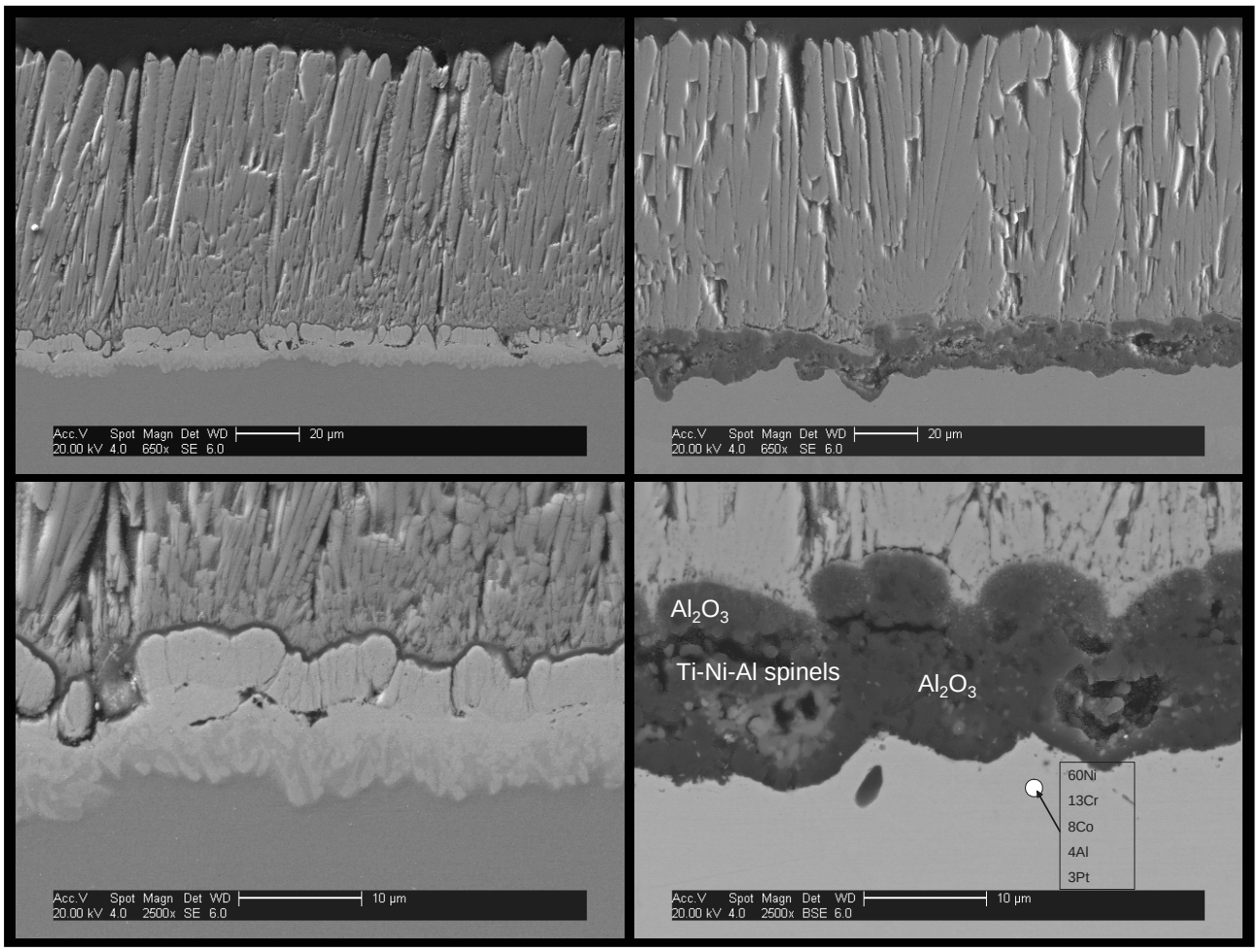

Figure 381 Two views of Blz38 grit blasted sample as deposited (left) and after 740 cycles (right).

Moreover, some features, often referred to "zirconia pegs" in the literature were observed. The mechanical griping of the YSZ onto the TGO is thought to be only a consequence of the as deposited roughness of the system: these pegs never get through the inner TGO scale.

The microstructure of the metal shows a Al poor Pt modified γ/γ' structure. The first microns are too poor in Al to contain γ': the first islands of this intermetallic appear 20 microns under the metal oxide interface. One can notice as well that no TCP phases are observed, as was already discussed before. Moreover, the bondcoat does not rumple and the failure occurrs within the TGO (actually between the two layers of the duplex TGO). This is thought to be due to the

formation of less tough spinel oxides rather than due to local shear stress as induced by undulations.

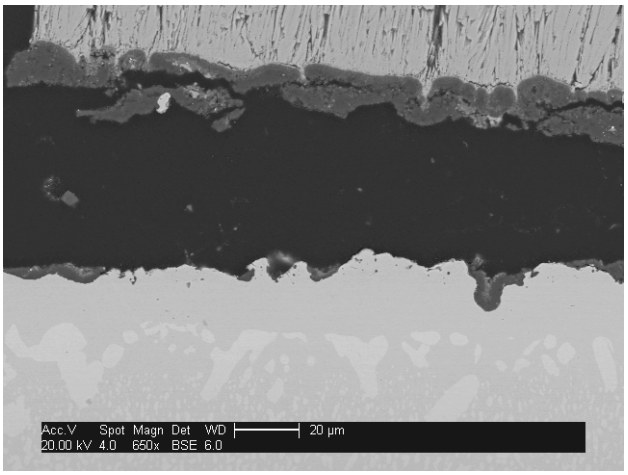

Figure 382 Blz38 failure: duplex TGO

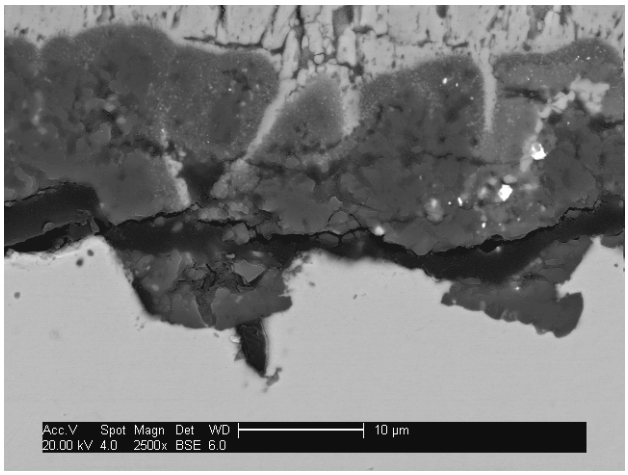

Figure 383 Blz38 zirconia pegs within the TGO

A possible model for the ageing behaviour of these systems is given in Figure 384:

✓ Prior to oxidation, the system has a convoluted bondcoat due to the grit blasting, with a thin TGO appearing during the ceramic deposition. The interface between the bondcoat and the superalloy presents some defects (voids+grit particles)

✓ Then the bondcoat oxidises during the thermal cycling. The Al content under the bondcoat reduces, so the γ' precipitation front grows deeper into the substrate. A γ Al depleted region is formed above this but below the oxide scale.

✓ When the bondcoat is entirely consumed, the first microns of the substrate (Pt γ/γ') system oxides.

✓ When this system gets to be poor in Aluminium, spinels start to form at the former superalloy/bondcoat interface, leading to the failure of the whole system

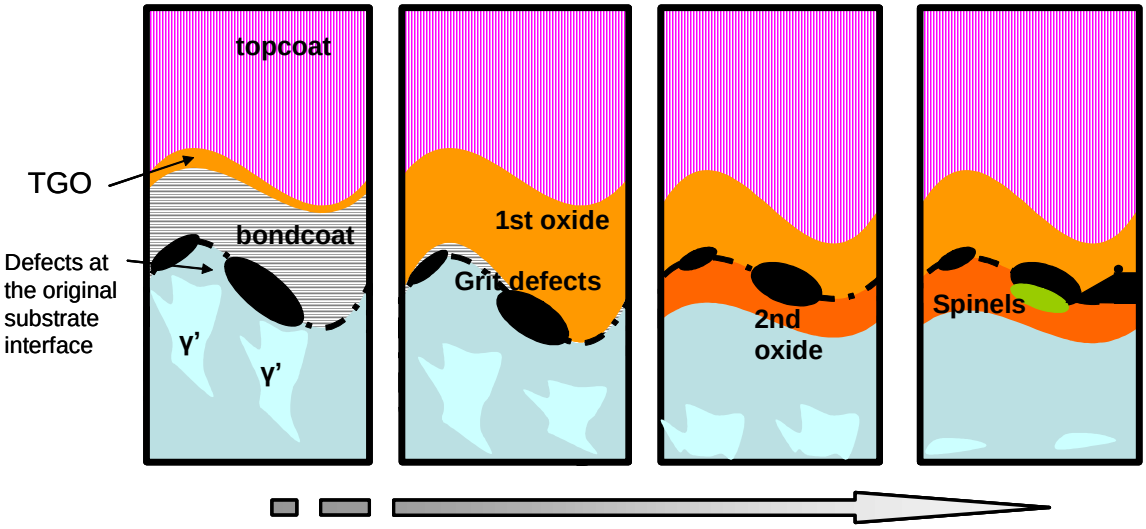

Figure 384 Possible failure mechanism for grit blasted samples

The bondcoat free AM1 samples display excellent lifetimes when compared with other systems. The observation of microstructures after failure shows that some alumina was formed (the TGO is over 10 microns thick). However, the fast growth of the oxide on this alloy led to the formation of vacancy induced voids under the scale. Some internal oxidation was also observed (chromia and Ni/Al spinel oxides). These excellent lifetimes are still not fully understood, but might be linked to the low sulphur content of this superalloy. However, this experiment shows the critical role of the surface roughness on TBC failure lifetime. How the surface state can reduce in plane stress, allowing thicker scales to grow. In this case, the crack may be running through a Cr_2O_3 rich region. This would mean a chemical failure.

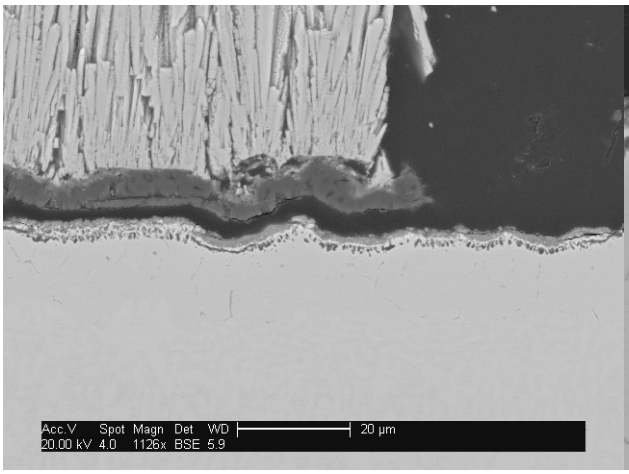

Figure 385 Bondcoat free AM1 failure

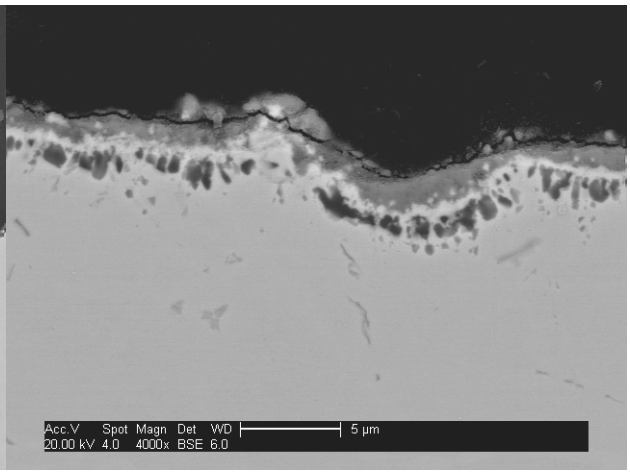

Figure 386 Bondcoat free AM1 failure

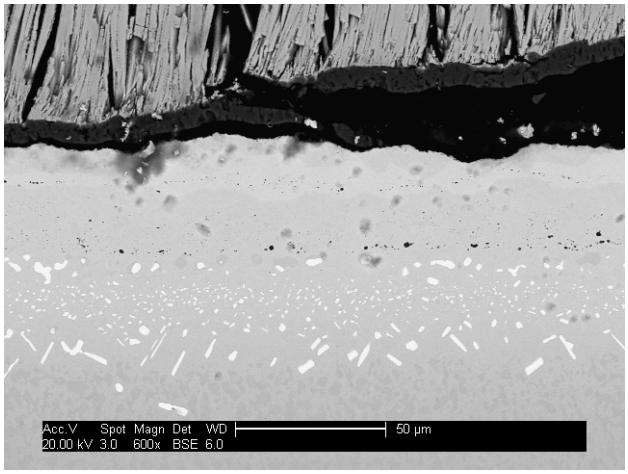

Figure 387 CN91 failure profile

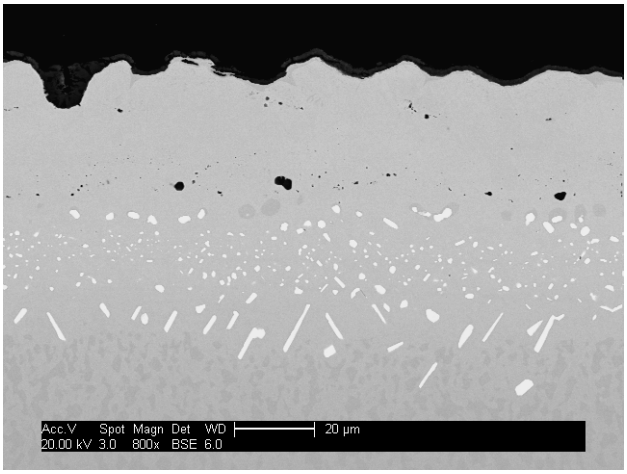

Figure 388 CN91: protective reoxidation and TCP's

In these cyclic oxidation tests, the failure of the reference CN91 sample is similar to the behaviour reported in the literature[34;128]. Failure occurs at the bondcoat/TGO interface. Thanks to the Al reservoir, no spinel oxides were observed: failure is mechanically induced: TGO growth rate + surface rumpling. After over 1100 cycles at 1100°C, some β-phase is left (roughly 10 µm) over a Pt modified γ/γ' structure with precipitation of TCP phases, extending into the substrate.

VII.2.3 Thermal cycling of α-phase bondcoat based TBC's: Conclusions and future works

These thermal cycling experiments gave some information on α phase based coatings. Although there structures transforms rapidly into γ/γ' system, the process route permits the modification of the alloy surface composition, which results in the coating exhibiting a characteristic behaviour. At first, a fast oxidation is observed with formation of transient alumina taking place. This is unlike isothermal oxidation, and thought to be due to cracking of the oxide scale upon cooling, promoting the transient oxidae cationic growth. This step last for approximately 5 hours at 1100°C. Then the protective α-alumina grows on the system. The first oxide loss appearing after 100 cycles at 1100°C.

With a ceramic top coat, lifetime is obviously driven by the surface finish. For ground sample, periodic defects such as grinding marks or mud flat cracks initiate fast diffusion short circuit paths leading to a general failure of the system, typically before 200 cycles at 1100°C. When the substrate is grit blasted prior to bondcoat deposition, failure is chemically induced by the impoverishment in Al and the formation of spinel oxides underneath the alumina, which are less tough oxides, at the former bondcoat/superalloy interface. An interesting point on the manufacturing point of view is the fact that carrying out the annealing in situ of the EB-PVD coater during heating up did not influence the TBC lifetime.

Some works could be very interesting to carry out in order to improve the understanding of these systems:

- ✓ Carrying out Raman spectroscopy for stress comparison between a ground and a grit blasted system and better characterisation of transient alumina.
- ✓ Manufacturing a β-phase bondcoat of 60µm thick with the same deposition route as blz37: this is the most promising lifetime/Pt content ratio.
- ✓ Manufacture a α-phase bondcoat of 15µm thick on grit blasted surface: this would be the ultimate system regarding to Pt content for a α-phase bondcoat.
- ✓ Adding a fourth element such as reactive elements (Hf, Y, or Zr) known as improving the scale adhesion. This process would allow to have an excellent control of the content throughout the coating thickness.

Chapter VIII

Conclusions and Future works

The use of Thermal Barrier Coatings for high temperature protection of gas turbines parts is a key issue for manufacturers. Although it has been used for over a decade, many challenges still remain in understanding failure mechanisms, in developing new materials, and new manufacturing routes. This domain of research and development is highly competitive as it is often supported by industrial partners.

This project started from two points. At first, a concept for manufacturing intermetallic compound coatings which was already partially developed on platinum aluminides at Cranfield. Secondly a new compound from the (Ni-Pt-Al) system which could be used as a coating for high temperature protection of superalloys, and/or as a bondcoat for TBC systems.

In the present work, physical properties of this new compound, called α-phase, were studied. The equilibrium stability field at high temperature was investigated with over ten samples of bulk material produced. These results confirm the work which was carried out at the same time by B.Gleeson: it is a tetragonal $L1_0$ phase with a large phase field at 1100°C, centred on the $NiPt_2Al$ stoichiometry. The melting point of this compound was measured for various compositions: it is relevant with surrounding compounds although it is lower than NiAl which is commonly used for high temperature protection. The energy released during the formation of the intermetallic from metallic state (sputtered multilayers) was measured by DSC, and is as well slightly lower in absolute than enthalpy of formation of other intermetallics, suggesting α-phase is not as stable as other known compounds from the (Ni-Al) or the (Pt-Al) systems.

Manufacturing such a material as a coating was not straightforward. The concept of the low mass bondcoat process is to sputter thin layers of pure metal onto the substrate, followed by an annealing under protective atmosphere in order to trigger the reaction of the metallic layers into the expected intermetallic compound.

Such coatings were at first manufactured on Nimmonic75 substrates. It appears that the loss of adherence of the film due to volume shrinkage during the reaction could not be overcome. Systems up to 25 layers for a 5μm total thickness were manufactured in order to improve coatings homogeneity, with no success. Changing heat treatment parameters did not improve adherence either. However, the synthesis of α-phase coatings by this route was proven to be possible. An important point revealed by these preliminary works is the consequence of the alternation pattern of metal multilayers in the resulting compound, primarily due to the fact that Al is the predominant diffusing species in the reacting system.

Simply changing the substrate material to Ni-based superalloy (AM1) did not improve the adherence: after reaction of the layers, voids at the former Al layer dramatically reduces the coating toughness.

Therefore, the deposition process was rethought, with lower deposition rates in order to reduce stress build up while depositing the metallic layers, and increasing even more the number of layer by an automated rotation of the substrate holder in the sputtering chamber. Calibration was as well improved compared to conventional thin film methods. This overhaul of the process enabled the production of numerous samples on sound bases. This manufacturing route is now "on shelf" for reproducible and controlled production of α-phase based coatings, but as well for β-(Ni-Pt)Al or platinum aluminides with the same low mass bondcoat concept. Over 80 samples of coated superalloy discs were produced with varied deposition parameters, such as number of layer, total thickness, surface roughness or coating composition.

Some of these samples were exposed to isothermal oxidation, at 1100°C in air for relatively short exposure times (1 to 50 hours). The ageing behaviour of these systems is not conventional, due to the original manufacturing route. The voids created during the reaction of the metallic layers are anchored within the coating, and do not evolve with time at temperature. However, the chemistry of the coating changes drastically with time, due to the high content of Pt. Platinum diffuses rapidly to the substrate, resulting in a global shift in composition to a Pt modified γ/γ' microstructure (after 1h only at 1100°C for the 5µm thick coatings). Some traces from the superalloy substrate are also observed within the coating such as Titanium based compounds (AM1 is a Titanium rich superalloy). Another interesting point is that no transient alumina could be measured by XRD, even after short time exposure at 1100°C in air.

Under thermal cycling at 1100°C, bare coatings behave slightly differently. Transient alumina is observed, with typical needle like scale. However, weight gain during the first hours is not as important as reference commercial coating CN91. After 100 cycles of 1 hour at 1100°C, the scale starts spalling, with the formation of less protective oxides due to the low aluminium reservoir of such coatings. After 400 cycles of 1 hour exposure, no bondcoat is left: it was all consumed by oxidation, only remains the oxide scale which grew on this Pt modified γ/γ' structure. Another feature of these types of bondcoat compared to conventional diffusion coating is the absence of TCP phases which are commonly described as reducing the mechanical properties of the superalloy.

Over 40 samples of low mass bondcoat topped with standard EB-PVD YSZ were produced and thermal cycled at 1100°C. Thermal cycling of TBC's is the conventional benchmarking experiment as it exposes TBC to high temperature oxidation, and to thermal fatigue due to CTE mismatches between involved materials. Surface preparation of the substrate prior to deposition of the bondcoat is the main factor affecting lifetime. Samples with ground substrate fail due to mechanical failure: periodic preferential oxidation paths are induced by the grinding defects, inducing global lack of adherence of the topcoat. A model for this mechanism was proposed. Whatever the composition or the thickness of the coating, the ceramic fails roughly after 200 cycles. Samples with grit blasted substrate last over 600 cycles (maximum is close to 900 cycles). This is due to the fact that mechanical gripping of the ceramic is enhanced, leading the system to fail chemically: the overlay bondcoat is entirely consumed. Another model was proposed for this type of failure.

The work presented in this thesis opens many directions for further investigations. At first, Raman spectroscopy could be used for a better understanding of the oxidation mechanism. This would give much information on the presence of transient oxides, and will enable to compare stress levels of the oxide scale grown on this new type of coating with conventional systems. Further TGA experiments would as well improve the knowledge on oxidation kinetic of α-phase (on bulk material or double sided coatings).

On a manufacturing point of view, it would be interesting to add a fourth material to the versatile process developed during this thesis. Reactive elements such as Zr or Hf would most certainly reduce the oxidation rate of α-phase based coating. Moreover, a diffusion barrier such as those described in the first chapter of this thesis may be added in order to reduce the interdiffusion with the substrate, and then sustaining the α-phase for longer time at high temperature.

At last, in order to finally conclude about the benchmarking of low mass bondcoat based TBC systems, it would be very interesting to manufacture a 15 µm thick α-phase based low mass bondcoat, with grit blasted substrate. This would give the actual lifetime comparison with commercial coatings, for the same amount of deposited platinum. A 60 µm thick low mass bondcoat of β(Ni,Al)Pt would as well give some information: it was the most promising lifetime/Pt content ratio.

Chapter IX

Figures, Tables & References

List of Figures

List of Tables

Reference List

1. Goward, G.W. Progress in coatings for gas turbine airfoils. Surface and Coatings Technology **108-109**, 73-79 (1998).

2. Wood, J.H. and Goldman, E.H. Protective coatings. In Simms, C.T., Stoloff, N.S., and Hagel, W.C. (eds.) Superalloys II - High Temperature Materials For Aerospace and Industrial Power. Wiley, New York (1987).

3. Bunshah, R.F. Handbook of deposition processes for films and coatings- Science technology and applications. William Andrew, Noyes (1994).

4. Pomeroy, M.J. Coatings for gas turbine materials and long term stability issues. Materials and Design **26**, 223-231 (2005).

5. Nicholls, J.R. and Stephenson, D.J. High temperature coatings for gas turbines. In Westbrook, J.H. and Fleisher, R.L. (eds.) Intermetallic compounds, principles and practice, volume 2. John Wiley and Sons, Chichester (1995).

6. Warnes, B.M. and Punola, D.C. Clean diffusion coatings by CVD. Surface and Coatings Technology **94-95**, 1-6 (1997).

7. Choy, K.L. Chemical vapour deposition of coatings. Progress in Materials Science **48**, 57-170 (2003).

8. Jackson, M.R. and Rairden, J.R. The Aluminization of platinum and platinum-coated IN-738. Metallurgical Transactions A **8A**, 1697-1707 (1977).

9. Mazars, P. Les procédés industriels de protection des superalliages. Traitements Thermiques **149**, 37-42 (1980).

10. Bunshah, R.F. Evaporation: processes, bulk microstructures and mechanical properties. In Bunshah, R.F. (ed.) Handbook of deposition technologies for films and coatings. Knovel ,(1994).

11. Bunshah, R.F. Deposition technologies: an overview . In Bunshah, R.F. (ed.) Handbook of deposition technologies for films and coatings. Knovel,(1994).

12. Thornton, J.A. and Greene, J.E. Sputter deposition processes. In Bunshah, R.F. (ed.) Handbook of deposition technologies for films and coatings. Knovel,(1994).

13. Chapman B. Glow discharge processes. Wiley-Interscience, New York (1980).

14. Rossnagel, S. Sputtering and sputter deposition. In Seshan, K. (ed.) Handbook of thin-film deposition processes and techniques: principles, methods, equipment and applications.(2002).

15. Holland, L. A review of plasma process studies. Surface Technology **11**, 145-169 (1980).

16. Nadel, S.J. *et al.* Advanced generation of rotatable magnetron technology for high performance reactive sputtering . Thin Solid Films **502**, 15-21 (2006).

17. Mochvan, B.A. and Demichishin, A.V. Study of the structure and properties of thick vacuum condensates of nickel, titanium, tungsten, aluminium oxide and zirconium oxide. Physics Metals Metallurgic **4**, 83-90 (1969).

18. Thornton. J.A. Influence of apparatus geometry and deposition conditions on the structure and topography of thick sputtered coatings. Journal of vacuum science and technology **11**, 666-670 (1974).

19. Tucker, R.C. Advanced thermal spray deposition techniques. In Bunshah, R.F. (ed.) Handbook of deposition technologies for films and coatings. Knovel,(1994).

20. Zhang, Y.J. *et al.* A comparative study of DS NiCrAlY coating and LPPS NiCrAlY coating. Materials Science and Engineering A **360**, 65-69 (2003).

21. Zhang, Y.J., Sun, X.F., Guan, H.R., and Hu, Z.Q. 1050°C isothermal oxidation behavior of detonation gun sprayed NiCrAlY coating. Surface and Coatings Technology **161**, 302-305 (2002).

22. Schwartz, M. Deposition from aqueous solution: an overview. In Bunshah, R.F. (ed.) Handbook of deposition technologies for films and coatings. Knovel,(1994).

23. Curran, J.A. and Clyne, T.W. The thermal conductivity of plasma electrolytic oxide coatings on aluminium and magnesium. Surface and Coatings Technology **199**, 177-183 (2005).

24. Goward, G.W. and Boone D.H. Mechanisms of formation of diffusion aluminide coatings on nickel base superalloys. Oxidation of metals **3**, 475-495 (1971).

25. Birks, N., Meier, G.H., and Pettit, F.S. Introduction to the high temperature oxidation of metals. Cambridge University Press, Cambridge (1983).

26. Pichoir R. Influence of the mode of formation on the oxidation and corrosion beahviour of NiAl type protective coatings. In Holmes, D.R. and Rahmel, A. (eds.) Materials and coatings to resist high temperature corrosion. Applied Science publishers,(1978).

27. Goward, G.W. and Cannon, W.R. Pack cementation coatings for superalloys: a review of history theory and practice. Journal of engineering for gas turbines and power **110**, 150-153 (1988).

28. Smith, A.B., Kempster, A., and Smith, J. Characterisation of aluminide coatings formed on nickel base superalloys by vapour aluminising. In Nicholls, J.R. and Rickerby, D.S. (eds.) High temperature surface engineering. IOM communications, London (2000).

29. Nicholls, J.R. Designing oxidation-resistant coatings. JOM **52**, 28-35 (2000).

30. St.Pierre, G.R. Advanced materials and coatings for energy conversion systems. Energy Conversion Management **38**, 1035-1041 (1997).

31. Stringer, J. Coatings in the electricity supply industry: past, present, and opportunities for the future. Surface and Coatings Technology **108-109**, 1-9 (1998).

32. Lehnert, G. and Meinhardt, H.W. A new protective coating for nickel alloys. Electrodeposition and surface treatment **1**, 189-267 (1973).

33. Angenete, J. and Stiller, K. A comparative study of two inward grown Pt modified Al diffusion coatings on a single crystal Ni base superalloy. Materials Science and Engineering A **316**, 182-194 (2001).

34. Angenete, J. and Stiller, K. Comparison of inward and outward grown Pt modified

aluminide diffusion coatings on a Ni based single crystal superalloy. Surface and Coatings Technology **150**, 107-118 (2002).

35. Streiff, R., Cerclier, O., and Boone, D.H. Structure and hot corrosion behavior of platinum-modified aluminide coatings. Surface and Coatings Technology **32**, 111-126 (1987).

36. Krishna, G.R., Das, D.K., Singh, V., and Joshi, S.V. Role of Pt content in the microstructural development and oxidation performance of Pt-aluminide coatings produced using a high activity aluminizing process. Materials Science and Engineering A **251**, 40-47 (1998).

37. Purvis, A.L. and Warnes, B.M. The effect of platinum concentration on the oxidation resistance of superalloys coated with single-phase platinum aluminides. Surface and Coatings Technology **146-147**, 1-6 (2001).

38. Benoist, J., Badawi, K.F., Malié, A., and Ramade, C. Microstructure of Pt-modified aluminide coatings on Nibased superalloys. Surface and Coatings Technology **182**, 14-23 (2004).

39. Nicholls, J.R. Advances in coating design for high performance gas turbines. MRS bulletin **September**, 659-670 (2003).

40. Wang, B., Gong, J., Sun, C., Huang, R.F., and Wen, L.S. The behavior of MCrAlY coatings on Ni_3Al-base superalloy. Materials Science and Engineering A **357**, 39-44 (2003).

41. American Society for Metals. Metals Handbook 8th edition volume 8 : Metallography, structures and phase diagrams. ed, Taylor Lyman, (1973).

42. Nash, P. and Kleppa, O. Composition dependance of the enthalpies of formation of NiAl. Journal of Alloys and Compounds **321**, 228-231 (2001).

43. Paul, A., Kodenstov, A.A., and van Loo, F.J.J. On diffusion in the B-NiAl phase. Journal of Alloys and Compounds **403**, 147-153 (2005).

44. Ross, E.W. and Sims, C.T. Nickel base alloys. In Sims, C.T., Stoloff, N.S., and Hagel, W.C. (eds.) Superalloys II - High Temperature Materials For Aerospace and Industrial Power. Wiley, New York (1987).

45. Jiang, C. and Gleeson, B. Site preference of transition metal elements in Ni3Al. Scripta

Materialia **55**, 433-436 (2006).

46. Jiang, C., Sordelet, D., and Gleeson, B. Site preference of ternary alloying elements in Ni3Al: a first principle study. Acta Materialia **54**, 1147-1154 (2006).

47. Colgan, E.G. Phase transformation and dissociation in the thin film Pt/Al system. Journal of Applied Physics **62**, 1224-1231 (1987).

48. Brindley, W.J. and Miller, R.A. TBCs for better engine efficiency. Advanced MAterials and Processes **8**, 29-36 (1989).

49. Stoeven, D. and Funke, C. Directions of the development of thermal barrier coatings in energy applications. Materials Processing Technology **92-93**, 195-202 (1999).

50. Alperine, S. , Derrien, M., Jaslier, Y., and Mevrel, R. Thermal barrier coatings: the thermal conductivity challenge. Proceedings of the 85th Meeting of the AGARD Structures and Materials Panel. 11-20. 98. Neuilly sur Seine, AGARD.

51. Nicholls, J. R., Lawson, K. J., Rickerby, D. S., and Morrell, P. Advanced processing of TBCs for reduced thermal conducivity. Proceedings of the 85th Meeting of the AGARD Structures and Materials Panel. 61-69. 98. Neuilly su Seine, AGARD.

52. Padture, N.P., Gell, M., and Jordan, E.H. Thermal barrier coatings for gas-turbine engine applications. Science **296**, 280-284 (2002).

53. Schulz, U. *et al.* Some recent trends in research and technology of advanced TBCs. Aerospace Science and Technology **7** , 73-80 (2003).

54. Bose, S. and DeMasi-Marcin, J.T. TBC experience in gas turbine engines at Pratt &Whitney. Thermal Barrier Coating Workshop, NASA, Lewis Research Centre **3312**, 63-78 (1995).

55. Morrell, P. and Rickerby, D. S. Advantages/Disadvantages of various TBC systems as perceived by the engine manufacturer. Proceedings of the 85th Meeting of the AGARD Structures and Materials Panel. 20.1-20.9. 98. Neuilly su Seine, AGARD.

56. Nicholls, J.R., Jaslier, Y., and Rickerby, D.S. Erosion and foreign object damage of TBCs. Materials Science Forum **251-254**, 935-948 (1997).

57. Raetzer-Scheibe, H.J., Schulz, U., and Krell, T. The effect of coating thickness on the thermal conductivity of EB-PVD PYSZ TBCs. Surface and Coatings Technology **200**, 5636-5644 (2006).

58. Schulz, U., Menzebach, M., Leyens, C., and Yang, Y.Q. Influence of substrate material on oxidation behaviour and cyclic lifetime of EB-PVD TBC systems. Surface and Coatings Technology **146-147**, 117-123 (2001).

59. Voisey, K.T. and Clyne, T.W. Laser drilling of cooling holes through plasma sprayed TBCs. Surface and Coatings Technology **176**, 296-306 (2004).

60. Lugscheider, E. *et al.* EB-PVD TBCs on laser drilled surfaces for transpiration cooling. Surface and Coatings Technology **133-134**, 49-53 (2000).

61. Laschet, G. Homogenization of the thermal properties of transpiration cooled multi-layer plates. Computer Methods in Applied Mechanics and Engineering **191**, 4535-4554 (2002).

62. Kaysser, W. A., Peters, M., Fritscher, K., and Schulz, U. Processing, characterisation and testing of EB-PVD TBC. Proceedings of the 85th Meeting of the AGARD Structures and Materials Panel. 91-101. 98. Neuilly-sur-Seine, AGARD.

63. Rigney, D. V., Viguie, R., and Wortman, D. J. PVD TBC application and process development for aircraft engines. Thermal Barrier Coating Workshop, 1995. NASA conference publication 3312.

64. Schiller, S. , Heisig, U., and Panzer, S. Electron beam technology. John Wiley and Sons, (1982).

65. Schulz, U., Fritscher, K., Ratzer-Schreibe, H. J., Kaysser, W. A., and Peters, M. Thermocyclic behaviour of microstructurally modified EB-PVD TBC. Proceedings of the 4th International Symposium on High Temperature Corrosion and Protection of Materials. 2, 957-964. 97. Switzerland, Trans Tech Publications.

66. Schulz, U., Terry, S.G., and Levi, C.G. Microstructure and texture of EBPVD TBCs grown under different rotation modes. Materials Science and Engineering A **360**, 319-329 (2003).

67. Evans, A.G., Mumm, D.R., Hutchinson, J.W., Meier, G.H., and Pettit, F.S. Mechanisms

controlling the durability of thermal barrier coatings. Progress in Materials Science **46**, 505-553 (2001).

68. Jones, R. Some aspect of the hot corrosion of TBC. Thermal Barrier Coating Workshop, NASA, Lewis Research Centre **3312**, 217-233 (1995).

69. Miller, R.A. TBC for aircraft engines, History and Directions. Thermal Barrier Coating Workshop, NASA, Lewis Research Centre **3312**, 17-34 (1995).

70. Hass, D. D. Thermal barier coatings via direct vapor deposition. 2001. Virginia, University of Virginia.

71. Hass, D.D., Slifka, A.J., and Wadley, H.N.G. Low thermal conductivity vapour deposited zirconia microstructures. Acta Materialia **49**, 973-983 (2001).

72. Scott, M.G. Phase relationship in the Zirconia Yttria system. Journal of Materials Science **10**, 1527-1535 (1975).

73. Jaslier, Y. and Alperine, S. Electron beam physical vapour deposition TBCs: a comparative evaluation of competing deposition technologies. Proceedings of the 85th Meeting of the AGARD Structures and Materials Panel. 81-90. 98. Neuilly-sur-Seine, AGARD.

74. Beele, W., Marijnissen, G., and van Lieshout, A. The evolution of TBCs, status and upcoming solutions for today's key issues. Surface and Coatings Technology **120-121**, 61-67 (1999).

75. Brady, M.P., Gleeson, B., and Wright, I.G. Alloy designe strategies for promoting protective oxide-scale formation. JOM **52**, 16-21 (2000).

76. Ellingham, H.J.T. Reducibility of oxides and sulfides in metallurgical processes. Journal of the society of chemical industry, transactions and communications **63**, 125-133 (1944).

77. Wagner, C. Beitrag zur Theorie des Anlaufvorgangs. Z. Physikalische Chemie **21**, (1933).

78. Smialek, J.L. and Meier, G.H. High-Temperature Oxidation. In Simms, C.T., Stoloff, N.S., and Hagel, W.C. (eds.) Superalloys II - High Temperature Materials For Aerospace and Industrial Power. Wiley, Weineim (1987).

79. Grabke, H. J. Oxidation of Aluminides. Proceedings of the 4th International Symposium on High Temperature Corrosion and Protection of Materials. 1, 149-161. 97. Switzerland , Trans Tech Publications.

80. Grabke, H.J. and Schutze, M. Oxidation of Intermetallics. Wiley-VCH, Weinheim (1998).

81. Grabke, H.J. Oxidation of NiAl anf FeAl. Intermetallics **7**, 1153-1158 (1999).

82. Doychak, J., Smialek, J.L., and Mitchell, T.E. Transient oxidation of single crystal β. Metallurgical Transactions **20A**, 499-518 (1989).

83. Prasanna, K.M.N., Khanna, A.S., Chandra, R., and Quadakkers, J. Effect of θ-alumina formation on the growth kinetics of alumina forming superalloys. Oxidation of Metals **47**, 1-20.

84. Stott, F. H. The oxidation of alumina forming alloys. Streiff, R., Stringer, J., Krutenat, R. C., Caillet, M., and Rapp, R. A. Proceedings of the 4th International Symposium on High Temperature Corrosion and Protection of Materials. 1, 19-32. 97. Switzerland, Trans Tech Publications.

85. Kao, H.C. and Wei, W.C. kinetics and microstructural evolution of heterogeneous transformation of θ-Al_2O_3 and α-Al_2O_3. Journal of the American Ceramic Society **83**, 362-368 (2000).

86. Strauss, D. *et al.* Oxide scale growth on MCrAlY bond coatings after pulsed electron beam treatment and deposition of EBPVD-TBC. Surface and Coatings Technology **135**, 196-201 (2001).

87. Lau, H., Leyens, C., Schulz, U., and Friedrich, C. Influence of bondcoat pre-treatment and surface topology on the lifetime of EB-PVD TBCs. Surface and Coatings Technology **165**, 217-223 (2003).

88. Alibhai, A.A., Chater, R.J., McPhail, D.S., and Shollock, B.A. Use of isotopic tracers and SIMS analysis for evaluating the oxidation behaviour of protective coatings on nickel based superalloys. Applied Surface Science **203-204**, 630-633 (2003).

89. Garriga-Majo, D.P., Shollock, B.A., McPhail, D.S., Chater, R.J., and Walker, J.F. Novel

strategies for evaluating the degradation of protective coatings on superalloys. International journal of inorganic materials **1**, 325-336 (1999).

90. Haynes, J.A. , Lance, M.J., Pint, B.A., and Wright, I.G. Characterisation of commercial EB-PVD TBC systems with CVD (Ni,Pt)Al bond coatings. Surface and Coatings Technology **146-147**, 140-146 (2001).

91. Cadoret, Y. Effet du Platine et du Soufre sur l'Oxydation des Revetements Protecteurs beta-NiAl a Haute Temperature. Application aux Barrieres Thermiques. Ph.D. Thesis. 2005.

92. Zhang, Y. *et al.* Synthesis and cyclic oxidation behavior of a (Ni,Pt)Al coating on a desulfurized Ni-Base superalloy. Metallurgical and Materials Transactions **A(30)**, 2679-2687 (1999).

93. Haynes, J.A. Potential influences of bondcoat impurities and void growth on premature failure of EB-PVD TBCs. Scripta Materialia **44**, 1147-1152 (2001).

94. Kiely, J.D., Yeh, T., and Bonnell, D.A. Evidence for the segregation of sulphur to Ni-alumina interfaces. Surface sciences **393**, 126-130 (1997).

95. Smialek, J.L., Jayne, D.T., Schaeffer, J.C., and Murphy, W.H. Effect of hydrogen annealing, sulphur segregation and diffusion on the cyclic oxidation resistance of superalloys: a review. Thin Solid Films **235**, 285-292 (1994).

96. Grabke, H.J. , Wiemer, D., and Viefhaus, H.V. Segregation of sulphur during growth of oxide scales. Applied Surface Science **47**, 243-250 (1991).

97. Sarioglu, S. , Blachere, J. R., Pettit, F. S., Meier, G. H. , and Smialek, J. L. The effect of reactive element additions, sulphur removal, and specimen thickness on the oxidation behavior of alumina-forming Ni and Fe-base alloys. Proceedings of the 4th International Symposium on High Temperature Corrosion and Protection of Materials. 2, 405-412. 97. Switzerland, Trans Tech Publications.

98. Guerre, C., Molins, R., and Remy, L. Study of the coating stability of a TBC system. Materials at High Temperatures **17**, 197-203 (2000).

99. Bouhanek, K. *et al.* Isothermal and thermal cyclic oxidation behaviour of TBCs: Pt aluminide

bond coats. Materials at High Temperatures **17**, 185-196 (2000).

100. Vialas, N. Etude de la deterioration par oxydation haute temperature et interdiffusion de systemes revetement/superalliage ŕ base de nickel. prevision de durée de vie. 2004. PhD Thesis, INP Toulouse.

101. Chen, J.H. and Little, J.A. Degradation of the platinum aluminide coating on CMSX4 at 1100°C . Surface and Coatings Technology **92**, 69-77 (1997).

102. Meier, G.H. and Pettit, F.S. High temperature corrosion of alumina forming coatings for superalloys. Surface and Coatings Technology **39-40**, 1-17 (1989).

103. Tawancy, H.M., Abbas, N.M., and Rhys-Jones, T.N. Role of platinum in aluminide coatings. Surface and Coatings Technology **49**, 1-7 (1991).

104. Gleeson, B. , Wang, W., Hayashi, S., and Sordelet, D. Effects of Platinum on the Interdiffusion and Oxidation Behavior of Ni-Al-Based Alloys. Materials Science Forum. Proceedings of the 6th International Symposium on High Temperature Corrosion and Protection of Materials. 2004. Switzerland, Trans Tech Publications.

105. Felten, E.J. and Pettit, F.S. Development, growth and adhesion of Al2O3 on platinum-aluminium alloys. Oxidation of Metals **10**, 189-223 (1976).

106. De Witt, J.H.W. and Van Manen, P.A. The precious metal effect in high temperature corrosion. Materials Science Forum **154**, (1994).

107. Farrell, M.S., Boone, D.H., and Streiff, R. Oxide adhesion and growth characteristics on platinum-modified aluminide coatings. Surface and Coatings Technology **32**, 69-84 (1987).

108. Haynes, J.A., Pint, B.A., Porter, W.D., and Wright, I.G. Comparison of thermal expansion and oxidation behaviour of various high temperature coatings materials and superalloys. Materials at High Temperatures **21**, 87-94 (2004).

109. Fisher, G., Datta, P.K., Burnell-Gray, J.S., Chan, W.Y., and Soares, J.C. The effects of active element additions on the oxidation performance of a platinum aluminides coating at 1100°C. Surface and Coatings Technology **110**, 24-30 (1998).

110. Golightly, A., Stott, F.H., and Wood, G.C. The influence of Yttrium addition on the oxide scale adhesion to an iron chromium aluminium alloy. Oxidation of Metals **10**, 163-187 (1976).

111. Pint, B.A. *et al.* Substrate and bondcoat compositions: factors affecting alumina scale adhesion. Materials Science and Engineering A **245**, 201-211 (1998).

112. Pint, B.A. The oxidation behavior of oxide -dispersed ß-NiAl: I. Short term performance at 1200°C. Oxidation of metals **49**, 531-559 (1998).

113. Hou, P. Beyond sulphur effect. Oxidation of Metals **52**, 337-351 (1999).

114. Grabke, H.J., Kurbatov, G., and Schmutzler, H.J. Segregation beneath oxide scales. Oxidation of Metals **43**, 97-114 (1995).

115. Pint, B.A., Martin, J.R., and Hobbs, L.W. The oxidation mechanism of theta alumina scales. Solid state Ionics **78**, 99-107 (1995).

116. Tawancy, H.M., Abbas, N.M., and Bennet, A. Role of Y during high temperature oxidation of an MCrAlY coating on an Ni-base superalloy. **68-69**, 10-16 (1994).

117. Warnes, B.M. Reactive element modified chemical vapour deposition low activity platinum aluminides coatings. Surface and Coatings Technology **146-147**, 7-12 (2001).

118. Xiang, Z.D. and Datta, P.K. Conditions for pack coeposition of Al and Hf on nickel-base superalloys. Surface and Coatings Technology **179**, 95-102 (2004).

119. Pint, B.A. The role of chemical composition on the oxidation performance of aluminide coatings. Surface and Coatings Technology **188-189** , 71-78 (2004).

120. Zhang, Y., Pint, B.A., Haynes, J.A., and Wright, I.G. A platinum enriched gamma/gamma' two phase bondcoat on Ni based superalloys. Surface and Coatings Technology **200**, 1259-1263 (2005).

121. Tolpygo, V.K. and Clarke, D.R. Surface rumpling of a (Ni,Pt)Al bondcoat induced by cyclic oxidation. Acta Materialia **48**, 3283-3293 (2000).

122. Panat, R., Zhang, S., and Hsia, K.J. Bond coat surface rumpling in TBC. Acta Materialia **51**, 239-249 (2003).

123. Tolpygo, V.K. and Clarke, D.R. Rumpling induced by thermal cycling of an overlay coating: the effect of coating thickness. Acta Materialia **52**, 615-621 (2004).

124. Tolpygo, V.K. and Clarke, D.R. On the rumpling mechanism in nickel-aluminide coatings. Part I: an experimental assessment. Acta Materialia **52**, 5115-5127 (2004).

125. Tolpygo, V.K. and Clarke, D.R. On the rumpling mechanism in nickel-aluminide coatings. Part II: characterisation of surface undulations and bondcoat swelling. Acta Materialia **52**, 5129-5141 (2004).

126. Zhang, Y., Haynes, J.A., Pint, B.A., Wright, I.G., and Lee, W.Y. Martensitic transformation in CVD NiAl and (Ni,Pt)Al bond coatings. Surface and Coatings Technology **163/164**, 19-24 (2003).

127. Chen, M.W., Livi, K.J.T., Wright, P.K., and Hemker, K.J. Microstrucutural characterisation of a platinum-modified diffusion aluminide bond coat for TBC . Metallurgical and Materials Transactions **34A**, 2289-2299 (2003).

128. Pan, D., Chen, M.W., Wright, P.K., and Hemker, K.J. Evolution of a diffusion aluminide bond coat for thermal barier coatings during thermal cycling. Acta Materialia **51**, 2205-2217 (2003).

129. Kim, H.J. and Walter, M.E. Characterization of the degraded microstructures of a platinum aluminide coating. Materials Science and Engineering A **360**, 7-17 (2003).

130. Tolpygo, V.K., Clarke, D.R., and Murphy, K.S. The effect of grit blasting on the oxidation behavior of a platinum-modified nickel aluminide coating. Metallurgical and Materials Transactions **32A**, 1467-1478 (2001).

131. Warnes, B.M., Purvis, A.L., and Schilbe, J.E. The manufacture and fatigue cracking resistance of grit ree aluminide diffusion coatings. Surface and Coatings Technology **163-164**, 100-105 (2003).

132. Levi, C.G., Sommer, E., Terry, S.G., Catanoiu, A., and Ruhle, M. Alumina grown during

deposition of TBC on NiCrAlY. Journal of the American Ceramic Society **86**, 676-685 (2003).

133. Brickey, M.R. and Lee, J.L. Strucutural and chemical analyses of a thermally grown oxide scale in TBC containing a Pt-Ni-Al bondcoat. Oxidation of metals **54**, 237-254 (2000).

134. Murphy, K.S., More, K.L., and Lance, M.J. As-deposited mixed zone in thermally grown oxide beneath a TBC. Surface and Coatings Technology **146-147**, 152-161 (2001).

135. Laxman, S., Franke, B., Kempshall, B.W.S.Y.H., Giannuzzi, L.A., and Murphy, K.S. Phase transformations of TGO on (Ni,Pt)Al bondcoat during electron physical vapor deposition and subsequent oxidation. Surface and Coatings Technology **177-178**, 121-130 (2004).

136. Atkinson, A., Selcuk, A., and Webb, S.J. Variability of stress in alumina corrosion layers formed in thermal barrier coatings. Oxidation of metals **54**, 371-384 (2000).

137. Selcuk, A. and Atkinson, A. The evolution of residual stress in the TGO on Pt diffusion bon coats in TBCs. Acta Materialia **51**, 535-549 (2003).

138. Xie, L., Sohn, Y.H., Jordan, E.H., and Gell, M. The effect of bond coat grit blasting on the durability and TGO stress inan EB-PVD TBC. Surface and Coatings Technology **176**, 57-66 (2003).

139. He, M.Y., Evans, A.G., and Hutchinson, J.W. The ratcheting of compressed thermally grown thin films on ductile substrates. Acta Materialia **48**, 2593-2601 (2000).

140. Tolpygo, V.K. and Clarke, D.R. Wrinkling of alpha-alumina films grown by thermal oxidation - I. Quantitative studies on single crystals of Fe-Cr-Al. Acta Materialia **46**, 5153-5166 (1998).

141. Su, Y.J., Trice, R.W., Faber, K.T., Wang, H., and Porter, W.D. Thermal conductivity, phase stability and oxidation resistance of YAG and YSZ TBC's. Oxidation of Metals **61**, 253-271 (2004).

142. Lughi, V., Tolpygo, V.K., and Clarke, D.R. Microstructural aspects of the sintering of TBCs. Materials Science and Engineering A **368**, 212-221 (2004).

143. Sohn, Y.H., Lee, E.Y., Nagaraj, B.A., Biederman, R.R., and Sisson Jr, R.D. Microstrucutural

characterization of TBCs on high pressure turbine blades. Surface and Coatings Technology **146-147**, 132-139 (2001).

144. Hutchinson, R.G., Fleck, N.A., and Cocks, A.C.F. A sintering model for TBCs. Acta Materialia **54**, 1297-1306 (2006).

145. Zhao, X., Wang, X., and Xiao, P. Sintering and failure behaviour of AB-PVD thermal barrier coating after isothermal treatment. Surface and Coatings Technology **200**, 5946-5955 (2006).

146. Wang, X. and Xiao, P. Residual stresses and constrained sintering of YSZ/Al2O3 composite coatings. Acta Materialia **52**, 2591-2603 (2004).

147. Wellman, R.G. and Nicholls, J.R. Some observations on the erosion mechanism of EB-PVD TBC. Wear **242**, 89-96 (2000).

148. Wellman, R.G. and Nicholls, J.R. A mechanism for the erosion of EB-PVD TBCs. Materials Science Forum 531-538 (2001).

149. Schmitt-Thomas, Kh.G. and Hertter, M. Improved oxidation resistance of thermal barrier coatings. Surface and Coatings Technology **120-121**, 84-88 (1999).

150. Chen, X. Calcium-magnesium alumina silicate (CMAS) delamination mechanisms in EBPVD TBCs. Surface and Coatings Technology **200**, 3418-3427 (2006).

151. Mercer, C., Faulhaber, S., Evans, A.G., and Darolia, R. A delamination mechanism for thermal barrier coatings subject to calcium-magnesium-alumino-silicate (CMAS) infiltration. Acta Materialia **53**, 1029-1039 (2005).

152. Kraemer, S. , Yang, J.Y., Johnson, C.A., and Levi, C.G. Thermochemical interactions of thermal barrier coatings with molten CaO-MgO-Al2O3-SiO2 (CMAS) deposits. Journal of the American Ceramic Society **89**, 3167-3175 (2006).

153. Kimmel, J., Mutasim, Z., and Brentnall, W. Effect of alloy composition on the performance of yttria stabilized zirconia TBC. Journal of Engineering for Gas Turbines and Power **122**, 393-400 (2000).

154. Leyens, C., Schulz, U., Pint, B.A., and Wright, I.G. Influence of EB-PVD TBC

microstructure on TBC system performance under cyclic oxidation conditions. Surface and Coatings Technology **120-121**, (1999).

155. Tawancy, H.M., Mohamed, A.I., Abbas, N.M., and Rickerby, D.S. Effect of superalloy substrate composition on the performance of a TBC system. Journal of Materials Science **38**, 3797-3807 (2003).

156. Alperine, S., Steinmetz, P., Friant-Costantini, A., and Josso, P. Structure and high temperature performance of various palladium-modified aluminide coatings: a low cost alternative to platinum aluminides. Surface and Coatings Technology **43/44**, 347-358 (1990).

157. Li, M.J., Sun, X.F., Guan, H.R., Jiang, X.X., and Hu, Z.Q. Cyclic oxidation behavior of palladium-modified aluminide coating. Surface and Coatings Technology **167**, 106-111 (2003).

158. Rickerby, D. S., Bell, S. R., and Wing, R. G. Method of applying a TBC to a superalloy article and a TBC. Chromalloy UK and Rolls-Royce plc. 97.

159. Rickerby, D. S., Bell, S. R., and Wing, R. G. Method of applying a thermal barrier coating to a superalloy article and a thermal barrier coating . Chromalloy UK limited and Rolls-Royce plc. 95.

160. Ning, B. and Weaver, M.L. A preliminary study of DC magnetron sputtered NiAl-Hf coatings. Surface and Coatings Technology **177-178**, 113-120 (2004).

161. Ning, B., Shamsuzzoha, M., and Weaver, M.L. Microstructure and properties of DC magnetron sputtered NiAl-Hf coatings. Surface and Coatings Technology **179**, 201-209 (2004).

162. Naploszek-Bilnik, I., Budniok, A., and Lagiewka, E. Electrolytic production and heat-treatment of Ni-based composite layers containing intermetallic phases. Journal of Alloys and Compounds **382**, 54-60 (2004).

163. Nicholls, J.R., Simms, N.J., Chan, W.Y., and Evans, H.E. Smart overlay coatings - Concept and Practice. Surface and Coatings Technology **149**, 236-244 (2002).

164. Fritscher, K., Leyens, C., and Peters, M. Development of a low expansion bond coating for

Ni-base superalloys. Materials Science and Engineering A **190**, 253-258 (1995).

165. Ke, P.L. *et al.* Study on TBCs deposited by detonation gun spraying. Surface and Coatings Technology (*In Press*).

166. Wu, Y.N., Ke, P.L., Wang, Q.M., Sun, C., and Wang, F.H. High temperature properties of TBCs obtained by detonation spaying. Corrosion Science **46**, 2925-2935 (2004).

167. Cremer, R., Witthaut, M., Reichert, K., Schierling, M., and Neuschutz, D. Thermal stability of Al-O-N PVD diffusion barriers. Surface and Coatings Technology **108-109**, 48-58 (1998).

168. Muller, J. and Neuschutz, D. Efficiency of alpha alumina as diffusion barrier between bondcoat and bulk material of gas turbine blades. Vacuum **71**, 247-251 (2003).

169. Wu, F., Murakami, H., and Suzuki, A. Development of an iridium-tantalum modified aluminide coating as a diffusion barrier on nickel base single crystal superalloy TMS-75. Surface and Coatings Technology **168**, 62-69 (2003).

170. Haynes, J.A. *et al.* High temperature diffusion barriers for protective coatings. Surface and Coatings Technology **188-189**, 153-157 (2004).

171. Yoshida, D. , Shibata, Y., Hayashi, S., and Narita, T. Changes of an outer betaNiAl and inner alphaCr coating on Ni40Cr alloy during oxidation at 1373°K in air. Oxidation of metals **64**, 119-130 (2005).

172. Clarke, D.R. Materials selection guidelines for low thermal conductivity TBC. **163/134**, 67-74 (2003).

173. Matsumoto, M., Yamaguchi, N., and Matsubara, H. Low thermal conductivity and high temperature stability of ZrO2-Y2O3-La2O3 coatings paroduced by EB PVD. Scripta Materialia **50**, 867-871 (2004).

174. Saruhan, B. , Francois, P., Fritscher, K., and Schulz, U. EBPVD processing of pyrochlore-structured $La_2Zr_2O_7$ based TBCs. Surface and Coatings Technology **182**, 175-183 (2004).

175. Portinha, A. *et al.* Stabilisation of ZrO2 PVD coatings with Gd2O3. **188-189**, 107-115 (2004).

176. Madhwall, M., Jordan, E.H., and Gell, M. Failure mechanisms of dense vertically cracked TBCs. Materials Science and Engineering A **384** , 151-161 (2004).

177. Yang, Y.G., Hass, D.D., and Wadley, H.N.G. Porosity control in zig-zag vapour deposited films. Thin Solid Films **471**, 1-11 (2005).

178. Gu, S., Lu, T.J., Hass, D.D., and Wadley, H.N.G. Thermal conductivity of zirconia coatings with zig-zag microstructures. Acta Materialia **49**, 2539-2547 (2001).

179. Wolfe, D.E. , Singh, J., Miller, R.A., Eldridge, J.I., and Shu, D.M. Tailored microstructure of EB-PVD 8YSZ TBCs with low thermal conductivity and high themal reflectivity for turbine applications. Surface and Coatings Technology **190**, 132-149 (2005).

180. Tu, R., Kimura, T., and Goto, T. High speed deposition of YSZ by MOCVD. Surface and Coatings Technology **187**, 238-244 (2004).

181. Taylor, R.E., Wang, X., and Xu, X. Thermophysical properties of TBCs. Surface and Coatings Technology **120-121**, 89-95 (1999).

182. Feist, J.P. , Heyes, A.L., and Nicholls, J.R. Phosphor thermometry in an EB-PVD TBC doped with dysprosium. Proceedings of the Institution of Mechanical Engineers **215**, 333-341 (2001).

183. Anonymous. Phosphors light way to longer life. Modern Power System 40-41 (2003).

184. Gentleman, M.M. and Clarke, D.R. Concepts for luminescence sensing of thermal barrier coatings. Surface and Coatings Technology **188-189**, 93-100 (2004).

185. Spitsberg I.T. and Putyera, K. Depth profile and quantitative trace element analysisod diffusion aluminided type layers on Ni based superalloys using high resolution glow discharge mass spectroscopy. Surface and Coatings Technology **139**, 35-43 (2001).

186. Clarke, D.R., Christensen, R.J., and Tolpygo, V.K. The evolution of oxidation stresses in zirconia thermal barrier coated superalloy leading to spalling failure. Surface and Coatings Technology **94-95**, 89-93 (1997).

187. Tolpygo, V.K., Clarke, D.R., and Murphy, K.S. Evaluation of interface degradation during

cyclic oxidation of EB-PVD thermal barrier coatings and correlation with TGO luminescence. Surface and Coatings Technology **188-189**, 62-70 (2004).

188. Wen, M., Jordan, E.H., and Gell, M. Analysis of localized damage in EBPVD/(Ni,Pt)Al TBC. Surface and Coatings Technology **200**, 5193-5202 (2006).

189. Newaz, G. and Chen, X. Progressive damage assessment in TBCs using thermal wave imaging technique. Surface and Coatings Technology **190**, 7-14 (2005).

190. Ferber, M.K., Wereszczak, A.A., Lance, M., and Haynes, J.A. Application of infrared imaging to the study of controlled failure of TBCs. Journal of Materials Science **35**, 2643-2651 (2000).

191. Ogawa, K., Minkov, D., Shoji, T., Sato, M., and Hashimoto, H. NDE of degradation of TBC by means of impedance spectroscopy. NDT&E International **32**, 177-185 (1999).

192. Wu, N.Q., Ogawa, K., Chyu, M., and Mao, S.X. Failure detection of TBCs using impedance spectroscopy. Thin Solid Films **457**, 301-306 (2004).

193. Song, S.H. and Xiao, P. Relation of the microstructural and compositional features to the electrical properties in degraded TBC system. Journal of Materials Science **38**, 1661-1665 (2003).

194. Jayaraj, B. , Vishweswaraiah, S., Desai, V.H., and Sohn, Y.H. Electrochemical impedance spectroscopy of TBCs as a function of isothermal and cyclic exposure. Surface and Coatings Technology **177-178**, 140-151 (2004).

195. Kulkarni, A. *et al.* Advanced neutrin and Xray techniques for insights into the microstrucure of EB-PVD TBCs. Materials Science and Engineering A **426**, 43-52 (2006).

196. Monceau, D. and Poquillon, D. Continuous thermogravimetry under cyclic conditions. **61**, 143-163 (2004).

197. Ducros, C., Benevent, V., and Sanchette, F. Deposition, characterization and machining performance of multilayer PVD coatings on cemanted carbide cuting tools. Surface and Coatings Technology **163-164**, 681-688 (2003).

198. Schulz, U., Fritscher, K., and Leyens, C. `Two-source jumping beam evaporation for

advanced EB-PVD TBC systems. Surface and Coatings Technology **133-134**, 40-48 (2000).

199. Preauchat, B. and Drawin, S. Isothermal and cycling properties of zirconia-based TBC deposited by PECVD. Surface and Coatings Technology **146-147**, 94-101 (2001).

200. Movchan, B.A. and Yakovchuk. K.Yu. Graded TBC deposited by EB-PVD. Surface and Coatings Technology **188-189**, 85-92 (2004).

201. Hayashi, S. *et al.* alpha-NiPt(Al) and phase equilibria in the Ni-Al-Pt system at 1150°C. Acta Materialia **53**, 3319-3328 (2005).

202. Kamm, J.L. and Milligan, W.W. Phase stability in $(Ni,Pt)_3Al$ alloys. Scripta Metallurgica et Materialia **31**, 1461-1464 (1994).

203. Meininger, H. and Ellner, M. Phase transformation and the type of lattice distorsion os some platinum-rich phases belonging to the Cu family. Journal of Alloys and Compounds **353**, 207-212 (2003).

204. Larikov, L.N. Diffusion. In Westbrook, J.H. and Fleisher, R.L. (eds.) Intermetallic compounds, principles and practice. John Wiley and Sons,(1995).

205. Deakin, M. J. Surface coatings on titanium alloys to limit oxygen ingress. 95. Cranfield University.

206. Deakin, M. J. and Nicholls, J. R. Diffusion barrier layers - GB 9302978.3 -. 93.

207. Saint-Ramond, B. Low mass platinum aluminide bondcoat for thermal barrier coatings. 2001. M.Phil. Thesis Cranfield Universiy.

208. M. Silva. A new, low mass, bondcoat technology for TBC. 2005. Ph.D. Thesis Cranfied University.

209. Saint-Ramond, B, Carlin, M., Silva, M., and Nicholls, J. R. Low Mass Bondcoats for Robust TBCs. Materials Science Forum. Proceedings of the 6th International Symposium on High Temperature Corrosion and Protection of Materials. 2004. Switzerland, Trans Tech Publications.

210. Forwood, C.T. and Clarebrough, L.M. Electron microscopy of interfaces in metals and alloys. A. Hilger, Bristol, England (1991).

211. Keyse, R.J. Introduction to scanning transmission electron microscopy. Bios Scientific Publishers, Oxford (1998).

212. Thomas, G. Transmission electron microscopy of metals . Wiley, New York (1962).

213. Sauthoff, G. Intermetallics. VCH, Weinheim (1995).

214. Cullity, B.D. Elements of X-Ray diffraction. Addison-Wesley, Reading (1978).

215. CaRIne Crystallography. Boudias, C. and Monceau, D. 97. Divergent SA. 89-97.

216. Huang, C., Yamabe-Mitarai, Y., and Harada, H. the stabilization of Pt3Al phase with L12 structure in Pt-Al-Ir-Nb and Pt-Al-Nb alloys. Journal of Alloys and Compounds **366**, 217-221 (2004).

217. Oramus, P. *et al.* Dynamics of atomic ordering in intermetallics. Materials Science and Engineering A **365**, 166-171 (2004).

218. Skomski, R., Kashyap, A., and Zhou, J. Atomic and micromagnetic aspects of L10 magnetism. Scripta Materialia **53**, 389-394 (2005).

219. Nastasi, M., Hung, L.S., and Mayer, J.W. Phase formation by ion beam mixing in Ni/Al, Pd/Al and Pt/Al bilayers. Applied Physic letters **43**, (1983).

220. Colgan, E.G., Li, C.Y., and Mayer, J.W. Interfacial reaction induced morphological instabilities in thin Al/Pt and Al/Pd films. Journal of Materials Research **2**, (1987).

221. Zhao, X.A., Ma, E., Yang, H.Y., and Nicolet, M.A. Study of the initial aluminide phase growth in Al/Pt couples. Thin Solid Films **153**, (1987).

222. Colgan, E.G. A review of thin film aluminide formation. Materials Science Reports **5**, (1980).